SYNTHESIS AND APPLICATIONS OF HIGH-SPIN IRON TETRA-AZAMACROCYCLIC COMPLEXES

by

SAMANTHA BREWER OCHOA

Associate of Arts, 2008
Tarrant County Community College
Fort Worth, Texas

Bachelor of Science, 2012
University of North Texas
Denton, Texas

Submitted to the Graduate Faculty of the
College of Science and Engineering
Texas Christian University
in partial fulfillment of the requirements
for the degree of

Doctor of Philosophy

August 2018

SYNTHESIS AND APPLICATIONS OF HIGH-SPIN IRON TETRA-AZAMACROCYCLIC COMPLEXES

by

Samantha Brewer Ochoa

Dissertation approved:

Kayla Green
Major Professor

For The College of Science and Engineering

Acknowledgements

It takes a village. -*Anonymous*

The above quote summarizes my graduate career. The completion of this journey would not have been possible without my advisor Kayla Green, our collaborators, Brad Pierce and Tim Hubin, my committee Dr. Coffer, Dr. Janesko, and Dr. Neilson, my fellow graduate students, my husband, my parents, and funding from the College of Science and Engineering at TCU.

Dr. Green, words cannot convey my gratitude. I thank God daily for the events that led me to join your lab. Thank you for the countless hours you have invested in my personal and professional development. It is no small feat to guide a graduate student through the preparation and delivery of a forty-five-minute literature seminar. Especially, when that student has never read a single scientific paper or presented for more than twelve-minutes. You have molded me into a professional who is organized, attentive, and knowledgeable. Not to mention the impact you have had on my writing…need I say anymore? Thank you, for your patience and hard work.

To my committee, thank you for the time and feedback you have given on my progress report, proposal, and this dissertation. Dr. Coffer, thank you for sharing the sacred knowledge, and the occasional "go-get'em" gesture in the hallway. It's the little things that encouraging. Dr. Janesko, thank you for teaching the computational course for experimentalist. I am by no means expert, but I am able to understand and perform simple computational studies. Dr. Nielson, although I never attended one of your courses, tutoring your general chemistry students increased my knowledge and has provided future course materials.

Anne do you remember? "Everyone is having a life, and all I have is grad school."-me, 2015? Thank you for traveling with me and supporting me through this journey called graduate school. Thank you for all the talks and all the times you played devil's advocate. Your friendship and willingness to

allow me to be a part of your life has greatly enriched mine. I will always be impressed by the way you navigate the most difficult of circumstances. Watching you and Dr. Green gives me hope that one day, I too, will be able to balance family and work. I know you will find your next journey in life soon. One question, when did we become grown-ups?

Hannah, wow. I do not know what my graduate career would look like without you in it. I might still be trying to figure out how to make the ligands. OK, that might be an exaggeration. Really, thank you for all the help along the way, both emotional and academic. Your positive attitude, love of science, and easy-going nature has held me together. I can't wait to see what your future holds.

Marianne, I have been impressed by you since the day you joined the lab. You have taught me many things: organization, the usefulness of literature, and how to find my voice. Knowing you has made me a better scientist and a stronger person. I have no doubt that you will thrive in whatever life holds for you. Thank you for all the encouraging words and problem-solving sessions.

Paulina, although we only worked together for a limited time, you were a pillar that got me through my first year in the program. Thank you. However, I could have done without Henry's glove balloons.

Akop, thank you for the crash course in column chromatography and all the synthetic suggestions. You, Charles, and Adam have taught me so much; I am eternally grateful.

To all the students I had the privilege of working with, thank you. Teaching you was a high-light of graduate school. It is very true that the student teaches the teacher. I would like to especially thank Magy Mekhail, Trang Nguyen, Jack Parker, and Tim Schwartz who not only furthered my scientific progress, but each in their own way provided a breath of fresh air. Travis Hayden, Ryan Itoh, Nhan Pham, Matthew Canipe, Lara Turan, and Hunter Scarborough it was a pleasure to learn beside you.

To my husband, Charles. Thank you for loving me and understanding the numerous sacrifices we made throughout graduate school. Thank you for always challenging me, even when it hurt, or I didn't want to hear it. You enrich my life daily. I am so grateful for all the scientific talks and the encouragement to just relax.

Mom, thank you for always believing in me, and telling me that I could do anything. Growing up watching you work so hard to better our lives has been a continues motivation. You instilled in me the desire to work as harder and achieve my goals no matter how many obstacles arose.

Dad and Sue thank you for all the emotional support along the years. I hope Charles and I can provide the love and values to our family that you have provided to me.

Bobby, thank you for always being there when I needed you. I have thoroughly enjoyed our lunches, building projects, and jam sessions.

Table of Contents

List of Figures

List of Appendix Figures

List of Tables

List of Appendix Tables

List of Schemes

Chapter 1. Introduction

1.1 Approaches and challenges in the development of iron-catalyzed reactions

There is a growing interest in replacing palladium with iron, as iron is more abundant and less expensive.[1-2] Studies employing iron catalysts are making strong contributions to the field of cross-coupling reactions.[1-18] Due to the strong reactivity of iron complexes, unpaired electrons complicating NMR spectroscopy, and transient nature of the iron-containing intermediate species,[1-2, 12-16] mechanistic insights and thorough catalyst characterizations are much more challenging than the palladium counterparts. Two distinct approaches have been employed for the development of new iron-catalyzed processes. The first approach concentrates on optimizing the catalyst,[19-20] and the second focuses on optimizing the substrates and reaction conditions. [10, 21-22]

1.2 Mononuclear iron-containing metalloenzymes

Iron-containing enzymes exist in many forms, including, monomeric heme, non-heme and diiron heme, non-heme complexes.[23-27] These iron-based enzymes are capable of both oxidative and reductive chemistry. The study of metalloenzymes is intertwined with the fundamental study of synthetic iron complexes. For example, the structures of iron-catalysts are often designed based on the binding motifs found in enzymes. The increased simplicity and control over the properties of synthetic iron complexes compared to iron-containing enzymes has been used to identify and isolate the active species in many systems.[28-30] Such work has resulted in the identification and characterize of several active iron species (Fe(III)OOH, Fe(IV)=O, or Fe(V)=O) as key players in both oxidative iron catalysis and enzymatic reactions.[17, 29, 31]

1.2.1 Hemoglobin and cytochrome P450

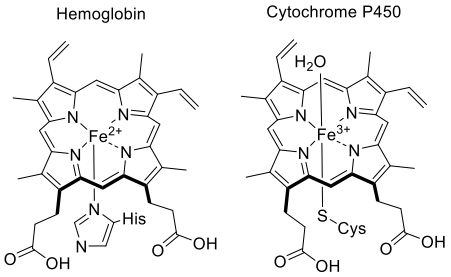

Figure 1.1. *Active site of hemoglobin and cytochrome P450.*

Tetra-azamacrocycles are cyclic organic molecules that contain four nitrogen atoms, which typically serve as coordinate covalent donors to metal ions. The most classic examples of such molecules are the naturally-occurring porphyrins. Porphyrins are known to bind iron in the 2+ and 3+ oxidation state. Iron-containing porphyrins represent a class of molecules known as hemes and are active sites of many enzymes. Figure 1.1 shows the active site of hemoglobin and cytochrome P450. In hemoglobin the axial site is filled with a histidine residue; the histidine can tune the reactivity of the iron center to facilitate the reversible coordination to dioxygen. The resulting hemoglobin-dioxygen adduct does not afford chemical transformations, which contrasts with cytochrome P450. The axial site in cytochrome P450 is occupied by a cysteine residue that facilitates the formation of high-valent iron species.[32] Cytochrome P450 catalyzes several organic transformations such as hydroxylation, epoxidation, oxidative cyclization, and C-C coupling.[33-34] The cytochrome P450 enzyme has been thoroughly studied and a rebound mechanism has been proposed for the hydroxylation of alkanes (Scheme 1.1).[33] In the resting state, the enzyme contains a ferric ion and metal bound water molecule. The substrate enters the protein and binds close to the iron-active site. Although the substrate does not bind to the iron center, it displaces the water molecule resulting in a five-coordinate iron. The iron can then accept an electron from NADPH and bind dioxygen. Through a series of electron transfers and protonation events several active species form, specifically, an iron(III) peroxo (compound 0), Iron(V) oxo (compound I), iron(IV) hydroxyl (compound II), and an organic radical (Scheme 1.1). The iron(III) peroxo has been

shown to catalyzes epoxidation and C-C coupling reactions, and the iron(V) oxo species has been implicated as the active catalyst in hydroxylation reactions.[33] The iron(IV) hydroxyl is capable of hydrogen atom abstraction as well as desaturation of alkanes.[33] The organic radical can participate in radical rearrangements resulting in C-C bond formation.[33] For a more comprehensive review of the reactivity and mechanistic explanation for the reactions described above the reader should refer to the recently published review by Guengerich and Yoshimoto.[33]

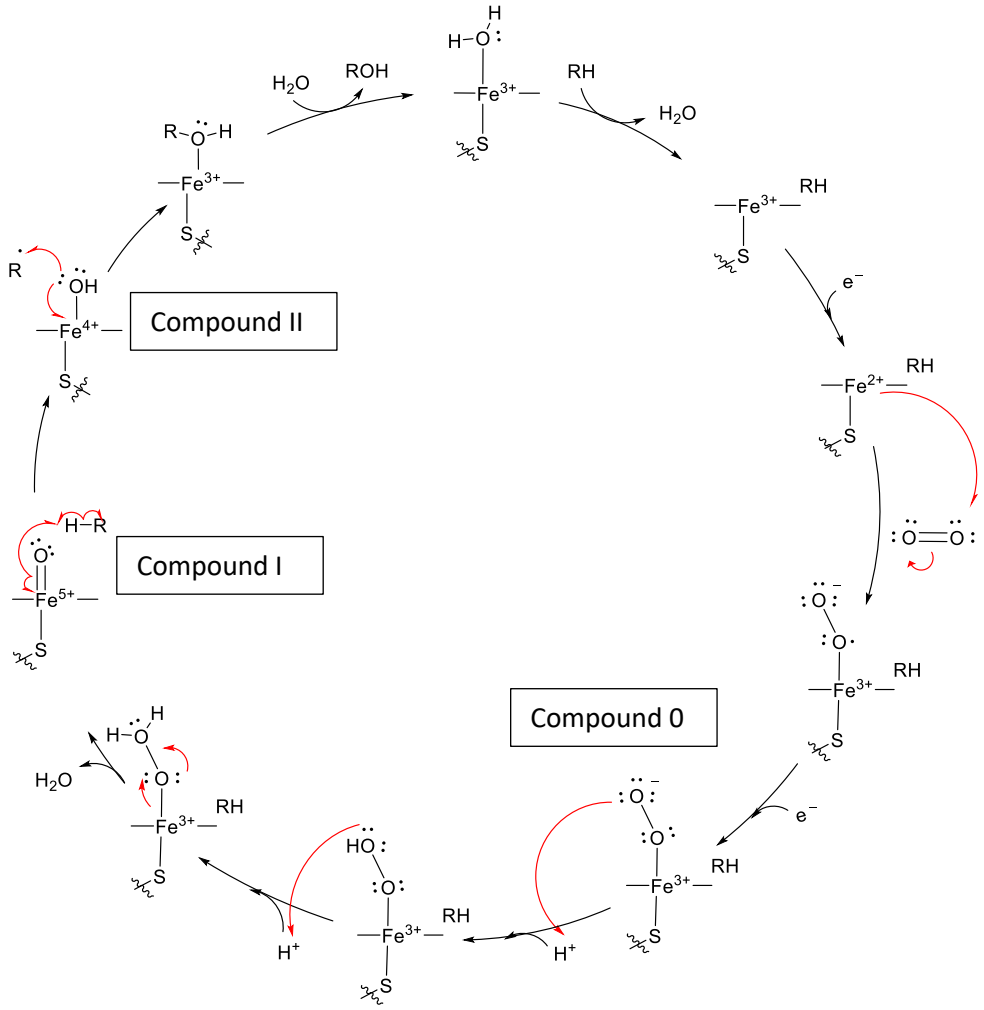

Scheme 1.1. *Proposed mechanism for the hydroxylation of alkanes by cytochrome P450.*

1.2.2 Diiron containing enzymes

Nature also uses dimeric iron species to facilitate a wide range of chemical reactions such as those shown in Figure 1.2.[24] The enzymes that catalyze each process are located over the reaction arrow in blue text. Mechanistic investigations of diiron enzymes have implicated a range of pathways through which diiron enzymes activate oxygen (Scheme 1.2). To date, three active species have been identified: a mixed valent $Fe(III)O_2/Fe(II)$, μ-O_2 diferric, and μ-O diiron(IV). The catalytic mechanisms shown in Schemes 1.1 and 1.2 illustrate the complexity of iron-based enzymes. The intricacy of these processes stem from the ability of iron complexes to form multiple species and activate dioxygen by more than one pathway.[24] The identification of the active iron species in enzymes has led to the development of synthetic iron complexes designed to harness the reactivity described here.

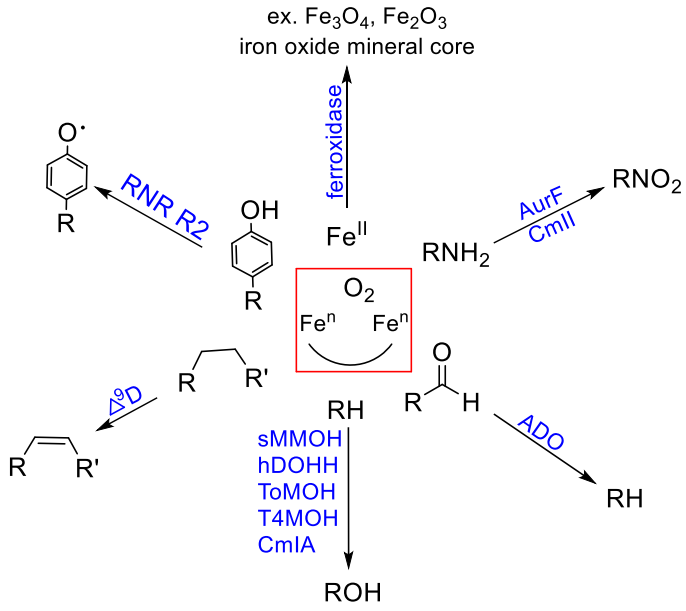

Figure 1.2. *Chemical transformation performed by various diiron enzymes. Modified from the recent review, reference 24. The pre-catalyst is indicated by a red box, and the enzymes which afford the specific transformation are shown in blue.*

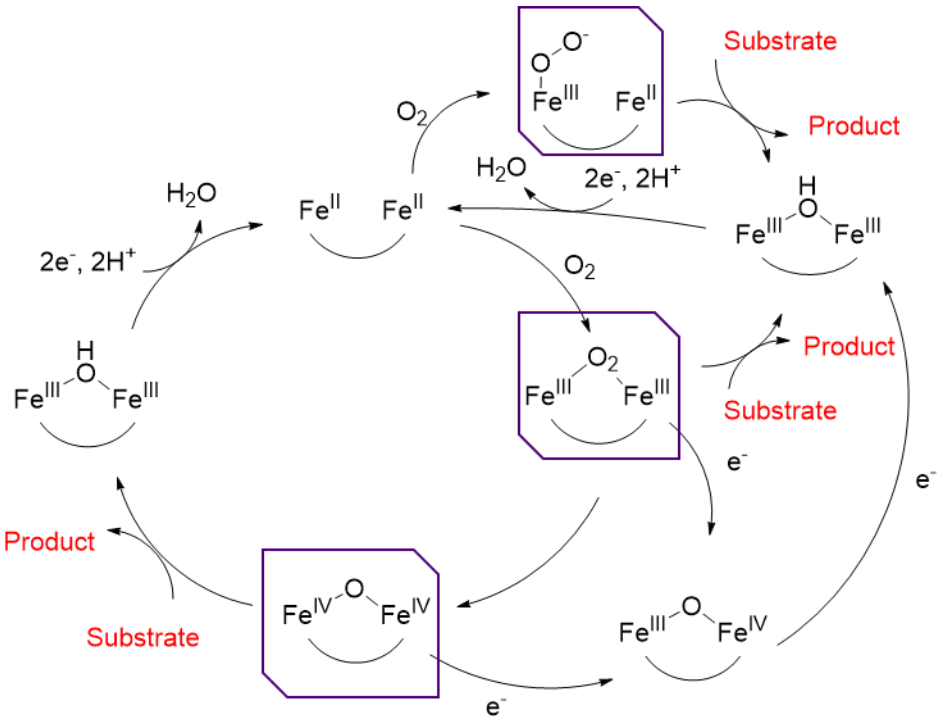

Scheme 1.2. *Possible oxygen activation pathways of diiron enzymes. Modified from the recent review, reference 24. The active iron species are indicated by a purple box.*

1.3 Tetra-azamacrocyclic complexes

Synthetic tetra-azamacrocycles were initially developed to determine how the cyclic nature of porphyrin ligands effect the metal center in biological systems.[35] This could not be determined using the natural systems because porphyrins are not only cyclic, but contain an extended π-system and two anionic nitrogen donors. These three properties lead to complex ligand-metal interactions that cannot be separated from the interactions due solely to the effect of a cyclic ligand scaffold. However, saturated tetra-azamacrocycles containing secondary amines (Figure 1.3) exhibited a more straightforward metal-ligand bonding, due to presence of only σ-donating ligands and a lack of steric bulk. The use of the synthetic macrocycles allowed investigations which determined the effect of cyclic chelates, such as porphyrins, on metal centers.[35]

The first two synthetic non-porphyrin tetra-azamacrocyclic complexes were reported in 1965 by Bosnich and co-workers (**[*trans*-Ni^{2+}Cyclam$(Cl)_2$]** and **[*trans*-Co^{3+}Cyclam$(Cl)_2]^+$**).[36] By 1979 saturated macrocyclic ligands with varying ring sizes (12-16 membered) had been synthesized.[35, 37-38] The macrocyclic complexes were shown to be more thermodynamically and kinetically stable than the open chain counter-parts.[39-40] Furthermore, varying the ring size, rigidity, and charge of the macrocycle were shown to tune the properties of the metal complexes in predictable ways.[35] Specifically, decreasing the size of the macrocyclic core increased ligand field strength. The tuning power of macrocyclic ligands illustrated that the reactivity of hemoglobin and cytochrome P450 can, in part, be attributed to the complexation of iron to the porphyrin ligand.

1.3.1 Speciation of iron-containing tetra-azamacrocycles

The ligand effects described above are based on investigations performed on the *trans* isomers of the 13- to 16-membered macrocyclic nickel and cobalt complexes.[35] The iron(II) complexes of the 13- to 16-membered tetra-azamacrocycles were first published in 1976 by Watkins Jr. and co-workers.[37] In this later series, three spin-states of the iron(II) complexes were identified as S = 1/2, 0, 2. The different spin-states obtained were attributed to the effect of ring size on ligand field strength, decreased size leads to increased ligand field strength of the macrocycle. All ring sizes afforded monomeric *trans* isomers; however, a *cis*-isomer was observed in the presence of a 15-membered macrocycle.[37] The ability to modulate spin-state by varying the size of the macrocyclic ring speaks to the tunability of tetra-macrocycles. Like porphyrins, the macrocyclic cavity of the 14-membered cyclam (Figure 1.3) is large enough to fully encapsulate a ferric or ferrous ion as observed in heme containing enzymes.[37] Porphyrins (16-membered macrocycles) are very rigid ligand scaffolds due to the presence of an extended π-system; therefore, these species only form *trans*- iron complexes. However, due to the saturated nature of the ring, cyclam is not as rigid as the porphyrins. The flexibility and ability of the ligand to fully encapsulate the iron center allows for the formation of both *trans* and *cis* isomers (Figure 1.4). The spin-

state of the iron center has been shown to differ between these species. The complex ***cis*-[Fe^{3+}Cyclam$(N_3)_2$]$^+$** contains a ferric iron in the high-spin state (S = 5/2). When the *cis*-complex is heated to 50 °C, a low-spin (S= ½) complex, ***trans*-[Fe^{3+}Cyclam$(N_3)_2$]$^+$**, is formed.[41] Reduction in the size of the macrocycle from 14- to 12-membered results in a macrocyclic cavity too small to fully engulf the iron center. Therefore, only *cis*-isomers form, independent of the temperature at which the complex is synthesized. Like the *cis*-cyclam complexes, **[Fe^{3+}Cyclen$(Cl)_2$]$^+$** contains a high-spin iron center. Although the use of cyclen prevents the formation of the *trans-*species, it does not result in the formation of only one type of iron complex. The monomeric complexes of cyclen-based ligands readily form μ-oxodiiron species such as **[μ-O(Fe^{3+}LCl$)_2$]$^{2+}$** shown in Figure 1.3.[42]

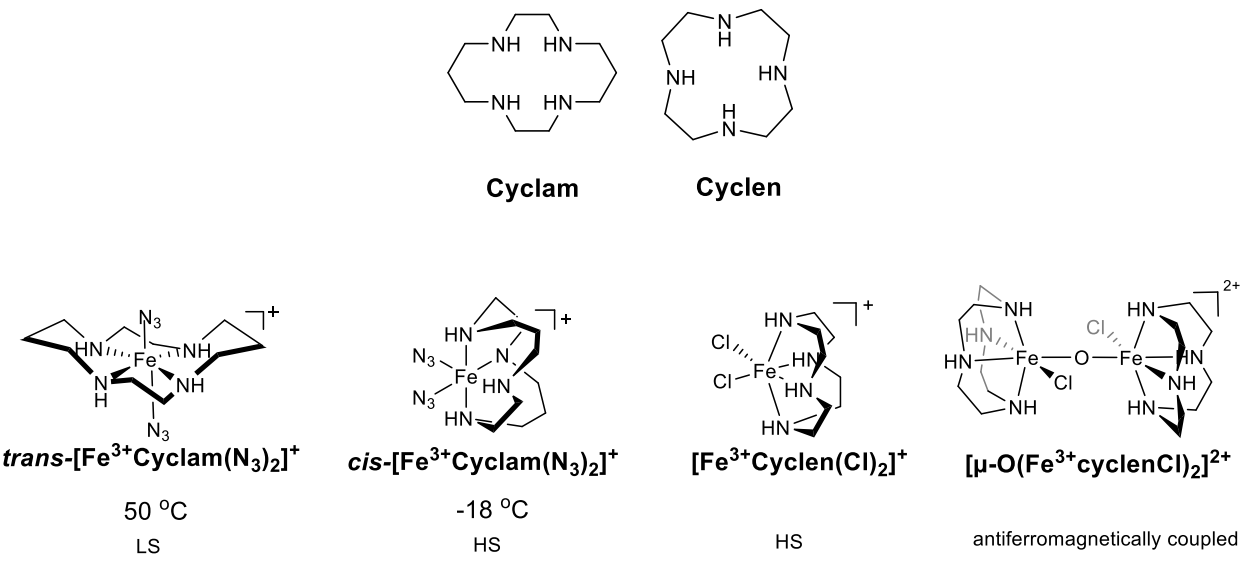

Figure 1.3. *(Top) Structure of cyclen and cyclam. (Bottom) Possible species that may form upon complexation of iron with cyclam- and cyclen-based ligands.*

1.3.2 Oxidative reactivity of iron-containing tetra-azamacrocycles

As stated above, tetra-azamacrocycles were developed to gain insight into the metal-based properties of iron-containing enzymes.[35] Amine-containing macrocycles and open chain iron complexes

that harness the oxidative reactivity of natural systems have become an important part of bioinorganic chemistry. Several review articles which outline the structure, reactivity, and active iron species of these synthetic complexes have been reported, providing invaluable spectroscopic comparisons to metalloenzymes in nature.[5, 20, 23, 28-29, 43-46]

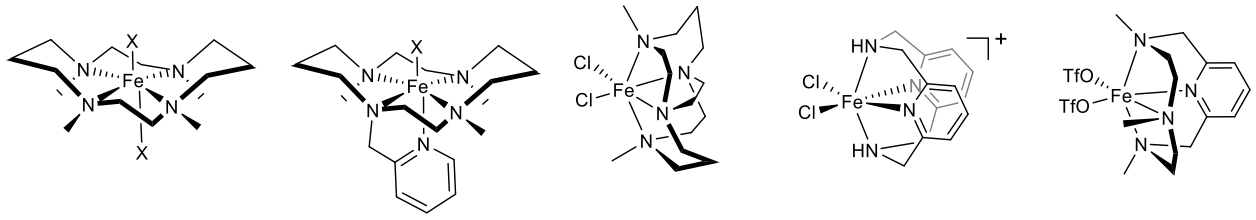

Figure 1.4. *Tetra-azamacrocyclic iron complexes that catalyze oxidation of organic substrates.*

Figures 1.3 and 1.4 show examples of tetra-azamacrocyclic complexes that have been tested as catalysts for the oxidation of organic substrates. Table 1.1 lists the reactions tested for each complex shown in Figures 1.3 and 1.4, along with the oxidants used. The iron(III)-cyclen complex catalyzes water oxidation in the presence of $[Ru(bpy)_3]Cl_2$,[47] and ***cis*-$[Fe^{3+}Cyclam(OTf)_2]^+$** catalyzes electrochemical water oxidation.[23] The *trans* isomer, ***trans*-$[Fe^{3+}Cyclam(OTf)_2]^+$**, was not tested for use in water oxidation, as it has shown that water oxidation is only catalyzed by complexes with labile *cis*-sites.[23] Instead, ***trans*-$[Fe^{3+}Cyclam(OTf)_2]^+$** was shown to catalyze the epoxidation of alkenes.[48] The methylated derivative **$[Fe^{2+}TMC(OTf)_2]$** was also investigated for the ability to functionalize olefins and perform water oxidation, however, no catalytic activity of this kind was observed.[23, 49] Although **$[Fe^{2+}TMC(OTf)_2]$** did not show catalytic activity like the cyclam derivatives, it proved to stabilize high-valent iron-oxo species allowing for the first single-crystal XRD analysis of an iron(IV)=O complex (**$[Fe^{4+}TMC(O)CH_3CN)]^{2+}$**).[50-52] Since this report, **$[Fe^{3+}TMC\text{-}O_2]^+$**, **$[Fe^{3+}TMC\text{-}(OH)]^{2+}$** and **$[Fe^{3+}TMC\text{-}OOH]^{2+}$** have also been synthesized.[53-54] The **$[Fe^{3+}TMC\text{-}(OH)]^{2+}$** species is capable of oxidizing TEMPOH.[54]

Table 1.1. *Reactivity of complexes in Figure 1.3 and 1.4.*

Catalyst	Reaction	Oxidant	No Reaction
$[Fe^{3+}Cyclen(Cl)_2]^+$	Water oxidation[47]	$[Ru(bpy)_3]Cl_2$	
***trans*-$[Fe^{2+}Cyclam]^{2+}$**	Alkene epoxidation[48]	H_2O_2	cis-hydroxylation[48]
***cis*-$[Fe^{3+}Cyclam(OTf)_2]^+$**	water oxidation[23]	Electrochemical	
$[Fe^{2+}TMC(X)_2]$	Aldehyde deformylation[51]	O_2	Epoxidation/cis-hydroxylation[49]
			water oxidation[23]
$[Fe^{3+}TMC\text{-}py(OH)]^{2+}$	Oxidation of TEMPOH[54]	-	
$[Fe^{2+}L8(Cl)_2]$	Epoxidation and cis-hydroxylation of alkene[49]	H_2O_2	Kumada type C-C coupling[15]
$[Fe^{3+}L8(Cl)_2]^+$	water oxidation[55]	$NaIO_4$	
	oxidation of alcohols[55]	$NaIO_4$	
$[Fe^{3+}LN_4H_2(Cl)_2]^+$	Epoxidation of cyclooctene[56]	Oxone	
$[Fe^{3+}LN_4Me_2(Cl)_2]^+$	Water oxidation[57]	*CAN or Oxone	
	Cis-hydroxylation of cyclooctene[56]	Oxone	
	Intradiol cleavage[58]	O_2	
$[Fe^{2+}L4(OTf)_2]$	Oxidation of alkenes[17-18]	peracetic acid	

*CAN ($[NH_4]_2[Ce^{4+}(NO_3)_6$)

The compound **L8** represents a class of ligands that contain an ethylene cross-bridge. These ligands are designed to prevent the formation of μ-oxodiiron species and guarantee iron complexes with two *cis*-labile ligands. The ferrous and ferric complexes of **L8** have also been synthesized. The ferrous complex catalyzes epoxidation and *cis*-hydroxylation of alkenes,[49] while the ferric complex catalyzes the oxidation of water and alcohols.[55] The incorporation of one or two pyridine rings into 12-membered macrocyclic ligands has also been accomplished, resulting in ligands **LN_4H_2**, **LN_4Me_2**, and **L4**.[18, 59-61] Iron complexes of each have been studied. The epoxidation of cyclooctene can be catalyzed by **$[Fe^{3+}LN_4H_2(Cl)_2]^+$** in the presence of oxone,[56] while the methylated congener **$[Fe^{3+}LN_4Me_2(Cl)_2]^+$** will catalyzes the *cis*-hydroxylation of cyclooctene opposed to the epoxidations chemistry demonstrated with the LN_4H_2 congener.[56] **$[Fe^{3+}LN_4Me_2(Cl)_2]^+$** also catalyzes water oxidation and intradiol cleavage, making it the most versatile ligand in this series, to date.[57] Lastly, **$[Fe^{2+}L4(OTf)_2]$** facilitates the oxidation of alkenes.[17-18] The active catalytic species in each of these reactions has been identified as either an

Fe(III)OOH, Fe(IV)=O, or Fe(V)=O species. In all cases, these species have been spectroscopically characterized. For example, the oxidation catalyst **[Fe^{2+}L4$(OTf)_2$]** has been shown to form an iron(V)=O, which has been characterized by EPR spectroscopy and exhibits three signals consistent with a S = ½ species.[18]

1.4 C-C coupling reactions

Carbon-carbon cross-coupling reactions catalyzed by transition metals are invaluable components in a chemist's toolbox.[16] Palladium is the most common metal used to facilitate these transformations despite the low availability and cost of the precious metal.[1-2, 12-16] Several types of palladium-catalyzed coupling reactions have been developed including Suzuki-Miyaura and Kumada.[62-63] Typical palladium-catalyzed C-C coupling reactions require a palladium source, aryl halide, and an electron deficient substrate. In Suzuki-Miyaura reactions the electron deficient substrate is a boronic acid or ester. In contrast, the Kumada reactions the electron deficient substrate is Grignard reagent. The majority of palladium catalyzed reactions are thought to follow the mechanism shown in Scheme 1.3. The first step of the mechanism is oxidative addition of an aryl halide to the Pd(0). The $ArPd^{2+}X$ species reacts with the electron deficient substrate via transmetalation to produce $ArPd^{2+}R$. The formation of a C-C bond occurs through a reductive elimination step, thus regenerating the catalyst.

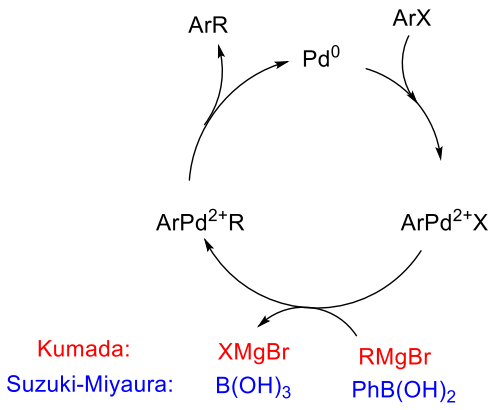

Scheme 1.3. *Accepted mechanism of palladium-catalyzed coupling reactions.*

1.4.1 Iron-catalyzed Kumada-type C-C coupling reactions

The complex **$[Fe^{2+}L8(Cl)_2]$** has also been tested for the ability to catalyze Kumada type C-C coupling reactions, however, under the conditions tested no catalysis was observed.[15] Iron-catalyzed Kumada type C-C coupling reactions are proposed to produce low-valent iron(I) species rather than the high-valent species proposed in oxidative chemistry. This low-valent iron(I) species has also been characterized by EPR spectroscopy and identified as a S = ½ species.[64] Therefore, a mechanism like Pd-catalyzed C-C coupling has been proposed and is shown in Scheme 1.4.

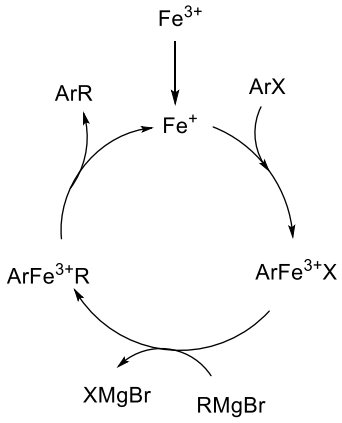

Scheme 1.4. *Proposed mechanism for iron-catalyzed Kumada-type C-C coupling.*

1.4.2 Iron-catalyzed Suzuki-Miyaura-type C-C coupling reactions

The studies that investigate other iron-catalysts for C-C bond formation focus largely on the scope of the catalysts and less on the properties of the active metal center or catalyst itself. Suzuki-Miyaura C-C coupling reactions facilitated by iron have been pioneered by Hu and co-workers.[3, 65] Tetra-azamacrocycles and iron(II) salts were shown to catalyze the coupling of pyrrole and phenylboronic acid only in the presence of oxygen.[19] In a preliminary mechanistic investigation, an iron-oxo species was proposed as the active catalyst. Initial attempts to characterize the active iron species *in-situ* were inconclusive. The only other mechanistic study performed on iron-catalyzed direct Suzuki-Miyaura coupling that employed tetra-azamacrocyclic ligands was performed by Dong *et al.* Using mass spectrometry and computational methods the authors purposed a catalytic cycle in which the active catalyst is an iron(III)-oxo species.[3] The two catalytic mechanisms proposed for iron-catalyzed Suzuki-Miyaura-type C-C coupling reactions are shown in Scheme 1.5.

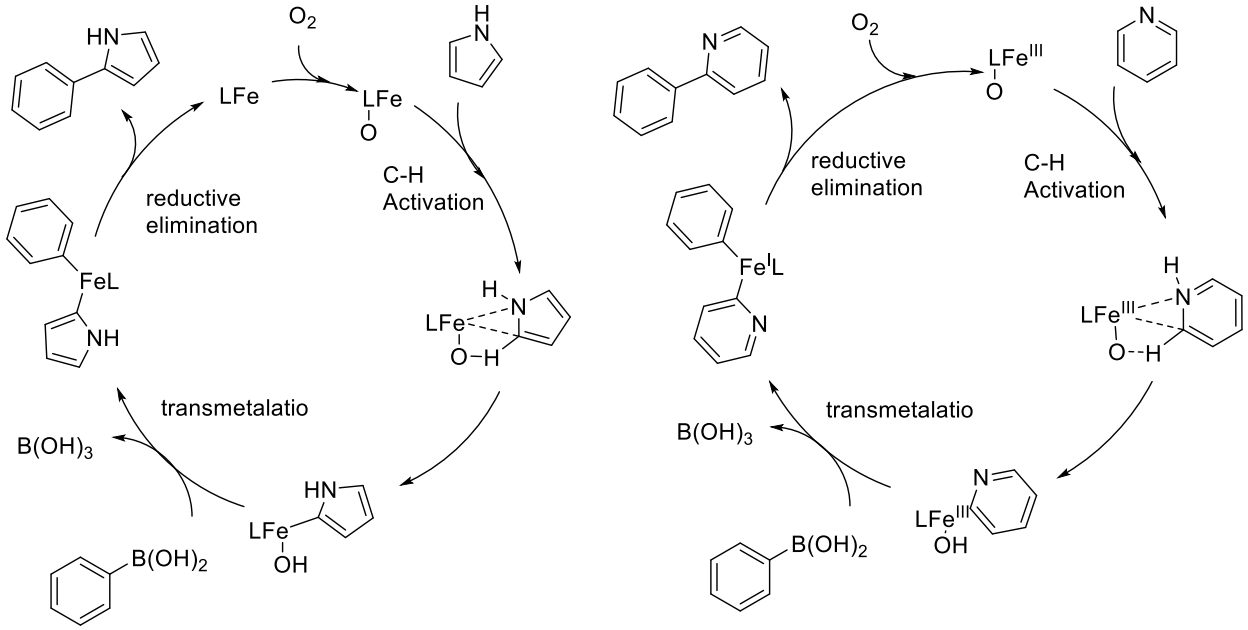

Scheme 1.5. *Proposed mechanism for iron-catalyzed Suzuki-Miyaura-type C-C coupling, (left) mechanism purposed by Wen et al. and (right) mechanism purposed by Dong et al.*[3, 19]

Although not explicitly stated in the main text, Wen *et al.* suggested an iron(IV)-oxo species performs the C-H activation step.[19] Dong *et al.* suggested an iron(III)-oxo species performs the C-H activation.[3] The two mechanisms are similar yet conflicting. Both mechanism resemble the palladium catalyzed process consisting of three-steps, C-H activation, transmetalation, and reductive elimination. However, the mechanisms differ in the assignment of the oxidation state of the iron center throughout the catalytic cycle.

Several mechanistic questions remain. Specifically, the identity of the iron complex throughout the catalytic cycle, the ability of the ligand to enhance catalytic yields, the role of the sacrificial oxidant, the participation of a radical, and the presence of off-cycle species. Therefore, in this dissertation several iron complexes were investigated as catalysts in the coupling of pyrrole and phenylboronic acid. The oxidation state and spin state of the iron complexes were characterized using X-ray crystallography, UV-vis absorbance spectroscopy, electron paramagnetic resonance spectroscopy, cyclic voltammetry, and mass spectrometry. Characterization of the iron complexes and subsequent catalytic testing were used to obtain a more detailed understanding of the catalytic mechanism. Furthermore, the results indicated that the iron(III) complexes are essential for catalytic and regioselective production of the 2-phenylpyrrole product.

Chapters 2-4 will focus on the investigations into the iron-catalyzed C-C coupling of pyrrole and phenylboronic acid. Chapter 2 describes the synthesis, characterization, and catalytic application of three high-spin iron complexes. Chapter 3 compares a library of eight iron complexes with tetra-azamacrocyclic ligands to determine the ligand properties that promote catalytic activity. In Chapter 4, a series of studies were conducted to expand the mechanistic understanding of iron-catalyzed Suzuki-Miyaura C-C coupling reactions facilitated by macrocyclic supported complexes.

1.5 MRI contrast agents

Gadolinium agents shorten the longitudinal and transverse relaxation times of bulk water protons, thus increasing signal intensity in T_1-weighted images.[66] Although gadolinium agents give good resolution, they are unable to respond to environmental factors that could give information related to disease states. In contrast, chemical exchange saturation transfer (CEST) agents can be sensitive to changes in the environment.[67] CEST agents must have exchangeable protons, for example -NH, -OH, or water. To produce a CEST image, these protons are spin saturated by the application of a specific radio-frequency pulse in the presence of a magnetic field. When the condition $K_{eq} \leq \Delta\omega$ (K_{eq} is the water exchange rate, $\Delta\omega$ is the frequency separation between the bulk water resonance and the resonance of the exchangeable proton) is satisfied, the exchange of irradiated protons with bulk water protons results in MRI images with increased contrast. Put simply, when $\Delta\omega$ is small the water exchange rate must be slow; increasing $\Delta\omega$ allows for protons with faster exchange rate to produce a CEST spectrum.[67] The $\Delta\omega$ may be increased by the presence of paramagnetic metal ions, which shifts the resonance of the exchangeable proton out of the diamagnetic NMR spectrum range. CEST is a versatile approach as it can be turned on or off by using or not using pre-saturation pulse. The effectiveness of CEST agents are tied to the water exchange process. The water exchange process is defined as the interchange of bulk water with the water molecule(s) covalently interacting with the metal center. In Ln^{3+} complexes the water exchange rate must be slow to intermediate. The Eu^{3+} ion has a co-ordination number of 8-9 (in equilibrium) and the slowest water exchange rate of the lanthanides.[67] The Eu^{3+} species is the lanthanide of choice for PARACEST applications to date because it has the slowest water exchange rate and low paramagnetic relaxation enhancement.[67] In contrast to Eu^{3+} systems, iron-complexes typically have a coordination number of 6, but 7- and 8- coordinate iron complexes have also been reported. Due to the lower coordination number of iron compared to europium complexes, iron-based CEST agents are not affected by the water exchange rate. Instead, exchange rate of -OH or -NH protons are responsible for

CEST behavior. Due to the fast relaxivity of water and protons that are in proximity to the iron(III) ions, only iron(II) complexes result in viable CEST agents. In 2011 Morrow and co-workers reported the first iron-based contrast agents.[68] Since this time, a range of agents containing 9-, 12-, 14-, and 15-membered macrocycles have also been reported. The next section details the PARACEST behavior of several transition metal complexes containing macrocyclic ligands.

1.5.1 Advances in transition-metal PARACEST agents

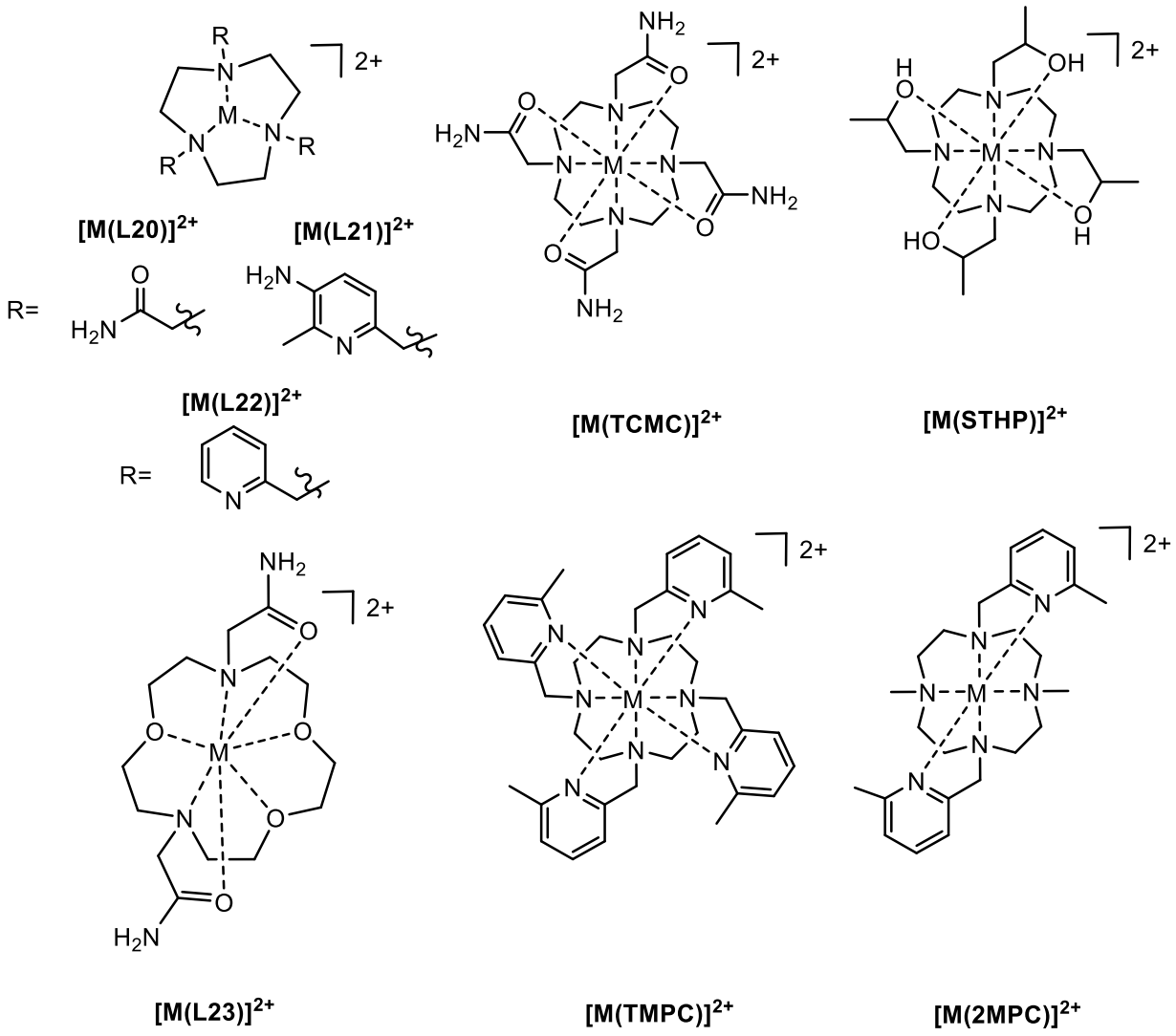

Figure 1.5. *Macrocyclic transition metal complexes synthesized and test by Morrow and co-workers as CEST agents.*[68-73]

The first transition-metal based PARACEST agents reported were the iron(II) complexes of **L20**, **L21**, and **L22**.[68] Each ligand stabilized the 2+ oxidation of the iron center, even in the presence of air. The ligands were designed to be 6-coordinate and contained a 9-membered tri-azamacrocycle (TACN) with varying pendant arms (Figure 1.5; **L20** (amide pendant arms), **L21** (5-amino-6-methyl-2-pyridyl), **L22** (2-pyridyl). At a pH of 7 the PARACEST signal varied greatly among the series. Complexes **[Fe(L20)]$^{2+}$**and **[Fe(L21)]$^{2+}$** exhibited signals at 69 ppm and 6 ppm downfield of bulk water, respectively. However, complex **[Fe(L22)]$^{2+}$** did not afford a CEST signal, most likely due to the lack of exchangeable protons or a water molecule. The following year, Morrow and co-workers studied the iron(II) complexes of **TCMC** and ***s*-THP**.[69] **TCMC** and ***s*-THP** contain a 12-membered tetra-azamacrocycle, but differ in the identity of pendent arms. **TCMC** (also referred to as **DOTAM** throughout literature) contains 4 pendant amide arms and ***s*-THP** contains four pendant hydroxypropyl arms (Figure 1.5). The iron complexes exhibit CEST signals at 50 ppm (**[Fe(TCMC)]$^{2+}$**) and 54 ppm (**[Fe(*s*-THP)]$^{2+}$**) downfield of bulk water. The CEST signal of these complexes were pH dependent between pH 6 and 8. The pH dependence was studied because identification of pH *in-vivo* may allow differentiation between malignant tumors and benign growths.[69] The iron complexes showed great stability even in the presence of Zn(II), Cu(II), carbonate, phosphate, and NaCl.[70] Furthermore, *in-vitro* studies concluded that the complexes should be non-toxic as redox cycling was not observed in presence of ascorbate/oxygen or ascorbate/H_2O_2. The three studies mentioned above were summarized in a perspective and a microreview published in 2012.[71-72] In 2014, the iron(II), cobalt(II), and nickel(II) complexes of **L23** were synthesized. The ligand **L23** is a 15-membered macrocycle containing 2 nitrogen and 3 oxygen donors and is functionalized with 2 pendant amide arms (Figure 1.5).[73] The iron complex, **[Fe(L23)]$^{2+}$**, was determined to be 7-coordinate and adopt a pentagonal bipyramidal geometry; the complex afforded a CEST signal at 92 ppm downfield of bulk water. In 2014, Harris and co-workers reported two spin-crossover iron(II) complexes for use as PARACEST MRI thermometers as the determination of tissue temperature has many medical

applications.[74] Both complexes studied showed CEST signals that had linear temperature dependence of 0.23(1) ppm/^{o}C (**[Fe(3-bpp)$_2$]$^{2+}$**) and 1.02(1) ppm/^{o}C (**[(Me$_2$NPY$_5$Me$_2$)Fe(H$_2$O)]$^{2+}$**), for the high-spin species. Although the complexes exhibited a temperature-dependent CEST signals, they suffered from low stability, due to the use of open -chain ligands. Following the report by Harris, Morrow and co-workers reported a more stable complex, **[Co(TCMC)]$^{2+}$**, with a linear temperature-dependence of -0.66 ppm/^{o}C.[75] Overall, Morrow's work has shown that amine functionalized pyridine-, amide-, and isopropyl-containing macrocyclic complexes result in iron(II) and Co(II) complexes that produce CEST spectra sensitive to pH and temperature, and may function as sensory contrast agents.[75]

Given our extensive experience in the synthesis and characterization of iron macrocyclic complexes, alternative applications for daughter complexes of **L1**, **L2**, and **L3** were explored. Chapter 5 consists of the synthesis and application of several pentadentate ligands for use as iron-based contrast agents. The preliminary studies are presented to establish a foundation for future synthetic methods in the Green Research Group, which will potentially lead to the production of responsive, theranostic, and non-toxic europium- and iron-based PARACEST agents.

Chapter 2. Isolation and identification of the pre-catalyst in iron-catalyzed direct arylation of pyrrole with phenylboronic acid

2.1 Introduction

In 2010, Wen *et al*. reported that the tetra-azamacrocycles (**cyclen**, **L1**. **LN_4H_2** and **Me_4cyclen**) shown in Figure 2.1, when mixed with iron(II) salts in the presence of oxygen, facilitate direct arylation of pyrrole with phenylboronic acid to form 2-phenylpyrrole.[19] A preliminary mechanism was proposed in which an iron-oxo species acts as the active catalyst; however, no metal oxidation states were assigned or catalyst characterization reported, aside from a mass spectrum that proved to be tenuous in its assignment. Since the release of this publication, it has been cited over 70 times [3, 6, 11, 21-22, 76-140] To date the synthesis and characterization of iron complexes of **LN_4H_2** and **cyclen** have been reported (Figure 2.2). [44, 47, 141-142] Both complexes **$[(LN_4H_2)Fe(Cl)_2]^+$** and **$[(cyclen)Fe(Cl)_2]^+$** were identified as high-spin iron(III) systems. Of the four mixtures tested for catalytic ability by Wen and co-workers, the mixture containing **L1** afforded the highest yield. Therefore, and reported here, we identified the spin-state and oxidation state of the complex formed by **L1** and iron(II) in the presence of oxygen and compared the structural and electronic properties to **$[(LN_4H_2)Fe(Cl)_2]^+$**, **$[(cyclen)Fe(Cl)_2]^+$**, and other iron(III) complexes. We have previously explored **L1** and its derivatives (**L2** and **L3**, Figure 2.3) as chelates for Cu(II), Ni(II), and Zn(II); the donor capacity of the ligand was affected by the presence and position of the hydroxyl group.[143] In this chapter, the iron complexes of **L1**, **L2,** and **L3** were also isolated, characterized, and compared within the series. The *bona-fide* iron(III) high-spin complexes derived from **L1**, **L2**, and **L3** were identified as pre-catalysts for *direct* Suzuki-Miyaura coupling of pyrrole and phenylboronic acid to yield 2-phenylpyrrole. A pre-catalyst is a species which, *in-situ*, undergoes further derivatization resulting in an active catalytic species. In nature, the pre-catalyst is often referred to as the resting state of an enzyme. Finally, further experiments suggested that **L2** and **L3** can promote a small amount of background reactivity yielding multiple products. However, the iron(III) pre-catalysts are critical for

focusing the reactivity to produce only 2-phenylpyrrole, thus validating the need for the intact iron complex as the catalyst. The goal of this chapter is to demonstrate that **$[Fe^{3+}L1(Cl)_2]^+$**, **$[Fe^{3+}L1(Cl)_2]^+$**, and **$[Fe^{3+}L3(Cl)_2]^+$** are capable of coupling pyrrole and phenylboronic acid, and that the coupling does not occur when an iron salt or tetra-azamacrocycle are used independently.

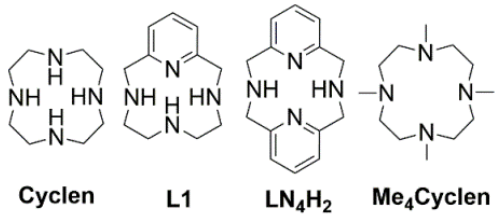

Figure 2.1. *Tetra-azamacrocycles studied by Wen* et al. *in combination with iron(II) salts to facilitate the coupling of pyrrole and phenylboronic acid to produce 2-phenylpyrrole.*[19]

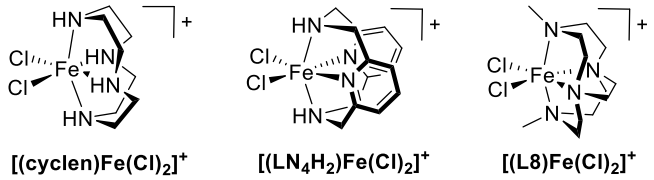

Figure 2.2. *Iron(III) complexes derived from* ***cyclen***, ***LN_4H_2***, *and* ***L8***.

2.2 Results and discussion

2.2.1 Synthesis and characterization

The corresponding iron complexes of **L1**-**L3**, shown in Figure 2.3, were synthesized in water at pH ~5 to compensate for the protonation of the isolated ligands. An iron(II) salt was used in metalation of **L1**-**L3** and was oxidized in air to iron(III) prior to isolation of the **$[Fe^{3+}L1(Cl)_2]^+$** -**$[Fe^{3+}L3(Cl)_2]^+$** complexes. The iron(II) perchlorate salt was exploited to facilitate the growth of X-ray quality crystals, discussed below. Attempts to form complex using $Fe(ClO_4)_3$ did not afford product in water. The presence and position of the hydroxyl group on the aromatic ring of the ligand affected the metalation efficiency and solubility of the resulting complexes;

therefore, divergent synthetic strategies were developed for each complex produced. For example, mixtures of CH_3CN/Et_2O or DMF/Et_2O were used to isolate metal complexes **$[Fe^{3+}L1(Cl)_2]^+$** (62% yield) and **L3Fe** (63% yield), respectively, as solids precipitates. **L2Fe** was easily isolated as a precipitate from the aqueous reaction mixture, albeit with a low yield (30%). Nevertheless, the resulting ferric complexes of **L1-L3** were stable to both air and light and can be stored indefinitely once isolated as dark red (**$[Fe^{3+}L3(Cl)_2]^+$**) or light brown (**$[Fe^{3+}L1(Cl)_2]^+$**, **$[Fe^{3+}L2(Cl)_2]^+$**) solids.

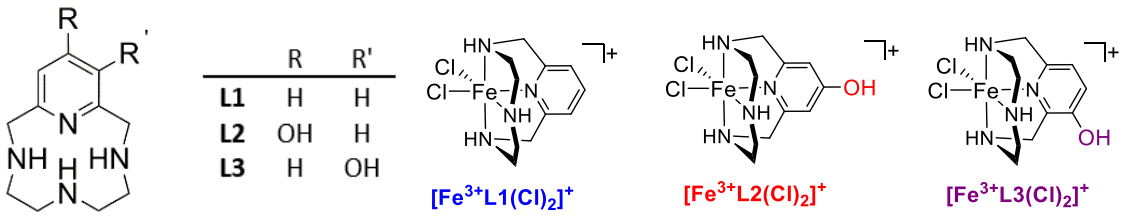

***Figure 2.3**. Chemical structure of ligands **L1-L3** (**L1** = 1,4,7,10-tetra-aza-2,6-pyridinophane, [35, 144] **L2** = 1,4,7,10-tetra-aza-2,6-pyridinophane-14-ol, [145] **L3** = 1,4,7,10-tetra-aza-2,6-pyridinophane-13-ol).[143] Pictorial representation of **$[Fe^{3+}L1(Cl)_2]^+$**, **$[Fe^{3+}L2(Cl)_2]^+$**, and **$[Fe^{3+}L3(Cl)_2]^+$**.*

2.2.2 X-ray crystallography

Figure 2.4 shows the results of single crystal diffraction analysis on crystalline solids of **$[Fe^{3+}L1(Cl)_2]^+$**, **$[Fe^{3+}L2(Cl)_2]^+$**, and **$[Fe^{3+}L3(Cl)_2]^+$**. Yellow, X-ray quality crystals of **$[Fe^{3+}L1(Cl)_2]^+$** were obtained through vapor diffusion of diethyl ether into a solution of DMF; yellow **$[Fe^{3+}L2(Cl)_2]^+$** and brown **$[Fe^{3+}L3(Cl)_2]^+$** crystalline materials were isolated by slow evaporation of aqueous solutions. Table A 1 contains the crystal data, intensity collections, and structure refinement parameters; a full list of bond lengths and angles are also located in the supporting information. Analysis of the structures determined through X-ray diffraction experiments showed that each complex adopts a six coordinate, distorted octahedral geometry (N(2)-Fe-N(4), ~85°; N(1)-Fe-N(3), ~147°). The coordination sphere consists of four nitrogen donors from the ligand set and two chloride ions.

Each complex adopts a *cis*-folded geometry due to the rigidity of the 12-membered ligand set, in which one chloride is *cis* and the other is *trans* to the pyridol ring.[16] This finding is consistent with previous structure determination of **$[Fe^{3+}L1(Cl)_2]BF_4$**, reported by Alcock *et al*.[146] The charge of the **$[Fe^{3+}Lx(Cl)_2]^+$** systems are balanced by one perchlorate counter ion. The position of the hydroxyl group and the flexibility of the aliphatic portion of the ligand results in an enantiomeric mixture of **$[Fe^{3+}L3(Cl)_2]^+$**. The hydroxyl group was modeled for disorder to account for both enantiomers, as shown in Figure 2.4c.

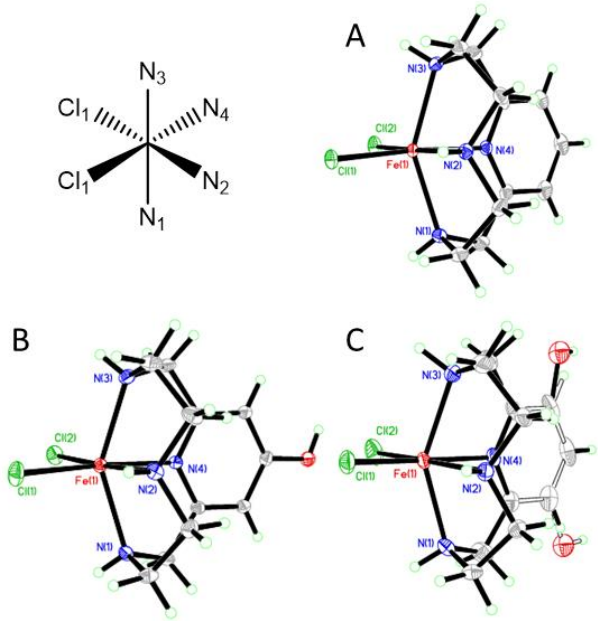

Figure 2.4. *ORTEP (50%) representations of* **$[Fe^{3+}L1(Cl)_2]^+$** *(A),* **$[Fe^{3+}L2(Cl)_2]^+$** *(B), and* **$[Fe^{3+}L3(Cl)_2]^+$** *(C). The perchlorate anion has been omitted for clarity; modelling of disorder for* **$[Fe^{3+}L3(Cl)_2]^+$** *is shown in grey. All complexes take on a* cis*-folded distorted octahedral geometry. The Fe-N bond lengths are greater than 2.0 Å, consistent with other high-spin ferric systems.*[44, 142, 147]

The geometry of complexes **$[Fe^{3+}L1(Cl)_2]^+$** - **$[Fe^{3+}L3(Cl)_2]^+$** can be compared to other macrocycles in the literature. For example, N(1)-Fe-N(3) bond angles have been reported for two 12-membered macrocycles (Figure 2.1), **$[(LN_4H_2)Fe(Cl)_2]^+$** (142.41°) and **$[(LN_4Me_2)Fe(Cl)_2]^+$** (146.55°), where the latter complex provides the closest bond angle to the **$[Fe^{3+}L1(Cl)_2]^+$**-**$[Fe^{3+}L3(Cl)_2]^+$** systems.[56, 142, 148] The **$[Fe^{3+}L2(Cl)_2]^+$** complex provides slightly longer Fe-N bonds

compared to **[Fe^{3+}L1(Cl)$_2$]$^+$** and **[Fe^{3+}L3(Cl)$_2$]$^+$**. For example, the Fe-N(2) bond of **[Fe^{3+}L2(Cl)$_2$]$^+$** was determined to be 2.2023(10) Å, while **[Fe^{3+}L1(Cl)$_2$]$^+$** and **[Fe^{3+}L3(Cl)$_2$]$^+$** were slightly shorter with 2.2001(6) and 2.181(2) Å, respectively. The only exception was observed with the Fe-N(4) bond, which was slightly shorter in **[Fe^{3+}L2(Cl)$_2$]$^+$** (2.0967(10) Å) compared to **[Fe^{3+}L1(Cl)$_2$]$^+$** (2.1074(5) Å) and **[Fe^{3+}L3(Cl)$_2$]$^+$** (2.107(2) Å). The difference in the equatorial Fe-N(4) pyridine-derived bond length is consistent with a stronger interaction between the pyridol nitrogen of **L2** vs. **L1** and **L3**. Throughout the series, the equatorial Fe-N(2) (pyridine atom) bond is the longest and thus the weakest Fe-N interaction. The Fe-N bond lengths of **[Fe^{3+}L1(Cl)$_2$]$^+$**- **[Fe^{3+}L3(Cl)$_2$]$^+$** are greater than 2.00 Å (Tables 2.1-2.2 and Figure 2.4) and are consistent with iron(III) high-spin systems.[149] For example, the iron center of **[(LN$_4$Me$_2$)Fe(Cl)$_2$]$^+$** was assigned as a high-spin iron(III) by EPR, and the Fe-N bond lengths within the high-spin complex were measured as 2.128 and 2.221 Å.[148, 150] Altogether, the results indicate that ligands **L1**-**L3** stabilize the high-spin iron(III) in similar manner and that **L2** is a slightly stronger σ-donor to iron(III) compared to **L1** and **L3**. However, the differences in bond lengths and angles within **[Fe^{3+}L1(Cl)$_2$]$^+$**- **[Fe^{3+}L3(Cl)$_2$]$^+$** are much smaller than the nickel(II), copper(II), and zinc(II) congeners of **L1**-**L3**.[143]

Table 2.1. Selected bond lengths and angles of complexes **[Fe^{3+}L1(Cl)$_2$]$^+$** - **[Fe^{3+}L3(Cl)$_2$]$^+$**.

Bond Length (Å)	**[Fe^{3+}L1(Cl)$_2$]$^+$**	**[Fe^{3+}L2(Cl)$_2$]$^+$**	**[Fe^{3+}L3(Cl)$_2$]$^+$**
Fe(1)-N(1)	2.1641(6)	2.1787(11)	2.162(2)
Fe(1)-N(2)	2.2001(6)	2.2023(10)	2.181(2)
Fe(1)-N(3)	2.1676(6)	2.1812(11)	2.172(2)
Fe(1)-N(4)	2.1074(5)	2.0970(10)	2.107(2)
Bond Angle (°)			
N(1)-Fe(1)-N(3)	147.25(2)	146.70(4)	147.17(8)
N(2)-Fe(1)-N(4)	85.56(2)	85.47(4)	85.72(8)

2.2.3 Mass spectrometry

Mass spectrometry further confirmed the oxidation state of the iron(III) in **$[Fe^{3+}L1(Cl)_2]^+$**-**$[Fe^{3+}L3(Cl)_2]^+$**. The mass spectrum obtained for **$[Fe^{3+}L1(Cl)_2]^+$** consisted of three isotopic envelopes that correspond to the complex: 260.1519 m/z = $[L1Fe(III)\text{-}2H^+]^+$, 296.1358 m/z = $[L1Fe(III)Cl^-\text{-}H^+]^+$, and 322.1209 m/z = $[L1Fe(III)2Cl^-]^+$ (Figure A 4). Similar fragmentation patterns were obtained for complexes **$[Fe^{3+}L2(Cl)_2]^+$** and **$[Fe^{3+}L3(Cl)_2]^+$** and are detailed in experimental methods related to each complex. Mass spectrometry analysis of the coupling reaction performed by Wen *et al.* revealed three isotopic envelopes: m/z = 207.1532, 353.1956, and 369.1956.[19] The isotopic envelopes were assigned as $[L1]^+$, $[L1 + Fe + C_2O_4]^+$, and $[L1 + Fe + C_2O_4 + O]^+$, respectively, with no indication of iron oxidation states or charge balance. The isotopic envelope observed at m/z = 207.1532 indeed corresponds to the singly protonated free ligand $[L1 + H^+]^+$, which we observe as well with studies of free ligand **L1**. However, the assignment of m/z = 353.1965 as $[L1 + Fe + C_2O_4]^+$ is incorrect, as the exact mass the expected species is modeled to have m/z = 350.0672, three mass units less than the observed ion reported. Similarly, the assignment of m/z = 369.1897 as $[L1 + Fe + C_2O_4 + O]^+$ (Theoretical m/z = 366.0621) as a component of the catalytic reaction does not correlate as well. Therefore, the results reported herein serve as the first validation of the composition and oxidation state of the pre-catalyst involved in the C-C coupling of pyrrole and phenylboronic acid.

2.2.4 Spin-state determination

The spin and oxidation states of complexes **$[Fe^{3+}L1(Cl)_2]^+$** - **$[Fe^{3+}L3(Cl)_2]^+$** were also validated at low temperature via electron paramagnetic resonance (EPR) spectroscopy. As shown in Figure 2.5 (*left)*, the EPR spectra (*solid lines*) for all complexes (**$[Fe^{3+}L1(Cl)_2]^+$** - **$[Fe^{3+}L1(Cl)_2]^+$**) exhibit features typical of high-spin ferric iron (S = 5/2). For analytical purposes, all data were recorded under non-saturating microwave power. The simulations overlaid on each spectrum (*dashed lines*) consist of contributions from two separate doublets. As indicated by the energy diagram

shown in Figure 2.5 (*right*), the dominant transition for these complexes arises from the ground m_s = ± 1/2 doublet of a S = 5/2 spin state with near axial symmetry (E/D = 0.07). Transitions within this doublet yield the observed g-values of 7.6, 4.3, and 1.7. The linewidth of this transition can be reasonably simulated by assuming a Gaussian distribution in rhombicity (E/D) [designated $\sigma_{E/D}$], which broadens the g ~ 1.7 resonance significantly. The lower intensity features observed at g ~ 5.8 and 1.97 are nearly absent at low temperature (4 K) but reach a maximal intensity near ~8 K before decreasing again as temperature approaches 20 K. The alternating temperature dependence of these features confirm that this signal must originate from the middle m_s = ± 3/2 doublet of the S = 5/2 spin state. The magnitude of the zero-field splitting parameter ($|D|$ = 0.7 ± 0.2 cm^{-1}) was determined by plotting the EPR signal intensity of the m_s = ± 1/2 doublet versus 1/T and fitting the data to a Boltzmann population distribution for a 3-level system. Additional corroboration of the axial zero-field splitting term was obtained by simultaneous simulation of EPR spectra collected at temperatures ranging from 4 to 20 K (n = 5). Within this temperature regime, all simulations accurately reproduce the relative intensity for each transition (± 1/2 and ± 3/2 m_s-states) using a D-value of 0.7 ± 0.2 cm^{-1}. Within error, all complexes (**$[Fe^{3+}L1(Cl)_2]^+$** - **$[Fe^{3+}L3(Cl)_2]^+$**) exhibited equivalent temperature dependence and thus all EPR simulations shown in Figure 2.5 utilized the same axial zero field splitting term. Indeed, except for minor perturbations in the extent of E/D-distribution ($\sigma_{E/D}$), all complexes **$[Fe^{3+}L1(Cl)_2]^+$** - **$[Fe^{3+}L3(Cl)_2]^+$** exhibit nearly equivalent EPR spectroscopic properties. The near equivalent of EPR spectra observed for these complexes is understandable given the close agreement in Fe-coordination sphere bond length and coordination geometry observed crystallographically (Table 2.1).

Table 2.2. *Comparison of spin-state and bond lengths within iron(III) complexes derived from 12-membered tetra-azamacrocyclic ligands.*[11,12]

Complex	Spin State	Fe-N4 (Å)	Fe-N2 (Å)	N1-Fe-N3 (°)	Ref.
[(cyclen)Fe(Cl)$_2$]Cl	5/2	-	2.1461(16)	146.40(6)	44
[(LN$_4$H$_2$)Fe(Cl)$_2$]Cl	*	2.094(1)	2.189(1)	142.41(7)	56, 142, 148
[(L8)Fe(Cl)$_2$]PF$_6$	5/2	-	2.163 (2)	153.20	147
[Fe^{3+}L1(Cl)$_2$]ClO$_4$	5/2	2.1074(5)	2.2001(6)	147.25(2)	This work
[Fe^{3+}L2(Cl)$_2$]ClO$_4$	5/2	2.0967(10)	2.2023(10)	146.71(4)	This work
[Fe^{3+}L3(Cl)$_2$]ClO$_4$	5/2	2.107(2)	2.181(2)	147.19(8)	This work

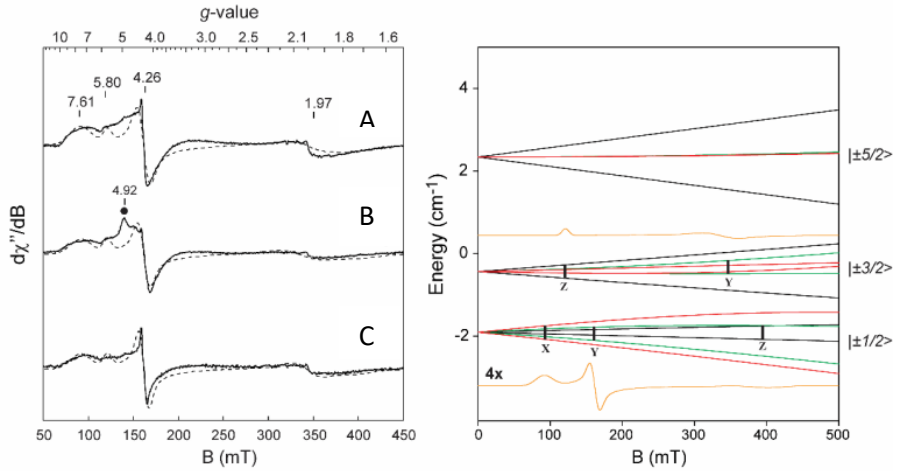

Figure 2.5. *(left) X-band EPR spectra of* ***[Fe^{3+}L1(Cl)$_2$]$^+$*** *(A),* ***[Fe^{3+}L2(Cl)$_2$]$^+$*** *(B), and* ***[Fe^{3+}L3(Cl)$_2$]$^+$*** *(C). Quantitative simulations (dashed lines) are overlaid on each spectrum for comparison. The black circle observed at g ~ 4.92 in* ***[Fe^{3+}L2(Cl)$_2$]$^+$*** *is from a minor (< 10%) high-spin iron(III)-impurity. Instrumental parameters: frequency, 9.643 GHz, microwave power, 6 µW; modulation amplitude, 0.9 mT; temperature, 10 K. Simulation parameters: S = 5/2; $g_{1,2,3}$ ~2.0; |D|, 0.7 ± 0.2 cm^{-1}; E/D, 0.07; $\sigma_{E/D}$, 0.01; σ_B, 0.9 mT. (right) Energy level diagram illustrating the splitting of doublets within the S = 5/2 spin state along each principle axis (X, red; Y, green; Z, black).*

2.2.5 Electrochemistry

Cyclic voltammetry was used to evaluate the electrochemical behavior of **$[Fe^{3+}L1(Cl)_2]^+$**-**$[Fe^{3+}L3(Cl)_2]^+$**. The cyclic voltammograms corresponding to the iron(III/II) couple of **$[Fe^{3+}L1(Cl)_2]^+$**-**$[Fe^{3+}L3(Cl)_2]^+$** are shown in Figure 2.6. Of the three complexes, **$[Fe^{3+}L2(Cl)_2]^+$** ($E_{1/2}$ = -486 mV) has the most negative half potential, followed by **$[Fe^{3+}L3(Cl)_2]^+$** ($E_{1/2}$ = -468 mV) and **$[Fe^{3+}L1(Cl)_2]^+$** ($E_{1/2}$ = -465 mV). The difference in the half potentials indicated derivatization of the pyridine ring effects the electron density around the iron center to a small extent. Figure 2.7 compares the electrochemical potentials of iron complexes containing 12-membered tetra-azamacrocycles; a wide range (-865 mV to -290 mV) of half potentials is achieved by changing the donor capacity of the ligand set, **L8** < **L1** ≈ **L3** < **L2** < **cyclen**.[94, 105, 122]

The reversibility of the redox process was investigated by determining the ΔE_p and I_{pa}/I_{pc}. The iron(III/II) redox processes are quasi-reversible (ΔE_p, I_{pa}/I_{pc}): **$[Fe^{3+}L1(Cl)_2]^+$** (105 mV, 1.2583), **$[Fe^{3+}L2(Cl)_2]^+$** (112 mV, 0.7264), and **$[Fe^{3+}L3(Cl)_2]^+$** (101 mV, 0.7485). Lastly, the electrochemical events are diffusion controlled for all three iron complexes, as shown by the linear relationship between I_p and the square-root of the scan rate (Figure A 6).[151]

It should be noted that an additional ligand-based oxidation event around 900 mV is observed in the full solvent window (1.4 to -1.2 mV, Figure A 5, *top*) for **$[Fe^{3+}L1(Cl)_2]^+$**-**$[Fe^{3+}L3(Cl)_2]^+$**. We have previously postulated that this event was ligand derived, based on electrochemical analysis of the corresponding zinc(II) complexes providing a similar behavior.[143] Electrochemical analysis of **L1**-**L3** in DMF solvent with TBAP electrolyte provide direct confirmation that this positive oxidation wave is ligand based (Figure A5, *bottom*).

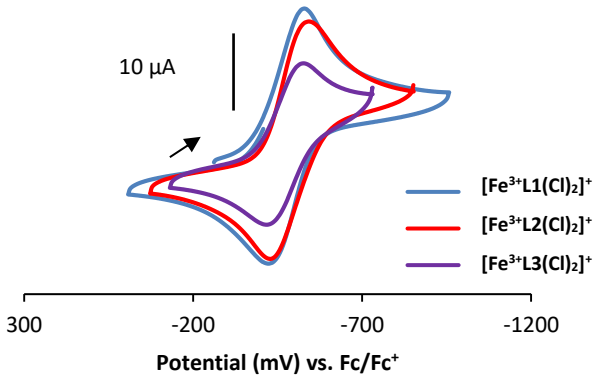

Figure 2.6. *Cyclic voltammogram overlay of the $Fe^{III/II}$ couple measured for* ***$[Fe^{3+}L1(Cl)_2]^+$-$[Fe^{3+}L3(Cl)_2]^+$*** *in DMF containing 0.1* M *$[Bu_4N][BF_4]$ as electrolyte, Ag/Ag^+ reference electrode, glassy carbon working electrode, and platinum auxiliary electrode at a scan rate of 100 mV/sec. All scans were referenced to Fc/Fc^+ = 0.00 mV.*

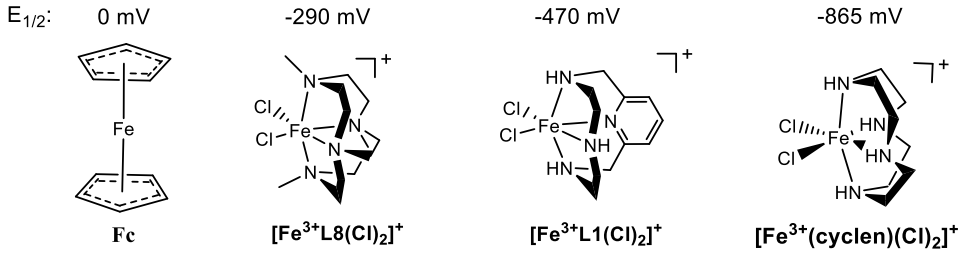

Figure 2.7. *Iron(III)/(II) halfway potentials of iron complexes in literature containing 12-membered tetra-azamacrocycles. The potentials are reported as referenced to Fc/Fc^+ = 0.00 mV.* [44, 147-148, 152]

Table 2.3. *The anodic wave potential (E_{pa}), cathodic wave potential (E_{pc}), peak potential separation (ΔE_p), and halfway potential ($E_{1/2}$) of* ***$[Fe^{3+}L1(Cl)_2]^+$*** *-* ***$[Fe^{3+}L3(Cl)_2]^+$****.* ***$[Fe^{3+}L2(Cl)_2]^+$*** *contains the most stable iron(III) ion in the series according to the $E_{1/2}$ values.*

Complex	E_{pc} (mV)	E_{pa} (mV)	$E_{1/2}$ (mV)	ΔE_p (mV)	I_{pc} (µA)	I_{pa} (µA)	I_{pa}/I_{pc}
$[Fe^{3+}L1(Cl)_2]^+$	-517	-412	-465	105	10.5837	-13.3181	1.2583
$[Fe^{3+}L2(Cl)_2]^+$	-542	-430	-486	112	18.4176	-13.3791	0.7264
$[Fe^{3+}L3(Cl)_2]^+$	-519	-418	-468	101	11.9661	-8.9570	0.7485

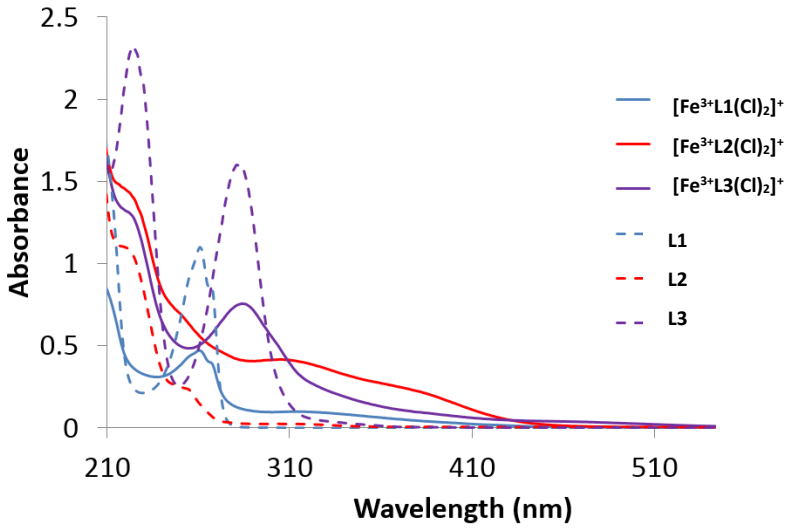

Figure 2.8. *The electronic absorbance spectra of ligands* ***L1-L3*** *and complexes* ***[Fe^{3+}L1(Cl)$_2$]$^+$-[Fe^{3+}L3(Cl)$_2$]$^+$*** *obtained in 1 M HCl.*

2.2.6 Electronic absorbance spectroscopy

The spectrophotometric behaviors of **[Fe^{3+}L1(Cl)$_2$]$^+$** - **[Fe^{3+}L3(Cl)$_2$]$^+$** are shown in Figure 2.8. The aromatic components of the ligands (*sans metal*) result in absorbance bands between 210 and 290 nm when measured in 1 *M* HCl, which was used to avoid the formation of multiple protonated species in solution. The iron(III) complexes showed no appreciable shift in the $\pi \rightarrow \pi^*$ region (210-300 nm). Instead, the appearance of LMCT bands were observed at wavelengths greater than 300 nm: **[Fe^{3+}L1(Cl)$_2$]$^+$** (311 nm), **[Fe^{3+}L2(Cl)$_2$]$^+$** (306 and 356 nm), **[Fe^{3+}L3(Cl)$_2$]$^+$** (458 nm), which is consistent with high-spin d^5 complexes.[153] These metal based assignments are supported by comparison to the 12-membered macrocycle, **[(cyclen)Fe(NCMe)$_2$]$^{3+}$** that Hua *et al.* reported to have absorbance bands at 259 and 358 nm and corresponding extinction coefficients below 500 $M^{-1}cm^{-1}$.[153] Furthermore, the difference in the absorbance spectra of **[Fe^{3+}L1(Cl)$_2$]$^+$**, **[Fe^{3+}L2(Cl)$_2$]$^+$**, and **[Fe^{3+}L3(Cl)$_2$]$^+$** is reflected in the visible color of the complexes. The **[Fe^{3+}L1(Cl)$_2$]$^+$** and **[Fe^{3+}L2(Cl)$_2$]$^+$** complexes are light brown solids, while **[Fe^{3+}L3(Cl)$_2$]$^+$** is a red solid; in solution **[Fe^{3+}L1(Cl)$_2$]$^+$** and **[Fe^{3+}L2(Cl)$_2$]$^+$** are yellow and **[Fe^{3+}L3(Cl)$_2$]$^+$** is brown. Low solubility of

the complexes in other solvents precluded a full study of solvent effects. The electronic absorption differences between **[Fe^{3+}L3(Cl)$_2$]$^+$** compared to the **[Fe^{3+}L1(Cl)$_2$]$^+$** and **[Fe^{3+}L2(Cl)$_2$]$^+$** complexes could be attributed to the lack of symmetry originating from the hydroxyl-moiety in the meta-position of the pyridine ring of the ligand.

Table 2.4. Catalytic reaction yields of 2-phenylpyrrole in the presence of 10 mole% **[Fe^{3+}L1(Cl)$_2$]$^+$** - **[Fe^{3+}L3(Cl)$_2$]$^+$**.

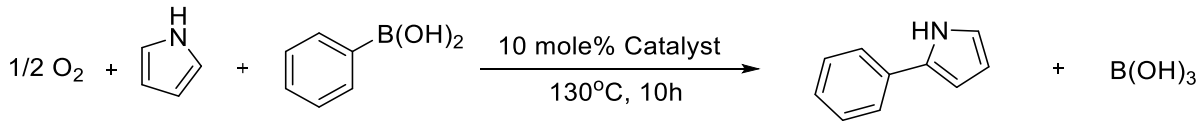

Catalyst	Yield (%)
[Fe^{3+}L1(Cl)$_2$]$^+$	57 ± 3
[Fe^{3+}L2(Cl)$_2$]$^+$	58 ± 7
[Fe^{3+}L3(Cl)$_2$]$^+$	52 ± 7

2.2.7 Catalytic activity of iron(III) complexes

Motivated by the report that addition of a tetra-azamacrocycle, iron(II) salt, and oxygen to phenylboronic and pyrrole results in the formation of 2-phenylpyrrole,[19] we explored the oxidation state of the pre-catalyst by testing **[Fe^{3+}L1(Cl)$_2$]$^+$**, **[Fe^{3+}L2(Cl)$_2$]$^+$**, and **[Fe^{3+}L3(Cl)$_2$]$^+$** for catalytic activity. Yields are shown in Table 2.4. In this series of experiments, each catalyst was tested at 10% loading, open to air. The ferric complexes afforded 2-phenylpyrrole in yields of 57% (**[Fe^{3+}L1(Cl)$_2$]$^+$**), 58% (**[Fe^{3+}L2(Cl)$_2$]$^+$**), and 52% (**[Fe^{3+}L3(Cl)$_2$]$^+$**), thereby identifying the oxidation state of the pre-catalyst as an iron(III) species. The realization that the iron(III) complexes enter the catalytic cycle will allow for better foundation to determine the oxidation state and identity of the active catalytic species. The following discussion focuses on the experiments used to

validate that the iron + ligand catalyst species is solely responsible for providing the selective reactivity observed.

Table 2.5. *Control reactions used to determine the yield of product in the absence of the high-spin iron(III) complexes.*

Test Compound	Oxidant	Yield (%)
*	*	0
*	20 eq. oxygen	0
$Fe(ClO_4)_3$	20 eq. oxygen	0
L1	20 eq. oxygen	0
L2	20 eq. oxygen	Trace
L3	20 eq. oxygen	Trace
L3	Atmosphere	Trace

*Not present

Control reactions were performed to ensure that the catalytic reactivity observed with **$[Fe^{3+}L1(Cl)_2]^+$**, **$[Fe^{3+}L2(Cl)_2]^+$**, and **$[Fe^{3+}L3(Cl)_2]^+$** was due only to the iron complexes. The substrates, pyrrole and phenylboronic acid, were heated to 130 ^oC in both the absence or presence of oxygen (Table 2.5). No reaction was observed under these conditions. This indicates that the reaction requires a catalyst to proceed. Additionally, four control reactions consisting of iron(III) perchlorate, **L1**, **L2**, and **L3** were performed in the presence of 10 mL O_2. The production of 2-phenylpyrrole was determined by both GC-MS and NMR due to the low quantities observed. Iron(III) perchlorate and **L1** did not afford 2-phenylpyrrole, however, **L2** and **L3** afforded trace amounts of 2-phenylpyrrole. Interestingly GC-MS analysis of the control reaction, which included

pyrrole, phenylboronic acid, **L3**, and atmospheric air also showed the formation of trace amounts of 2-phenylpyrrole, 3-phenylpyrrole, and two butenolides. The formation of 3-phenylpyrrole and butenolides was previously observed by Campi *et al*. when 3-phenylprop-2-yn-1-amine is exposed to CO/H_2 at 400 psi at 70°C for 20 hours in the presence of a rhodium catalyst. These results indicate that the ligand is capable of background reactivity thus producing pyrrole derivative. Additionally, it indicates that the derivatives produced are controlled by the composition of the oxidant (O_2 and CO_2) used in the reaction. Importantly, comparison of the products formed in the presence of **L3** and **$[Fe^{3+}L3(Cl)_2]^+$** and atmosphere showed that the use of the iron complex is *essential* to obtain catalytic and regioselective production of 2-phenylpyrrole product.

2.3 Conclusions

The addition of iron(II) perchlorate to the tetra-azamacrocycles **L1**, **L2**, and **L3** in the presence of oxygen yielded high-spin iron(III) complexes **$[Fe^{3+}L1(Cl)_2]^+$**, **$[Fe^{3+}L2(Cl)_2]^+$**, and **$[Fe^{3+}L3(Cl)_2]^+$** as shown by X-ray crystallography and EPR spectroscopy. Furthermore, it was demonstrated that the high-spin iron(III) complexes participate in the coupling of pyrrole and phenylboronic acid to produce 2-phenylpyrrole. Although a small amount of background reactivity was observed with **L2** and **L3**, the results showed that the iron complexes are responsible for controlling the reaction to produce 2-phenylpyrrole alone. Finally, the characterization of the complexes using electrochemistry, UV-vis spectroscopy, and mass spectrometry lays a foundation for mechanistic investigations concerning the oxidation state of the iron center throughout the catalytic process.

2.4 Experimental methods

General methods: Iron(II) perchlorate was freeze dried prior to use, all other reagents were obtained from commercial sources and used as received, unless noted otherwise. NMR spectra were obtained on a 400-MHz Bruker Advance spectrometer, using deuterated solvents ($CDCl_3$). NMR spectra were referenced using the corresponding solvent resonance (in parts per million; $CDCl_3$ δ = 7.26).[154] The following abbreviations were used for proper identification of the NMR signals: s = singlet, d = doublet, t = triplet, m = multiplet. ESI-MS experiments were carried out using an Agilent 6224 Accurate-Mass Time-of-Flight (TOF) mass spectrometer using 175 V to ionize the complexes. Elemental analysis was performed by Canadian Microanalytical Service Ltd. Electronic absorption spectra were recorded on a DU 800 UV-vis spectrophotometer (Beckman Coulter) using a 3 mL quartz cuvette with a 1 cm path length. GC-MS analysis was carried out using a Bruker Scion 436-GC-MS equipped with an auto sampler 8410 and a Br-5ms column 29.9m.

Synthesis of ligands: Stability of transition-metal complexes containing a tetra-azamacrocycle are facilitated by the macrocyclic effect. The ease with which these processes occur depends upon ring size, the number of donor atoms, electronic characteristics, and other factors.[35, 39] The formation of 14-membered tetra-azamacrocyclic ligands, for example, typically involves the use of transition metal ions to template the cyclization step between two independent units to form the ligand. The product of this reaction is, therefore, a transition metal macrocyclic complex. However, tetra-azamacrocyclic amines, comprised of 12 atoms in the ring, form through metal-independent cyclization pathways.[155-161] Therefore, for the work described herein, the 12-membered pyridine and pyridol based tetra-azamacrocyclic amines ligands, **L1**-**L3**, were produced previously reported procedures developed in our group and isolated as the

corresponding HCl salts.[143, 145] **Caution!** Perchlorate salts are explosive and should be handled in small quantities. Such compounds should never be heated as solids.

$[Fe^{3+}L1(Cl)_2]ClO_4$: Ligand (**L1·3HCl**) (101.1 mg, 0.3216 mmol) and $Fe(ClO_4)_2$ (83.7 mg, 0.330 mmol) were dissolved in 3 mL DI water; the solution was adjusted to pH= 6 using 1*M* KOH. The resulting red solution was stirred open to air for 15 hours at 40°C. After 15 hours, a tan precipitate was removed by centrifugation followed by filtration using a 0.45 μm PTFE filter. The water was removed using an azeotrope formed with acetonitrile. The resulting solid was taken up in CH_3CN and dried with Na_2SO_4. The addition of Et_2O to the CH_3CN solution, followed by centrifugation yielded the product as a brown powder. Yield: 62% (92.8 mg, 0.198 mmol). Yellow X-ray quality crystals were obtained by slow diffusion of ether into DMF at 4°C, CCDC# 1422489. ESI-MS (m/z) Found: 260.1515, $[L1Fe(III)\text{-}2H^+]^+$, (34%); 296.1360, $[L1Fe(III)Cl\text{-}H^+]^+$, (58%), 332.1209, $[L1Fe(III)2Cl^-]^+$, (14%). Theoretical: 260.0724, $[L1Fe(III)\text{-}2H^+]^+$, 296.0491, $[L1Fe(III)Cl\text{-}H+]^+$, 332.0258, $[L1Fe(III)2Cl^-]^+$. UV-vis, $\lambda_{max,}$ ε ($M^{-1}\cdot cm^{-1}$): 261 nm (3,600), 311 nm (800), 416 nm (170). Elemental analysis: **$[L1Fe^{3+}(Cl)_2]ClO_4$** (Formula:$C_{11}H_{18}N_4FeO_4Cl_3$); Calc(Found): C 30.50, (30.66); H 4.20, (4.09); N 12.95, (13.04).

$[Fe^{3+}L2(Cl)_2]ClO_4$: Ligand (**L2·3HCl**) (65.0mg, 0.208 mmol) was dissolved in 2.5 mL DI water. The pH of the solution was adjusted to 5 using 1*M* KOH. $Fe(ClO_4)_2$ (53.6 mg, 0.211 mmol) was dissolved in 1 mL DI water and added dropwise to the ligand solution; the pH was maintained between 3.5 and 5.2. After all iron(II) solution was added, the pH was adjusted to 5.3. The solution was allowed to stir open to air 2 days resulting in precipitation of a brown solid that was isolated by centrifugation. Yield: 30% (27.4 mg, 0.061 mmol). Yellow crystals suitable for XRD analysis were obtained by slow evaporation of water at room temperature, CCDC # 1422490. ESI-MS (m/z)

Found: 276.1529, [L2Fe(III)-2H$^+$]$^+$ (35%); 312.1377, [L2Fe(III)Cl-H$^+$]$^+$ (45%). Theoretical: 276.0674, [L2Fe(III)2-H$^+$]$^+$; 312.0440 [L2Fe(III)Cl-H$^+$]$^+$. UV-vis, λ_{max}, ε ($M^{-1}\cdot cm^{-1}$): 249 nm (6,700), 306 nm (4,000), 356 nm (2,700). Elemental analysis: **[Fe^{3+}L2(Cl)$_2$]ClO$_4$** (Formula: $C_{11}H_{18}N_4FeO_5Cl_3$); Calc (Found): C 29.46, (29.88); H 4.05, (4.08); N 12.49, (11.75).

[Fe^{3+}L3(Cl)$_2$]ClO$_4$: Ligand (**L3·3HCl**) (206.4 mg, 0.6223 mmol) was dissolved in 20 mL DI water and the pH was adjusted to 5 using 1*M* KOH. Fe(ClO$_4$)$_2$ (164 mg, 0.6155 mmol) was dissolved in 10 mL DI water, added drop wise to ligand, and the pH was re-adjusted to 5. The solution was allowed to stir open to air for 2 days at 40°C. The solvent was removed under reduced pressure. The resulting dark brown solid was dissolved in DMF, dried with Na_2SO_4, and filtered. Ether was added to the DMF solution and a red-brown powder was isolated by centrifugation. Yield = 63.2% (235.6 mg, 0.3932 mmol). Brown crystals suitable for XRD analysis were obtained by slow evaporation from water at room temperature, CCDC # 950048. ESI-MS (m/z) Found: 276.1481, [L3Fe(III)-2H$^+$]$^+$ (30%), 312.1322, [L3Fe(III)Cl-H$^+$]$^+$ (55%). Theoretical: 276.0674, [L3Fe(III)2-H$^+$]$^+$ 312.0440 [L3Fe(III)Cl-H$^+$]$^+$. UV-vis, λ_{max}, ε ($M^{-1}\cdot cm^{-1}$): 205 nm (14,000), 219 nm (10,000), 284 nm (5,600), 458 nm (300). Elemental analysis: **[Fe^{3+}L3(Cl)$_2$]ClO$_4$** (Formula: $C_{11}H_{18}N_4FeO_5Cl_3$); Calc(Found): C 29.46, (29.03); H 4.05, (4.05); N 12.49, (12.57).

X-ray diffraction analysis: Crystal diffraction data were collected at 100 K on a Bruker D8 Quest Diffractometer. Data collection, frame integration, data reduction (multi-scan), and structure determination were carried out using APEX2 software.[162] Structural refinements were performed with XSHELL (v 6.3.1), by the full-matrix least-squares method.[163] All non-hydrogen atoms were refined using anisotropic thermal parameters, while the hydrogen atoms were

treated as mixed. The ORTEP molecular plots (50%) were produced using APEX2 (Version 2014.9-0).

Electrochemistry: Cyclic voltammetry experiments were obtained using 2.2 mM complex and 100 *mM* tetrabutylammonium tetraflouroborate as the supporting electrolyte in DMF. The electrochemical cell was composed of a working glassy carbon electrode, a Pt auxiliary electrode, and a silver wire as the reference electrode. To facilitate solubility, all samples were first dissolved in 1*M* HCl, thoroughly dried, and then dissolved in DMF for electrochemical analysis. the potential was scanned in the negative direction at a rate of 100 mV/s, starting at the open circuit potential. The potential values presented here have been normalized to the half-wave potential of the Fc/Fc^+ redox couple set equal to 0.00 V. For comparison purposes half-wave potential in cited references were converted to reflect Fc/Fc^+ = 0 mV; **$[Fe^{3+}L8(Cl)_2]PF_6$**, (Fc/Fc^+ = 400 mV), and **$[Fe^{3+}$(cyclen) $(Cl)_2]Cl$**, (Fc/Fc^+ = 515 mV).[44, 147-148]

X-band EPR spectroscopy and analytical simulations: X-band (9 GHz) EPR spectra were recorded on a Bruker EMX Plus spectrometer equipped with a bimodal resonator (Bruker model 4116DM). Low-temperature measurements were made using an Oxford ESR900 cryostat and an Oxford ITC 503 temperature controller. A modulation frequency of 100 kHz was used for all EPR spectra. All experimental data used for spin-quantitation were collected under non-saturating conditions. Analysis of the EPR spectra utilized the general spin Hamiltonian,

$$\widehat{H} = \boldsymbol{D}\left(\hat{S}_Z^2 - \frac{S(S+1)}{3}\right) + \boldsymbol{E}\left(\hat{S}_X^2 + \hat{S}_Y^2\right) + \beta \mathbf{B} \cdot \boldsymbol{g} \cdot \boldsymbol{S}$$

Equation 1

where *D* and *E* are the axial and rhombic zero-field splitting parameters and *g* is the *g*-tensor.[164] EPR spectra were simulated and quantified using Spin Count (ver. 5.8.6218.29549), written by

Professor M. P. Hendrich at Carnegie Mellon University. The simulations were generated with consideration of all intensity factors, both theoretical and experimental, to allow concentration determination of species. The only unknown factor relating the spin concentration to signal intensity was an instrumental factor that depended on the microwave detection system. However, this was determined by the spin standard, Cu(EDTA), prepared from a copper atomic absorption standard solution purchased from Sigma–Aldrich.

2-phenylpyrrole yield determination: Phenylboronic acid (24 mg, 0.2 mmol) and crystalline material of the iron complex (0.02 mmol) were added to a 5 or 10 mL flask equipped with a stir bar. Pyrrole (1 mL) was added to flask, the mixture was heated to 130°C for 10 hours. The reaction was cooled to room temperature and the pyrrole was removed under vacuum until no visible liquid was present. Increasing the time the reaction was kept under reduced pressure decreased yields. The product mixture was dissolved in a minimum amount of $CDCl_3$, 5 µL of dimethyldiphenylsilane was added to the solution. The solution was filtered through a 0.2 µm nylon filter and a known amount of sample was added to a pre-weighed NMR tube. Yield determinations were performed using three resonances 6.875, 6.532, and 6.307 ppm corresponding to 2-phenylpyrrole and a resonance at 0.533 ppm corresponding to dimethyldiphenylsilane. The reported values are averages of all resonances; each measurement was run in triplicate.

Control reactions: Phenylboronic acid (24 mg, 0.2 mmol) and ligand (0.02 mmol), if used, were added to a 2 mL flask equipped with a stir bar, the system was then placed under an atmosphere of nitrogen. Pyrrole (1 mL) was added to flask and the mixture was heated to 130 °C for 15

minutes, if used, 10 mL O_2 was injected directly into the pyrrole, the system was closed, and heated for 10 hours. Yields were determined as stated above.

GC-MS details: Method, 80°C 2 min, ramp 5°C/min to 170°C, ramp 20°C/min to 300°C, hold 5 min. GC-MS Compound Identification **L3** coupling: 3-methyl-4-phenylfuran-2(5H)-one: (trace) RT. 14.909 min. Found (Cal.): $M^{+\cdot}$ 174.1 (174.1); (6%) 3-phenylpyrrole: RT. 15.002 min. Found (Cal.) $M^{+\cdot}$ 142.9 (143.0); (trace) 3-methyl-5-phenylfuran-2(4H)-one: 16.330 min. Found (Cal.) 174.1 (174.1); (16%) 2-phenylpyrrole: RT: 16.460 min Found (Cal.): $M^{+\cdot}$ 142.9 (143.0).

Chapter 3. Increase of direct C-C coupling reaction yield by identifying structural and electronic properties of high-spin iron tetra-azamacrocyclic complexes

3.1 Introduction

This chapter seeks to evaluate the effect of five different properties (1. coordination number, 2. redox properties, 3. complex rigidity/topological constraint, 4. resistance to oxidative degradation, and 5. complex geometric parameters) on the catalytic efficiency of a series of iron complexes. Our approach, below, will discuss each parameter separately. However, these parameters cannot be considered completely in isolation from one another, as they are related in a complex interplay that defines a given transition metal catalyst (relationships are discussed in respective sections).

A comparison of the catalytic reaction yields of four high-spin iron(III) and four high-spin iron(II) complexes for the coupling of phenylboronic acid and pyrrole to form 2-phenylpyrrole were used to identify key properties of the iron catalyst responsible for providing enhanced yields. Specifically, the ligands in Figure 3.1 were chosen to vary five properties: 1) the coordination requirements of the catalyst, 2) increasing oxidative stability of the complex, 3) topological constraint/rigidity, 4) N-atom modification(s), and 5) geometric parameters around the metal center of the complexes. Complexes **$[Fe^{2+}L5(Cl)]Cl$**, **$[Fe^{2+}L6(Cl)_2]$**, **$[Fe^{3+}L7(Cl)_2]PF_6$**,[165] **$[Fe^{3+}L8(Cl)_2]PF_6$**,[165] **$[Fe^{2+}L9(Cl)]PF_6$**, and **$[Fe^{2+}L10(Cl)]PF_6$**[152], were synthesized by Hubin and co-workers. However, complexes **$[Fe^{3+}L4(Cl)_2]PF_6$** and **$[Fe^{3+}L1(Cl)_2]Cl$** were produced by Green and co-workers. As noted above, many of these ligands or similar systems have been used to support metal-catalyzed oxidation, hydroxylation, or other reactions.[56,166-168,71] This study serves to show the versatility of macrocyclic systems and specific features that should be retained in these ligands to obtain optimized yields in the coupling C-C coupling of phenylboronic acid and pyrrole.

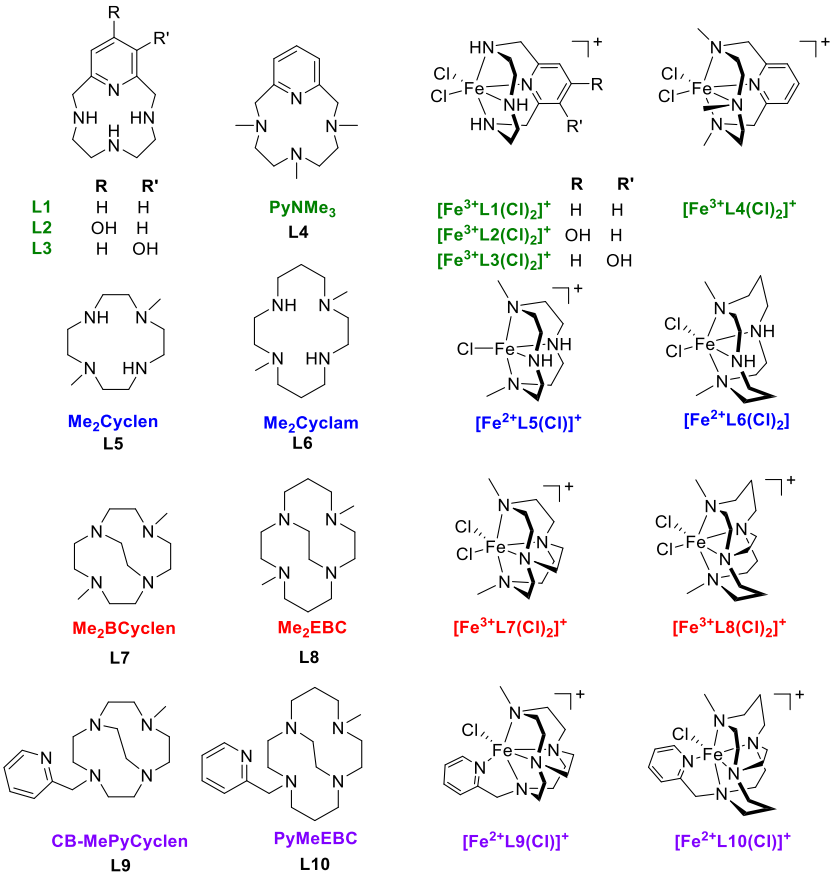

Figure 3.1. *Tetra-azamacrocycles and high-spin iron catalysts described herein and comparison of structures.*[144, 169, 19, 170, 171 172 165, 169, 152]

Table 3.1. *Detailed comparison of tetra-azamacrocycles described in Chapter 3.*

Ligand	Size of Macrocycle	N-Donor Atoms				Cross-Bridged (CB)
		-NH	-NMe	-N(CB)N-	-PyN	
L1-L3	12	3	0	0	1	X
L4	12	0	3	0	1	X
L5	12	2	2	0	0	X
L6	14	2	2	0	0	X
L7	12	0	2	2	0	✓
L8	14	0	2	2	0	✓
L9	12	0	2	2	1	✓
L10	14	0	2	2	1	✓

3.2 Results and discussion

As previously shown in chapter 2, the iron(III) complexes **[Fe^{3+}L1$(Cl)_2$]$^+$**, **[Fe^{3+}L2$(Cl)_2$]$^+$**, and **[Fe^{3+}L3$(Cl)_2$]$^+$** catalyze the C-C coupling reaction between pyrrole and phenylboronic acid to yield 2-phenylpyrrole.[169] This study established that the macrocyclic ligand, iron salt, and oxygen were all required for the reaction to proceed, and that **L1**-**L3** iron(III) complexes provided similar reaction yields. Encouraged by our preliminary results, the availability of a library of macrocyclic scaffolds, and the positive attributes of an iron catalyst to carry out direct C-C coupling reactions, we set out to (1) exemplify/expand the versatility of macrocyclic ligands, previously shown to facilitate other catalytic transformations,[12,166-168,71] to C-C chemistry to produce 2-phenylpyrrole for the first time and (2) identify properties of such an iron catalyst that result in increased catalytic yields. Modifications to tetra-azamacrocyclic ligands abound in the literature and are known to impact electronic and structural features of metal complexes.[11, 56, 140, 142, 148-149, 153, 165, 173-176] The complexes **[Fe^{3+}L1$(Cl)_2$]$^+$**, **[Fe^{3+}L4$(Cl)_2$]$^+$**, **[Fe^{2+}L5(Cl)]$^+$**, **[Fe^{2+}L6$(Cl)_2$]**, **[Fe^{3+}L7$(Cl)_2$]$^+$**, **[Fe^{3+}L8$(Cl)_2$]$^+$**, **[Fe^{2+}L9(Cl)]$^+$**, and **[Fe^{2+}L10(Cl)]$^+$** (Figure 3.1) were studied to determine impact electronic and structural variation of macrocyclic iron complexes have on the catalytic production of 2-phenylpyrrole. At 10% loading, catalytic yields ranging from 19-81% were achieved (Table 3.2). The reported catalytic reactions yields were determined after a ten-hour reflux and are based on the amount of phenylboronic acid used. Given that each catalyst was isolated and characterized prior to the catalytic studies, the inorganic properties of the iron catalysts could be compared for correlations to catalytic yield.

3.2.1 Rationale for ligand/complex comparison

As detailed in Figure 3.1 and Table 3.1, ligands **L1-L8** have four N-atom donor atoms but vary from one another by ring size (12 versus 14), N-atom substitution (secondary versus tertiary amine), and the presence of the ethylene cross-bridge between N-atom donors. Ligands **L9-L10** are 12- and 14-

membered systems, respectively, and provide five N-atom donors. Therefore, the importance of coordination requirements (property 1) of the resulting iron catalyst was achieved by comparing complexes with tetra-dentate ligands (**[Fe^{3+}L7$(Cl)_2$]$^+$** and **[Fe^{3+}L8$(Cl)_2$]$^+$**) to penta-dentate ligands (**[Fe^{2+}L9(Cl)]$^+$** and **[Fe^{2+}L10(Cl**)]$^+$). The importance of the reductive and oxidative properties of the complexes (property 2) was determined by comparing the iron(III/II) half-wave potentials versus catalytic reaction yields of **[Fe^{3+}L1$(Cl)_2$]$^+$**, **[Fe^{3+}L4$(Cl)_2$]$^+$**, **[Fe^{2+}L5(Cl)]$^+$**, **[Fe^{2+}L6$(Cl)_2$]**, **[Fe^{3+}L7$(Cl)_2$]$^+$**, **[Fe^{3+}L8$(Cl)_2$]$^+$**, **[Fe^{2+}L9(Cl)]$^+$**, and **[Fe^{2+}L10(Cl)]$^+$**. The effect of rigidity/topological ligand constraint (property 3) was investigated by comparing the most rigid metal complexes (**[Fe^{3+}L7$(Cl)_2$]$^+$** and **[Fe^{3+}L8$(Cl)_2$]$^+$**) to the least rigid metal complexes (**[Fe^{3+}L1$(Cl)_2$]$^+$**, **[Fe^{2+}L5(Cl)]$^+$**, and **[Fe^{2+}L6$(Cl)_2$]**), based on the factors described in Chapter 1. The presence of tertiary amines has been shown to increase the stability of complexes toward oxidative degradation; therefore, the impact of complex stability against oxidative degradation (property 4) on C-C catalytic reaction yields was evaluated directly by comparing the **[Fe^{3+}L1$(Cl)_2$]**$^+$ (N-atom donors) with **[Fe^{3+}L4$(Cl)_2$]**$^+$ (-NMe donor atoms).[56] Finally, geometric parameters about the iron center (property 5) were probed by comparing geometric parameters of **[Fe^{3+}L1$(Cl)_2$]$^+$**, **[Fe^{2+}L6$(Cl)_2$]**, **[Fe^{n+}L7$(Cl)_2$]$^+$**, and **[Fe^{n+}L8$(Cl)_2$]$^+$** determined through X-ray diffraction analysis.

3.2.2 Property 1: Coordination requirements

Mechanistic studies pertaining to catalytic oxygen-atom transfer and insertion reactions indicate that two exchangeable *cis*-sites are needed for oxygen activation during the catalytic cycle.[49, 58] To date, the need for two *cis*-labile coordination sites has not been identified in iron-catalyzed direct Suzuki-Miyaura C-C coupling reactions. Herein, the requirement for two labile *cis*-cites was determined by comparing catalysts with one exchangeable site (**[Fe^{2+}L9(Cl)]$^+$**, **[Fe^{2+}L10(Cl)]$^+$**) versus two *cis*-sites (**[Fe^{3+}L7$(Cl)_2$]$^+$**, **[Fe^{3+}L8$(Cl)_2$]$^+$**). The loss of an exchangeable *cis*-site led to a 42% reduction in 2-phenylpyrrole formation (**[Fe^{3+}L7$(Cl)_2$]$^+$** (74 ± 3%), **[Fe^{2+}L9(Cl)]$^+$** (32 ± 5%)). Similarly, a yield decrease of

49% was observed when comparing **[Fe^{3+}L8(Cl)$_2$]$^+$** (68 ± 4%) with **[Fe^{2+}L10(Cl)]$^+$** (19 ± 2%). Next, catalytic yields obtained from a mixture of **L3** and iron(II) oxalate (an iron(II) complex of **L3** was not isolable) were compared to **[Fe^{3+}L1(Cl)$_2$]$^+$** (Table 3.2) to validate that it was not the iron(II) oxidation states of **[Fe^{2+}L9(Cl)]$^+$** and **[Fe^{2+}L10(Cl)]$^+$** that contribute to a decrease in catalytic yields versus the loss of a coordination site. As with all of the studies described herein, the conditions used mimic those reported previously.[19] The mixture of **L3** and iron(II) oxalate afforded 61 ± 5% of 2-phenylpyrrole, which is comparable to the 57 ± 3% obtained when **[Fe^{3+}L1(Cl)$_2$]$^+$** was used. Therefore, the use of an iron(II) complex as opposed to the iron(III) complex does not decrease the amount of 2-phenylpyrrole produced. This is further supported when comparing **[Fe^{2+}L5(Cl)]$^+$** (30 ± 3%) and **[Fe^{2+}L6(Cl)$_2$]** (81 ± 7%), which provide the lowest and highest reaction yields, respectively, within the series of four-coordinate ligand-based complexes explored. Furthermore, no significant differences are observed between catalytic yields of *bona fide* complexes with chloride or perchlorate counter ions versus conditions mixing iron oxalate and **L3** (Table 3.2).[19] This is in contrast to the results obtained by Wen *et al.*, which reported that when mixtures of iron salts and **L1** are used in the catalytic reaction, the oxalate salt afforded better yields than sulfate or chloride salts. The counter-ion effect previously reported may be attributed to solubility of the iron salts being prohibitive of catalyst formation *in situ*. Altogether, these results show that the addition of a 5th coordinating amine to the ligand scaffold significantly decreased catalytic yields, and therefore confirms the need for two exchangeable *cis*-sites.

3.2.3 Property 2: Reductive and oxidative properties of the complexes

Ligand modifications are known to result in tuning the redox potential of the subsequent metal ion complexes.[177-179] In nature, the electrochemical potential of metalloenzymes is tuned by the ligand environment to produce different reactivities.[180-182] Therefore, the catalytic reaction yields of **[Fe^{3+}L1(Cl)$_2$]$^+$**, **[Fe^{3+}L4(Cl)$_2$]$^+$**, **[Fe^{2+}L5(Cl)]$^+$**, **[Fe^{2+}L6(Cl)$_2$]**, **[Fe^{3+}L7(Cl)$_2$]$^+$**, **[Fe^{3+}L8(Cl)$_2$]$^+$**, **[Fe^{2+}L9(Cl)]$^+$**, and **[Fe^{2+}L10(Cl)]$^+$** were compared to the iron(III/II) electrochemical potential of each catalyst to determine if

the position of the iron redox potential affects the efficiency of 2-phenylpyrrole production (Table 3.2 and Figure 3.3 - 3.4). Cyclic voltammetry studies were carried out under identical conditions to one another and standardized to Fc/Fc^{+} (0.00 mV). As indicated in Figure 3.2, each scan was collected beginning with the resting potential of each complex. The results indicate that the **$[Fe^{3+}L1(Cl)_2]^{+}$** complex affords the

most negative iron(III/II) half potential (-465 mV), followed by **$[Fe^{2+}L5(Cl)]^{+}$** (-442 mV), **$[Fe^{2+}L6(Cl)_2]$** (-405 mV), **$[Fe^{3+}L7(Cl)_2]^{+}$** (-391 mV), **$[Fe^{3+}L8(Cl)_2]^{+}$** (-306 mV), **$[Fe^{3+}L4(Cl)_2]^{+}$** (-285 mV), **$[Fe^{2+}L9(Cl)]^{+}$** (-232 mV), and **$[Fe^{2+}L10(Cl)]^{+}$** (73 mV). The more positive half-wave potentials derived from the pyridine pendant arm containing complexes, **$[Fe^{2+}L9(Cl)]^{+}$** and **$[Fe^{2+}L10(Cl)]^{+}$**, could be related to having only one negatively charged chloride ion to stabilize the higher oxidation state of the iron center versus two in the remainder of the complexes. This observation is in accordance with previous reports of similar manganese complexes.[152] The half potentials of the iron complexes, thereby, indicates that **L1** is the most donating followed by **L5 > L6 > L7 > L8 > L4** > **L9** > **L10**. This order is in accordance to ring size and modifications of the N-atom donors from the macrocycle scaffold. Overall, the 14-membered complexes result in more positive iron(III/II) potentials compared to 12-membered congeners; e.g. a shift of +85 mV is observed for **$[Fe^{3+}L7(Cl)_2]^{+}$** versus **$[Fe^{3+}L8(Cl)_2]^{+}$**. Conversion of –NH to –NMe donors also results in a shift to more positive potentials, consistent with the N-atoms becoming weaker donors upon methylation. For example, a difference of +180 mV is observed for **$[Fe^{3+}L1(Cl)_2]^{+}$** versus **$[Fe^{3+}L4(Cl)_2]^{+}$**. Finally, the topological constraint obtained by substituting the -NH donor ligands (**L5** and **L6**) with an ethylene cross-bridge (**L7** and **L8**) results in a more positive iron(III/II) potential; **$[Fe^{3+}L5(Cl)]^{+}$** versus **$[Fe^{2+}L7(Cl)_2]^{+}$** results in a shift of +51 mV.

Figure 3.3 shows a plot of the iron(III/II) half-potentials versus catalytic reaction yields for each complex. Both a linear and Lorentzian relationship between catalytic yield and half-wave potential were considered. A linear relationship was realized; however, to obtain a statistically reasonable fit of the

data, two catalysts **[Fe^{3+}L5(Cl)]$^{+}$** and **[Fe^{2+}L9(Cl)]$^{+}$** must be excluded. Conversely, Lorentzian fitting of the data (including **[Fe^{3+}L5(Cl)]$^{+}$** and **[Fe^{2+}L9(Cl)]$^{+}$**) afforded a statistically reasonable fit and predicts that a complex with iron(III/II) potentials in the range of -325.5 to -389.0 mV would be optimal for this C-C coupling reaction. The Lorentzian fitting parameters can be found in the supporting information (Table A 8). The use of a Lorentzian function is further supported by the Sabatier's principle, which states that the most active catalyst for a given process must not bind too strongly or weekly to the substrates.[183] Analysis of the direct relationship between catalytic reaction yield and iron(III/II) redox potentials suggests that the reaction mechanism depends upon an iron-based electron transfer, which can be modulated by ligand choice. Altogether, this comparison shows redox potentials of the iron center should be a factor to consider when tuning a catalyst. This redox potential is clearly tied to the rigidity and modification to the donor and could serve as a more direct predictor for catalytic success. Finally, this result helps to explain why the C-C coupling reaction does not proceed without a ligand donor present;[169] the redox chemistry of the iron center needs to be tuned to match that of the key step(s) involved in the C-C coupling reaction cycle being carried out.

Table 3.2. *Half-potential and catalytic reaction yield of iron complexes used to couple pyrrole and phenylboronic acid to produce 2-phenylpyrrole using 10% catalyst loading in the presence of air.*

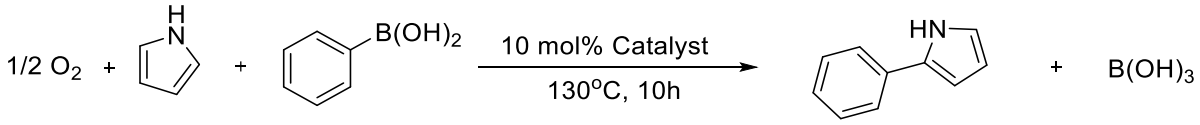

Catalyst	Yield (%)[a]	$E_{1/2}$ (mV)[b]	Catalyst	Yield (%)[a]	$E_{1/2}$ (mV)[b]
[Fe^{3+}L1(Cl)$_2$]$^{+}$	57 ± 3	-465	**[Fe^{3+}L8(Cl)$_2$]$^{+}$**	68 ± 4	-306
[Fe^{3+}L4(Cl)$_2$]$^{+}$	60 ± 1	-285	**[Fe^{2+}L9(Cl)]$^{+}$**	32 ± 5	-285
[Fe^{2+}L5(Cl)]$^{+}$	30 ± 2	-442	**[Fe^{2+}L10(Cl)]$^{+}$**	19 ± 2	73
[Fe^{2+}L6(Cl)$_2$]	81 ± 7	-405	**L3 + FeC$_2$O$_4$·2H$_2$O**	61 ± 5	-
[Fe^{3+}L7(Cl)$_2$]$^{+}$	74 ± 3	-391			

[a] Yields determined by NMR analysis.

[b] Referenced vs. Fc/Fc^{+} 0.0 mV.

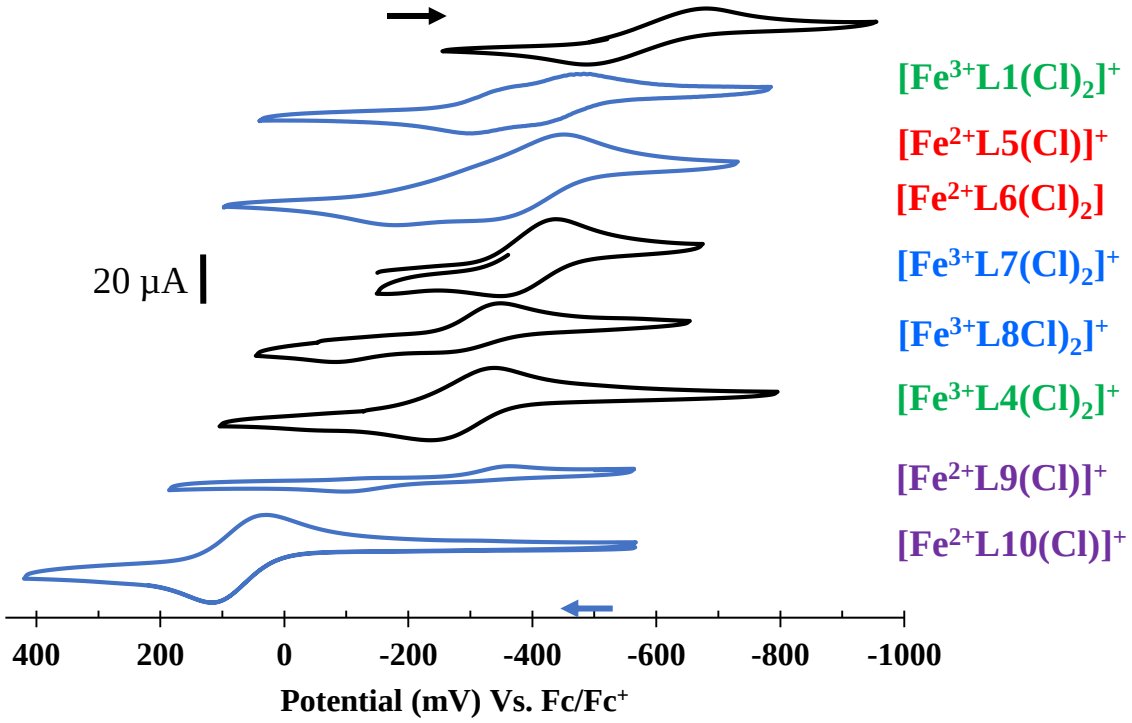

Figure 3.2. *Cyclic voltammogram overlay of the iron(III/II) couple measured for* ***$[Fe^{3+}L1(Cl)_2]^+$***, ***$[Fe^{3+}L4(Cl)_2]^+$***, ***$[Fe^{2+}L5(Cl)]^+$***, ***$[Fe^{2+}L6(Cl)_2]$***, ***$[Fe^{3+}L7(Cl)_2]^+$***, ***$[Fe^{3+}L8(Cl)_2]^+$***, ***$[Fe^{2+}L9(Cl)]^+$***, and* ***$[Fe^{2+}L10(Cl)]^+$*** *in DMF containing 0.1 M $[Bu_4N][BF_4]$ as electrolyte, Ag wire as the reference electrode, a glassy carbon working electrode, and a platinum auxiliary electrode at a scan rate of 100 mV/s. The trace color indicates the initial direction of each scan: Black trace (toward more positive potential), Blue trace (toward more negative potential).*

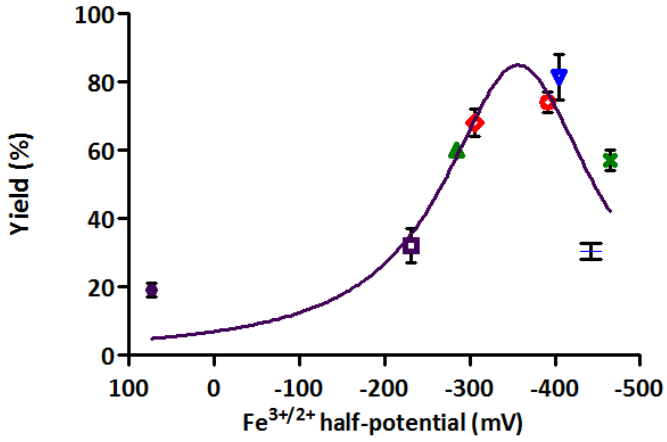

Figure 3.3. *Plot of iron(III/II) half-potentials versus yield for complexes:* ***$[Fe^{2+}L10(Cl)]^+$*** *(●);* ***$[Fe^{2+}L9(Cl)]^+$*** *(□);* ***$[Fe^{3+}L4(Cl)_2]^+$*** *(Δ);* ***$[Fe^{3+}L8(Cl)_2]^+$*** *(◊);* ***$[Fe^{3+}L7(Cl)_2]^+$*** *(○);* ***$[Fe^{2+}L6(Cl)_2]$*** *(▽);* ***$[Fe^{2+}L5(Cl)]^+$*** *(-);* ***$[Fe^{3+}L1(Cl)_2]^+$*** *(x).*

3.2.4 Property 3: Effect of rigidity/topological constraint

The series of cross-bridge free (**$[Fe^{3+}L1(Cl)_2]^+$**, **$[Fe^{2+}L5(Cl)]^+$**, and **$[Fe^{2+}L6(Cl)_2]$**) versus cross-bridged complexes (**$[Fe^{3+}L7(Cl)_2]^+$** and **$[Fe^{3+}L8(Cl)_2]^+$**) provide a good comparison to evaluate the impact of rigidity on catalytic reaction yields as they vary by both ring size and presence of the rigidifying ethylene cross-bridge (CB). To the best of our knowledge, the incorporation of a cross-bridge into a ligand has not been explored as supports for *direct* C-C coupling reactions, particularly iron catalysts. For an example of a cross-bridged ligand supporting *indirect* C-C coupling (pre-activated substrates), see reference [15]. The rigidity of a complex can be controlled by the presence of an ethylene cross-bridge and the size of the macrocyclic ligand (12 versus 14).[42] Specifically, topological constraint,[35] a term that describes making a ligand's donor atoms more interconnected, leads to more kinetically stable interactions between the metal ion and the ligand.[184] Topological constraint has been observed experimentally and is similar to the macrocyclic effect. The simple bridging of two nitrogen atoms of a cyclic ligand by a two-carbon chain dramatically changes how the ligand coordinates the metal ion, vastly increases the kinetic stability and ability to catalyze oxidation reactions.[49, 168] In addition, smaller macrocyclic rings (12- versus 14- membered rings) also impart greater rigidity through ring strain that results when metals bind to the donor atoms. Based on these principles, the order of rigidity in the series studied is **$[Fe^{3+}L7(Cl)_2]^+$** (12-membered, CB) > **$[Fe^{3+}L8(Cl)_2]^+$** (14-membered, CB) > **$[Fe^{3+}L1(Cl)_2]^+$** (12-membered) **≥ $[Fe^{2+}L5(Cl)]^+$** (12-membered) > **$[Fe^{2+}L6(Cl)_2]$** (14-membered). The catalytic reaction yields do not parallel the rigidity/topological constraint: **$[Fe^{2+}L6(Cl)_2]$** (81 ± 7%) > **$[Fe^{3+}L7(Cl)_2]^+$** (74 ± 3%) > **$[Fe^{3+}L8(Cl)_2]^+$** (68 ± 4%) > **$[Fe^{3+}L1(Cl)_2]^+$** (57 ± 3%) > **$[Fe^{2+}L5(Cl)]^+$** (30 ± 2%). The results indicated that cross-bridged complexes (**$[Fe^{3+}L7(Cl)_2]^+$** and **$[Fe^{3+}L8(Cl)_2]^+$**) in general result in higher yields compared to 12-membered noncross-bridged complexes (**$[Fe^{3+}L1(Cl)_2]^+$** and **$[Fe^{2+}L5(Cl)]^+$**). Conversely, the absence of a cross-bridge in **$[Fe^{2+}L6(Cl)_2]$** compared to **$[Fe^{2+}L8(Cl)_2]$** results in a higher (+13 %) catalytic reaction yield. This supported that the presence of a cross-bridge and ring strain (12- versus 14-membered rings)

tunes the reactivity. However, the effect on reduction and oxidation properties was dominant compared to structural and stability considerations typically associated with cross-bridged systems alone.

3.2.5 Property 4: Stability of the complex against oxidative degradation

The comparison of protected versus unmodified N-atoms in the ligands was prompted by Chow and co-workers, who reported that the use of iron catalysts for oxygen atom transfer reactions derived from azamacrocycle ligands with the N-atoms methylated (-NMe) afforded a 99% conversion of substrate. [56] This is in contrast to the non-methylated congeners, which resulted in only 38% substrate conversion. The observed increase in conversion with N-atom protected complexes was attributed to the presence of tertiary versus secondary amine donors, that provided an increased stability by resistance to oxidative degradation of the catalyst.[56] The effect of increased stability against oxidative degradation through protection of the N-atoms was evaluated for C-C coupling chemistry by comparison of **$[Fe^{3+}L1(Cl)_2]^+$** and **$[Fe^{3+}L4(Cl)_2]^+$**, which utilize unprotected, secondary (-NH) amine donors versus tertiary (-NMe) donors, respectively (Figure 3.1). The **$[Fe^{3+}L1(Cl)_2]^+$** (57 ± 3%) and **$[Fe^{3+}L4(Cl)_2]^+$** (60 ± 1%) complexes afforded comparable yields under identical conditions. Therefore, the substitution of the N-atoms as protection from catalyst decomposition is not a property to be considered in catalyst design for this reaction. Furthermore, this, along with the need for oxygen, suggests that the catalytic cycle may not involve highly reactive oxidative intermediates or conditions.

3.2.6 Property 5: Effect of geometric parameters

A brief structural comparison between the novel catalysts presented here and related literature analogues may be helpful to orient the rationalization of catalytic performance with structural parameters. Figure 3.4 contains solid-state structures of each relevant complex and Table 3.3 includes useful geometric parameters for comparison.

Table 3.3. *Comparison of the catalytic reaction yields and useful geometric parameters, derived from solid-state structural data.*

Fig. 3.4	Complex (Coord Geometry)	Catalytic Yield (%)	M^{n+}	[a]r (pm)	N_{ax}-Fe-N_{ax} Angle (°)	N_{eq}-Fe-N_{eq} Angle (°)	Cl-Fe-Cl Angle (°)	Cl-Cl Bond Dist (Å)	M-N Bond Dist (Å)	M-Cl Bond Dist (Å)	Ref
a	**$[Fe^{2+}L7(Cl)_2]^+$** (Octahedral)	(74)	Fe^{2+}	92	145.78	77.31	93.42	3.511	2.276 2.269 2.248 2.240	2.416 2.407	168
b	**$[Fe^{2+}L8(Cl)_2]$** (Octahedral)	(68)	Fe^{2+}	92	161.88	78.36	95.53	3.593	2.275 2.287 2.257 2.263	2.426 2.427	168
c	**$[Fe^{3+}L7(Cl)_2]^+$** (Octahedral)	74	Fe^{3+}	79	153.20	77.81	95.10	3.377	2.179 2.158 2.171 2.163	2.2853 2.2911	147
d	**$[Fe^{3+}L8(Cl)_2]^+$** (Octahedral)	68	Fe^{3+}	79	166.8	79.8	95.70	3.412	2.188 2.197 2.223 2.229	2.278 2.288	185
e	**$[Fe^{2+}L5Cl]^+$** (Square Pyramidal (τ) = 0.098[b])	30	Fe^{2+}	92	131.14	125.27	-	-	2.296 2.278 2.228 2.232	2.304	This Work
f	**$[Fe^{2+}L6(Cl)_2]$** (Octahedral)	81	Fe^{2+}	92	162.4	91.5	94.4	3.58	2.27 2.31	2.438 2.438	This work
g	**$[Fe^{3+}L1(Cl)_2]^+$** (Octahedral)	57	Fe^{3+}	79	146.68	86.62	95.78	3.388	2.181 2.182 2.161 2.098(N_{py})	2.2862 2.2805	This work
h	**$[Fe^{2+}L10(Cl)]^+$** (Octahedral)	19	Fe^{2+}	92	168.27	80.82	-	-	2.204 2.232 2.246 2.285 2.215(N_{py})	2.3805	152

[a] Shannon, R. D. *Acta Crystallogr. Sect. A* **1976**, *32*, 751-767.
[b] Addison, A. W. *et al. J Chem Soc Dalton* **1984**, 7, 1349-1356.
Values in () indicate yields based on congener with complementary oxidation state to the species used for catalysis.

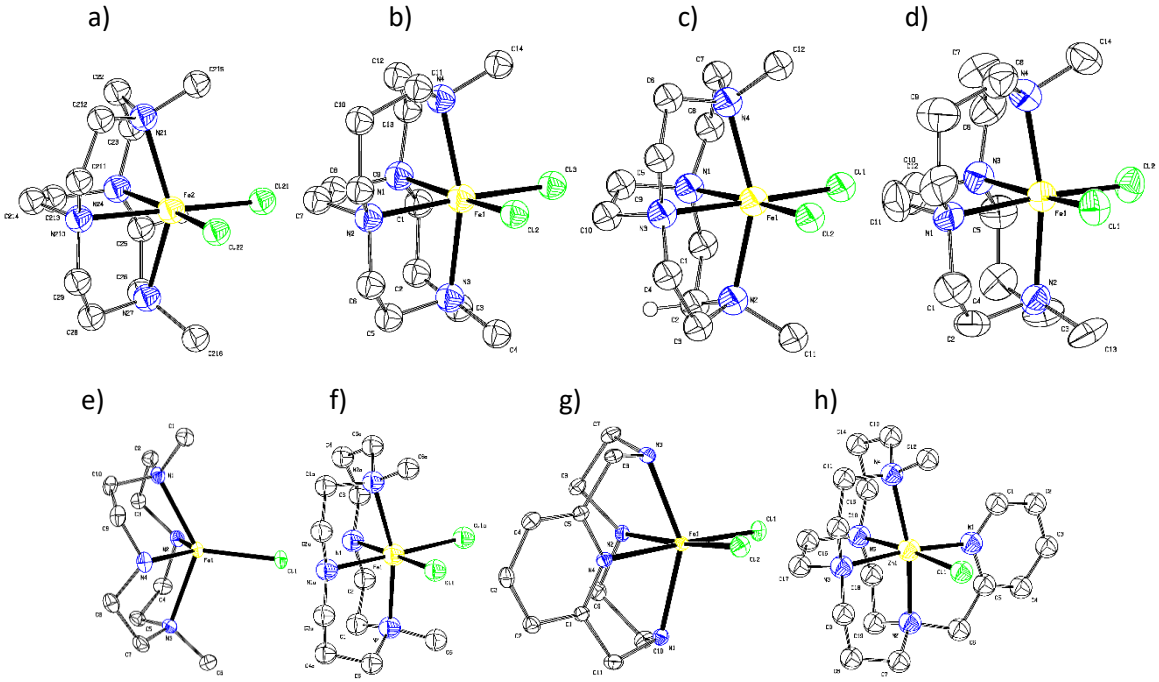

Figure 3.4. *ORTEP (50% TELP) representation of a)* ***[Fe^{2+}L7(Cl)$_2$]****, b)* ***[Fe^{2+}L8(Cl)$_2$]****, c)* ***[Fe^{3+}L7(Cl)$_2$]$^+$****, d)* ***[Fe^{3+}L8(Cl)$_2$]$^+$****, e)* ***[Fe^{2+}(L5)Cl]$^+$****, f)* ***[Fe^{2+}(L6)Cl$_2$]****, g)* ***[Fe^{3+}L1(Cl)$_2$]$^+$****, h)* ***[Fe^{2+}L10(Cl)]$^+$****. Hydrogen atoms and counter-ions have been omitted for clarity.*[147, 168, 185]

The X-ray derived crystal structures of iron(II) and (III) dimethyl cross-bridged cyclen and cyclam complexes are found in Figure 3.4a-d and all have distorted octahedral geometries with the macrocyclic nitrogen atoms at the axial and two *cis* equatorial positions, leaving the remaining *cis* equatorial positions filled by chloro- ligands. The iron(II) complexes (Figure 3.4a-b,h) are presented for comparison with the other iron(II) structures, since we were unable to obtain iron(III) structures of **[Fe^{2+}L5(Cl)]$^+$**, **[Fe^{2+}(L6)Cl$_2$]**, and **[Fe^{2+}L10(Cl)]$^+$**. For our purposes, these structures mainly differ by the extent to which the metal ion extends from the macrocyclic cavity to be available for catalytic reactivity. The iron ion extends further from the cavity in both cyclen analogues (**L5**, **L7**) than the larger cyclam analogues (**L6**, **L8**), which can more fully engulf the metal ion and thereby more closely approach octahedral geometry. Finally, the larger iron(II) cations are extended further away from the macrocycle cavity than the smaller iron(III) cations.

The unbridged analogues (**[Fe^{2+}L5(Cl)]$^{+}$** and **[Fe^{2+}(L6)Cl_2])** of these just-discussed iron(II) complexes are found in Figure 3.4e-f and demonstrate the enhanced flexibility available without the ethylene cross-bridges. A direct comparison can be made between both octahedral cross-bridged cyclam complexes, which have N_{eq}-Fe-N_{eq} bond angles of 79.8° and 78.36°, respectively, to the N_{eq}-Fe-N_{eq} bond angle of 91.5° in the likewise octahedral **[Fe^{2+}L6$(Cl)_2$]** (Figure 3.4f). The Fe-N and Fe-Cl bond distances change less than 0.02 Å between the cross-bridged and unbridged iron(II) complexes even as the bond angles are adjusted. The unbridged ligand has more nearly octahedral bond angles and likely better orbital overlap for bonding, while the cross-bridged complex has gained topological constraint that is most readily demonstrated as higher kinetic stability.[40] The **[Fe^{2+}L5(Cl)]$^{+}$** (Figure 3.4e) complex, on the other hand, has a unique 5-coordinate geometry that is best described as distorted square pyramidal (τ = 0.098).[186] The flexible cyclen macrocycle unfolds from its tight *cis*-configuration in the two cross-bridged cyclen octahedral structures in Figure 3.4a,c which have N_{eq}-Fe-N_{eq} bond angles of 77.81° and 77.3°, respectively, to the analogous smallest N_{eq}-Fe-N_{eq} bond angle of 125.27° in the square pyramidal structure of **[Fe^{2+}L5(Cl)]$^{+}$**. This expansion of the macrocycle around the "equator" allows steric space for only one chloro-ligand, which is more tightly held, as would be expected, in this 5-coordinate complex (Fe^{2+}-Cl = 2.304 Å) than in the octahedral iron(II) bridged cyclen complex (Fe^{2+}-Cl = 2.407 Å and 2.416 Å). Presumably, the unbridged ligand could have folded more tightly to accommodate an octahedral structure with a second chloro-ligand, but at least in the solid state, the 5-coordinate mono chloro-complex was favored.

The **[Fe^{3+}L1$(Cl)_2$]$^{+}$** complex (Figure 3.4g) is pseudo-octahedral, folded like the cross-bridged ligands, with two *cis* chloro-ligands and the pyridine donor located equatorially. This complex has a N_{eq}-Fe-N_{eq} bond angle of 86.62°, which is larger than the 77.81° of the constrained complex **[Fe^{3+}L7$(Cl)_2$]$^{+}$**, but much smaller than the highly flexible 125.27° of **[Fe^{2+}L5(Cl)]$^{+}$**. Interestingly, the N_{ax}-Fe-N_{ax} bond angle of 146.68° for **[Fe^{3+}L1$(Cl)_2$]$^{+}$** is also intermediate between the 153.20° of **[Fe^{3+}L7$(Cl)_2$]$^{+}$** and the 131.14° of

[Fe^{2+}L5(Cl)]$^{+}$. It appears that inclusion of a pyridine in the macrocyclic ring is an effective strategy to select these intermediate bond angles between those of the ethylene cross-bridged and unbridged cyclen analogues and could be used for tuning complexes in future ligand design.

Finally, the octahedral **[Fe^{2+}L10(Cl)]$^{+}$** complex (Figure 3.4h) has metric parameters fairly similar to its **L8** analogue (Figure 3.4b), with the trend of slightly larger N-Fe-N bond angles, as the pyridine pendant arm helps pull the iron(II) ion more fully into the ligand cavity.[152] However, this ligand is pentadentate donor, and its pendant pyridine may interfere with the catalytic process rather than enhance it, as the catalytic yield of **[Fe^{2+}L10(Cl)]$^{+}$** is the lowest studied. Presumably, the **[Fe^{2+}L9(Cl)]$^{+}$** complex, though no crystal structure was obtained, would also have a pentadentate macrocyclic ligand and was likewise not a very active catalyst.

In summary, comparison of the N-Fe-N angles versus reaction yields indicate that equatorial space about the exchangeable *cis*-sites and/or iron accessibility does not correlate to increased catalytic reaction yield; the N_{eq}-Fe-N_{eq} and N_{ax}-Fe-N_{ax} were 91.5^{o} and 162.4^{o} for **[Fe^{2+}L6(Cl)$_2$]**, 86.62^{o} and 146.68^{o} for **[Fe^{3+}L1(Cl)$_2$]$^{+}$**, 79.83^{o} and 166.8^{o} for **[Fe^{3+}L8(Cl)$_2$]$^{+}$**, and 79.62^{o} and 153.20^{o} for **[Fe^{3+}L7(Cl)$_2$]$^{+}$**. Likewise, the differences in the corresponding Cl-Fe-Cl(°) and Cl-Cl(Å) geometric parameters for the *cis*-chloride ions are derived from the chelate composition and were analyzed as well. Small variations between **[Fe^{3+}L1(Cl)$_2$]$^{+}$** (95.78^{o}, 3.388 Å), **[Fe^{3+}L7(Cl)$_2$]$^{+}$** (95.10^{o}, 3.377 Å), and **[Fe^{3+}L8(Cl)$_2$]$^{+}$** (95.70^{o}, 3.412 Å) are noted, but, like N-Fe-N angles, none correlate to the observed trends in catalytic yields. These studies help to support that the redox chemistry of the iron center plays the key role in controlling the catalytic reaction yields. Although, the accessibility to the iron center is a factor to consider, as shown by the need for two labile *cis* sites (property 1), the small changes in the axial and equatorial iron angles within the series studied does not correlate to catalytic reaction yields. This encourages the use of the range of tetra azamacrocycles available to synthetic chemists as considerations for tuning redox potentials to optimal ranges for this reaction.

3.3 Conclusion

Catalytic reaction yields of a library of high-spin iron complexes **$[Fe^{3+}L1(Cl)_2]^+$**, **$[Fe^{3+}L4(Cl)_2]^+$**, **$[Fe^{2+}L5(Cl)]^+$**, **$[Fe^{2+}L6(Cl)_2]$**, **$[Fe^{3+}L7(Cl)_2]^+$**, **$[Fe^{3+}L8(Cl)_2]^+$**, **$[Fe^{2+}L9(Cl)]^+$**, and **$[Fe^{2+}L10(Cl)]^+$** has been determined for the C-C coupling reaction that yields 2-phenylpyrrole. Complex **$[Fe^{2+}L6(Cl)_2]$** afforded the highest yield (81%). The systematic evaluation of the coordination requirements, the reductive and oxidative properties of the complex, rigidity/topological constraint of the complex, the stability of the complex toward oxidative degradation, and geometric parameters about the iron center revealed that optimized iron redox potential are responsible for the increase in catalytic reaction yield. The need for two labile *cis*-sites was probed and confirmed as a 42% decrease in yield was observed when only one labile labile-site was present. Altogether the fundamental approach to this series of catalysts for C-C coupling reactions shows some similarities to iron catalysts used in oxidation catalytic reactions, but there are differences that should be taken in to consideration when carrying out these reactions. The studies in this chapter suggested that electronic control of the iron center via rationalized modification of the macrocycle ring size, modification to the N-atoms (methylation or cross-bridging) and/or further modification to the pyridine for electronic tuning could be used to improved yields obtained to date. Such a new class of molecules is the focus of our future studies. Altogether, this work provides an inorganic/coordination chemistry focused approach to optimizing catalytic reactions and expands the applications in which macrocycles and cross-bridged macrocycles are used.

3.4 Experimental methods

General methods: Pyrrole was distilled under reduced pressure prior to use; all other reagents including anhydrous iron(II) chloride (Sigma Aldrich) used were obtained from commercial sources and used as received, unless noted otherwise. ^{1}H-NMR spectra were obtained on a 300- or 400-MHz Bruker Avance spectrometer using deuterated solvents and spectra were referenced using the corresponding solvent

resonance (in parts per million; $CDCl_3$, δ = 7.26 ppm).[154] No NMR data were obtainable for **$[Fe^{3+}L4(Cl)_2]PF_6$** and **$[Fe^{3+}L1(Cl)_2]Cl$**. Elemental analysis was performed by Canadian Microanalytical Service Ltd. The following compounds were synthesized using previously published procedures: **L1** – **L3**,[143, 145] **$PyNMe_3$** (**L4**),[59] **Me_2Cyclen** (**L5**;1,7-dimethyl-1,4,7,10-tetraazacyclododecane)[187], **Me_2Cyclam** (**L6**; 1,8-dimethyl-1,4,8,11-tetraazacyclotetradecane)[188], **Me_2BCyclen** (**L7**),[171] **Me_2EBC (L8)**,[168] **CB-MePyCyclen (L9)**,[172] **PyMeEBC** (**L10**),[152] **$[Fe^{3+}L7(Cl)_2]PF_6$**,[165] **$[Fe^{3+}L8(Cl)_2]PF_6$**,[165] and **$[Fe^{2+}L10]PF_6$**.

Synthesis. *$[Fe^{3+}L4(Cl)_2]PF_6$*: $FeCl_3 \cdot 6H_2O$ (109 mg, 0.404 mmol) was dissolved in 9 mL methanol and added drop-wise to **L4** (124 mg, 0.500 mmol) dissolved in minimum volume of methanol. A large amount of precipitate formed when half of the iron solution was added, the reaction was allowed to stir overnight at which time the majority of precipitate re-dissolved. The remaining solid was removed by filtration through celite, and $[(Bu)_4N]PF_6$ (787 mg, 2.03 mmol) was added as a solid resulting in precipitate of a yellow powder. The product was isolated via filtration and washed with small amount of methanol. Yield: 78% (164 mg, 0.316 mmol). ESI-MS^+ Calc (Found): 374.0727 (373.9824). Absorption spectrum (CH_3CN), $\lambda_{max,}$ (ε, $M^{-1} \cdot cm^{-1}$): 326 (5,000) and 408 (sh; 1,400) nm; (**$[Fe^{3+}L4(Cl)_2]^+$**). Elemental Analysis: Calc. (Found) for $C_{14}H_{24}Cl_2FeN_4PF_6$: C, 32.33(32.15); H, 4.65(4.90); N, 10.77(10.67).

$[Fe^{3+}L1(Cl)_2]Cl$: Ligand (**L1**) (252 mg, 0.799 mmol) was dissolved in 3 mL DI water. Iron(III) chloride hexahydrate (222.3 mg, 0.823 mmol) was dissolved in 3 mL methanol, the metal was added dropwise to the ligand. Slow evaporation of methanol yielded yellow X-ray quality crystals. Yield: 12% (34 mg, 0.0932 mmol). Absorption spectrum (CH_3CN), $\lambda_{max,}$ (ε, $M^{-1} \cdot cm^{-1}$): 319 (4,500) and 390 (sh; 1,600) nm. Elemental analysis: Calc (Found) for $C_{12}H_{18}Cl_3FeN_4 \cdot 3H_2O$: C 35.85(35.29); H 4.92(4.95); N 15.20(14.92). ESI-MS^+ was consistent with the ClO_4^- congener from previous reports.[169]

Catalytic Reactions: Phenylboronic acid (24 mg, 0.20 mmol) and iron complex (0.02 mmol) were added to a 2-10 mL flask equipped with a stir bar. Pyrrole (1 mL) was added to flask, the mixture was heated to 130 ^{o}C for 10 hours.

Yield determination: Reactions were cooled to room temperature, and the pyrrole was removed *in vacuo* until no visible liquid was present. Care was taken to avoid product loss under high vacuum. The reaction was dissolved in a minimum amount of $CDCl_3$ and 5 µL of dimethyldiphenyl silane was added. The solution was filtered through a 0.2 µm nylon filter and a known amount of sample was added to a pre-weighed NMR tube. Yield determinations were performed using three resonances 6.875, 6.532, and 6.307 ppm, corresponding to 2-phenylpyrrole and a resonance at 0.533 ppm corresponding to dimethyldiphenyl silane. The reported values are averages of all resonances; each reaction was run in triplicate.

Electrochemistry: Cyclic voltammetry experiments utilized 2-3 mM complex and 100 mM tetrabutylammonium hexafluoroborate in DMF. The electrochemical cell was composed of a working glassy carbon electrode, a Pt auxiliary electrode, and a silver wire as the reference electrode. The potential values presented here are normalized to the half-wave potential of the Fc^{+}/Fc = 0.00 mV.

X-ray crystallography: Crystal diffraction data for **$[Fe^{3+}L1(Cl)_2]^{+}$** were collected at 100 K on a Bruker D8 Quest Diffractometer. Data collection, frame integration, data reduction (multi-scan) were carried out using APEX3 software.[162] The structure was solved via intrinsic phasing methods using ShelXT[189] and refined with ShelXL[189] within the Olex2 graphical user interface.[190] All non-hydrogen atoms were refined using anisotropic thermal parameters, while the hydrogen atoms were treated as mixed. The ORTEP molecular plots (50 %) were produced using Platon.[191]

Chapter 4. Mechanistic insight into iron-catalyzed Suzuki-Miyaura type C-C coupling

4.1 Introduction

Direct Suzuki-Miyaura C-C coupling reactions facilitated by iron have been pioneered by Wen and co-workers.[65] Using tetra-azamacrocycles and iron salts, pyridine and pyrrole were independently coupled to phenylboronic acid to produce 2-phenylpyridine (41%) and 2-phenylpyrole (66%), respectively. The coupling of pyridine and phenylboronic acid was performed in the presence of an iron(III) salt. Conversely, pyrrole coupling to phenylboronic acid was performed using an iron(II) salt. Wen and co-workers proposed mechanism for the iron(II)-catalyzed coupling of pyrrole and phenylboronic acid. In this mechanism, shown in Scheme 1.5 *(left)*, the iron(II) complex enters that catalytic cycle and is activated by oxygen to form an Fe-O species. The Fe-O species is proposed to activate the C_2-H bond of pyrrole. Following the report by Wen and co-workers, Dong *et al.* showed by mass spectrometry that an iron(III)-oxo species is present in the iron(III)-catalyzed Suzuki-Miyaura C-C of pyridine and phenylboronic acid.[3] An Fe(III)/Fe(I) process was proposed based on a computational study that began with the iron(III)-oxo species. Although some mechanistic studies have been performed on the iron-catalyzed Suzuki-Miyaura reaction, several questions remain: (1) Do the iron(III) complexes act as stoichiometric reagents to afford Suzuki-Miyaura type reactions? (2) Does oxygen oxidize pyrrole or the metal center? (3) What type of interaction does oxygen have with iron(III) catalysts? (4) Are any off-cycle species formed that may decrease catalytic efficiency? (5) What is the oxidation state of the active catalytic species?

Here we investigate (1) the ability of the iron(III) complexes to act as stoichiometric reagents to afford Suzuki-Miyaura type reactions, (2) the role of oxygen, (3) the type of interaction that occurs between the iron catalyst and oxygen, and (4) the presence of off-cycle species such as μ-oxodiiron complexes. The ability of the iron complex to act as a stoichiometric reagent (1) was investigated by altering the reaction conditions to eliminate all sources of oxygen, including dioxygen, water, and oxy-

containing counter-ions. Next, the role of oxygen (2) was investigated by determining if 3-pyrroline-2-one could serve as a starting martial in the production of 2-phenylpyrrole. The radical nature of the iron-oxygen interaction (3) was tested by varying the radical scavenging ability of the catalyst used. Finally, the formation of μ-oxodiiron complexes under reaction conditions (4) was studied using absorbance spectroscopy. Overall this study provides a more detailed mechanism for the iron-catalyzed Suzuki-Miyaura C-C coupling process.

4.2 Results and discussion

4.2.1 ***[Fe^{3+}L2(Cl)$_2$]Cl*** as a stochiometric reagent in Suzuki-Miyaura type coupling

To determine if the iron-complexes act as a stoichiometric reagent in Suzuki-Miyaura type coupling, the iron catalyst **[Fe^{3+}L2(Cl)$_2$]Cl** was tested for the ability to produce 2-phenylpyrrole in the absence of oxygen. When **[Fe^{3+}L2(Cl)$_2$]Cl** was loaded at 100 mole% and the reaction was heated for 10 hours under anaerobic conditions (Table 4.1) no 2-phenylpyrrole was produced. Therefore, the coupling only occurs in the presence of an oxygen source, and a stoichiometric pathway does not need to be included in the catalytic mechanism. Interestingly, the use of **[Fe^{3+}L2(Cl)$_2$]ClO$_4$** at 100% loading under anaerobic conditions resulted in 16 ± 4% product formation. Indicating that the perchlorate counter-ion is capable of acting as sacrificial oxidant in iron catalysis. Although the perchlorate counter-ion was able to act as a sacrificial oxidant, a 1:1 mole ratio of perchlorate to iron was not able to produce comparable yields to those obtained when 10 mole% **[Fe^{3+}L2(Cl)$_2$]Cl** was used open to air (58 ± 7%). This can be explained in one of two ways: 1) the perchlorate is not as effective an oxidant as air or 2) more than one equivalent oxidant is required to facilitate one turnover.

Table 4.1. *Catalytic yields used to determine the role of the sacrificial oxidant in the coupling reaction.*

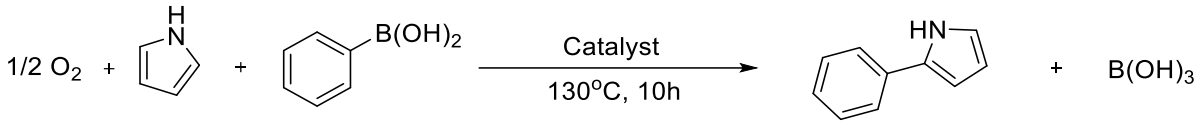

Loading	Catalyst	Oxidant	Yield (%)
10%	**$[Fe^{3+}L2(Cl)_2]Cl$**	air	58 ± 7
100%	**$[Fe^{3+}L2(Cl)_2]ClO_4$**	*	16 ± 4
100%	**$[Fe^{3+}L2(Cl)_2]Cl$**	*	Trace

* excluded

4.2.2 The role of oxygen in the catalytic cycle

After establishing the need for an oxidant, *vide infra*, an alternative mechanism to metal oxidation was considered. Specifically, pyrrole has been shown to oxidize to 3-pyrroline-2-one; therefore, oxidation of the reagent prior to entering the catalytic cycle was explored.[192] To evaluate this, 3-pyrroline-2-one was independently synthesized using a previously reported procedure in which hydrogen peroxide is used to oxidize pyrrole in the presence of $Ca(CO_3)_2$ (Scheme 4.1).[193] No 2-phenylpyrrole was isolated when 3-pyrroline-2-one was combined with phenylboronic acid in the presence of **$[Fe^{3+}L1(Cl)_2]^+$**. Based on these results, oxygen is required for oxidation chemistry with the iron and not the pyrrole substrate.

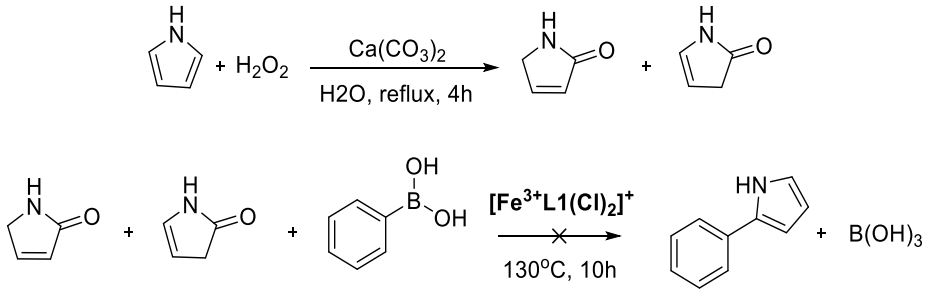

Scheme 4.1. *Synthesis 3-pyrroline-2-one as a potential starting material for pyrrole and phenylboronic acid coupling, 2-phenylpyrrole is not produced.*

4.2.3 Radical participation

Many catalytic processes progress through a mechanism involving radicals.[23, 194-195] Therefore, the catalytic coupling of pyrrole with phenylboronic acid was evaluated to determine if a radical species is involved. Previously, the ligands **L1**, **L2**, and **L3** were tested for radical scavenging ability using the DPPH (2,2-diphenyl-1-picrylhydrazyl) assay, which allows for analysis of radical scavenging ability in solution.[196-198] When DPPH is dissolved in ethanol an intense purple solution is obtained, with a corresponding absorbance band at 515 nm. The intensity of the absorbance band is concentration dependent, therefore, as radical scavenging systems react with DPPH the intensity of the absorbance band decreases. The decrease in intensity of the absorbance band at 515 nm is directly related to the radical scavenging ability of the test compound. Quantification of radical scavenging ability is obtained by comparison to a positive control such as BHT (2,6-di-tert-butyl-4-methylphenol). Ligands **L2** and **L3** were previously shown to be potent radical scavengers, but **L1** did not show any reactivity.[199-200] The radical scavenging activity of **L2** and **L3** was attributed to the pyridol moiety, which scavenges radicals in a similar manner to tannins. However, the radical scavenging activity of metal congeners was not explored. Therefore, a DPPH assay was performed with **$[Fe^{3+}L1(Cl)_2]^+$**, **$[Fe^{3+}L2(Cl)_2]^+$**, and **$[Fe^{3+}L3(Cl)_2]^+$** (Figure 4.1); complex **$[Fe^{3+}L1(Cl)_2]^+$** did not scavenge radicals at or below 0.75 mM. In contrast, **$[Fe^{3+}L2(Cl)_2]^+$** and **$[Fe^{3+}L3(Cl)_2]^+$** provided concentration-dependent radical scavenging activity at concentrations greater than 250 µM. The catalytic yields obtained in the presence of 198 mM **$[Fe^{3+}L1(Cl)_2]^+$**, **$[Fe^{3+}L2(Cl)_2]^+$**, and **$[Fe^{3+}L3(Cl)_2]^+$** were compared to the radical scavenging ability of a 1 mM solution of each complex (Table 4.2). Complex **$[Fe^{3+}L1(Cl)_2]^+$**, **$[Fe^{3+}L2(Cl)_2]^+$**,and **$[Fe^{3+}L3(Cl)_2]$** afforded 57 ± 3%, 58 ± 7%, and 52 ± 7% 2-phenylpyrrole and a 0%, 50%, and 50% reduction of the DPPH radical, respectively. Therefore, a radical process is not plausible because the radical scavenging activity differs among the iron complexes, but the catalytic yields for each are nearly identical.

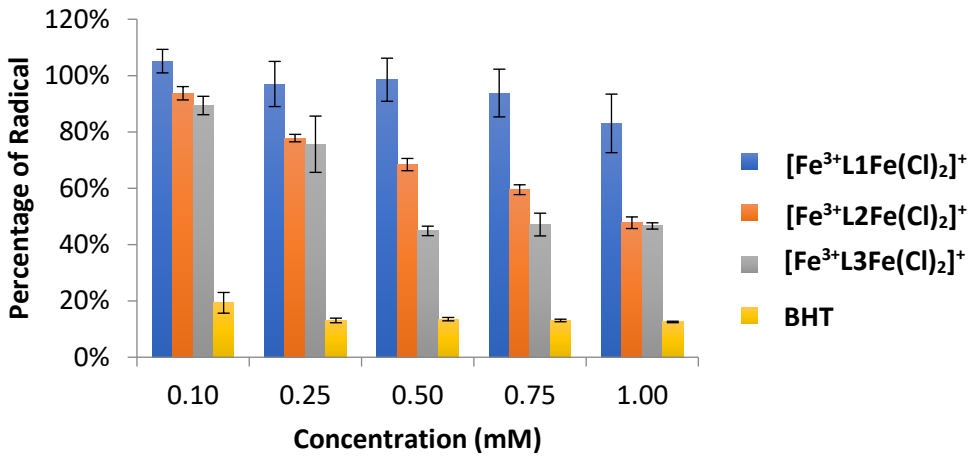

Figure 4.1. *DPPH assay showing radical scavenging ability of* ***$[Fe^{3+}L1(Cl)_2]^+$***, ***$[Fe^{3+}L2(Cl)_2]^+$***, *and* ***$[Fe^{3+}L3(Cl)_2]^+$***; *BHT serves as a positive control.*

Table 4.2*. Catalytic yields obtained for* ***$[Fe^{3+}L1(Cl)_2]^+$***, ***$[Fe^{3+}L2(Cl)_2]^+$***, *and* ***$[Fe^{3+}L3(Cl)_2]^+$***.*

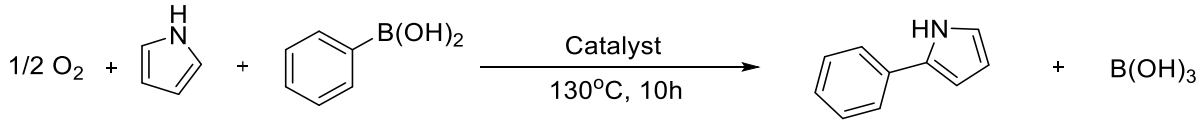

Catalyst	Yield (%)
$[Fe^{3+}L1(Cl)_2]^+$	57 ± 3
$[Fe^{3+}L2(Cl)_2]^+$	58 ± 7
$[Fe^{3+}L3(Cl)_2]^+$	52 ± 7

4.2.4 Implication and participation of μ-oxodiiron complexes in C-C coupling reactions

μ-oxodiiron complexes are known to play a role in oxygen atom transfer reactions, but their role in C-C coupling reactions has not been established.[26, 201-235] The complexes **$[Fe^{3+}L1(Cl_2)]^+$**, **$[Fe^{3+}L4(Cl_2)]^+$**, and **$[Fe^{3+}L7(Cl)_2]^+$** were explored due to the well-documented and facile formation of μ-oxodiiron complexes in solutions with a pH above 1.[236-238] In the presence of triethylamine and water, **$[Fe^{3+}L1(Cl_2)]^+$** and **$[Fe^{3+}L4(Cl_2)]^+$** readily formed μ-oxodiiron complexes **1** and **2** (Scheme 4.2). However, **$[Fe^{3+}L7(Cl)_2]^+$**

formed a monomeric species **3** (Scheme 4.2). The inability of **[Fe^{3+}L7$(Cl)_2$]$^+$** to form diiron species under basic conditions expands on previous reports that dimer formation is not observed upon oxidation of the iron(II) complex to the iron(III) in the presence of O_2.[147, 236-237] The participation of a μ-oxo dimer in the catalytic mechanism is unlikely because increased catalytic yields were observed with **[Fe^{3+}L7$(Cl)_2$]$^+$** compared to **[Fe^{3+}L1(Cl_2)]$^+$** and **[Fe^{3+}L4(Cl_2)]$^+$**. The μ-oxo complexes **1** and **2** (Figure 4.2) were characterized by single crystal X-ray diffraction, NMR, and absorbance spectroscopy, which are discussed in depth below. Moreover, the absorbance spectra of **[Fe^{3+}L1(Cl_2)]$^+$** in the presence of pyrrole showed the formation of **1.** Therefore, **1** and **2** are assigned as off-cycle species that decrease catalytic efficiency of **[Fe^{3+}L1(Cl_2)]$^+$** and **[Fe^{3+}L4(Cl_2)]$^+$**.

4.2.5 Reactivity of [Fe^{3+}L1(Cl_2)]$^+$, [Fe^{3+}L4(Cl_2)]$^+$, and [Fe^{3+}L7$(Cl)_2$]$^+$ with Et_3N and H_2O

As noted above, **[Fe^{3+}L1$(Cl)_2$]$^+$**, **[Fe^{3+}L4$(Cl)_2$]$^+$**,and **[Fe^{3+}L7$(Cl)_2$]$^+$** were treated with Et_3N in the presence of water in either methanol (**[Fe^{3+}L1$(Cl)_2$]$^+$**) or acetonitrile (**[Fe^{3+}L4$(Cl)_2$]$^+$**and **[Fe^{3+}L7$(Cl)_2$]$^+$**) as shown in Scheme 4.2. Dimers **1** (**[μ-O(Fe^{3+}L1Cl)$_2$]$^{2+}$**) and **2** (**[μ-O(Fe^{3+}L4Cl)$_2$]$^{2+}$**), as well as, monomer **3** (**[Fe^{3+}L7(Cl)(OH)]$^+$**) were isolated from the reaction mixtures as X-ray quality crystalline materials. Complex **1** crystalized in two separate forms, **1a** and **1b**, depending on the solvent used for crystal growth. Due to the small amount (3 mg) of **[Fe^{3+}L7$(Cl)_2$]$^+$** available, the only characterization possible on complex **3** was solid state determination.

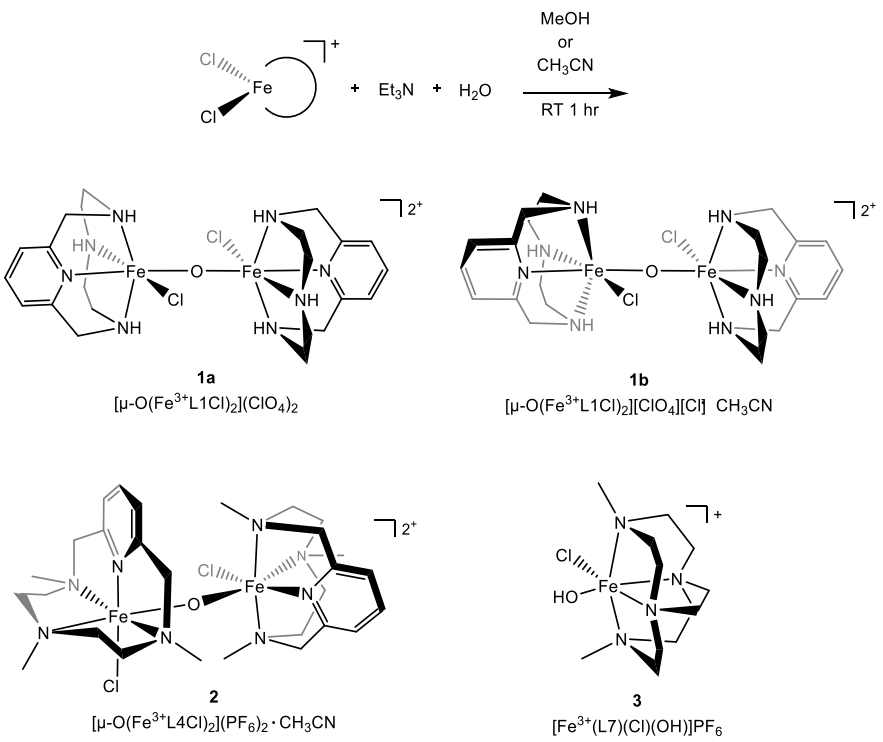

Scheme 4.2. *Synthesis and structures of **1** and **2**, and monomer **3**.*

*4.2.6 Solid-state structure determination of **1**, **2**, and **3**.*

The solid-state structures of **1a**, **1b**, **2**, and **3** are shown in Figure 4.2 and selected bond lengths and angles are in Table 4.3. X-ray quality crystals of **1a** were obtained by slow evaporation of methanol; isolation of the X-ray quality crystals resulted in a 50% yield. The crystals of **1a** were dark brown with a brick morphology. Several unsuccessful attempts were made to slow the crystallization process, to eliminate the presence of disorder, twinning, and pseudo-symmetry found when crystals were grown by slow evaporation at room temperature. The twinning and pseudo-symmetry were identified using the program PLATON. The diffraction data for **1a** was refined in the space group C2 rather than C2/m, because the crystallographic data did not support a centrosymmetric system. Like **$[Fe^{3+}L1(Cl)_2]^+$**, the ferric iron took on a *cis*-distorted octahedral geometry in which the equatorial plane was occupied by two nitrogen atoms of the macrocycle, a bridging-oxide, and a chloride; the axial positions were filled by the two remaining nitrogen atoms in the macrocycle completing the coordination sphere.

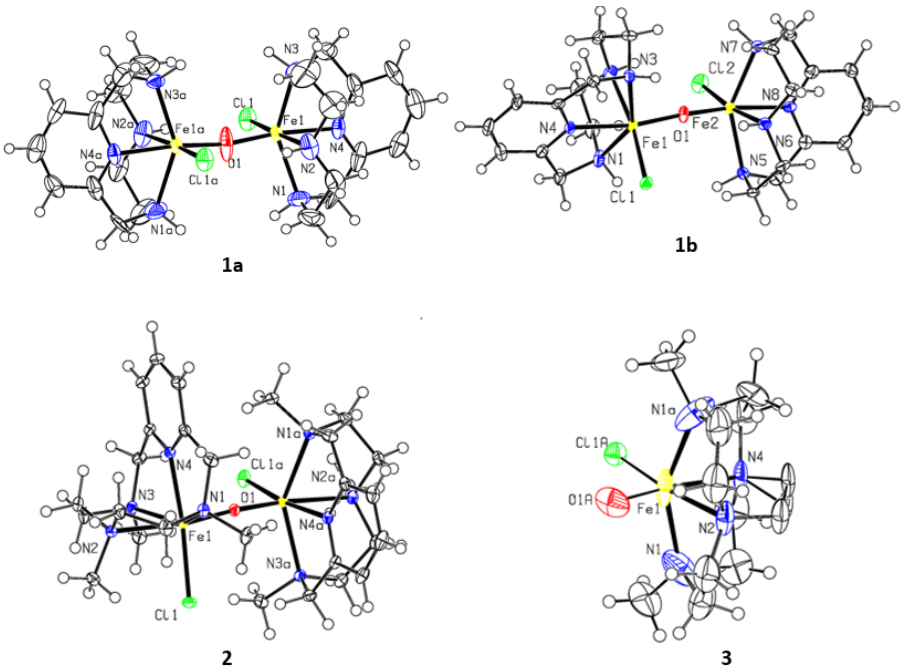

Figure 4.2. *ORTEP (50% TELP) representation of solid-state structure of* ***1a****,* ***1b****,* ***2****, and* ***3****. Counter-ions and solvent molecules have been removed for clarity.*

Table 4.3. *Selected bond lengths and angles for* ***1a****,* ***1b****,* ***2****, and* ***3****.*

Bond Length (Å)	**1a**	**1b**	**2**	**3**	Bond Length (Å)	**1b'**
Fe(1)-O(1)	1.765(3)	1.775(4)	1.80035(16)	1.75(3)	Fe(2)-O(1)	1.782(4)
Fe(1)-Cl(1)	2.3230(15)	2.3298(17)	2.2857(3)	2.283(8)	Fe(2)-Cl(2)	2.3279(19)
Fe…Fe	3.592	3.533	3.592	-		
Bond Angle (°)	**1a**	**1b**	**2**		Bond Angle (°)	**1b'**
Fe-O(1)-Fe	171(2)	166.7(3)	171.91(6)	-	Fe(1)-O(1)-Fe(2)	166.7(3)
Twist Angle	0*	35.53(4)	90*	-		

*Assigned based on point group symmetry

Table 4.4. *Crystal data, intensity collections, and structure refinement parameters* ***1a***, ***1b***, ***2,*** *and* ***3****.*

Complex	**1a**	**1b**	**2**	**3**
Formula	$C_{22}H_{36}Cl_4Fe_2N_8O_9$	$C_{24}H_{39}Cl_4Fe_2N_9O_5$	$C_{32}H_{54}Cl_2F_{12}Fe_2N_{10}OP_2$	$C_{12}H_{19}Cl_{1.5}F_4FeN_4O_{2.83}P_{0.67}$
M.W.	810.09	787.14	1067.39	470.32
Unit cell	Monoclinic	Tetragonal	Monoclinic	Hexagonal
Space group	C2	$I4_1/a$	C2/c	$P6_3/m$
a (Å)	12.6640(7)	31.963(2)	14.6320(8)	13.5637(16)
b (Å)	10.3637(6)	31.963(2)	13.1936(7)	13.5637(16)
c (Å)	12.2668(7)	12.5812(10)	23.4564(13)	17.377(2)
α	90°	90°	90°	90°
β	103.254(2)°	90°	92.817(2)°	90°
γ	90°	90°	90°	120°
Volume ($Å^3$)	1567.08(15)	12854(2)	4522.8(4)	2768.6(8)
Z	2	16	4	6
$D_{calc.}$(g/cm^3)	1.717	1.627	1.568	1.692
Reflections Collected	32172	134293	86353	66760
Independent Reflections	3063	6578	6649	1636
R_{int}	0.0516	0.1629	0.0257	0.0731
Completeness to θ	99.3%	99.8%	99.7%	100%
GooF	1.041	1.144	1.082	2.221
R1,wR2 [I>2sigma(I)]	R1 = 0.0429 wR2 = 0.0965	R1 = 0.0926 wR2 = 0.1619	R1 = 0.0223 wR2 = 0.0544	R1 = 0.1529 wR2 = 0.4561
R1, wR2	R1 = 0.0648 wR2 = 0.1072	R1 = 0.1194 wR2 = 0.1729	R1 = 0.0249 wR2 = 0.0561	R1 = 0.1686 wR2 = 0.47211

The asymmetric unit of **1a** consisted of half of the molecule (O-Fe^{3+}L1(Cl)) and two perchlorate counter-ions. The complete complex is symmetry generated by a two-fold rotation about the oxygen atom, resulting in a 180° twist angle between the two pyridine moieties of the **L1** backbone. The Fe-O bond

length, Fe(1)-O-Fe(1A) bond angle, and Fe…Fe distance (1.765(3) Å, 170.30°, 3.592 Å, respectively) are consistent with previously reported μ-oxodiiron species containing chloride ligands.[211, 236]

The inability to avoid twinned crystals of **1a** using slow evaporation of methanol prompted us to investigate other crystal growth conditions. The slow diffusion of ether into a solution of **1a** in CH_3CN afforded dark brown brick shaped X-ray quality crystals that formed in the $I4_1/a$ point group. The asymmetric unit consisted of the diiron(III) complex (L1ClFe-O-FeL1Cl), a perchlorate counter-ion, a chloride counter-ion, and a molecule of CH_3CN. This was the first indication that **1** may exist in multiple isomers. The orientation of the ligands with respect to one another was quantified by the twist angle between the pyridine moieties. The twist angle of **1b** was 35.53(4)°, a difference of 144° compared to **1a**. Otherwise, the Fe(1)-O bond length (1.775(4) Å), the Fe(2)-O bond length (1.782(4) Å), Fe(1)-O-Fe(2) bond angle (166.7(3)°), and the Fe...Fe distance (3.533 Å) are comparable to **1a**. The ability to isolate multiple solid-state species of **1** indicated that multiple isomers may be thermodynamically similar in energy.

X-ray quality crystals of **2** were obtained by slow diffusion of ether into CH_3CN at room temperature. A 55% yield was achieved by isolation of the brown brick-shaped crystals. As shown in Figure 4.2, the complex crystalized in the space group C2/c and a *cis*-folded octahedral geometry. The *cis*-coordination sites of both ferric ions were filled by a μ-oxide and a chloride ligand. The asymmetric unit of **2** resembled that of **1a** rather than **1b**, and consisted of one half of the dimer, two PF_6 counter-ions, and a molecule of CH_3CN. The oxygen atom was positioned on a 2_1-screw axis resulting in a 90° twist angle between the pyridine moieties. The Fe(1)-O bond length (1.775(4) Å), Fe(2)-O bond length (1.782(4) Å), Fe(1)-O-Fe(2) bond angle (166.7(3)°), and Fe...Fe distance (3.592 Å) were consistent with those observed in **1a** and **1b.**

Slow evaporation of the reaction solution containing CH_3CN, triethylamine, water, and $\mathbf{[Fe^{3+}L7(Cl)_2]^+}$ resulted in red plate-shaped X-ray quality crystals of **3**. The solid-state structure, shown in

Figure 4.2, indicated that **3** is a stable ferric hydroxide containing species, **[Fe^{3+}L7(OH)(Cl)]$^{+}$**. The asymmetric unit consisted of half of the molecule (L7$_{1/2}$Fe(O)(Cl)), two water molecules, and one-third of the PF_6 counter-ion. Over half of the molecule exhibits disorder and two solvent water molecules are located on a special position (Figure A15). The combination of many distorted atoms and the presence of water molecules on special positions explains the unfavorable statistical values corresponding the refinement model (Table 4.4). Therefore, this is considered an accurate representation of the complex. The presence of an Fe-OH bond was supported by the Fe(1)-O(1a) bond length of 1.75(3) Å, which is much longer than a typical Fe(IV)=O bond (1.6 Å) and much shorter than an Fe(III)-Cl bond (2.3 Å).[239-241]

The higher catalytic efficiency of **[Fe^{3+}L7(Cl)$_2$]$^{+}$** compared to **[Fe^{3+}L1(Cl)$_2$]$^{+}$** and **[Fe^{3+}L4(Cl)$_2$]$^{+}$** in combination with the stability of **[Fe^{3+}L7(OH)(Cl)]$^{+}$**, suggested that the active catalytic species is an iron(III) hydroxide or an iron(V)-oxo species. Attempts to spectroscopically characterize or isolate a high valent species were unsuccessful. However, Serrano-Plana *et al.* have reported an acylperoxo-Fe(III) in equilibrium with an oxo-Fe(V) when **[Fe^{2+}L4(OTf)$_2$]** is exposed to excess peracetic acid.[17]

*4.2.7 ^{1}H-NMR analysis of **1a** and **2**.*

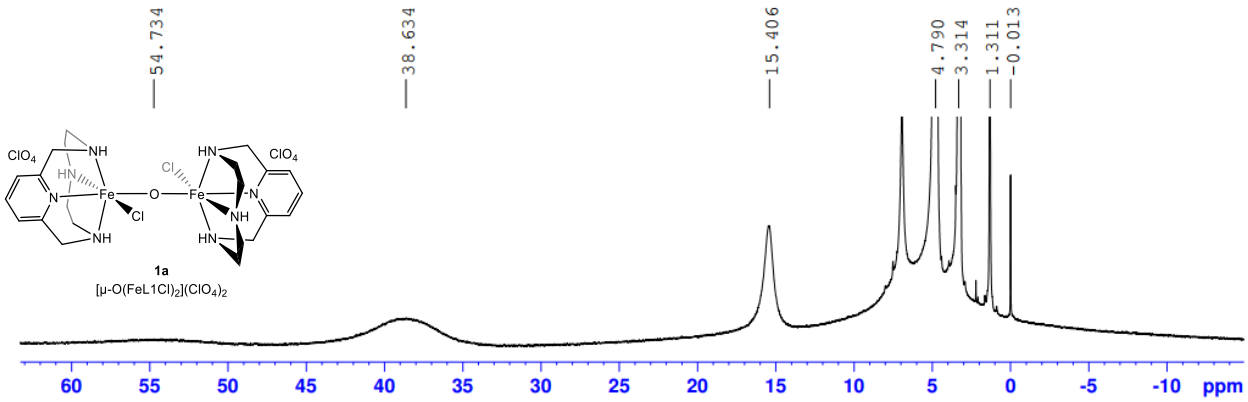

Figure 4.3. *^{1}H-NMR of **1a** in MeOD.*

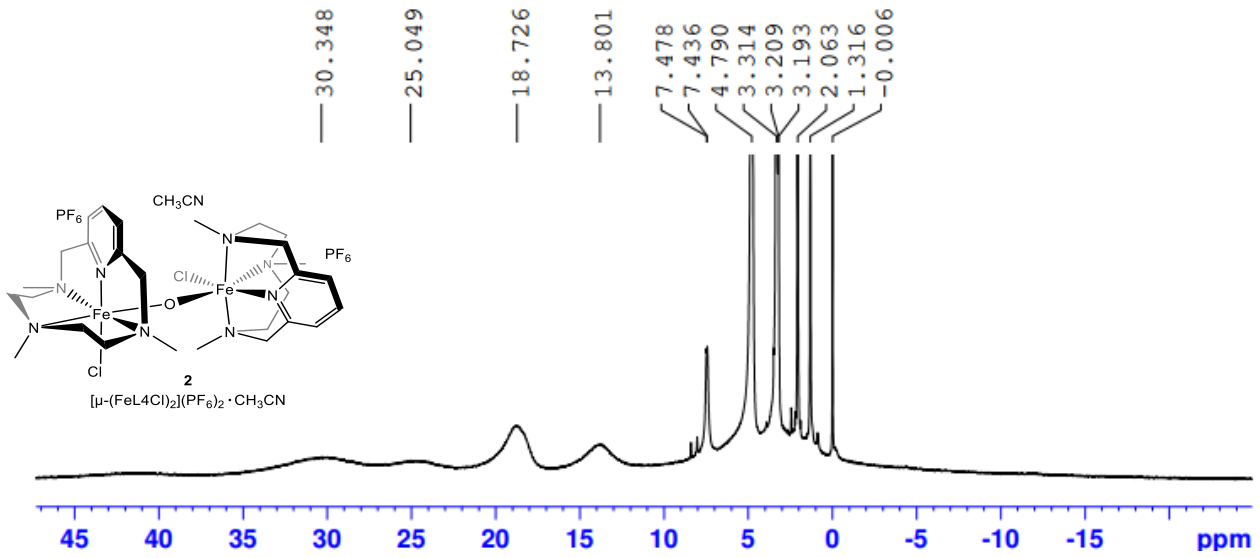

Figure 4.4. *^{1}H-NMR of **2** in MeOD.*

The stability and magnetic properties of **1** and **2** in methanol were studied using ^{1}H-NMR (Figure 4.3 and 4.4). Both complexes exhibit resonances between 0-40 ppm. The presence of paramagnetically shifted resonances indicated that the dimers are stable in methanol because the monomeric congeners of **1** and **2** are not visible by NMR. Furthermore, the observation of resonances at 40 ppm are typical for large antiferromagnetically coupled iron centers.[223]

*4.2.8 Absorbance analysis of **1a** and **2** in MeOH and CH_3CN*

The absorbance spectra of μ-oxodiiron(III) complexes have been shown to exhibit three types of transitions in the visible region: an allowed oxo-Fe charge transfer (LMCT) (300-400 nm), d-d transition (400-550 nm), and a forbidden oxo-Fe CT (550-700 nm).[238] The allowed oxo-Fe CT is believed to alter the electronics of μ-oxodiiron(III) complexes in such a way that the spin forbidden d-d and oxo-Fe CT are observed. This principle is explained fully in reference 242 and summarized here. The identity of the transitions were assigned based on the analysis of absorbance spectra of a series of $[Fe_2(TPA)_2O(L)](ClO_4)_n$ complexes; variations in the ligand field strength of L resulted in Fe-O-Fe bond angles ranging from 125° to 180°.[242] The series of $[Fe_2(TPA)_2O(L)_2](ClO_4)_n$ complexes exhibited a band at

490 nm indicating that this transition was not affected by the Fe-O-Fe angle or ligand field strength. Therefore, the transition was assigned as a spin-forbidden $^6A_1 \rightarrow (^4E$ and $^4A_1)$, because the d^5 Tanabe-Sugano diagram showed that the energy of two states, ^4E and $^4A_1$, are independent of ligand field strength in high-spin complexes. This transition was assigned as a forbidden oxo-Fe CT Because the absorbance bands between 550-700 nm varied with Fe-O-Fe angle and are accompanied by a low extinction coefficient. For linear μ-oxodiiron(III) complexes absorbance bands at 550-580 nm are expected corresponding to a d-d and oxo-Fe CT transition.[211, 223, 238, 242]

***Table 4.5**. Absorbance data and transition assignments for **$[Fe^{3+}L1(Cl)_2]^+$**, **$[Fe^{3+}L4(Cl)_2]^+$**, **1a**, and **2** in acetonitrile, and **$[Fe^{3+}L1(Cl)_2]^+$** and **1a** in methanol.*

Complex	λ in nm (ε in $M^{-1}cm^{-1}$)			
Acetonitrile	MLCT	Allowed oxo-Fe CT	$^6A_1 \rightarrow (^4E, ^4A_1)$	oxo-Fe CT
$[Fe^{3+}L1(Cl)_2]^+$	319 (4 500)	390 (sh; 1 600)		
$[Fe^{3+}L4(Cl)_2]^+$	326 (5 000)	408 (sh; 1 400)		
1a	335 (10 000)*	381 (sh, 6 0863)	481 (932), 500 (878)	
2	332 (sh; 13 000)*	385 (10 000)*	495 (sh; 51)	567 (sh; 161)
Methanol				
$[Fe^{3+}L1(Cl)_2]^+$	319 (4 200)	390 (sh; 1 400)		
1a	330 (sh; 3 500)		500 (170)	

* MLCT & oxo-LMCT

Solid-state analysis showed that the use of methanol and acetonitrile for crystal growth resulted in two different complexes, **1a** (MeOH) and **1b** (CH_3CN). Examination of the Fe-O-Fe bond angle indicated that the absorbance spectra of **1a** would vary in MeOH vs CH_3CN, if **1a** and **1b** persist as independent species in solution. Therefore, the absorbance spectra of **1a** was obtained in MeOH and CH_3CN. The absorbance maxima are available in Table 4.5 and the absorbance spectra are shown in Figures 4.5 and 4.6, for MeOH and CH_3CN, respectively. When dissolved, the brown solution of **1a** exhibited absorbance bands between 330 and 600 nm. The allowed oxo-Fe charge transfer band of **1a**

was observed at 330 nm (3 500 M^{-1} cm^{-1}) in MeOH and 335 nm (10 000 $M^{-1}cm^{-1}$) in CH_3CN. In MeOH, the absorbance band at 500 nm (170 M^{-1}, cm^{-1}) was consistent with a $^6A_1 \rightarrow (^4E, ^4A_1)$ transition, however, in CH_3CN two absorbance bands are observed (481 nm, ε = 932 M^{-1}, cm^{-1}; 500 nm ε = 878 M^{-1}, cm^{-1}). The extinction coefficient observed in CH_3CN is inconsistent with a d-d transition and cannot be assigned at this time. However, computational studies are currently under way to determine species responsible. The forbidden oxo-Fe CT was not observed in methanol or acetonitrile.

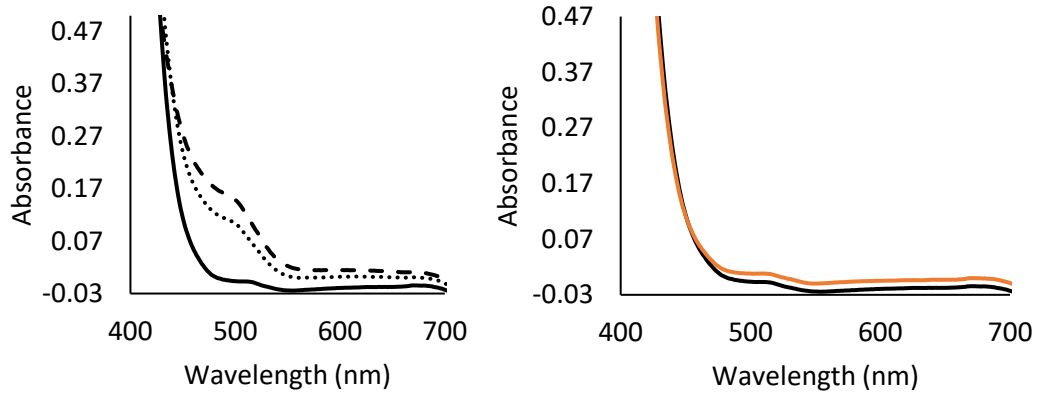

Figure 4.5 .(left) *Visible spectra of **1a** in methanol (dashed-line), **[Fe^{3+}L1(Cl)$_2$]$^+$** in 8% water/methanol (dotted-line), and **[Fe^{3+}L1(Cl)$_2$]$^+$** in 8% water/methanol/25 µL acid (solid-line).* (right) *Visible absorbance spectra of **[Fe^{3+}L1(Cl)$_2$]$^+$** in CH_3CN (tan) and 8% water/methanol solution after addition of 25 µL $HCl_{con.}$ (black).*

Attempts to compare spectra of **[Fe^{3+}L1(Cl)$_2$]$^+$** to **1a** in methanol were limited by solubility. Therefore, an 8% water/methanol solution was used to dissolve **[Fe^{3+}L1(Cl)$_2$]$^+$**. An absorbance band at 498 nm was observed, indicating that **1a** forms in the presence of water as (Figure 4.5). The addition of 25 µL of concentrated HCl resulted in the disappearance of the band at 498 nm, confirming the existence of an equilibrium between **1a** and **[Fe^{3+}L1(Cl)$_2$]$^+$**.

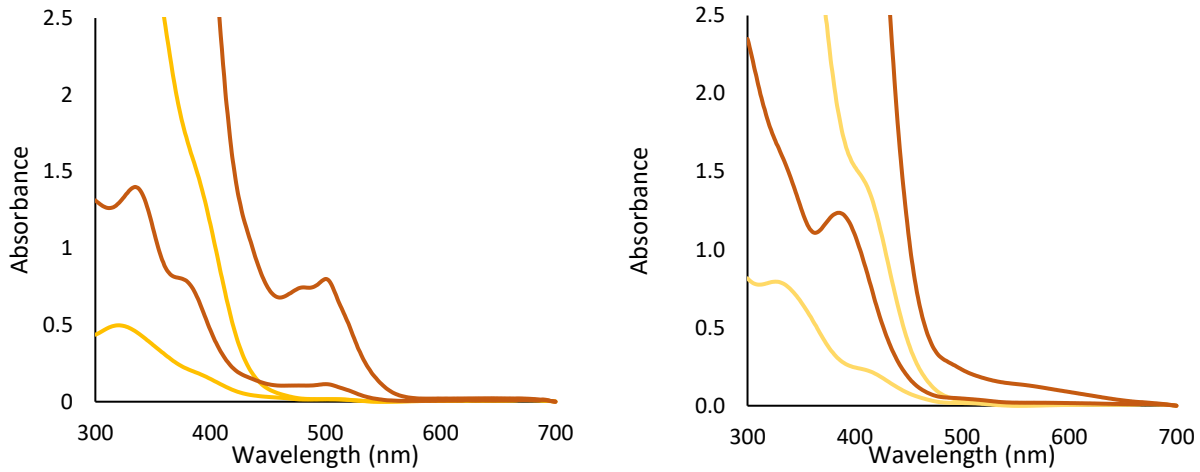

Figure 4.6. *The absorbance spectra of complexes* (left) ***[Fe^{3+}L1(Cl)$_2$]$^+$*** *(0.13 mM/0.94 mM) and* ***1a*** *(0.13 mM/ 0.99 mM);* (right) ***[Fe^{3+}L4(Cl)$_2$]$^+$*** *(0.16 mM/ 1.0 mM) and* ***2*** *(0.12 mM/1.0 mM) in CH_3CN. Monomers are represented in orange and dimers in yellow.*

Acetonitrile solutions of **[Fe^{3+}L1(Cl)$_2$]$^+$** and **[Fe^{3+}L4(Cl)$_2$]$^+$** were pale yellow, while **1a** and **2** were brown. The absorbance data can be found in Figure 4.6 and Table 4.5. Two LMCT bands are observed: **[Fe^{3+}L1(Cl)$_2$]$^+$**, at 319 nm (4 500 $M^{-1}cm^{-1}$) and 390 nm (sh; 1 600 $M^{-1}cm^{-1}$); and **[Fe^{3+}L4(Cl)$_2$]$^+$**, at 326 nm (5 000 $M^{-1}cm^{-1}$) and 408 nm (sh; 1 400 $M^{-1}cm^{-1}$). No other absorbance bands were observed for, **[Fe^{3+}L1(Cl)$_2$]$^+$** and **[Fe^{3+}L4(Cl)$_2$]$^+$**. Complexes **1a** and **2** exhibited four absorbance bands between 300 and 700 nm, which are consistent with other μ-oxodiiron(III) complexes.[211, 223, 242] The formation of an Fe-O-Fe bridged complex greatly increased the extinction coefficient of bands between 300 – 410 nm. This is attributed to a two-fold increase in iron atom concentration in combination with the additive effect of the LMCT and the oxo-Fe CT transitions. The signature absorbance bands at 490 nm and 550 nm corresponding to the forbidden $^6A_1 \rightarrow (^4E, {}^4A_1)$ and oxo-Fe CT are observed at 481 nm (932 $M^{-1}cm^{-1}$) and 500 nm (878 $M^{-1}cm^{-1}$) for **1a** and 495 nm (sh; 51 $M^{-1}cm^{-1}$) and 567 (sh; 161 $M^{-1}cm^{-1}$) for **2**.

4.2.9 Pyrrole promoted dimerization of ***[Fe^{3+}L1(Cl)$_2$]$^+$***

Finally, the ability of pyrrole to promote formation of **1a** was tested. Interestingly, the addition of up to 4 equivalents of pyrrole had no effect on the absorbance spectra of **[Fe^{3+}L1(Cl)$_2$]$^+$**, but the

addition of excess pyrrole, 200 µL (800 eq.), resulted in dimer formation based on the appearance of an absorbance band at 498 nm upon pyrrole addition (Figure 4.7). The conversion of monomeric iron complexes into µ-oxodiiron complexes may occur in the presence of excess water. Therefore, the large excess of pyrrole needed is most likely due to the low water continent in the pyrrole, however, the 200 µL used is 1/5th of the amount used during the catalytic reaction. These results indicate dimer formation can be promoted under coupling reaction conditions, due to the presence of water in the pyrrole used. In the catalytic cycle, complexes **1a** and **2** are assigned as off-cycle species. Therefore, the formation of **1a** and **2** may attribute to the decreased activity of **$[Fe^{3+}L1(Cl)_2]^+$** and **$[Fe^{3+}L4(Cl)_2]^+$** compared to **$[Fe^{3+}L7(Cl)_2]^+$** in the coupling of pyrrole and phenylboronic acid.

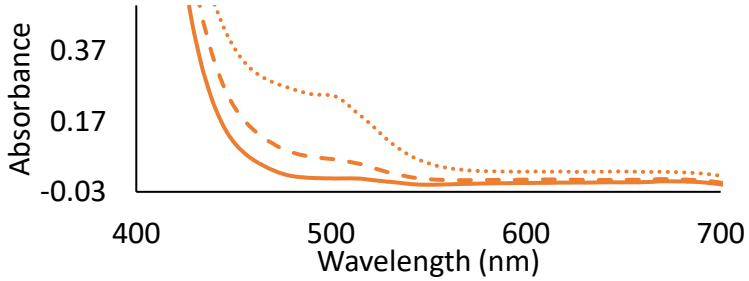

Figure 4.7. *Absorbance spectra of* ***$[Fe^{3+}L1(Cl)_2]^+$*** *in acetonitrile (solid-line),* ***$[Fe^{3+}L1(Cl)_2]^+$*** *after the addition of 200 µL pyrrole (dashed-line), and* ***$[Fe^{3+}L1(Cl)_2]^+$*** *after addition of 700 µL pyrrole (dotted-line) showing the effect of addition of excess pyrrole to* ***$[Fe^{3+}L1(Cl)_2]^+$*** *in CH_3CN. Under reaction conditions pyrrole promotes the formation of* ***1a*** *and other species.*

The identification of dimer formation in the presence of pyrrole, the need for oxygen, the inability of oxidized pyrrole to act as a starting material to produce 2-phenylpyrrole, and the fact that radical scavenging catalysts **$[Fe^{3+}L2(Cl)_2]^+$** and **$[Fe^{3+}L3(Cl)_2]^+$** give comparable yields to **$[Fe^{3+}L1(Cl)_2]^+$**. Have led to a more detailed mechanism shown in Scheme 4.3. Specifically, both possible oxidation state of the active catalyst and the off-cycle µ-oxodiiron species are represented.

4.3 Conclusion

In conclusion, it has been shown that an oxidant is needed in the iron(III)-catalyzed Suzuki-Miyaura C-C coupling reactions. Air and perchlorate are viable sacrificial oxidants; however, more experiments are needed to understand the true reactivity of perchlorate as a sacrificial oxidant. Oxidized pyrrole was tested and found unable to react with phenylboronic acid to produce 2-phenylpyrrole, thereby, implicating oxygen reacts with the iron center. Furthermore, the presence of radical scavengers in the form of complexes **$[Fe^{3+}L2(Cl)_2]^+$** and **$[Fe^{3+}L3(Cl)_2]^+$** did not decrease catalytic yields. Therefore, the participation of an iron(IV) species has been ruled out. The monomeric iron complexes **$[Fe^{3+}L1(Cl)_2]^+$** and **$[Fe^{3+}L4(Cl)_2]^+$** readily form μ-oxodiiron species in the presence of a base and water. The more topologically constrained **$[Fe^{3+}L7(Cl)_2]^+$** does not form a dimeric complex, but instead one chloride is replaced with a hydroxide. The formation of **$[Fe^{3+}L7(Cl)(OH)]^+$** is consistent with the first step in the proposed mechanism of μ-oxodiiron formation. Comparison of the absorbance spectra of **1a** in acetonitrile to that of the monomer **$[Fe^{3+}L1(Cl)_2]^+$** after addition of pyrrole, indicates that **1a** can form during the coupling of pyrrole and phenylboronic acid. The μ-oxodiiron species (**1** and **2**) are assigned as off-cycle complexes that lowers catalytic yield, because **$[Fe^{3+}L1(Cl)_2]^+$** affords less 2-phenylpyrrole than **$[Fe^{3+}L7(Cl)_2]^+$**. Additionally, it is known that the formation of μ-oxodiiron complexes proceeds through an $Fe^{3+}OH$ species. Therefore, iron-catalyzed Suzuki-Miyaura C-C coupling may include an $Fe^{3+}OH$ or an Fe(V)-O as the catalytically active species.[238] The studies presented here have resulted in experimental evidence to develop a more detailed catalytic mechanism for the coupling of pyrrole and phenylboronic acid in the presence of an iron(III) catalyst. To fully understand the catalytic process kinetic studies such as those reported by Blackmond are needed.[243]

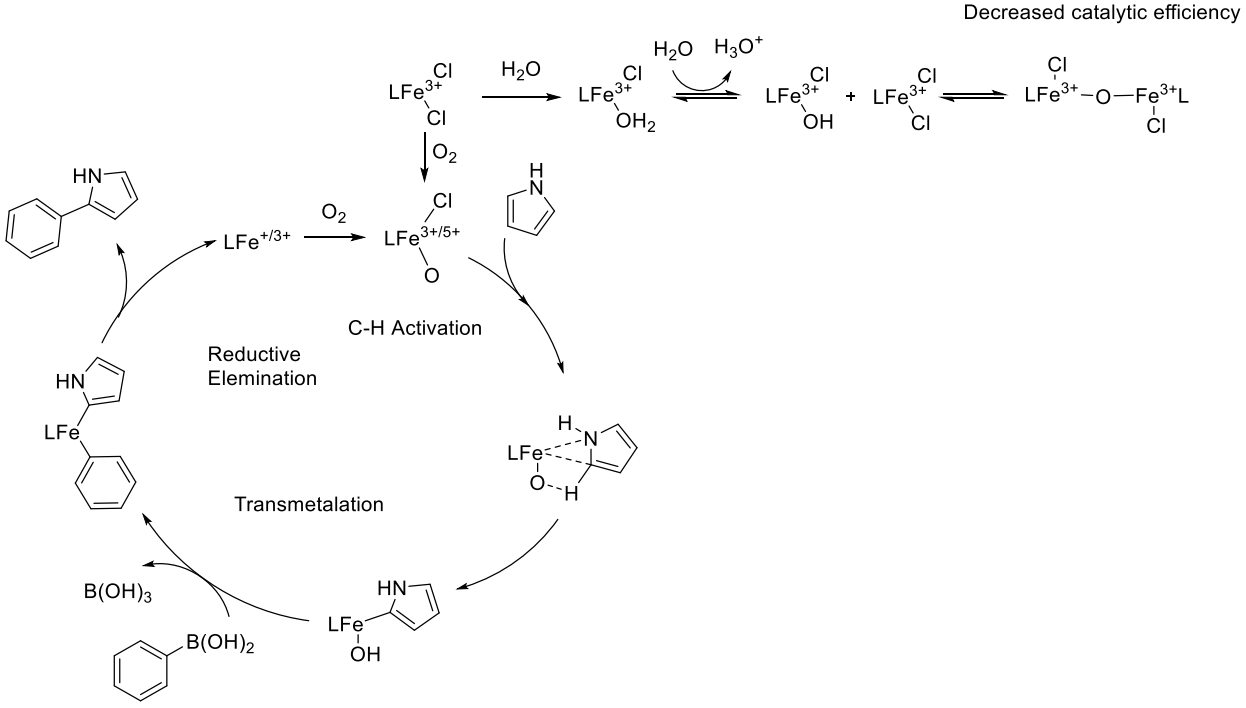

Scheme 4.3*. More detailed catalytic mechanism proposed for iron-catalyzed Suzuki-Miyaura C-C coupling.*

4.4 Experimental methods

General methods: Pyrrole was distilled before use, all other reagents were obtained from commercial sources and used as received, unless noted otherwise. NMR spectra were obtained on a 400-MHz Bruker Avance spectrometer, using deuterated solvents (MeOD, D_2O). NMR spectra were referenced using the corresponding solvent resonance (in parts per million; MeOD δ =3.31 D_2O δ = 4.79).[154] Elemental analysis was performed by Canadian Microanalytical Service Ltd. Electronic absorption spectra were recorded on a Cary 60 UV-vis spectrophotometer using a 3 mL quartz cuvette with a 1 cm path length. **Caution!** Perchlorate salts are explosive and should be handled in small quantities. In particular, such compounds should never be heated as solids.

X-ray diffraction analysis: Crystal diffraction data were collected at 100 K on a Bruker D8 Quest Diffractometer. Data collection, frame integration, data reduction (multi-scan), and structure

determination were carried out using APEX3 software.[162] Structural refinements were performed with XSHELL (v 6.3.1), by the full-matrix least-squares method.[163] All non-hydrogen atoms were refined using anisotropic thermal parameters, while the hydrogen atoms were treated as mixed. The ORTEP molecular plots (50 %) were produced using PLATON.

[μ-O(FeL1Cl)$_2$](ClO$_4$)$_2$ (**1a**) : Crystalline **[Fe^{3+}L1(Cl)$_2$]ClO$_4$** (34.0 mg, 0.08 mmol) was dissolved in 1 ml water and diluted with 5 ml methanol. Triethylamine (10.9 μL, 0.0786 mmol) was dissolved in 600 μL of methanol and added dropwise to **[Fe^{3+}L1(Cl)$_2$]ClO$_4$**. The solution was stirred for 1hr, followed by slow evaporation of solvent to afford black X-ray quality crystals over the course of several days. Yield: 100 % (32.0 mg, 0.04 mmol). Elemental analysis Calc (Found): $C_{22}H_{36}Cl_4Fe_2N_8O_9$: C 32.62 (32.22); H 4.48 (4.50); N 13.83 (13.70). CCDC # 1578765.

[μ-O(FeL4Cl)$_2$](PF$_6$)$_2$·CH$_3$CN (**2**): Complex **[Fe^{3+}L4(Cl)$_2$]PF$_6$** (39.7 mg, 0.076 mmol) was dissolved in 12.5 μL water and 1 mL CH_3CN. Triethylamine (16.17 μL, 0.116 mmol) was dissolved in 300 μL CH_3CN and added dropwise to [**Fe^{3+}L4(Cl)$_2$]PF$_6$**. The reaction was stirred for 1 hour, then placed in ether. Black X-ray quality crystals formed over the course of six hours. Yield: 55.2% (22.8 mg, 0.021 mmol). Elemental analysis Calc (Found): $C_{30}H_{51}N_8Fe_2Cl_2OP_2F_{12}$: C 35.11 (35.50); H 5.01 (5.09); N 12.28 (12.81). CCDC # 1813235.

2-phenylpyrrole yield determination: Phenylboronic acid (24 mg, 0.2 mmol) and crystalline material of the iron complex (0.02 mmol) were added to a 20 mL vial equipped with a stir bar in a glovebox. Degassed pyrrole (1 mL) was added to flask, the mixture was heated to 130^{o}C for 10 hours. The reaction was cooled to room temperature and the pyrrole was removed under vacuum until no visible liquid was present. Increasing the time the reaction was kept under reduced pressure decreased yields. The product mixture was dissolved in a minimum amount of

$CDCl_3$, 5 µL of dimethyldiphenylsilane was added to the solution. The solution was filtered through a 0.2 µm nylon filter and a known amount of sample was added to a pre-weighed NMR tube. Yield determinations were performed using three resonances 6.875, 6.532, and 6.307 ppm corresponding to 2-phenylpyrrole and a resonance at 0.533 ppm corresponding to dimethyldiphenylsilane. The reported values are averages of all resonances; each measurement was run in triplicate.

Coupling reactions oxidation amount controlled: Phenylboronic acid (24 mg, 0.20 mmol) and catalyst (0.02 mmol, 0.20 mmol), if used, were added to a 2 mL flask equipped with a stir bar, the system was then placed under an atmosphere of nitrogen. Pyrrole (1ml) was added to flask and the mixture was heated to 130°C for 10 hours.

3-pyrroline-2-one coupling reactions: *Open to Air*: Phenylboronic acid (24 mg, 0.20 mmol) and **[Fe^{3+}L1$(Cl)_2$]ClO_4** (8 mg, 0.02 mmol) were added to a test tube equipped with a stir bar. 3-pyrroline-2-one (1 mL) was added to flask and the mixture was heated to 130 °C. After 10 hours at refluxed the reaction was cooled to room temperature, the crude product was dried under reduced pressure until no visible liquid was present. NMR of the crude reaction showed no formation of 2-phenylpyrrole. *Inert atmosphere*: Phenylboronic acid (24 mg, 0.20 mmol) and **[Fe^{3+}L1$(Cl)_2$]ClO_4** (8 mg, 0.02 mmol) were added to a 2 mL reaction vessel equipped with a stir bar, the system was placed under an inert atmosphere using Schlenk techniques, 1 mL 3-pyrroline-2-one was added and the system was heated to 130°C for 10 hour. Formation of 2-phenylpyrrole was not observed.

DPPH assay: A 2,2-diphenyl-1-picrylhydrazyl (DPPH) stock solution was made by dissolving 25 mg of DPPH in 100 mL of absolute EtOH. The solution was standardized to 1.32 absorbance units (0.137 mM) by dilution with absolute ethanol. 1 mg of each complex was dissolved in 2 mL of water to yield the following concentrations: 1.2 mM **$[Fe^{3+}L1(Cl)_2]ClO_4$**, 1.4 mM **$[Fe^{3+}L2(Cl)_2]ClO_4$**, 1.0 mM **$[Fe^{3+}L3(Cl)_2]ClO_4$**. The pH was adjusted with HCl gas to dissolve the compounds in water. 1 mg of BHT was dissolved in 2 mL of absolute EtOH to make a 2.3 mM stock solution of BHT. Each complex and BHT were diluted to reach the following concentrations: 0.75 mM, 0.5 mM, 0.25 mM, and 0.1 mM. 150 µL of each solution were put into a microplate well with 150 µL of 0.137 M DPPH. The solutions were incubated in the dark for 24 hours, and the absorbance was measured at 515 nm. The experiment was done in triplicate. A 50:50 mixture of EtOH and water served as the negative control. A mixture of 150 µL of water and 150 µL of DPPH, as well as, a mixture of 150 µL of absolute EtOH and 150 µL of DPPH served as positive controls for the complexes and BHT respectively.

Chapter 5. Synthesis, characterization, and application of hexa- and hepta-dentate pyridine-containing macrocycles

5.1 Introduction

Magnetic resonance imaging (MRI) is a noninvasive technique most commonly used to analyze soft tissue. Gadolinium-based contrast agents are often used to enhance the clarity of the images by altering the relaxation rate of bulk water protons.[72] Although gadolinium-based agents yield acceptable contrast, they can be toxic to patients with compromised renal function. Iron(II) and europium(III) complexes are currently being investigates as a less toxic alternative to gadolinium-based systems.[67, 70, 244-245]

Iron- and europium-based agents enhance MRI images through a process termed PARACEST (Paramagnetic Chemical Exchange Saturation Transfer).[67, 244] In the PARACEST process the paramagnetic nature of the metal ion results in a shift of the chelates protons resonance up to 300 ppm from the diamagnetic region (0-12 ppm) of the NMR spectrum.[71-72] The paramagnetically shifted protons are magnetically saturated by a radio frequency pulse. The exchange of these protons with the bulk water protons produces decrease the NMR signal of the bulk water protons resulting in a negative contrast.

Not all iron(II) or europium(III) complexes are satisfactory PARACEST agents. In fact, several properties must be considered concerning the metal and the ligand. First, the properties of the complex should be such that a ^{1}H-NMR of the complex exhibits paramagnetically shifted resonances without excess broadening of the resonances. For iron agents, this is typically observed in high-spin 2+ complexes; for europium agents the 3+ oxidation state is typically needed to achieve a suitable spectrum. Other considerations include ligand properties. The ligand should contain exchangeable paramagnetically shifted protons; this can be achieved by incorporation of amines and alcohols into the ligand scaffold or adjusting the denticity of the ligand to allow for an exchangeable water molecule.

In 2011, the first iron-based PARACEST contrasts agents were reported. The work of Morrow and coworkers, [68-73, 75, 244, 246-249] laid the foundation for the development of transition-metal based contrast agents. Furthermore, independent reports by Morrow and co-works and Harris and co-workers have shown that transition metal agents can be used in responsive and theranostic applications.[244, 250] The versatility of europium-agents has also been thoroughly studied.[67, 245, 251]

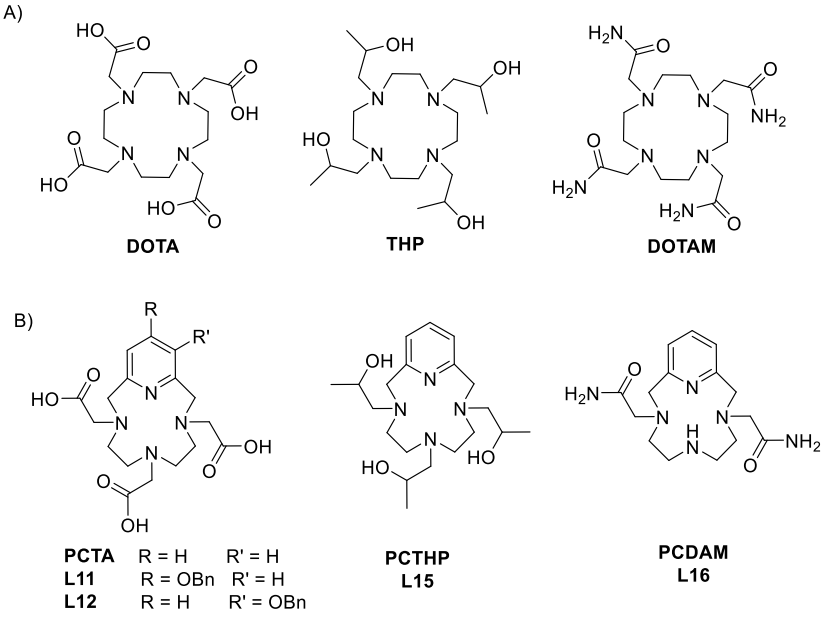

Figure 5.1. *A) Cyclen-based ligands used in previously reported contrast agents;[67, 246, 252] B) new ligands reported here, with the exception of* ***PCTA****.*

Decreased flexibility of the ligand backbone increased the thermodynamic stability of CEST contrast agents.[68, 253] Therefore, we set out to synthesize five ligands for use in PARACEST agents. The ligand designs are based on previously reported ligands shown in Figure 5.1a, which contain a cyclen core. Here, the tetra-azamacrocycle pyclen was used as the macrocyclic core (Figure 5.1b), as it should engender more rigidity and stability than the previously reported cyclen derivatives.[254] The ligands **PCTA**, **Bn*p*-PCTA** (**L11**), and **Bn*m*-PCTA** (**L13**) contain three carboxylic acid pendent arms but vary in the

presence and/or position of a benzyl protected alcohol. Ligand **PCTHP** (**L15**) contains three isopropanol arms, and ligand **PCDAM** (**L16**) contains two amide arms. The synthesis and characterization of these ligands, the synthesis and solid-state analysis of **[Fe^{3+}PCTA]**, and NMR and CEST analysis of **[Fe^{2+}PCTA]**$^{-}$ are presented here.

5.2 Results and discussion

5.2.1 Synthesis of PCTA

The synthesis and imaging applications of **PCTA** has been reported several times.[253, 255-258] In general, the synthesis of **PCTA** begins with a Richman-Atkins cyclization of an alkyl halide and a N-atom protected diethylenetriamine, establishing the macrocyclic core (Scheme 5.1b). After deprotection of the macrocycle, the acetate arms are added using potassium chloroacetate in an aqueous solution at pH= 10. Isolated yields of 64, 49, and 78% have been reported after chromatographic separation using sephadexG-10 or DOWEX 1X8 as the stationary phase.[253, 255-258] Here we report an alternate synthesis of **PCTA** that does not require chromatographic separation. Similar to previous reports, the macrocyclic core (**L1**) is constructed first by reacting an alkyl halide (2,6-bis(chloromethyl)pyridine (**1**)) with a secondary amine (1,4,7-tris(2-nitrobenzenesulfonyl)-1,4,7-triazaheptane (**7**)) in the presence of an inorganic base such as K_2CO_3. Deprotection of the cyclized product with thiophenol and KOH, followed by an acidic work-up yielded **L1·3HCl** (Scheme 5.1a). Contrary to previous reports, the carboxylic acid arms were added in acetonitrile. The use of acetonitrile simplified the synthesis as the pH of the solution did not need to be monitored, however, it was imperative to add the arms to the free base form of **L1**. After dropwise addition of tert-butyl bromoacetate to **L1** and K_2CO_3 in acetonitrile the reaction was stirred for 12 hours at which time all the **L1** had reacted based on TLC-analysis. The product **PCTA·4HCl** was obtained in 48% yield after recrystallization from a 60 ^{o}C, 20% HCl solution (scheme 5.1c). This synthetic route was followed because the use of expensive separation techniques was not required; despite the isolated yield is lower than those obtained by Aime *et al.* and Siaugue *et al.*[253, 258]

*5.2.2 Synthesis of **L11** and **L12***

Ligands **L13** and **L14** were designed with a goal to produce theranostic PARACEST agents. A theranostic agent is defined as an agent that can both treat and detect disease states. Ligands **L13** and **L14** were designed to incorporate the radical scavenging ability of **L2**, **L3**, **$[Fe^{3+}L2]^{+}$**, and **$[Fe^{3+}L3]^{+}$** with the high stability of **PCTA**. The synthetic route used to produce **PCTA** afforded the benzyl ethers, **L11** and **L12,** in 28 and 48% yields, respectively (Scheme 5.1). However, hydrogenation of **L11** and **L12** in acid solution using PdO resulted in partial dearomatization of the pyridine ring rather than formation of **L13** and **L14** (Scheme 5.1d). The dearomatization of pyridines in acidic media has been previously reported but using stronger catalysts and higher hydrogen pressure.[259-260] Furthermore, **BnL2** and **BnL3** do not undergo dearomatization under identical conditions. Multiple attempts to remove the dearomatized side product by chromatography were either unsuccessful or produced limited amount of product. When purification was unsuccessful, alternative deprotection methods were explored such as 12h reflux in TFA and hydrogenation using 10% Pd on carbon; no reaction occurred under these conditions. In future studies careful investigation of catalyst loading, hydrogen pressure, and reaction time ligand may yield **L13** and **L14**.

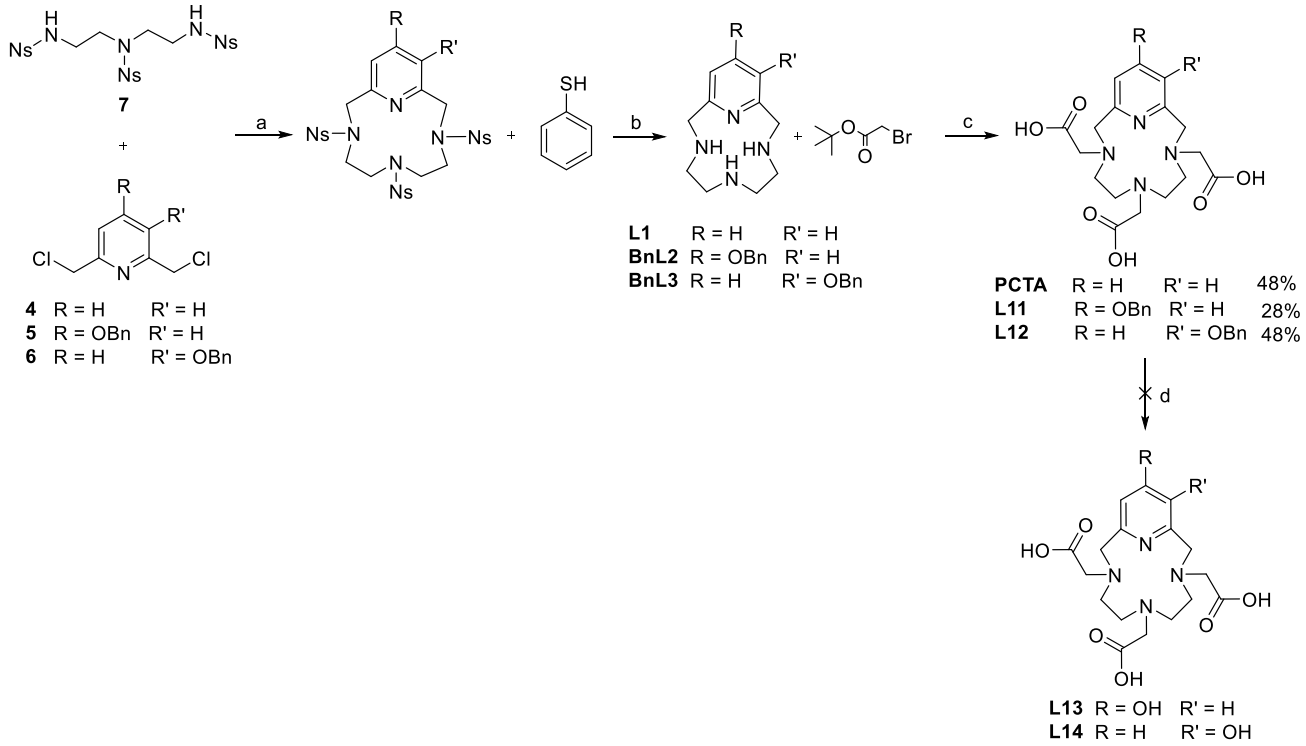

Scheme 5.1. *Synthesis of **PCTA**, **L11**, **L12**, **L13**, and **L14**. **PCTA** a) CH_3CN, K_2CO_3, 90 °C, 2d; b) CH_3CN, KOH, 60 °C, 12h; c) i. CH_3CN, K_2CO_3, RT, ii. 20% HCl, 12h, 60 °C to RT. **L13** a) DMF, K_2CO_3, 100 °C, 2d; b) DMF, KOH, 60 °C, 12h; c) i. CH_3CN, K_2CO_3, RT, ii. 20% HCl, 12h, 60 °C to RT (**L11**), d) PdO, 44 psi H_2O. **L14** a) DMF, K_2CO_3, 100 °C, 2d; b) DMF, KOH, 60 °C, 12h; c) i. CH_3CN, K_2CO_3, RT, ii. 20% HCl, 12h, 60 °C to RT (**L12**), d) H_2O, PdO, 44 psi H_2.*

*5.2.3 Alternative synthesis of **L11***

An alternative approach to synthesize **L11** was employed (Scheme 5.2). The alkylation of **BnL2** only afforded 315 mg of **L11** (28% yield), as opposed to the almost 50% yield obtained for **PCTA** and **L12**. When **BnL2** is alkylated to produce **L11,** 2.69 mmol of **5** are needed to produce 0.472 mmol of **L11·5HCl**. In an alternative, approach 0.851 mmol of **5** produce 0.305 mmol **L11·4HCl**, a 2.6-fold increase in yield. The first step in the alternative approach is the protection of diethylenetriamine. This protection is a two-step process, first an imine is formed using benzaldehyde to prevent over-alkylation of the amine. The imine is then reduced to an amine *in-situ*. Next, the now protected amine (**8**) is alkylated using tert-butyl bromoacetate in the presence of an inorganic base, K_2CO_3. At this point in the synthesis, the amine

(**9**) is purified by column chromatography, a technique not viable with the previously described macrocyclic ligands. Hydrogenation of the protected amine affords **10**. The cyclization was performed under optimized conditions reported by Ferroud *et al.* (Na_2CO_3 and 100 mM reactant concentrations).[261] In the same report it was also described that the use of chloride as a leaving group greatly decreased yields. Therefore, tetrabutylammonium iodide was added to the reaction mixture in catalytic amounts to produce the iodo-halide *in-situ*. This reaction is complete within 16 hours compared to the original approach which required 4 days. Overall this approach affords higher yields, decreased reaction times, and increased atom economy compared to alkylation of **BnL2**.

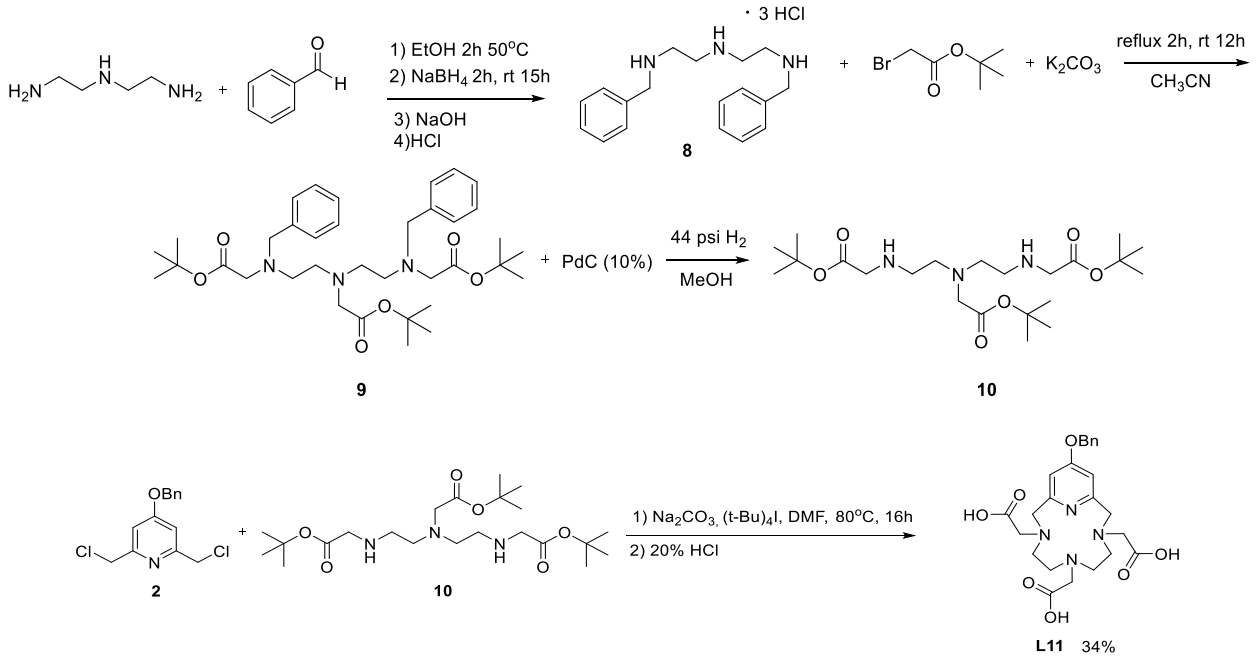

Scheme 5.2. *Alternative synthesis of* ***L11****.*

5.2.4 Synthesis of ***L15***

Churchill and co-workers have reported the synthesis of THP, a cyclen based ligand with four 2-hydroxypropyl pendent arms.[252] Here we present a similar synthetic route used to obtain **PCTHP** (**L15**). The macrocycle (**L1·3HCl**), K_2CO_3, and (±)-propylene oxide were dissolved in water and stirred at room temperature for 2 days (Scheme 5.3). The product (**L15·4.5HCl**) was precipitated by addition of ethanol

and HCl. The use of racemic propylene oxide resulted in several isomers. Each pendant arm of **L15** consists of a chiral center; therefore, four stereoisomers are possible (R, R, R; R, R, S; R, S, S; S, S, S). The presence of multiple isomers resulted in a very complex proton and carbon NMR spectra (Figure 5.2 and 5.3). However, the identity of the ligand was confirmed using HR-MS ([M+ H]$^+$ = 381.2849) and elemental analysis.

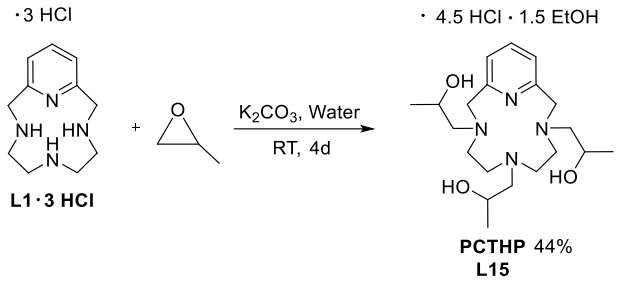

Scheme 5.3. *Synthesis of* ***PCTHP (L15)****.*

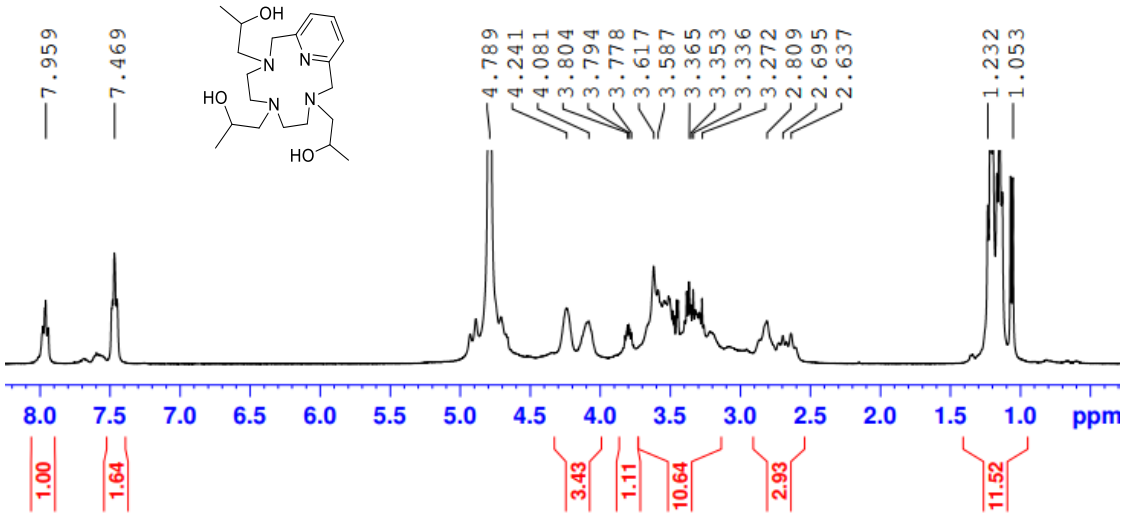

Figure 5.2. *^{1}H-NMR of* ***L15*** *in D_2O.*

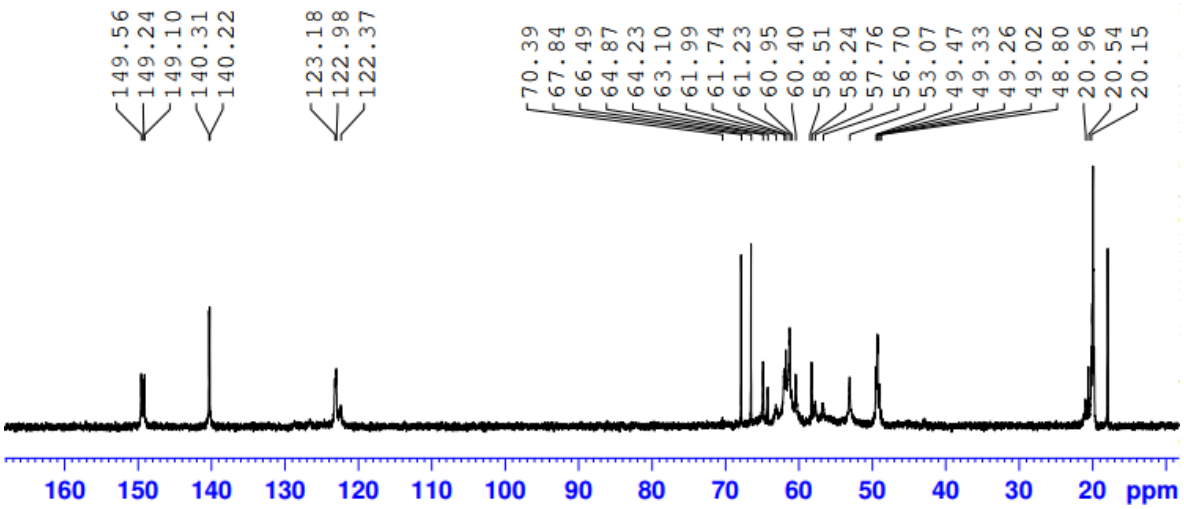

Figure 5.3. *^{13}C-NMR of **L15** in D_2O.*

*5.2.5 Synthesis of **L16***

The addition of amide arms to the macrocyclic core guarantees exchangeable protons into the ligand scaffold, which are necessary for PARACEST agents.[67] Amin *et al.* reported the synthesis of **DOTAM**, a cyclen based macrocycle with four amide pendant arms.[246] The synthesis of **L16** was performed in ethanol in the presence of triethylamine (base) and 2-bromoacetamide (alkylating agent, Scheme 5.4). Of the ligands synthesized, the alkylation of **L1** to form **L16** was the fastest; 1 hour after addition of triethylamine and 2-bromoacetamide the product had precipitated out of solution. After filtration **L16** was isolated in 81% yield as a white solid. Although excess 2-bromoacetamide was used (4.5 eq.), only two pendant arms were added to **L1**. A longer reaction time may afford the tri-substituted **PCTAM,** but this was not explored further. However, the isolation of **L16** will allow for comparison of hexadentate (**L16**) and heptadentate (**PCTA**, **L15**) ligands. Complex **L16** may allow enough space for an exchangeable water molecule as iron(II) systems have been reported to have coordination numbers of 6, 7, and 8.[73] The ability of iron to bind a water molecule even in the presence of a 6-coordinate ligand will be discussed further below. Attempts to synthesize **L16** in water using the alkylating agent 2-chloroacteamide were unsuccessful.

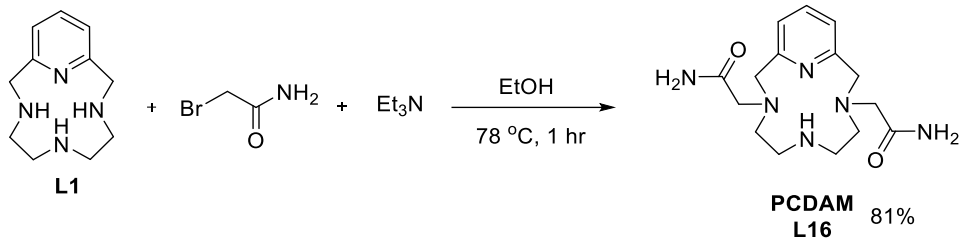

Scheme 5.4 *Synthesis of* ***L16****.*

5.2.6 Synthesis and solid-state XRD analysis of iron(III) PCTA

The synthesis of **[Fe^{3+}PCTA]** was achieved using iron(III) chloride hexahydrate in water at a pH of 7 (Scheme 5.5). After stirring for 13 days, the reaction mixture was filtered and dried under reduced pressure. X-ray quality crystals of **[Fe^{3+}PCTA]** were obtained by slow evaporation of ether into a solution of methanol. Isolation of the crystals resulted in 85% yield. The complex crystalized in the Pbca point group. The solid-state structure is shown in Figure 5.4 and selective bond lengths and angles are in Table 5.1. The iron(III) center coordinates to the four nitrogen atoms in the macrocycle and three carboxylate oxygen atoms. Seven coordinate metals, such as **[Fe^{3+}PCTA]** have been observed in three geometries: capped octahedral (C_{3v}, point group), capped trigonal prism (C_{2v}, point group), and pentagonal bipyramidal (D_{5h}, point group) (Figure 5.4).[262] Like the 7-coordinate iron(II) complexes reported by Morrow and Co-workers, **[Fe^{3+}PCTA]** adopts a pentagonal bipyramidal geometry. The 3+ charge of the iron center is balanced by the presence of the three carboxylate arms. The iron(III)-nitrogen and iron(III)-oxygen bond lengths are Fe(1)- O(1) 2.042(2), Fe(1)-O(3) 2.056(3), Fe(1)-O(2) 1.937(3), Fe(1)-N(4) 2.087(3), Fe(1)-N(1) 2.311(3), Fe(1)-N(3) 2.337(3), Fe(1)-N(2) 2.385(3) Å, which are consistent with iron(III) pentagonal bipyramidal complexes. The axial positions are occupied by N(4) and O(2); these bonds are overall shorter than the equatorial bonds. Such a decrease in the axial bond lengths is observed in other iron(II) and iron(III) pentagonal bipyramidal complexes as shown in Table 5.1. The compression of the axial bonds has been explained by a Hückel derived population analysis. The axial

ligands were shown to harbor more of the negative charge, which would result in shorter bond lengths.[263]

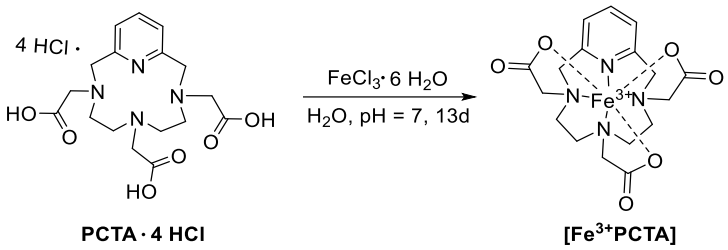

***Scheme 5.5**. Synthesis of **[Fe^{3+}PCTA]**.*

Table 5.1. Selected bond lengths for iron(II) and iron(III) pentagonal bipyramidal complexes.

Bond length (Å)	**[Fe^{3+}PCTA]**	**4Fe^{3+}**	**6Fe^{3+}**	**7Fe^{2+}**
Equatorial			Bond Length (Å)	
Fe-N	2.311(3)-2.385(3)	2.188(3), 2.194(3)	2.332(5) 2.185(6)	2.2873(11)-2.2896(11)
Fe-O	2.042(2)-2.056(3)	2.029(2),2.033(2)	2.163(4), 2.161(4)	2.1978-2.2952(9)
Axial				
Fe-N	2.087(3)	-	1.955(4), 2.153(4)	-
Fe-O	1.937(3)	2.033(2), 2.035(2)	-	2.0938(9)-2.0866(9)
Reference	*This Work*	264	265	73

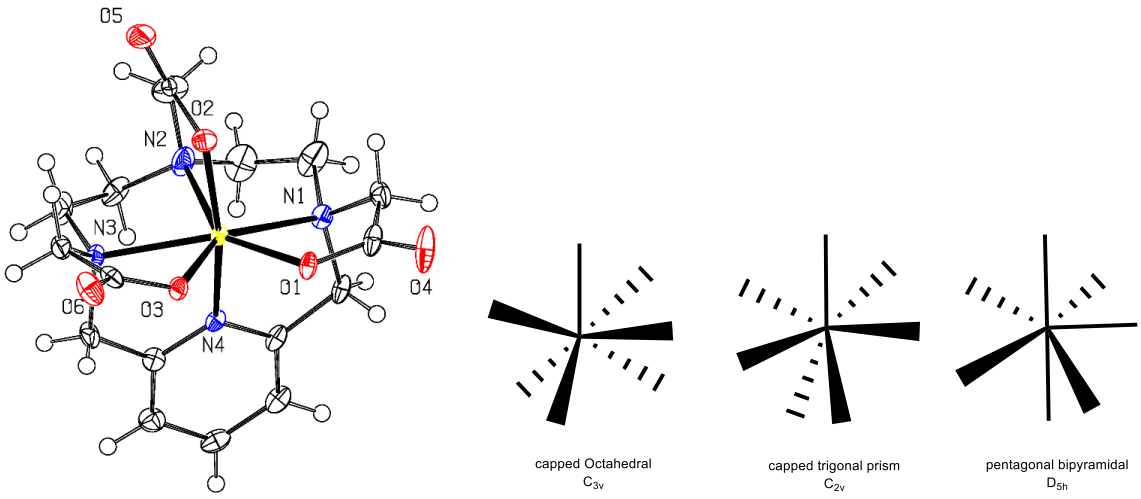

***Figure 5.4**. ORTEP (50% TELP) representation of **[Fe^{3+}PCTA]** and possible geometry of 7 coordinate systems.*

5.2.7 ^{1}H-NMR and CEST analysis of iron(II) PCTA

Ferrous and ferric iron exhibit different relaxivities. Only the ferrous species are visible by proton NMR and CEST experiments. Following the synthesis and solid-state analysis of the iron(III) PCTA complex, the iron(II) derivative was synthesized and characterized by ^{1}H-NMR *in-situ*. Due to the large donating capacity of PCTA, the iron(II) derivative readily oxidized to the iron(III) derivative. Therefore, **[Fe^{2+}PCTA]$^{-}$** was synthesized under inert conditions. The reduced iron(II) center of **[Fe^{2+}PCTA]$^{-}$** was confirmed by ^{1}H-NMR analysis. In DMSO-d_6 (*top* Figure 5.5) eight paramagnetically shifted resonances are observed (103.786, 88.960, 71.410, 63.038, 48.413, 30.208, 21.483, and -8.858 ppm). The ligand contains seven unique protons. Therefore, water (5 µL) was added to the NMR sample to determine if one of the resonances corresponded to a bound water molecule. The addition of water resulted in several changes in the proton spectra. After the addition of water, nine paramagnetically shifted resonances were observed (94.882, 87.659, 84.013, 75.668, 52.666, 24.965, 23.773, -3.016, and -8.345 ppm). A new resonance at -3 ppm is accompanied by a change of the chemical shift of all resonances. One explanation for the changes in the NMR spectra with the addition of water is the presence of an exchangeable water molecule. Encouraged by the change in the proton NMR spectrum upon the addition of water, **[Fe^{2+}PCTA]$^{-}$** was investigated for CEST properties. Analysis of the Z spectrum (M_z/M_o versus ppm) of **[Fe^{2+}PCTA]$^{-}$** (Figure 5.6) revealed no observable CEST effect. The lack of CEST may be due to absence of exchangeable protons or a rapid water exchange rate.[67]

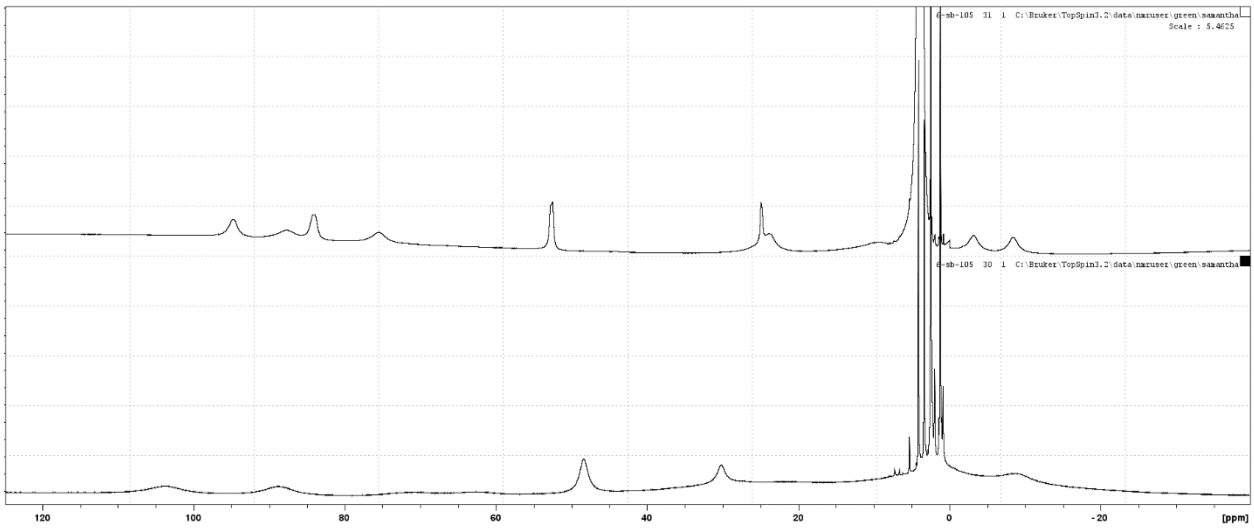

Figure 5.5. *^{1}H-NMR of **[Fe^{2+}PCTA]**, (*bottom*), in DMSO-d_6 (*top*) DMSO-d_6 with 5 µL H_2O.*

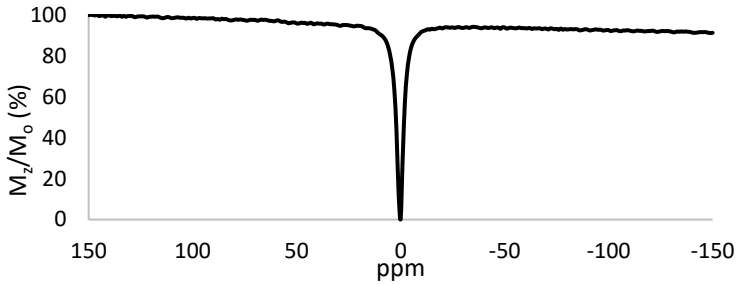

Figure 5.6. *The Z-spectrum of **[Fe^{2+}PCTA]**$^-$ obtained at 25^{o}C in H_2O.*

5.3 Conclusion

Five tetra-azamacrocyclic ligands have been synthesized for use in PARACEST imaging. Ligands **PCTA**, **L12**, **L15,** and **L16** were synthesized by direct alkylation of the macrocycle back-bone. An alternative pathway was used to synthesize **L11**. In this process the amine was functionalized with tert-butyl ester pendent arms. Ligand **L11** was thereby isolated after cyclization and acidic work-up. A preliminary CEST experiments performed on **[Fe^{2+}PCTA]**$^-$ indicated that carboxylic acid pendent side arms are not ideal for iron based PARACEST agent. Therefore, further CEST investigation of **L11** and **L13** should concentrate on the synthesis of Eu^{3+} complexes. The ligands **L15** and **L16** contain either

exchangeable -OH or -NH protons, making them better suited for iron based PARACEST agents. Future studies will concentrate on the synthesis of **$[Fe^{2+}L15]^{2+}$** and **$[Fe^{2+}L16]^{2+}$**.

5.4 Experimental methods

General methods:. All other reagents were obtained from commercial sources and used as received, unless noted otherwise. Ligands **L1-L3** were produced using methods previously reported by our group.[143, 145] 1H-NMR spectra were obtained on a 400-MHz Bruker Avance spectrometer, using deuterated solvents (D_2O and DMSO-d_6). NMR spectra were referenced using the corresponding solvent resonance (in parts per million; D_2O = 4.79; DMSO-d_6 = 2.50).[154] The following abbreviations were used for proper identification of the NMR signals: s = singlet, d = doublet, t = triplet, m = multiplet. Elemental analysis was performed by Canadian Microanalytical Service Ltd. Mass spectra were recorded using ion trap instruments (LCQ Deca or LTQ Velos Orbitrap Pro; Thermo Fisher Scientific, San Jose, CA, USA) using electrospray ionization (ESI). Samples were dissolved in methanol containing 1% (v/v) acetic acid, and the solutions were introduced into the ion source by the systems' built-in syringe pump. Accurate mass measurements, when required, were performed in the Orbitrap at mass resolution of >35,000 (specified at *m/z* 400).Crystal diffraction data were collected at 100 K on a Bruker D8 Quest Diffractometer. Data collection, frame integration, data reduction (multi-scan) were carried out using APEX3 software.[76] The structure was solved via intrinsic phasing methods using ShelXT[77] and refined with ShelXL[78] within the Olex2 graphical user interface.[79] All non-hydrogen atoms were refined using anisotropic thermal parameters, while the hydrogen atoms were treated as mixed. The ORTEP molecular plots (50%) were produced using Platon.[80]

PCTA·4HCl (1,4,7,10-tetra-aza-2,6-pyridinophane-1,4,7-triacetic acid): **L1·3HCl** was dissolved in 10 mL 50% NaOH, extracted three times with 20 mL DCM, dried with Na_2SO_4, and the solvent was removed under reduced pressure, 719.4 mg (3.492 mmol) of **L1** was obtained. Potassium carbonate (1.496 g,

10.82 mmol) and **L1** were dissolved in 10 mL of CH_3CN and heated to 60 °C. Tert-butyl bromoacetate (1.597 mL, 10.82 mmol) was dissolved in 10 mL CH_3CN and added drop-wise to the **L1** solution, the solution was stirred for twelve hours. Acetonitrile was removed and the resulting powder was dissolved in DCM, extracted 3x's with water, dried with Na_2SO_4. The DCM was removed under reduced pressure. The ligand was dissolved using 20% HCl solution preheated heated to 60°C. The solution was stirred for 12h at room temperature. A white solid formed, which was isolated by filtration and washed with methanol. Yield = 47.82% (878.7 mg, 1.669 mmol). ^{1}H-NMR (400 MHz, D_2O) δ: 8.068 (t, 1H), 7.548 (d, 1H), 4.876 (s, 4H), 4.273 (s, 4H), 3.682 (s, 2H), 3.566 (s, 4H) 2.996 (b, 4H). ^{13}C NMR δ: 174.53, 169.03, 149.65, 140.87, 122.57, 59.50, 56.41, 54.54, 54.31, 50.87. Elemental analysis: $C_{24}H_{30}N_4O_7$·5HCl Calc(Found): C, 38.80(38.50); H, 5.36(5.69); N, 10.65(10.47).

Bnp-PCTA (**L11**): (14-benzyloxy-1,4,7,10-tetra-aza-2,6-pyridinophane-triacetic acid): Potassium carbonate (770.9 g, 5.586 mmol) and **BnL2·3HCl** (409.1 g, 1.311 mmol) were dissolved in 30 mL DMF to this a solution of tert-Butyl bromoacetate (586 µL, 3.97 mmol) in 9 mL DMF was added at room temperature. The reaction was stirred under a blanket of nitrogen for 5 days. The reaction was filtered, and the DMF was removed with the aid of toluene under reduced pressure. Crude product was dissolved in DCM, washed three times with $NaHCO_{3\,(aq)}$, and dried with Na_2SO_4. After filtration, the DCM was extracted three times with 20% HCl (200 mL total). Pure white solid product was obtained after lyophilization of the water layer as a white solid. Yield = 27.49% (315.7 mg, 0.3603 mmol). ^{1}H NMR (400 MHz, D_2O, pD=3) δ: 7.534-7.429 (m, 5H), 7.262 (s, 2H), 5.387 (s, 2H), 4.514 (s, 4H), 4.003 (s, 4H),3.882 (s, 2H), 3.3.317-2.60 (broad, 8H). ^{13}C NMR δ: 172.79, 170.84, 170.26, 152.75, 134.34, 128.99, 128.94, 128.15, 110.12, 71.84, 57.95, 56.28, 54.56, 53.07, 51.33. ESI-MS (m/z) Found: 397.1247, $[M\text{-}Bn^+H^+]^+$ (44%), 487.1827, $[M+H^+]^+$ (100 %). Theoretical: 397.1723, $[M\text{-}Bn^+H^+]^+$ 487.2193 $[M+H^+]^+$. Elemental analysis: $C_{24}H_{30}N_4O_7$·5HCl Calc(Found): C, 43.10(42.97); H, 5.28(5.81); N, 8.38(8.70).

Bnp-PCTA(2) (**L11**)**:** Alkyl halide (240.9 mg, 0.8543 mmol) was dissolved in 8.86 mL DMF, to make a 0.1 M solution. The alkyl halide solution was added drop-wise to an 8.86 mL DMF solution at 80 °C containing amine (398.8 mg, 0.8950 mmol), sodium carbonate (383.6 mg, 3.6202), and a catalytic amount of tetrabutylammonium iodide. The reaction was stirred for 4 h at 80 °C and 12h at room temperature. The DMF was removed under reduced pressure. The resulting solid was dissolved in ether, extracted twice with water and once with brine. The ether was dried with Na_2SO_4 and removed under reduced pressure. The crude product was recrystallized from hot 20% HCl to yield a white solid. Yield = 34.02% (193.1 mg, 0.2906 mmol). Elemental analysis: $C_{24}H_{30}N_4O_7 \cdot 4HCl \cdot H_2O$ Calc(Found): C, 44.32(43.91); H, 5.58(6.00); N, 8.61(8.78).

Bnm-PCTA (**L12**) (13-benzyloxy-1,4,7,10-tetra-aza-2,6-pyridinophane-triacetic acid)**:** Potassium carbonate (1.395g, 10.11 mmol) and **BnL3·3HCl** (1.001g, 2.373 mmol) were dissolved in 20 mL CH_3CN. To this a 9 mL solution of tert-Butyl bromoacetate (1.06 mL, 7.179 mmol) was added at room temperature (**BnL3·3HCl** does not dissolve). The reaction was blanketed with $N_{2\ (g)}$ heated to 60 ^{0}C for 4 days and dried under reduced pressure. Crude product was dissolved in DCM and washed three times with $NaHCO_{3\ (aq)}$, and dried with Na_2SO_4. Pure product was obtained by recrystallization from 20% HCl. Excess water was removed by lyophilization, resulting in a white solid. Yield = 48 % (548.7 mg, 1.128 mmol). ^{1}H NMR (400 MHz, D_2O) δ 7.651 (d, 1H), 7.455-7.345 (m, 6H), 5.239 (s, 2H), 4.280 (s, 4H), 3.559 (s, 2H) 3.503 (b, 5H), 2.838 (b, 3-OH). ^{13}C NMR δ: 175.01, 168.61, 151.81, 140.53, 139.52, 135.53, 128.89, 128.79, 128.08, 123.66, 123.18, 71.80, 59.26, 56.71, 56.43, 53.43, 50.61, 50.55. Elemental analysis: $C_{24}H_{30}N_4O_7 \cdot 4$ HCl Calc(Found): C, 45.59(45.33); H, 5.42(5.75); N, 8.86(8.79).

PCTHP (**L15**) (1,4,7-tri(2-hydroxypropyl)-1,4,7,10-tetra-aza-2,6-pyridinophane): Potassium carbonate (1.417 g, 10.27 mmol) and **L1·3HCl** (500.0 mg, 1.587 mmol) were dissolved in 10 mL water. (±)-Propylene oxide (2.0 mL, 28 mmol) was added dropwise at room temperature, and the reaction was stirred for 4 days. Absolute ethanol (50 mL) and concentrated HCl (4 mL) was added to the reaction mixture resulting in a white solid. The crude product was recrystallized using ethanol and ethyl acetate. Yield = 44.4 % (434.0 mg, 0.706 mmol). ^{1}H NMR (400 MHz, D_2O) δ: 7.959 (t, 1H), 7.469 (d, 2H), 4.95-4.56, 4.241-2.637 (m, 20H), 1.417-0.963 (m, 12H). ^{13}C NMR δ: 149.56, 149.24, 149.10, 140.31, 140.22, 123.18, 122.98, 122.37, 70.39, 67.84, 66.49, 64.87, 64.23, 63.10, 61.66, 61.74, 61.23, 60.95, 60.40, 58.51, 58.24, 57.76, 56.70, 53.07, 49.47, 49.33, 49.26, 49.02, 48.80, 20.96, 20.54, 20.15, 20.02, 19.92, 19.75. Elemental analysis Cal (Found): $C_{20}H_{37}N_4O_3 \cdot 4.5\ HCl \cdot 1.5\ EtOH$: C 45.33 (45.15); H 8.88 (8.50); N 9.19 (9.00). FT-MS (m/z) Found: 191.14627, $[M+2H^+]^{2+}$ (100%), 381.28485 $[M+H^+]^+$ (55%). Theoretical: 191.14665, $[M+2H^+]^{2+}$, 381.28657 $[M+H^+]^+$.

PCDAM (**L16**) (1,4,7-di(amide)-1,4,7,10-tetra-aza-2,6-pyridinophane): **L1·3HCl** was dissolved in 10 mL 50% NaOH, extracted three times with 20 mL DCM, dried with Na_2SO_4, and the solvent was removed under reduced pressure, yielding 326.3 mg (1.584 mmol) of **L1**. Triethylamine (1.1 mL, 7.7 mmol) was added to oven dried 50 mL round bottom flask equipped with a stir bar. A 12 mL absolute ethanol solution of **L1** (326.3 mg, 1.584 mmol) was added followed by 2-bromoacetamide (984.7 mg, 7.138 mmol). The reaction was heated to 78 °C for 1 hour at which time a large amount of solid formed. The solid was isolated using a centrifuge, followed by 3 X 6 mL washes of absolute ethanol. The excess solvent was removed under reduced pressure yielding a white solid. Yield = 80.11% (409.6mg, 1.28 mmol). ^{1}H NMR (400 MHz, D_2O) δ: 7.747 (t, 1H), 7.253 (d, 2H), 3.783 (s, 4H), 3.367 (s, 4H), 2.579 (s, 4H), 2.087 (s, 4H). ^{13}C NMR δ: 176.62, 157.50, 138.55, 122.80, 60.82, 58.99, 51.70.

[Fe^{3+}PCTA]: Ligand **PCTA** (50.5 mg, 0.096 mmol) was dissolved in 1.6 mL water and 0.4 mL MeOH, the pH was adjusted to 4 using 1 *M* NaOH. Iron(III) chloride hexahydrate (27.0 mg, 0.100 mmol) was added as a solid. The pH was adjusted to 7.03 using 1 *M* NaOH; a precipitate formed at pH = 3. The reaction was stirred for 13 days at room temperature. The reaction was filtered and dried under reduced pressure. Orange X-ray quality crystal were obtained by slow diffusion of ether into methanol. Yield = 81% (35.6 mg, 0.0822 mmol).

[Fe^{2+}PCTA]$^{--}$: In a glovebox at 0.1 ppm O_2 **PCTA** (61.3 mg, 0.116 mmol) was dissolved in 2 mL water. The pH was adjusted to 11.11. Iron(II) chloride tetrahydrate was dissolved in 1 mL MeOH and added dropwise to ligand solution resulting in an orange solution. The pH was adjusted to 8 and allowed to stir for 10 days. The solvent was removed under reduced pressure resulting in a green solid. The green solid was dissolved in minimum amount of methanol and filtered through a 0.2 µm nylon filter. Methanol was removed under reduced pressure. ^{1}H NMR (400 MHz, DMSO-d_6): 103.786, 88.960, 71.410, 63.038, 48.413, 30.208, 21.483, -8.858.

Chapter 6. Conclusion

The first three studies contained herein shed new light on the iron-catalyzed Suzuki-Miyaura process. The analysis of several control reactions indicted that the coupling of pyrrole and phenylboronic acid only occurs in a stereoselective manner, when both an iron ion and a tetra-azamacrocycle are present. However, the use of hydroxyl containing macrocyclic ligand (**L3**) resulted in trace amounts of a mixture of products. Furthermore, it was shown that under the reaction condition used in the preliminary study by Wen *et al.* an iron(III) complex forms.

The use of isolated and fully characterized iron complexes established the identity of the pre-catalyst as a high-spin iron(III) species. Comparison of the catalytic reaction yields resulting from a library of ten iron-containing tetra-azamacrocyclic complexes revealed that the electrochemical potential of the iron center could be correlated to the amount of product formed. This relationship was used to predict an optimal range of electrochemical potentials (-325.5 to -389.0 mV) of iron catalysts in the coupling of pyrrole and phenylboronic acid.

Several additional studies are needed to determine the industrial relevance of the catalysts presented here, including: the ability to catalyze a large-scale coupling, the ability to recycle the catalyst, the amount of residual iron in the isolated product, the rate of the reaction, and turnover number for each catalyst. However, the best performing iron complex **[Fe^{2+}L6$(Cl)_2$]** afforded 23 mg of 2-phenylpyrrole an 81% yield; which compares well with yields obtain with industrial palladium-catalyzed Suzuki-Miyaura reactions (77 - 99%).[266] Furthermore, the iron catalysts require less additives than the palladium catalysts; making them an attractive alternative.

Lastly, the need for a sacrificial oxidant, two labile *cis* sites, a two-electron process, and the presence of an off-cycle -μ-oxodiiron species were established. Furthermore, solid-state structure of a

rare hydroxoiron(III) complexes was obtained,[54] indicating the active iron catalyst may contain an $Fe^{3+}OH$ or $Fe^{5+}=O$ species. These studies were used to propose a more complete catalytic cycle.

The final study presented here, has established several synthetic routes to a new hexadentate and four heptadentate ligands in iron and/or europium PARACEST contrast agent. Based on current literature the metal complexes may function as theranostic or sensory contrast agents.

Appendix

Table A 1. *Crystal data, intensity collections, and structure refinement parameters for* ***$[Fe^{3+}L1(Cl)_2]ClO_4$, $[Fe^{3+}L2(Cl)_2]ClO_4$,*** *and* ***$[Fe^{3+}L3(Cl)_2]ClO_4$.***

Complex	**$[Fe^{3+}L1(Cl)_2]ClO_4$**	**$[Fe^{3+}L2(Cl)_2]ClO_4$**	**$[Fe^{3+}L3(Cl)_2]ClO_4$**
Formula	$C_{11}H_{18}Cl_3FeN_4O_4$	$C_{11}H_{18}Cl_3FeN_4O_5$	$C_{11}H_{18}Cl_3FeN_4O_5$
M.W.	435.52	448.49	448.49
Unit cell	Monoclinic	Monoclinic	Triclinic
Space group	P 2 1/c	P 2 1/c	P 1
a (Å)	7.0287(10)	9.2816(7)	7.0773(3)
b (Å)	12.9457(19)	12.7956(9)	9.4652(4)
c (Å)	18.578(3)	14.4652(11)	12.9941(6)
α	90°	90°	85.329(2) °
β	90.850(6) °	95.565(3) °	81.642(2) °
γ	90°	90°	89.546(2) °
Volume ($Å^3$)	1690.3(4)	1709.8(2)	858.34(6)
Z	4	4	2
$D_{calc.}(g/cm^3)$	1.711	1.742	1.735
Reflections Collected	122566	32234	37488
Independent Reflections	15087	7088	3797
R_{int}	0.0310	0.0281	0.0565
Completeness to θ	99.6%	99.9%	99.8%
GooF	1.050	1.024	0.954
R1,wR2 [I>2sigma(I)]	R1 = 0.0289, wR2 = 0.0673	R1 = 0.0307, wR2 = 0.0779	R1 = 0.0358, wR2 = 0.0710
R1, wR2	R1 = 0.0431, wR2 = 0.0727	R1 = 0.0411, wR2 = 0.0828	R1 = 0.0520, wR2 = 0.0779

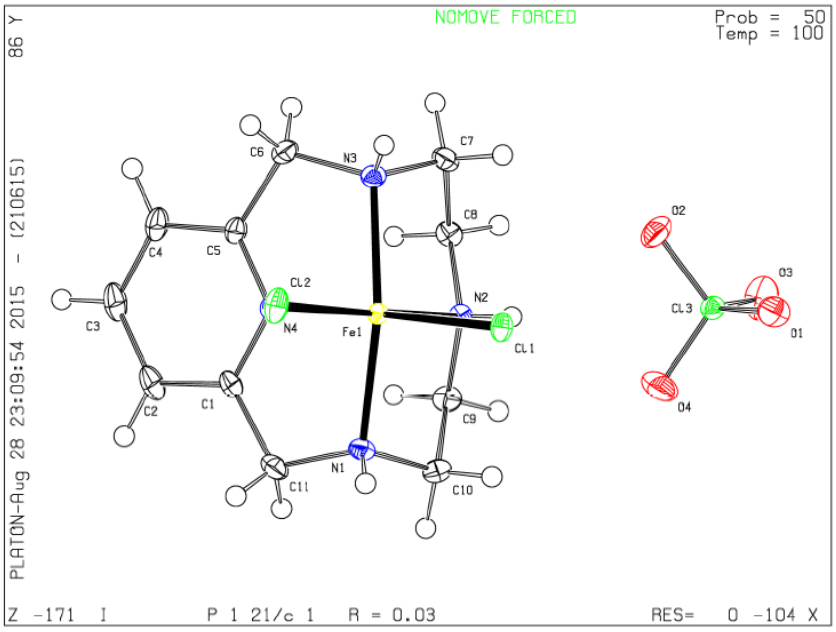

Figure A 1. *Solid state structure of* ***[Fe^{3+}L1(Cl)$_2$]ClO$_4$.***

Table A 2*. Bond lengths* ***[Fe^{3+}L1(Cl)$_2$]ClO$_4$.***

Atom	Atom	Length/Å	Atom	Atom	Length/Å
Fe1	N4	2.1074(5)	N4	C5	1.3394(8)
Fe1	N1	2.1641(6)	N3	C6	1.4835(9)
Fe1	N3	2.1676(6)	N3	C7	1.4917(9)
Fe1	N2	2.2001(6)	N2	C9	1.4756(8)
Fe1	Cl1	2.2638(3)	N2	C8	1.4770(8)
Fe1	Cl2	2.2819(3)	C11	C1	1.5061(10)
Cl3	O3	1.4304(7)	C1	C2	1.3913(9)
Cl3	O4	1.4381(7)	C5	C4	1.3882(9)
Cl3	O2	1.4492(6)	C5	C6	1.5061(9)
Cl3	O1	1.4497(6)	C7	C8	1.5136(9)
N1	C11	1.4869(9)	C9	C10	1.5149(10)
N1	C10	1.4894(9)	C4	C3	1.3927(11)
N4	C1	1.3388(8)	C3	C2	1.3881(12)

Table A 3. *Bond angles* ***[Fe^{3+}L1$(Cl)_2$]ClO_4.***

Atom	Atom	Atom	Angle/˚	Atom	Atom	Atom	Angle/˚
N4	Fe1	N1	76.75(2)	C1	N4	C5	121.60(5)
N4	Fe1	N3	76.93(2)	C1	N4	Fe1	119.15(4)
N1	Fe1	N3	147.25(2)	C5	N4	Fe1	118.31(4)
N4	Fe1	N2	85.56(2)	C6	N3	C7	113.37(5)
N1	Fe1	N2	79.72(2)	C6	N3	Fe1	110.99(4)
N3	Fe1	N2	79.15(2)	C7	N3	Fe1	108.58(4)
N4	Fe1	Cl1	172.862(15)	C9	N2	C8	116.24(5)
N1	Fe1	Cl1	98.990(17)	C9	N2	Fe1	109.79(4)
N3	Fe1	Cl1	104.983(15)	C8	N2	Fe1	110.15(4)
N2	Fe1	Cl1	88.044(18)	N1	C11	C1	111.89(5)
N4	Fe1	Cl2	87.187(19)	N4	C1	C2	120.65(6)
N1	Fe1	Cl2	100.485(17)	N4	C1	C11	115.58(5)
N3	Fe1	Cl2	97.332(16)	C2	C1	C11	123.66(6)
N2	Fe1	Cl2	172.500(15)	N4	C5	C4	120.76(6)
Cl1	Fe1	Cl2	99.297(12)	N4	C5	C6	115.46(5)
O3	Cl3	O4	110.65(5)	C4	C5	C6	123.67(6)
O3	Cl3	O2	109.47(4)	N3	C6	C5	112.07(5)
O4	Cl3	O2	109.31(5)	N3	C7	C8	109.75(5)
O3	Cl3	O1	109.07(4)	N2	C8	C7	106.53(5)
O4	Cl3	O1	109.94(4)	N2	C9	C10	107.18(5)
O2	Cl3	O1	108.36(4)	N1	C10	C9	109.30(5)
C11	N1	C10	113.27(5)	C5	C4	C3	118.33(7)
C11	N1	Fe1	112.56(4)	C2	C3	C4	120.24(6)
C10	N1	Fe1	107.19(4)	C3	C2	C1	118.41(7)

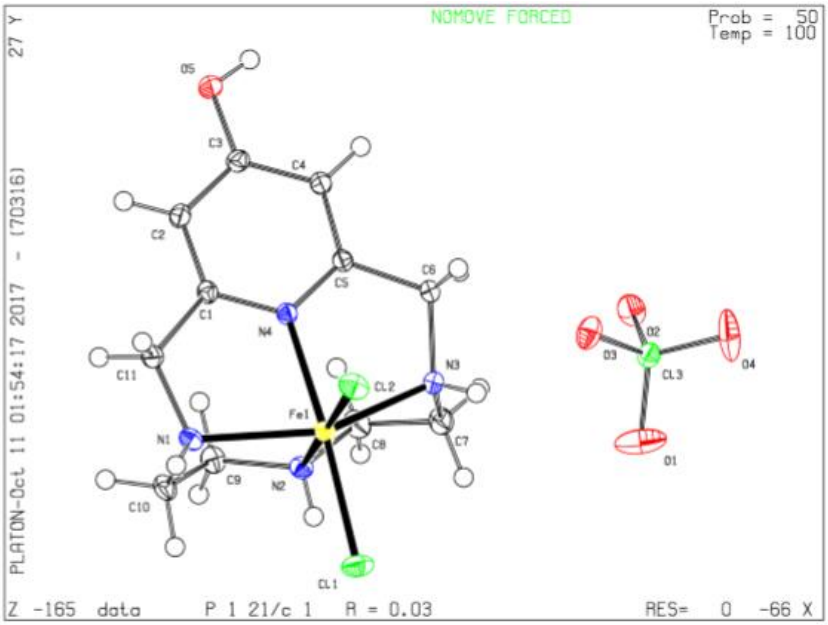

Figure A 2. *Solid state structure of* ***[Fe^{3+}L2(Cl)$_2$]ClO$_4$.***

Table A 4. *Bond lengths* ***[Fe^{3+}L2(Cl)$_2$]ClO$_4$.***

Atom	Atom	Length/Å	Atom	Atom	Length/Å
Fe1	Cl1	2.2852(4)	N3	C6	1.4880(16)
Fe1	Cl2	2.2666(4)	N4	C5	1.3410(15)
Fe1	N2	2.2023(10)	N4	C1	1.3422(15)
Fe1	N3	2.1812(11)	N1	C11	1.4885(16)
Fe1	N4	2.0970(10)	N1	C10	1.4902(16)
Fe1	N1	2.1787(11)	C8	C7	1.5183(19)
Cl3	O1	1.4337(12)	C6	C5	1.5021(16)
Cl3	O2	1.4603(10)	C5	C4	1.3821(16)
Cl3	O3	1.4453(10)	C1	C2	1.3801(16)
Cl3	O4	1.4231(12)	C1	C11	1.5116(17)
O5	C3	1.3499(14)	C2	C3	1.3989(17)
N2	C8	1.4758(16)	C3	C4	1.3950(17)
N2	C9	1.4740(16)	C10	C9	1.5144(18)
N3	C7	1.4870(17)			

Table A 5. *Bond angles* ***[Fe^{3+}L2(Cl)$_2$]ClO_4.***

Atom	Atom	Atom	Angle/˚	Atom	Atom	Atom	Angle/˚
Cl2	Fe1	Cl1	95.754(13)	C6	N3	Fe1	110.20(7)
N2	Fe1	Cl1	86.93(3)	C6	N3	C7	112.97(10)
N2	Fe1	Cl2	176.13(3)	C5	N4	Fe1	119.45(8)
N3	Fe1	Cl1	103.72(3)	C1	N4	Fe1	120.11(8)
N3	Fe1	Cl2	98.21(3)	C1	N4	C5	120.43(10)
N3	Fe1	N2	78.42(4)	C11	N1	Fe1	111.52(7)
N4	Fe1	Cl1	172.07(3)	C10	N1	Fe1	107.75(7)
N4	Fe1	Cl2	91.95(3)	C10	N1	C11	113.52(10)
N4	Fe1	N2	85.47(4)	C7	C8	N2	107.14(10)
N4	Fe1	N3	76.97(4)	C8	C7	N3	109.40(10)
N1	Fe1	Cl1	99.94(3)	C5	C6	N3	111.55(10)
N1	Fe1	Cl2	102.41(3)	C6	C5	N4	114.63(10)
N1	Fe1	N2	79.81(4)	C4	C5	N4	121.79(11)
N1	Fe1	N3	146.70(4)	C4	C5	C6	123.53(11)
N1	Fe1	N4	76.47(4)	C2	C1	N4	121.77(11)
O2	Cl3	O1	108.35(7)	C11	C1	N4	114.59(10)
O3	Cl3	O1	107.99(7)	C11	C1	C2	123.61(10)
O3	Cl3	O2	108.99(6)	C3	C2	C1	117.79(11)
O4	Cl3	O1	111.94(9)	C2	C3	O5	117.29(11)
O4	Cl3	O2	109.91(7)	C4	C3	O5	122.27(11)
O4	Cl3	O3	109.58(7)	C4	C3	C2	120.43(11)
C8	N2	Fe1	111.10(7)	C3	C4	C5	117.79(11)
C9	N2	Fe1	109.76(7)	C1	C11	N1	110.77(10)
C9	N2	C8	115.47(10)	C9	C10	N1	110.06(10)
C7	N3	Fe1	109.53(8)	C10	C9	N2	108.24(10)

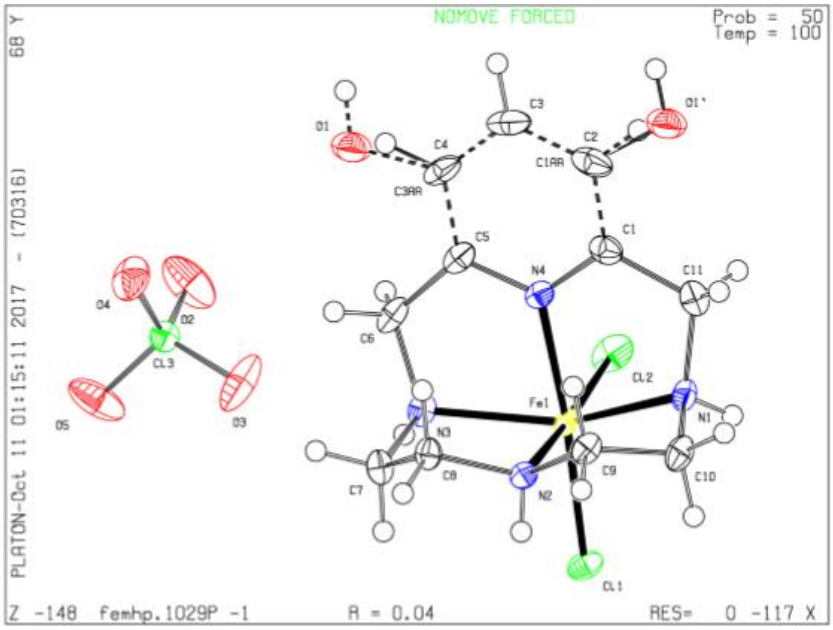

Figure A 3. *Solid state structure of* ***[Fe^{3+}L3(Cl)$_2$]ClO$_4$.***

Table A 6. *Bond Lengths* ***[Fe^{3+}L3(Cl)$_2$]ClO$_4$.***

Atom	Atom	Length/Å	Atom	Atom	Length/Å
Fe1	Cl1	2.2479(7)	C3AA	O1	1.485(7)
Fe1	Cl2	2.2880(7)	C3AA	C3	1.376(5)
Fe1	N2	2.181(2)	C4	C3	1.376(5)
Fe1	N3	2.172(2)	C3	C1AA	1.390(4)
Fe1	N4	2.107(2)	C3	C2	1.390(4)
Fe1	N1	2.162(2)	C1AA	C1	1.391(4)
N2	C8	1.473(3)	C2	O1'	1.425(4)
N2	C9	1.471(3)	C2	C1	1.391(4)
C8	C7	1.510(4)	C1	C11	1.504(4)
C7	N3	1.491(3)	C11	N1	1.484(4)
N3	C6	1.477(3)	N1	C10	1.487(3)
C6	C5	1.499(4)	C10	C9	1.509(4)
C5	N4	1.337(3)	Cl3	O2	1.430(2)
C5	C3AA	1.385(4)	Cl3	O3	1.425(2)
C5	C4	1.385(4)	Cl3	O4	1.431(2)
N4	C1	1.336(3)	Cl3	O5	1.429(2)

Table A 7. *Bond angles* ***[Fe^{3+}L3(Cl)$_2$]ClO_4.***

Atom	Atom	Atom	Angle/˚	Atom	Atom	Atom	Angle/˚
Cl2	Fe1	Cl1	97.55(3)	N4	C5	C6	116.0(2)
N2	Fe1	Cl1	87.96(6)	C5	N4	Fe1	118.52(17)
N2	Fe1	Cl2	174.37(6)	C1	N4	Fe1	119.10(17)
N3	Fe1	Cl1	100.09(6)	C1	N4	C5	122.1(2)
N3	Fe1	Cl2	100.40(6)	C3	C3AA	C5	119.1(3)
N3	Fe1	N2	79.71(8)	C3	C4	C5	119.1(3)
N4	Fe1	Cl1	173.33(6)	C1AA	C3	C3AA	120.1(3)
N4	Fe1	Cl2	88.82(6)	C2	C3	C4	120.1(3)
N4	Fe1	N2	85.72(8)	C1	C1AA	C3	118.5(3)
N4	Fe1	N3	76.71(8)	C1	C2	C3	118.5(3)
N1	Fe1	Cl1	104.24(6)	C11	C1	N4	115.8(2)
N1	Fe1	Cl2	97.93(6)	N1	C11	C1	111.3(2)
N1	Fe1	N2	79.47(8)	C11	N1	Fe1	112.56(16)
N1	Fe1	N3	147.17(8)	C10	N1	Fe1	107.45(15)
N1	Fe1	N4	76.68(8)	C10	N1	C11	113.3(2)
C8	N2	Fe1	109.97(14)	C9	C10	N1	109.6(2)
C9	N2	Fe1	110.72(15)	C10	C9	N2	106.9(2)
C9	N2	C8	116.07(19)	O3	Cl3	O2	111.55(17)
C7	C8	N2	107.1(2)	O4	Cl3	O2	108.16(15)
N3	C7	C8	109.6(2)	O4	Cl3	O3	107.78(14)
C7	N3	Fe1	107.59(15)	O5	Cl3	O2	110.17(14)
C6	N3	Fe1	111.71(16)	O5	Cl3	O3	109.87(16)
C6	N3	C7	112.9(2)	O5	Cl3	O4	109.22(15)
C5	C6	N3	111.7(2)				

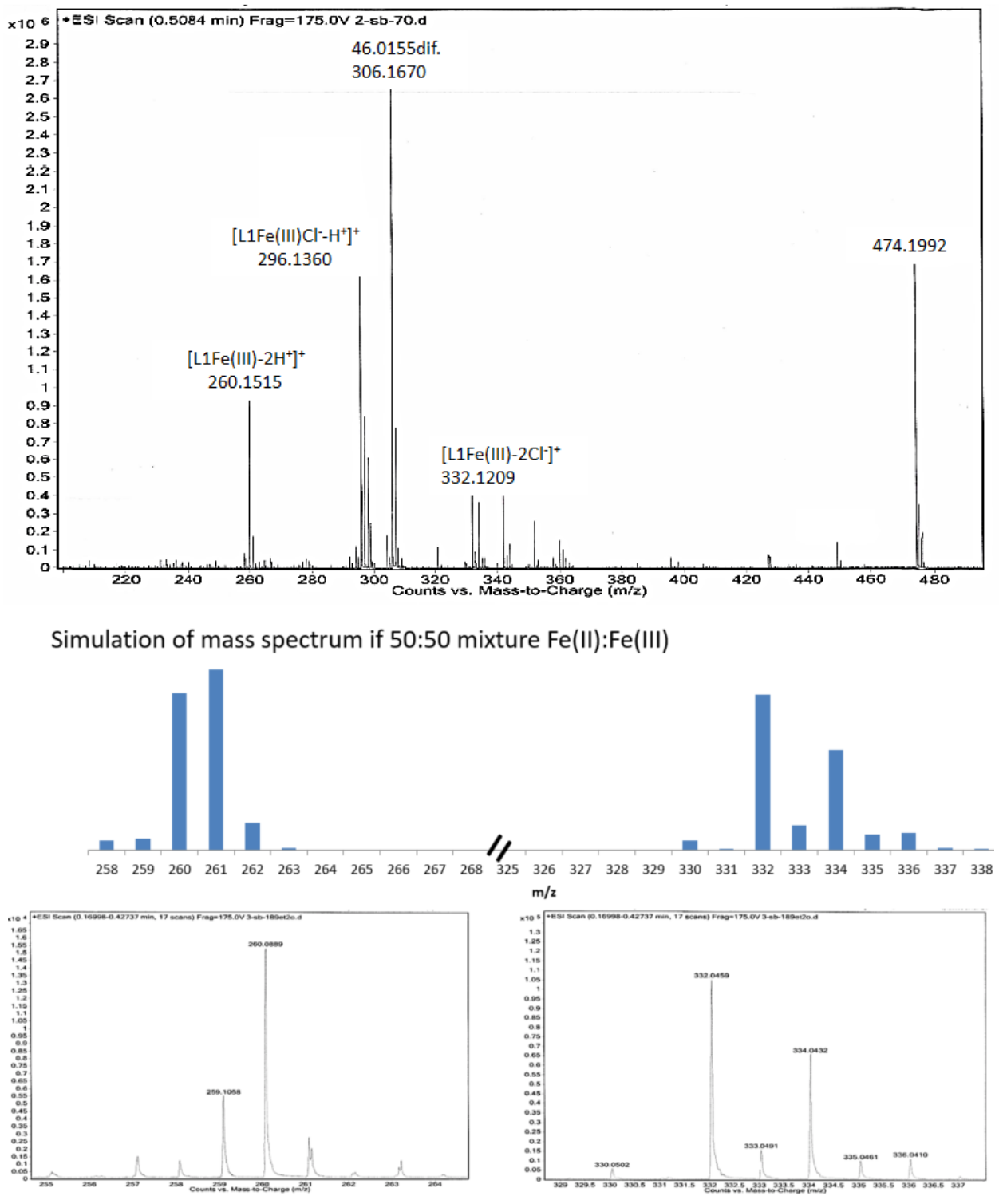

Figure A 4. *(a) Mass spectrometry of* ***[Fe^{3+}L1(Cl)$_2$]ClO$_4$*** *showing (m/z) = 260.1515, [L1Fe(III)-2H$^+$]$^+$, (34%), 296.1360, [L1Fe(III)Cl-H$^+$]$^+$, (58%), 332.1209, [L1Fe(III)2Cl$^-$]$^+$, (14%), all other complexes follow the same trend. (b) Comparison of experimental isotopic envelope vs calculated isotopic envelope showing that* ***[Fe^{3+}L1(Cl)$_2$]ClO$_4$*** *is reduced inside the mass spectrometer.*

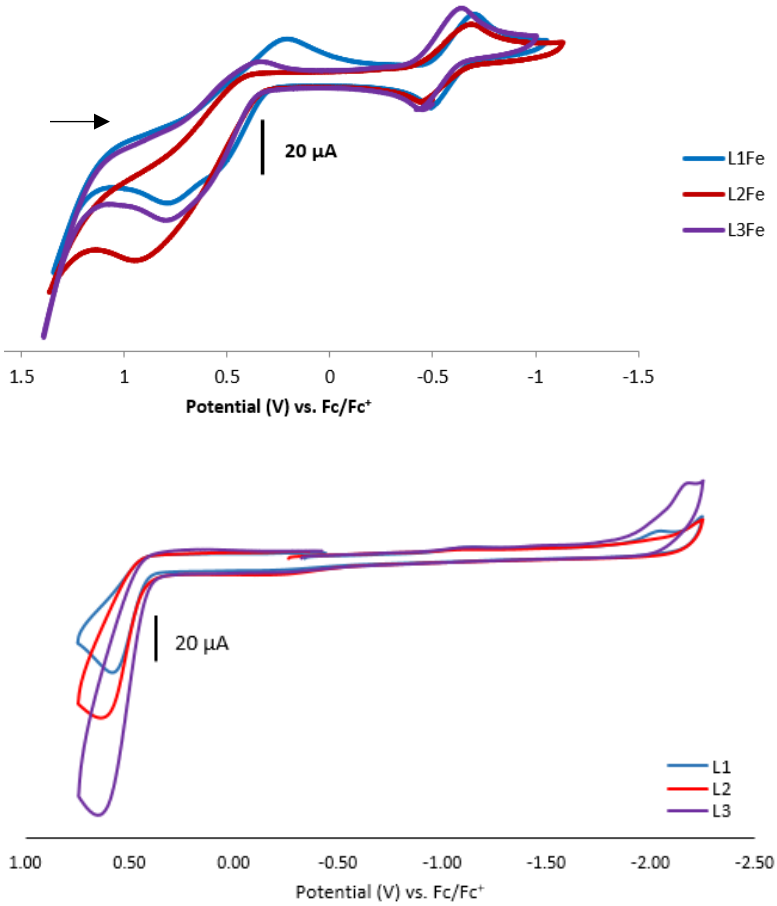

Figure A 5. *(Top) Cyclic voltammograms of* ***$[Fe^{3+}L1(Cl)_2]ClO_4$*** *-* ***$[Fe^{3+}L3(Cl)_2]ClO_4$*** *showing two electrochemical events, (bottom) cyclic voltammograms of* ***L1 – L3*** *showing a large positive oxidation event.*

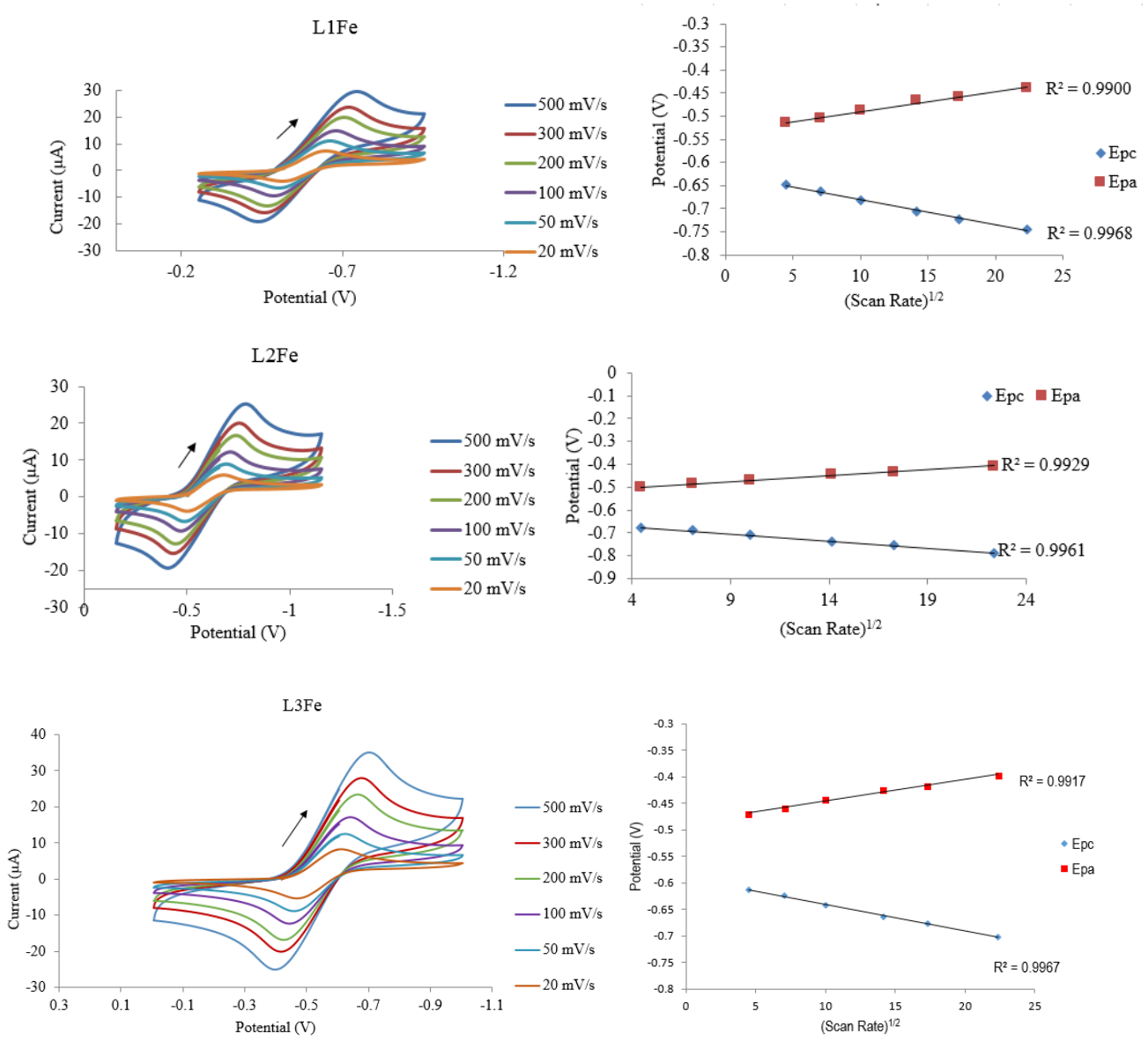

Figure A 6. *Cyclic voltammograms* ***[Fe^{3+}L1(Cl)$_2$]ClO$_4$*** *-* ***[Fe^{3+}L3(Cl)$_2$]ClO$_4$*** *at various scan rates with corresponding plots of the I_{pc} and I_{pa} versus $\sqrt{scan\ rate}$. The results indicate that the Fe$^{III/II}$ couples of* ***[Fe^{3+}L1(Cl)$_2$]ClO$_4$*** *-* ***[Fe^{3+}L3(Cl)$_2$]ClO$_4$*** *are diffusion controlled under the conditions used in the electrochemistry experiments.*

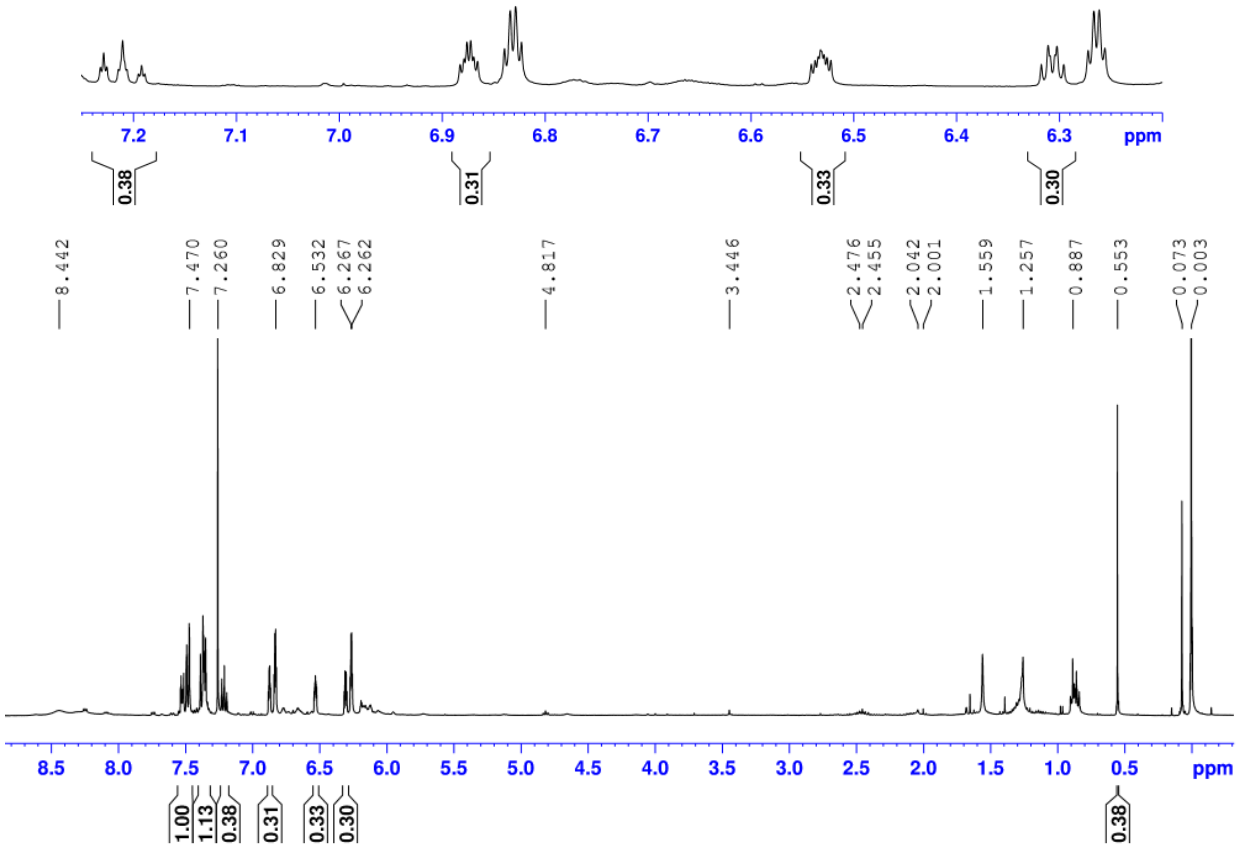

Figure A 7. *^{1}H-NMR of coupling reaction used to calculate percent yield obtained in $CDCl_3$.*

Mass spectrometry analysis of the coupling reaction performed by Wen. *et al.* revealed three isotopic envelopes, 207.1532, 353.1956, and 369.1956. The isotopic envelopes were assigned as $[L1]^+$, $[(L1)(Fe)(C_2O_4)]^+$, and $[(L1)(Fe)(C_2O_4)(O)]^+$, respectively. The isotopic envelope seen at 207.1532 corresponds to the singly protonated free ligand $[(L1)(H^+)]^+$ (Figure $S1_a$), which the authors may have considered apparent in the labeling $[L1]^+$. The assignment of 353.1965 as $[(L1)(Fe)(C_2O_4)]^+$ (Figure $S1_b$) is incorrect as the exact mass is 350.0672, three mass units less than the observed ion. Similarly, the assignment of 369.1956 as $[(L1)(Fe)(C_2O_4)(O)]^+$ (366.0621) shown in Figure $S1_c$ is three mass units less than the observed value of 369.1897.

a $[(L1)(H^+)]^+$

Theoretical: 207.1604

Found: 207.1532

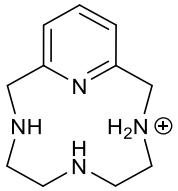

Chemical Formula: $C_{11}H_{19}N_4^+$

m/z: 207.1604 (100.0%), 208.1638 (11.9%), 208.1575 (1.5%)

b $[(L1)(Fe^{3+})(C_2O_4^{2-})]^+$

Theoretical: 350.0672

Found: 353.1956

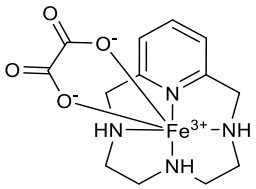

Chemical Formula: $C_{13}H_{18}FeN_4O_4^+$

m/z: 350.0672 (100.0%), 351.0706 (14.1%), 348.0719 (6.4%), 351.0677 (2.3%), 351.0642 (1.5%)

c $[(L1)(Fe^{5+})(C_2O_4^{2-})(O^{2-})]^+$

Theoretical: 366.0621

Found: 369.1897

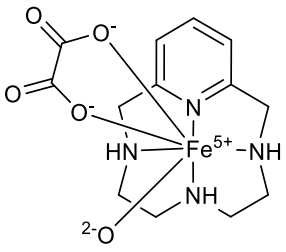

Chemical Formula: $C_{13}H_{18}FeN_4O_5^+$

m/z: 366.0621 (100.0%), 367.0655 (14.1%), 364.0668 (6.4%), 367.0626 (2.3%), 367.0591 (1.5%), 368.0664 (1.0%)

Figure A 8. *Exact mass analysis of the mass spectrometry assignments made by Wen et al.*[19]

Table A 8. *Lorentzian fitting parameters used to produce Figure 3.3.*

Lorentizan	
Best-fit values	
Amplitude	84.93
Center	-357.2
Width	106.4
Std. Error	
Amplitude	15.38
Center	12.35
Width	33.52
95% Confidence Intervals	
Amplitude	45.38 to 124.5
Center	-389.0 to -325.5
Width	20.21 to 192.6
Goodness of Fit	
Degrees of Freedom	5
R square	0.7159
Absolute Sum of Squares	1035
Sy.x	14.39
Number of points	
Analyzed	8

Table A 9. *Crystal data, intensity collections, and structure refinement parameters for* ***[Fe^{3+}L1(Cl)$_2$]Cl****,* ***[Fe^{3+}L2(Cl)$_2$]Cl****, and* ***[Fe^{3+}L3(Cl)$_2$]Cl****.*

Complex	**[Fe^{3+}L1(Cl)$_2$]Cl**	**[Fe^{3+}L2(Cl)$_2$]Cl**	**[Fe^{3+}L3(Cl)$_2$]Cl**
Formula	$C_{11}H_{21}Cl_3FeN_4$	$C_{11}H_{21}Cl_3FeN_4O$ + solvent	$C_{11}H_{19}Cl_3FeN_4O_2$
M.W.	371.52	384.49	400.68
Unit cell	Monoclinic	Monoclinic	Monoclinic
Space group	P 21/c	P 21/n	P 21/c
a (Å)	9.0709(12)	7.4373(3)	8.6125(5)
b (Å)	12.9066(16)	16.4820(6)	7.0103(4)
c (Å)	12.6919(16)	13.8530(6)	27.2333(13)
α	90°	90°	90°
β	90.823(6)°	101.807(2) °	98.438(2) °
γ	90°	90	90°
Volume (Å^3)	1475.4(3)	1662.20(12)	1626.44(15)
Z	4	4	4
$D_{calc.}$(g/cm^3)	1.673	1.536	1.636
Reflections Collected	65481	59062	67807
Independent Reflections	4302	4121	4720
R_{int}	0.0990	0.0614	0.0481
Completeness to θ	97.1%	99.7%	98.4%
GooF	1.070	1.082	1.257
R1,wR2 [I>2sigma(I)]	R1 = 0.0545, wR2 = 0.1368	R1 = 0.0374, wR2 = 0.0803	R1 = 0.0577, wR2 = 0.1196
R1, wR2	R1 = 0.0655, wR2 = 0.1437	R1 = 0.0525 wR2 = 0.0849	R1 = 0.0623, wR2 = 0.1213

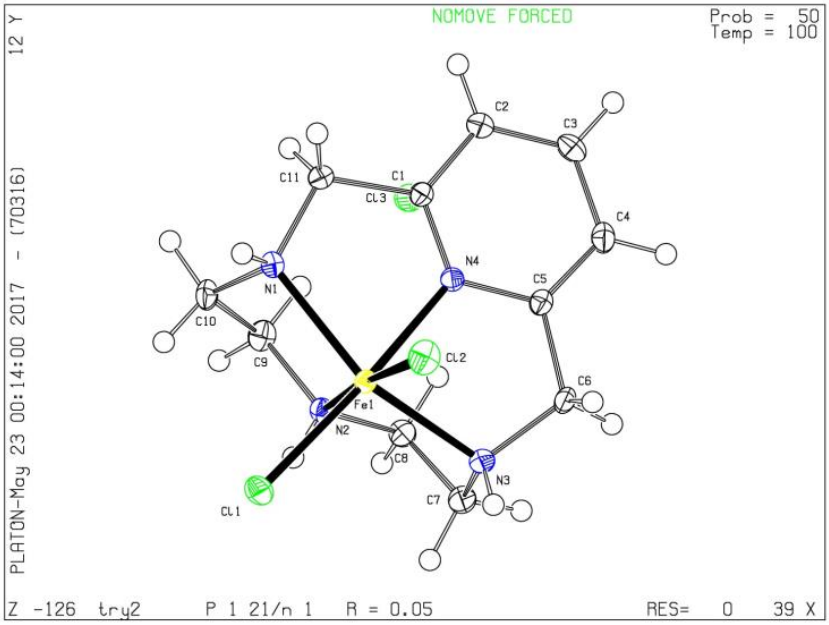

Figure A 9. *Solid-state structure of* ***[Fe^{3+}L1(Cl)$_2$]Cl****.*

Table A 10. *Bond lengths* ***[Fe^{3+}L1(Cl)$_2$]Cl****.*

Atom	Atom	Length/Å	Atom	Atom	Length/Å
Fe1	Cl1	2.2862(8)	N3	C7	1.489(4)
Fe1	Cl2	2.2805(8)	N4	C1	1.324(3)
Fe1	N1	2.181(2)	N4	C5	1.345(3)
Fe1	N2	2.182(2)	C1	C2	1.396(4)
Fe1	N3	2.161(2)	C1	C11	1.509(4)
Fe1	N4	2.098(2)	C2	C3	1.380(4)
N1	C10	1.487(4)	C3	C4	1.392(4)
N1	C11	1.485(4)	C4	C5	1.380(4)
N2	C8	1.469(4)	C5	C6	1.496(4)
N2	C9	1.476(4)	C7	C8	1.518(4)
N3	C6	1.483(4)	C9	C10	1.524(4)

Table A 11. *Bond angles* ***[Fe^{3+}L1$(Cl)_2$]Cl****.*

Atom	Atom	Atom	Angle/˚	Atom	Atom	Atom	Angle/˚
Cl2	Fe1	Cl1	95.78(3)	C6	N3	Fe1	107.75(17)
N1	Fe1	Cl1	99.28(7)	C6	N3	C7	113.4(2)
N1	Fe1	Cl2	104.56(7)	C7	N3	Fe1	110.84(18)
N1	Fe1	N2	79.93(9)	C1	N4	Fe1	121.03(19)
N2	Fe1	Cl1	86.35(7)	C1	N4	C5	121.3(2)
N2	Fe1	Cl2	174.59(7)	C5	N4	Fe1	117.58(18)
N3	Fe1	Cl1	104.59(7)	N4	C1	C2	120.9(3)
N3	Fe1	Cl2	95.89(7)	N4	C1	C11	116.0(2)
N3	Fe1	N1	146.67(9)	C2	C1	C11	123.1(2)
N3	Fe1	N2	78.76(9)	C3	C2	C1	118.4(3)
N4	Fe1	Cl1	172.25(7)	C2	C3	C4	120.0(3)
N4	Fe1	Cl2	91.50(7)	C5	C4	C3	118.5(3)
N4	Fe1	N1	76.26(9)	N4	C5	C4	120.8(3)
N4	Fe1	N2	86.62(9)	N4	C5	C6	114.2(2)
N4	Fe1	N3	77.19(9)	C4	C5	C6	125.0(3)
C10	N1	Fe1	106.00(17)	N3	C6	C5	111.6(2)
C11	N1	Fe1	113.96(17)	N3	C7	C8	110.8(2)
C11	N1	C10	112.1(2)	N2	C8	C7	106.7(2)
C8	N2	Fe1	110.64(17)	N2	C9	C10	108.9(2)
C8	N2	C9	115.5(2)	N1	C10	C9	108.9(2)
C9	N2	Fe1	110.75(18)	N1	C11	C1	111.4(2)

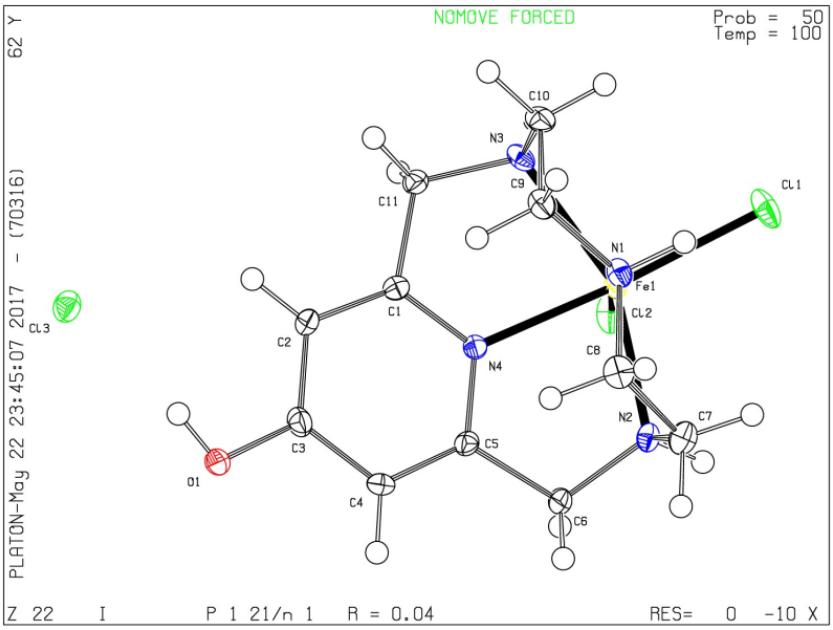

Figure A 10. Solid-state structure ***[Fe^{3+}L2(Cl)$_2$]Cl***. SQEEZE analysis was performed, asymmetric unit contains a molecule of methanol.

Table A 12. *Bond lengths* ***[Fe^{3+}L2(Cl)$_2$]Cl***.

Atom	Atom	Length/Å	Atom	Atom	Length/Å
Fe1	Cl1	2.2895(7)	N1	C11	1.482(3)
Fe1	Cl2	2.2563(7)	N4	C1	1.344(3)
Fe1	N2	2.200(2)	N4	C5	1.344(3)
Fe1	N3	2.173(2)	C1	C2	1.376(3)
Fe1	N1	2.178(2)	C1	C11	1.510(3)
Fe1	N4	2.0997(19)	C2	C3	1.399(3)
O1	C3	1.337(3)	C3	C4	1.400(3)
N2	C8	1.477(3)	C4	C5	1.378(3)
N2	C9	1.474(3)	C5	C6	1.511(3)
N3	C6	1.487(3)	C7	C8	1.513(3)
N3	C7	1.489(3)	C9	C10	1.517(3)
N1	C10	1.490(3)			

Table A 13. *Bond angles* ***[Fe^{3+}L2(Cl)$_2$]Cl.***

Atom	Atom	Atom	Angle/˚	Atom	Atom	Atom	Angle/˚
Cl2	Fe1	Cl1	96.94(3)	C11	N1	Fe1	111.78(14)
N2	Fe1	Cl1	85.38(5)	C11	N1	C10	112.41(19)
N2	Fe1	Cl2	175.18(6)	C1	N4	Fe1	120.15(15)
N3	Fe1	Cl1	104.22(6)	C5	N4	Fe1	119.52(15)
N3	Fe1	Cl2	95.59(6)	C5	N4	C1	119.2(2)
N3	Fe1	N2	79.73(7)	N4	C1	C2	122.5(2)
N3	Fe1	N1	147.49(8)	N4	C1	C11	113.5(2)
N1	Fe1	Cl1	99.07(6)	C2	C1	C11	124.0(2)
N1	Fe1	Cl2	103.86(6)	C1	C2	C3	118.1(2)
N1	Fe1	N2	79.87(8)	O1	C3	C2	123.0(2)
N4	Fe1	Cl1	169.80(6)	O1	C3	C4	117.3(2)
N4	Fe1	Cl2	93.02(5)	C2	C3	C4	119.7(2)
N4	Fe1	N2	84.85(7)	C5	C4	C3	117.9(2)
N4	Fe1	N3	76.91(7)	N4	C5	C4	122.6(2)
N4	Fe1	N1	76.28(7)	N4	C5	C6	113.3(2)
C8	N2	Fe1	110.06(14)	C4	C5	C6	124.1(2)
C9	N2	Fe1	109.49(14)	N3	C6	C5	110.33(18)
C9	N2	C8	116.38(19)	N3	C7	C8	110.49(19)
C6	N3	Fe1	110.59(14)	N2	C8	C7	107.41(19)
C6	N3	C7	112.67(19)	N2	C9	C10	107.01(19)
C7	N3	Fe1	107.75(14)	N1	C10	C9	109.75(19)
C10	N1	Fe1	106.91(15)	N1	C11	C1	110.11(19)

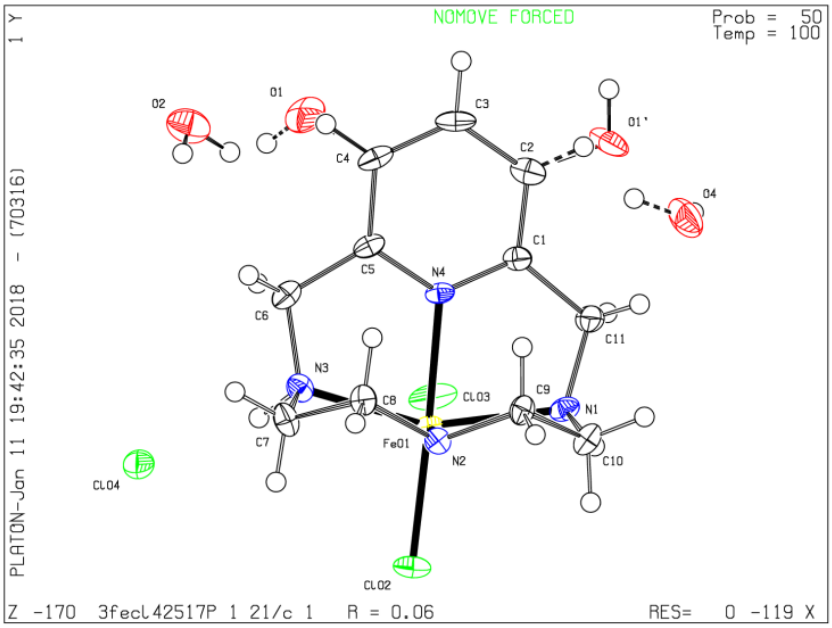

Figure A 11. *Solid-state structure* ***[Fe^{3+}L3(Cl)$_2$]Cl****, the hydroxyl group has been modeled for disorder.*

Table A 14. *Bond lengths* ***[Fe^{3+}L3(Cl)$_2$]Cl.***

Atom	Atom	Length/Å	Atom	Atom	Length/Å
Fe01	Cl02	2.2321(9)	N3	C6	1.481(4)
Fe01	Cl03	2.3036(9)	N3	C7	1.491(4)
Fe01	N4	2.115(3)	O1'	C2	1.361(7)
Fe01	N2	2.199(3)	C5	C4	1.390(4)
Fe01	N1	2.164(3)	C5	C6	1.506(5)
Fe01	N3	2.174(3)	C4	C3	1.383(5)
N4	C5	1.340(4)	C4	O1	1.23(3)
N4	C1	1.331(4)	C9	C10	1.517(5)
N2	C9	1.483(4)	C3	C2	1.389(5)
N2	C8	1.478(4)	C1	C2	1.386(5)
N1	C10	1.483(4)	C1	C11	1.506(5)
N1	C11	1.491(4)	C8	C7	1.521(5)

Table A 15. *Bond angles* ***[Fe^{3+}L3(Cl)$_2$]Cl.***

Atom	Atom	Atom	Angle/˚	Atom	Atom	Atom	Angle/˚
Cl02	Fe01	Cl03	97.82(4)	C11	N1	Fe01	110.7(2)
N4	Fe01	Cl02	174.06(8)	C6	N3	Fe01	112.2(2)
N4	Fe01	Cl03	87.85(7)	C6	N3	C7	112.8(3)
N4	Fe01	N2	86.36(10)	C7	N3	Fe01	107.1(2)
N4	Fe01	N1	77.18(10)	N4	C5	C4	119.9(3)
N4	Fe01	N3	76.53(11)	N4	C5	C6	115.2(3)
N2	Fe01	Cl02	88.14(8)	C4	C5	C6	124.8(3)
N2	Fe01	Cl03	172.30(8)	C3	C4	C5	118.8(3)
N1	Fe01	Cl02	104.02(8)	O1	C4	C5	118.1(11)
N1	Fe01	Cl03	94.14(8)	O1	C4	C3	123.0(11)
N1	Fe01	N2	79.63(10)	N2	C9	C10	106.6(3)
N1	Fe01	N3	147.55(11)	C4	C3	C2	120.1(3)
N3	Fe01	Cl02	100.32(8)	N4	C1	C2	120.4(3)
N3	Fe01	Cl03	103.52(8)	N4	C1	C11	115.9(3)
N3	Fe01	N2	80.05(10)	C2	C1	C11	123.7(3)
C5	N4	Fe01	119.4(2)	O1'	C2	C3	125.0(3)
C1	N4	Fe01	118.2(2)	O1'	C2	C1	116.4(3)
C1	N4	C5	122.3(3)	C1	C2	C3	118.6(3)
C9	N2	Fe01	110.15(19)	N2	C8	C7	107.0(3)
C8	N2	Fe01	109.82(19)	N3	C6	C5	112.0(3)
C8	N2	C9	115.0(3)	N1	C10	C9	111.0(3)
C10	N1	Fe01	108.5(2)	N3	C7	C8	110.3(3)
C10	N1	C11	113.5(3)	N1	C11	C1	111.2(3)

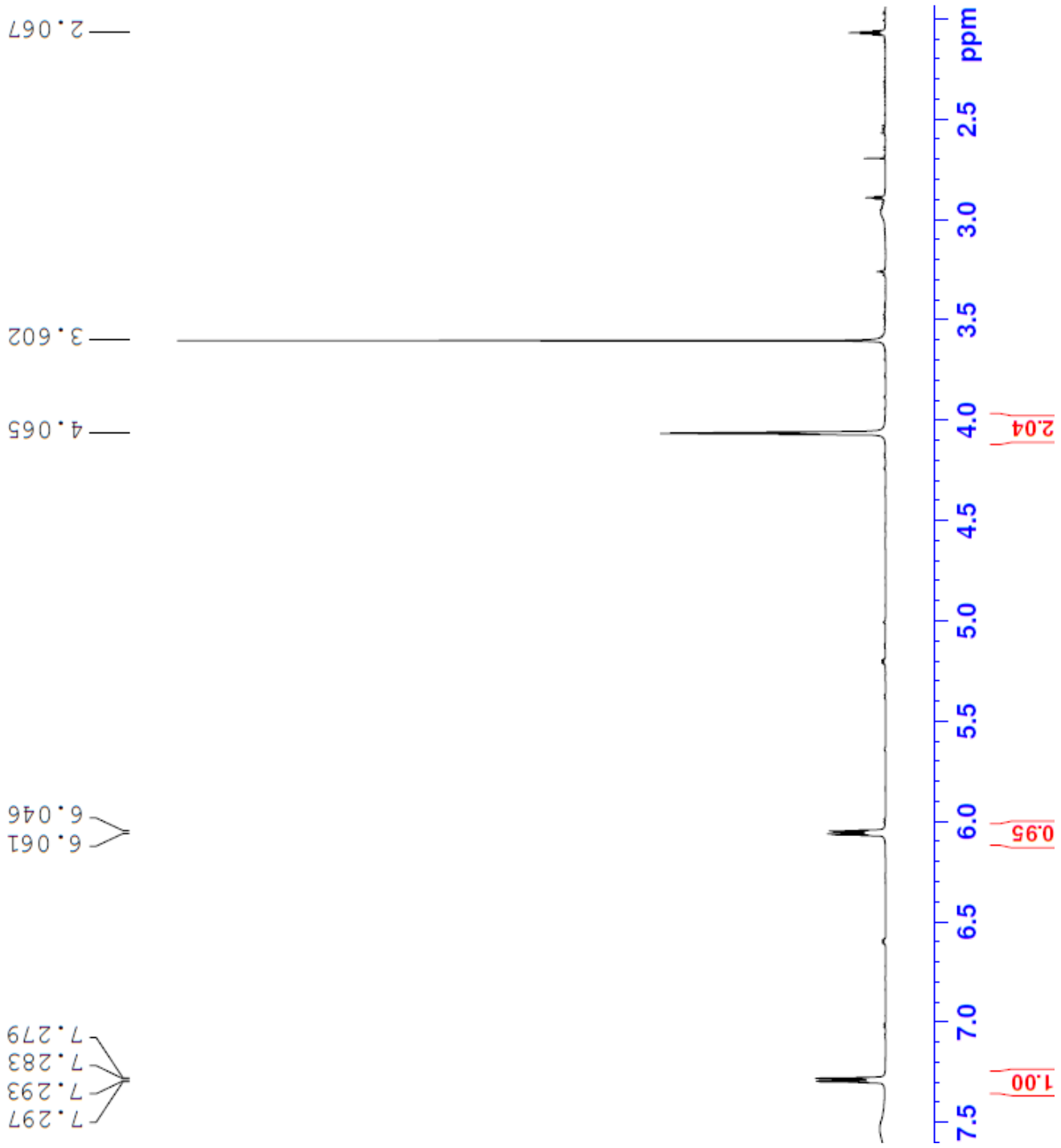

Figure A 12. *^{1}H-NMR of 3-pyrroline-2-one.*

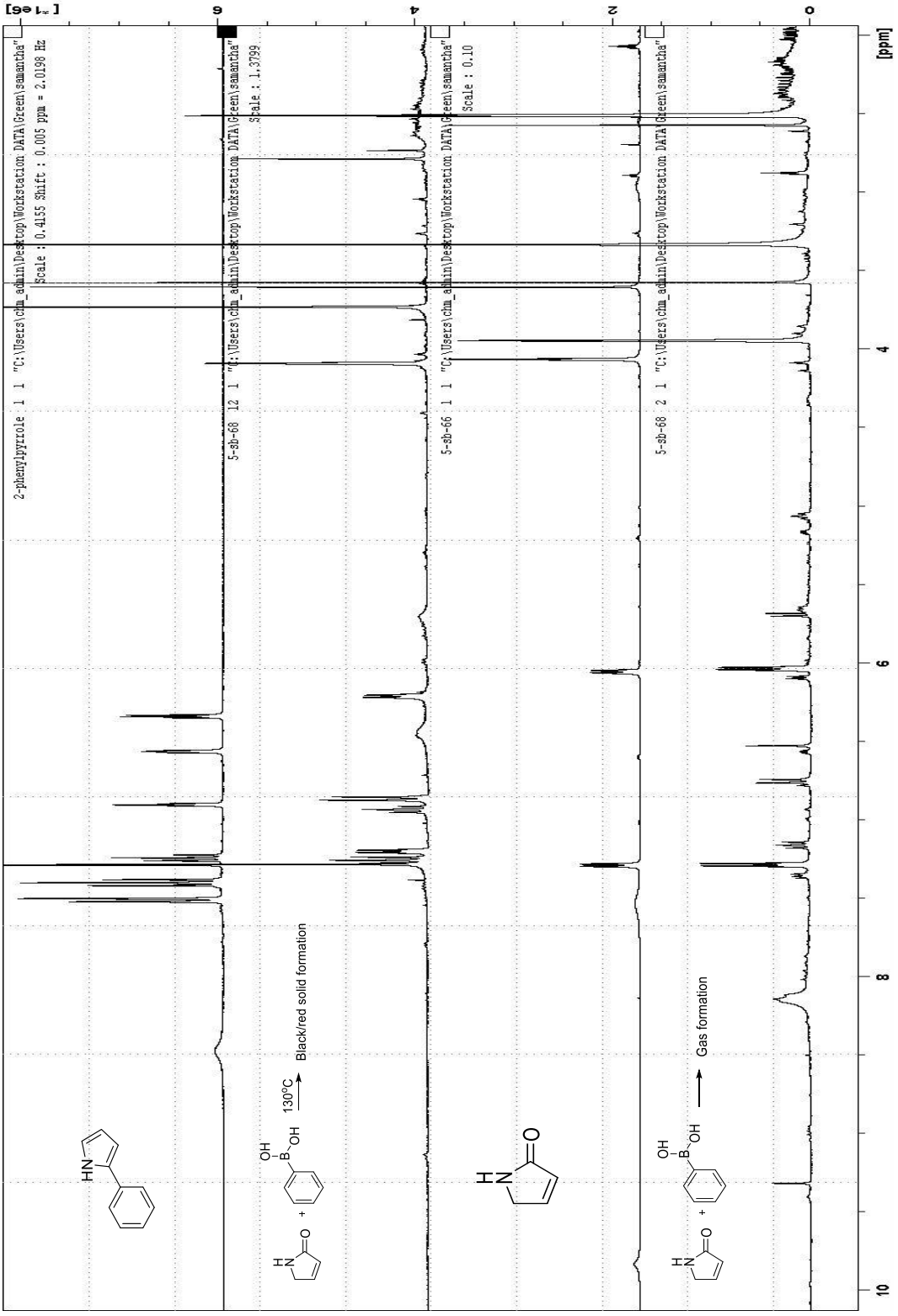

Figure A 13. *^{1}H-NMR comparing (a) 2-phenylpyrrole, (b) the result of mixing phenylboronic acid and 3-pyrroline-2-one at 130°C, (c) 3-pyrroline-2-one, and (d) the result of mixing phenylboronic acid and 3-pyrroline-2-one at room temperature.*

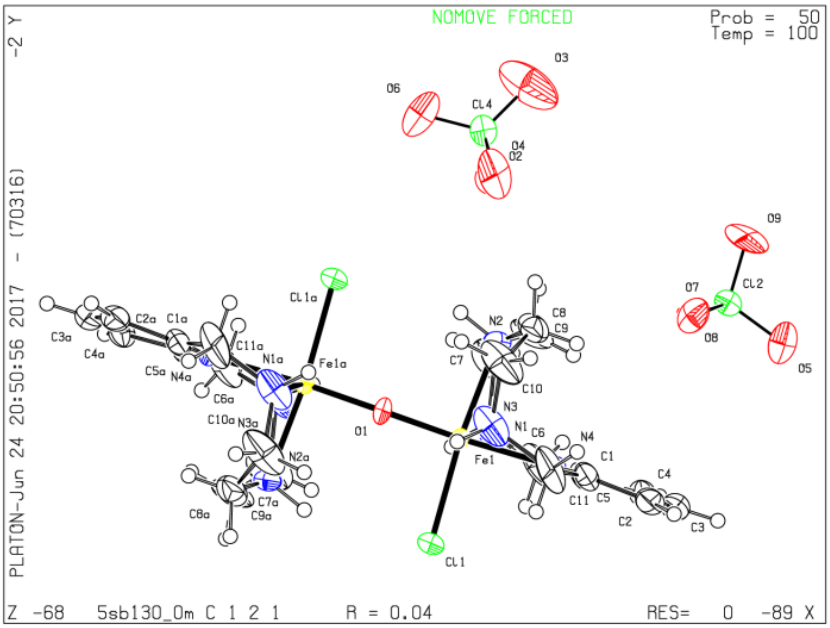

***Figure A 14**. Solid-state structure of **1a**.*

***Table A 16.** Bond lengths **1a**.*

Atom	Atom	Length/Å	Atom	Atom	Length/Å
Fe1	Cl1	2.3230(15)	C1	C11	1.44(2)
Fe1	O1	1.765(3)	C2	C3	1.377(16)
Fe1	N1	2.200(16)	C3	C4	1.340(15)
Fe1	N2	2.206(5)	C4	C5	1.358(19)
Fe1	N3	2.148(15)	C5	C6	1.55(2)
Fe1	N4	2.127(4)	C7	C8	1.34(3)
N1	C10	1.41(2)	C9	C10	1.65(3)
N1	C11	1.58(2)	Cl2	O5	1.443(19)
N2	C8	1.56(3)	Cl2	O7	1.430(16)
N2	C9	1.37(3)	Cl2	O8	1.454(16)
N3	C6	1.37(2)	Cl2	O9	1.424(18)
N3	C7	1.56(2)	Cl4	O2	1.508(14)
N4	C1	1.23(2)	Cl4	O3	1.366(13)
N4	C5	1.44(3)	Cl4	O4	1.502(13)
C1	C2	1.46(2)	Cl4	O6	1.378(10)

Table A 17. *Bond angles* ***1a*****.**

Atom	Atom	Atom	Angle/˚	Atom	Atom	Atom	Angle/˚
O1	Fe1	Cl1	93.70(5)	N4	C1	C2	115.8(16)
O1	Fe1	N1	100.0(11)	N4	C1	C11	112.3(15)
O1	Fe1	N2	91.59(14)	C11	C1	C2	131.2(14)
O1	Fe1	N3	107.7(11)	C3	C2	C1	122.2(11)
O1	Fe1	N4	173.2(11)	C4	C3	C2	121.9(9)
N1	Fe1	Cl1	99.6(5)	C3	C4	C5	112.7(12)
N1	Fe1	N2	78.5(8)	N4	C5	C6	116.7(14)
N2	Fe1	Cl1	174.63(17)	C4	C5	N4	126.4(15)
N3	Fe1	Cl1	99.9(4)	C4	C5	C6	116.8(15)
N3	Fe1	N1	144.8(2)	N3	C6	C5	109.8(13)
N3	Fe1	N2	79.3(7)	C8	C7	N3	110.5(16)
N4	Fe1	Cl1	89.32(13)	C7	C8	N2	105.4(18)
N4	Fe1	N1	73.5(7)	N2	C9	C10	108.3(16)
N4	Fe1	N2	85.32(19)	N1	C10	C9	109.2(14)
N4	Fe1	N3	77.7(7)	C1	C11	N1	112.6(12)
Fe1	O1	Fe11	171(2)	O5	Cl2	O8	107.8(14)
C10	N1	Fe1	110.9(13)	O7	Cl2	O5	109.4(16)
C10	N1	C11	114.7(17)	O7	Cl2	O8	109.8(14)
C11	N1	Fe1	106.9(10)	O9	Cl2	O5	109.8(14)
C8	N2	Fe1	107.1(12)	O9	Cl2	O7	110.2(17)
C9	N2	Fe1	112.5(13)	O9	Cl2	O8	109.8(15)
C9	N2	C8	114.0(6)	O3	Cl4	O2	110.4(14)
C6	N3	Fe1	117.0(12)	O3	Cl4	O4	111.5(16)
C6	N3	C7	113.0(17)	O3	Cl4	O6	120.6(10)
C7	N3	Fe1	105.0(11)	O4	Cl4	O2	97.6(7)
C1	N4	Fe1	126.1(14)	O6	Cl4	O2	108.8(13)
C1	N4	C5	120.5(7)	O6	Cl4	O4	105.5(13)
C5	N4	Fe1	113.3(11)				

[1]-X,+Y,-Z

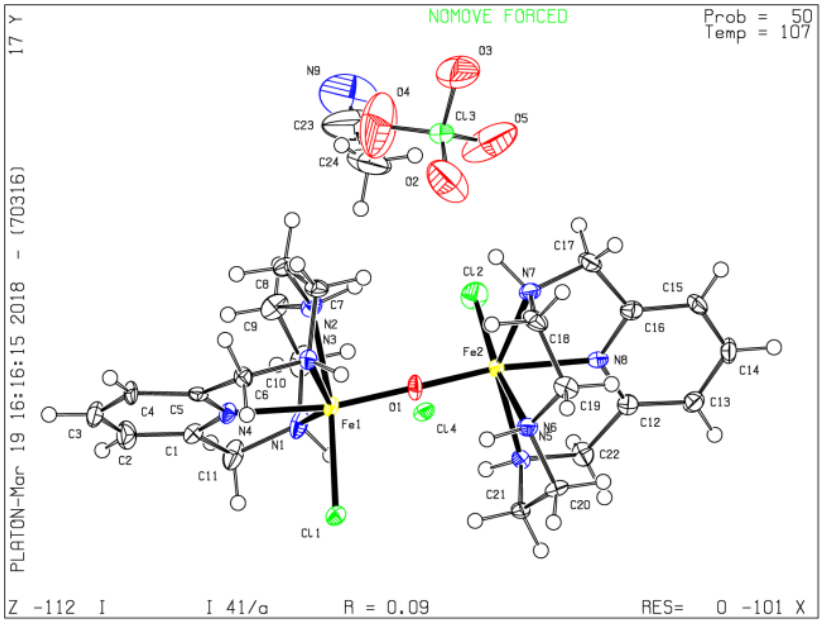

Figure A 15. *Solid-state structure of* ***1b****.*

Table A 18. *Bond length* ***1b.***

Atom	Atom	Length/Å	Atom	Atom	Length/Å
Fe1	Cl1	2.3298(17)	N7	C17	1.460(9)
Fe1	O1	1.775(4)	N1	C11	1.492(9)
Fe1	N4	2.137(5)	N1	C10	1.478(9)
Fe1	N3	2.187(5)	C6	C5	1.513(9)
Fe1	N2	2.215(5)	C5	C4	1.386(9)
Fe1	N1	2.202(5)	C12	C22	1.499(9)
Fe2	Cl2	2.3279(19)	C12	C13	1.371(9)
Fe2	O1	1.782(4)	C7	C8	1.520(9)
Fe2	N6	2.218(5)	C20	C21	1.513(9)
Fe2	N5	2.179(5)	C1	C11	1.502(9)
Fe2	N8	2.136(5)	C1	C2	1.379(10)
Fe2	N7	2.210(5)	C19	C18	1.511(9)
N6	C20	1.474(8)	C15	C16	1.376(10)
N6	C19	1.467(8)	C15	C14	1.383(10)
N5	C21	1.478(8)	C4	C3	1.386(10)
N5	C22	1.477(8)	C16	C17	1.513(9)
N4	C5	1.338(8)	C14	C13	1.382(10)
N4	C1	1.335(8)	C10	C9	1.514(10)
N3	C6	1.472(8)	C3	C2	1.378(10)
N3	C7	1.488(8)	N9	C23	1.084(15)
N8	C12	1.339(8)	C24	C23	1.550(18)
N8	C16	1.336(8)	Cl3	O2	1.417(8)
N2	C8	1.478(8)	Cl3	O5	1.391(9)
N2	C9	1.467(8)	Cl3	O3	1.441(8)
N7	C18	1.481(9)	Cl3	O4	1.388(9)

Table A 19. *Bond angles* ***1b****.*

Atom	Atom	Atom	Angle/˚	Atom	Atom	Atom	Angle/˚
O1	Fe1	Cl1	100.37(16)	C8	N2	Fe1	109.9(4)
O1	Fe1	N4	170.3(2)	C9	N2	Fe1	110.6(4)
O1	Fe1	N3	97.6(2)	C9	N2	C8	116.4(5)
O1	Fe1	N2	87.7(2)	C18	N7	Fe2	108.5(4)
O1	Fe1	N1	107.6(2)	C17	N7	Fe2	110.0(4)
N4	Fe1	Cl1	88.02(15)	C17	N7	C18	114.1(6)
N4	Fe1	N3	75.86(19)	C11	N1	Fe1	110.4(4)
N4	Fe1	N2	84.1(2)	C10	N1	Fe1	108.0(4)
N4	Fe1	N1	75.8(2)	C10	N1	C11	113.5(5)
N3	Fe1	Cl1	100.45(14)	N3	C6	C5	111.2(5)
N3	Fe1	N2	79.78(19)	N4	C5	C6	114.7(5)
N3	Fe1	N1	145.8(2)	N4	C5	C4	121.2(6)
N2	Fe1	Cl1	171.80(16)	C4	C5	C6	124.0(6)
N1	Fe1	Cl1	97.37(16)	N8	C12	C22	114.0(6)
N1	Fe1	N2	78.6(2)	N8	C12	C13	120.7(6)
O1	Fe2	Cl2	98.68(16)	C13	C12	C22	125.3(6)
O1	Fe2	N6	87.0(2)	N3	C7	C8	110.4(5)
O1	Fe2	N5	98.4(2)	N6	C20	C21	108.0(5)
O1	Fe2	N8	170.5(2)	N4	C1	C11	114.6(6)
O1	Fe2	N7	106.9(2)	N4	C1	C2	120.9(6)
N6	Fe2	Cl2	172.04(15)	C2	C1	C11	124.5(6)
N5	Fe2	Cl2	104.54(15)	N6	C19	C18	107.7(5)
N5	Fe2	N6	79.96(19)	C16	C15	C14	118.3(6)
N5	Fe2	N7	145.5(2)	C5	C4	C3	118.1(6)
N8	Fe2	Cl2	90.12(14)	N5	C21	C20	111.3(5)
N8	Fe2	N6	84.6(2)	N5	C22	C12	112.1(5)
N8	Fe2	N5	75.8(2)	N8	C16	C15	121.6(6)
N8	Fe2	N7	75.7(2)	N8	C16	C17	113.6(6)
N7	Fe2	Cl2	94.65(15)	C15	C16	C17	124.7(6)
N7	Fe2	N6	78.30(19)	N7	C18	C19	110.4(5)
Fe1	O1	Fe2	166.7(3)	N7	C17	C16	112.4(5)
C20	N6	Fe2	109.6(4)	C13	C14	C15	119.6(6)
C19	N6	Fe2	110.7(4)	N2	C8	C7	108.1(5)
C19	N6	C20	116.6(5)	N1	C11	C1	111.6(5)
C21	N5	Fe2	106.5(4)	C12	C13	C14	119.4(6)
C22	N5	Fe2	112.0(4)	N1	C10	C9	110.7(5)
C22	N5	C21	114.3(5)	C2	C3	C4	119.9(6)
C5	N4	Fe1	119.6(4)	N2	C9	C10	107.0(5)
C1	N4	Fe1	119.7(4)	C3	C2	C1	119.1(7)
C1	N4	C5	120.7(6)	N9	C23	C24	172.8(19)
C6	N3	Fe1	112.5(4)	O2	Cl3	O3	105.9(6)
C6	N3	C7	112.9(5)	O5	Cl3	O2	109.7(5)
C7	N3	Fe1	106.9(4)	O5	Cl3	O3	104.3(6)
C12	N8	Fe2	119.9(4)	O4	Cl3	O2	113.6(6)
C16	N8	Fe2	119.6(4)	O4	Cl3	O5	117.0(7)
C16	N8	C12	120.5(6)	O4	Cl3	O3	105.2(6)

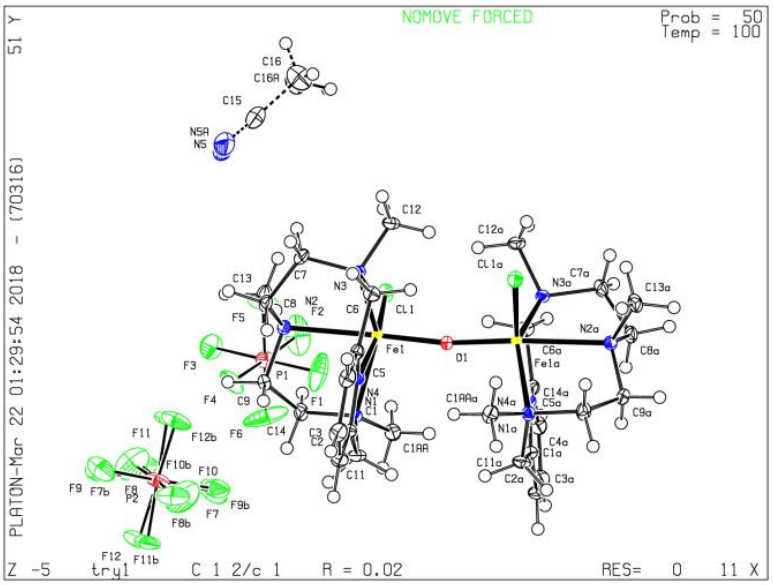

Figure A 16. *Solid-state structure of* ***2****.*

Table A 20. *Bond lengths of* ***2****.*

Atom	Atom	Length/Å	Atom	Atom	Length/Å
C1	C2	1.3924(14)	Fe01	N3	2.2230(8)
C1	C11	1.5032(14)	Fe01	N4	2.1174(8)
C1	N4	1.3378(12)	Fe01	O1	1.80035(16)
C2	C3	1.3860(17)	F4	P2	1.592(8)
C3	C4	1.3909(16)	F5	P2	1.585(9)
C4	C5	1.3887(13)	F6	P2	1.605(8)
C5	C6	1.5022(14)	F7	P2	1.590(9)
C5	N4	1.3397(12)	F8	P2	1.602(5)
C6	N3	1.4857(13)	F9	P2	1.578(5)
C7	C8	1.5170(15)	F10	F121	0.249(19)
C7	N3	1.4889(13)	F10	P3	1.590(9)
C8	N2	1.4773(13)	F11	F131	0.21(3)
C9	C10	1.5143(14)	F11	P3	1.601(10)
C9	N2	1.4815(13)	F12	P3	1.598(8)
C10	N1	1.4906(12)	F13	P3	1.594(10)
C11	N1	1.4873(13)	F14	F151	0.26(3)
C12	N1	1.4882(13)	F14	P3	1.597(11)
C13	N2	1.4821(13)	F15	P3	1.612(11)
C14	N3	1.4886(13)	C0AA	C16	1.489(11)
Cl1	Fe01	2.2857(3)	C0AB	C16	1.475(10)
Fe01	N1	2.2259(8)	C16	N0AA	1.144(11)
Fe01	N2	2.3669(8)	C16	N0AB	1.10(2)

[1]1/2-X,1/2-Y,1-Z

Table A 21. *Bond angles* ***2****.*

Atom	Atom	Atom	Angle/˚	Atom	Atom	Atom	Angle/˚
C2	C1	C11	124.11(9)	F152	F14	P3	89(5)
N4	C1	C2	120.58(10)	F142	F15	P3	82(5)
N4	C1	C11	115.18(8)	F102	P3	F10	180.0
C3	C2	C1	118.56(10)	F10	P3	F112	89.1(6)
C2	C3	C4	120.29(10)	F102	P3	F112	90.9(6)
C5	C4	C3	118.11(10)	F102	P3	F11	89.1(6)
C4	C5	C6	124.24(9)	F10	P3	F11	90.9(6)
N4	C5	C4	121.06(9)	F102	P3	F12	8.9(7)
N4	C5	C6	114.57(8)	F10	P3	F12	171.1(7)
N3	C6	C5	111.78(8)	F102	P3	F122	171.1(7)
N3	C7	C8	112.64(8)	F10	P3	F122	8.9(7)
N2	C8	C7	108.91(8)	F10	P3	F132	97.1(6)
N2	C9	C10	109.09(8)	F10	P3	F13	82.9(6)
N1	C10	C9	110.76(8)	F102	P3	F13	97.1(6)
N1	C11	C1	112.71(8)	F102	P3	F132	82.9(6)
Cl1	Fe01	N2	88.73(2)	F10	P3	F14	86.1(5)
N1	Fe01	Cl1	98.48(2)	F10	P3	F142	93.9(5)
N1	Fe01	N2	78.65(3)	F102	P3	F14	93.9(5)
N3	Fe01	Cl1	105.68(2)	F102	P3	F142	86.1(5)
N3	Fe01	N1	145.45(3)	F102	P3	F15	93.9(5)
N3	Fe01	N2	77.59(3)	F102	P3	F152	86.1(5)
N4	Fe01	Cl1	170.95(2)	F10	P3	F15	86.1(5)
N4	Fe01	N1	76.10(3)	F10	P3	F152	93.9(5)
N4	Fe01	N2	83.13(3)	F112	P3	F11	180.0
N4	Fe01	N3	76.47(3)	F11	P3	F152	90.1(5)
O1	Fe01	Cl1	98.763(19)	F112	P3	F152	89.9(5)
O1	Fe01	N1	102.41(4)	F112	P3	F15	90.1(5)
O1	Fe01	N2	172.14(2)	F11	P3	F15	89.9(5)
O1	Fe01	N3	97.97(3)	F12	P3	F112	82.0(6)
O1	Fe01	N4	89.55(3)	F12	P3	F11	98.0(6)
C10	N1	Fe01	107.35(6)	F122	P3	F11	82.0(6)
C11	N1	C10	110.24(8)	F122	P3	F112	98.0(6)
C11	N1	C12	109.46(8)	F12	P3	F122	180.0
C11	N1	Fe01	110.84(6)	F12	P3	F152	87.0(5)
C12	N1	C10	108.67(8)	F122	P3	F152	93.0(5)
C12	N1	Fe01	110.23(6)	F122	P3	F15	87.0(5)
C8	N2	C9	112.27(8)	F12	P3	F15	93.0(5)
C8	N2	C13	108.67(8)	F13	P3	F112	7.6(10)
C8	N2	Fe01	105.69(6)	F132	P3	F11	7.6(10)
C9	N2	C13	108.40(8)	F132	P3	F112	172.4(10)
C9	N2	Fe01	105.25(6)	F13	P3	F11	172.4(10)

C13	N2	Fe01	116.62(6)	F13	P3	F122	91.8(5)
C6	N3	C7	110.72(8)	F132	P3	F122	88.2(5)
C6	N3	C14	108.65(8)	F13	P3	F12	88.2(5)
C6	N3	Fe01	106.28(6)	F132	P3	F12	91.8(5)
C7	N3	Fe01	111.00(6)	F13	P3	F132	180.0
C14	N3	C7	108.30(8)	F132	P3	F142	88.5(5)
C14	N3	Fe01	111.88(6)	F132	P3	F14	91.5(5)
C1	N4	C5	121.37(9)	F13	P3	F14	88.5(5)
C1	N4	Fe01	120.45(7)	F13	P3	F142	91.5(5)
C5	N4	Fe01	117.97(6)	F13	P3	F15	85.5(5)
Fe01	O1	Fe011	171.91(6)	F132	P3	F15	94.5(5)
F4	P2	F6	177.8(4)	F132	P3	F152	85.5(5)
F4	P2	F8	89.6(2)	F13	P3	F152	94.5(5)
F5	P2	F4	90.6(5)	F14	P3	F11	95.4(5)
F5	P2	F6	89.5(4)	F142	P3	F11	84.6(5)
F5	P2	F7	179.5(5)	F14	P3	F112	84.6(5)
F5	P2	F8	89.9(4)	F142	P3	F112	95.4(5)
F7	P2	F4	89.5(4)	F142	P3	F12	86.1(5)
F7	P2	F6	90.3(5)	F14	P3	F122	86.1(5)
F7	P2	F8	89.7(3)	F142	P3	F122	93.9(5)
F8	P2	F6	88.2(4)	F14	P3	F12	93.9(5)
F9	P2	F4	91.2(5)	F14	P3	F142	180.0
F9	P2	F5	91.0(4)	F142	P3	F15	9.4(10)
F9	P2	F6	91.0(2)	F14	P3	F152	9.4(10)
F9	P2	F7	89.5(4)	F142	P3	F152	170.6(10)
F9	P2	F8	178.8(7)	F14	P3	F15	170.6(10)
F122	F10	P3	87(4)	F152	P3	F15	180.0
F132	F11	P3	84(6)	N0AA	C16	C0AA	174.0(8)
F102	F12	P3	84(4)	N0AB	C16	C0AB	178(4)
F112	F13	P3	88(6)				

[1]1-X,+Y,1/2-Z; [2]1/2-X,1/2-Y,1-Z

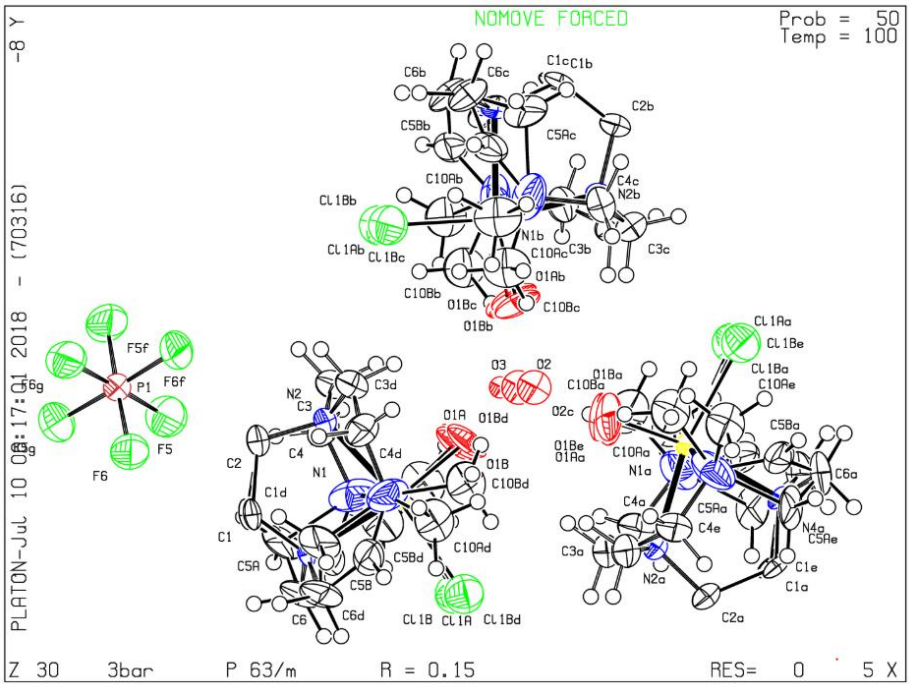

***Figure A 17**. Solid-state structure of **3**.*

***Table A 22.** Bond lengths **3**.*

Atom	Atom	Length/Å	Atom	Atom	Length/Å
Fe1	Cl1B1	2.395(9)	N2	C31	1.480(13)
Fe1	Cl1B	2.395(9)	N1	C4	1.478(14)
Fe1	O1B1	1.865(18)	N1	C5B	1.36(3)
Fe1	O1B	1.865(18)	N1	C10B	1.64(3)
Fe1	N4	2.208(11)	N1	C5A	1.75(3)
Fe1	N2	2.186(12)	N1	C10A	1.47(3)
Fe1	N11	2.177(14)	C1	C11	0.70(4)
Fe1	N1	2.177(14)	C1	C2	1.55(3)
Fe1	Cl1A	2.284(8)	C3	C4	1.48(2)
Fe1	O1A	1.65(4)	C5B	C6	1.547(19)
Cl1B	Cl1B1	1.155(18)	C6	C5A	1.526(18)
O1B	O1B1	1.18(3)	P1	F62	1.586(8)
N4	C11	1.46(2)	P1	F63	1.586(8)
N4	C1	1.46(2)	P1	F6	1.586(8)
N4	C61	1.516(12)	P1	F5	1.574(8)
N4	C6	1.516(12)	P1	F52	1.574(8)
N2	C2	1.443(19)	P1	F53	1.574(8)
N2	C3	1.480(13)			

1+X,+Y,3/2-Z; 2+Y-X,1-X,+Z; 31-Y,1+X-Y,+Z

Table A 23. *Bond angles of* ***3.***

Atom	Atom	Atom	Angle/˚	Atom	Atom	Atom	Angle/˚
O1B1	Fe1	Cl1B	93.5(9)	C61	N4	C6	113.8(13)
O1B	Fe1	Cl1B	102.4(9)	C2	N2	Fe1	117.3(10)
O1B	Fe1	N4	158.6(7)	C2	N2	C31	111.5(8)
O1B1	Fe1	N4	158.6(7)	C2	N2	C3	111.5(8)
O1B1	Fe1	N2	91.8(9)	C31	N2	Fe1	101.5(7)
O1B	Fe1	N2	91.8(9)	C3	N2	Fe1	101.5(7)
O1B	Fe1	N1	118.1(7)	C3	N2	C31	112.9(13)
O1B1	Fe1	N1	82.0(7)	C4	N1	Fe1	108.0(8)
N4	Fe1	Cl1B	92.3(4)	C4	N1	C10B	99.4(15)
N4	Fe1	Cl1B1	92.3(4)	C4	N1	C5A	98.1(13)
N4	Fe1	Cl1A	92.2(4)	C5B	N1	Fe1	104.0(13)
N2	Fe1	Cl1B1	162.6(3)	C5B	N1	C4	132.0(19)
N2	Fe1	Cl1B	162.6(3)	C5B	N1	C10B	112.4(17)
N2	Fe1	N4	77.1(4)	C10B	N1	Fe1	95.0(13)
N2	Fe1	Cl1A	169.3(4)	C5A	N1	Fe1	109.8(9)
N11	Fe1	Cl1B	113.2(4)	C10A	N1	Fe1	127.2(16)
N1	Fe1	Cl1B	85.9(3)	C10A	N1	C4	112.0(18)
N1	Fe1	Cl1B1	113.2(4)	C10A	N1	C5A	97.2(17)
N11	Fe1	Cl1B1	85.9(3)	N4	C1	C2	112.8(13)
N1	Fe1	N4	78.0(4)	C11	C1	N4	76.1(9)
N11	Fe1	N4	78.0(4)	C11	C1	C2	77.0(8)
N11	Fe1	N2	78.5(3)	N2	C2	C1	112.3(13)
N1	Fe1	N2	78.5(3)	N2	C2	C11	112.3(13)
N1	Fe1	N11	149.8(7)	C1	C2	C11	26.1(17)
N1	Fe1	Cl1A	99.5(3)	C4	C3	N2	109.4(10)
N11	Fe1	Cl1A	99.5(3)	C3	C4	N1	115.2(12)
Cl1A	Fe1	Cl1B1	14.0(2)	N1	C5B	C6	118.8(18)
O1A	Fe1	Cl1B1	100(2)	N4	C6	C5B	111.2(13)
O1A	Fe1	O1B1	18.5(6)	N4	C6	C5A	102.5(12)
O1A	Fe1	N4	167(2)	F62	P1	F63	92.2(5)
O1A	Fe1	N2	90(2)	F63	P1	F6	92.2(5)
O1A	Fe1	N11	99.7(6)	F62	P1	F6	92.2(5)
O1A	Fe1	N1	99.7(6)	F52	P1	F63	178.2(4)
O1A	Fe1	Cl1A	100(2)	F53	P1	F6	178.2(4)
Cl1B1	Cl1B	Fe1	76.0(2)	F5	P1	F62	178.2(4)
O1B1	O1B	Fe1	71.6(6)	F53	P1	F62	89.2(5)
C11	N4	Fe1	114.1(10)	F52	P1	F6	89.2(5)
C1	N4	Fe1	114.0(10)	F53	P1	F63	86.7(5)
C11	N4	C1	27.8(17)	F5	P1	F6	86.7(5)
C11	N4	C6	123.4(12)	F52	P1	F62	86.7(5)
C1	N4	C6	98.6(11)	F5	P1	F63	89.2(5)

C11	N4	C61	98.6(11)	F53	P1	F52	92.0(6)
C1	N4	C61	123.4(12)	F53	P1	F5	92.0(6)
C6	N4	Fe1	102.7(7)	F52	P1	F5	92.0(6)
C61	N4	Fe1	102.7(7)	C6	C5A	N1	99.3(14)

[1]+X,+Y,3/2-Z; [2]+Y-X,1-X,+Z; [3]1-Y,1+X-Y,+Z

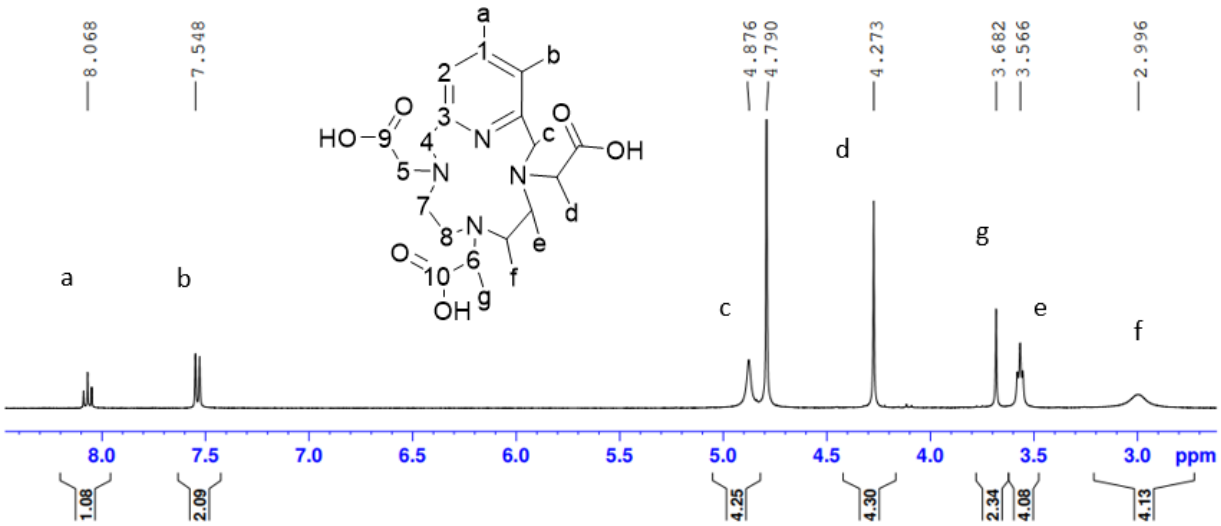

Figure A 18. *[1]H-NMR of* ***PCTA*** *in D_2O.*

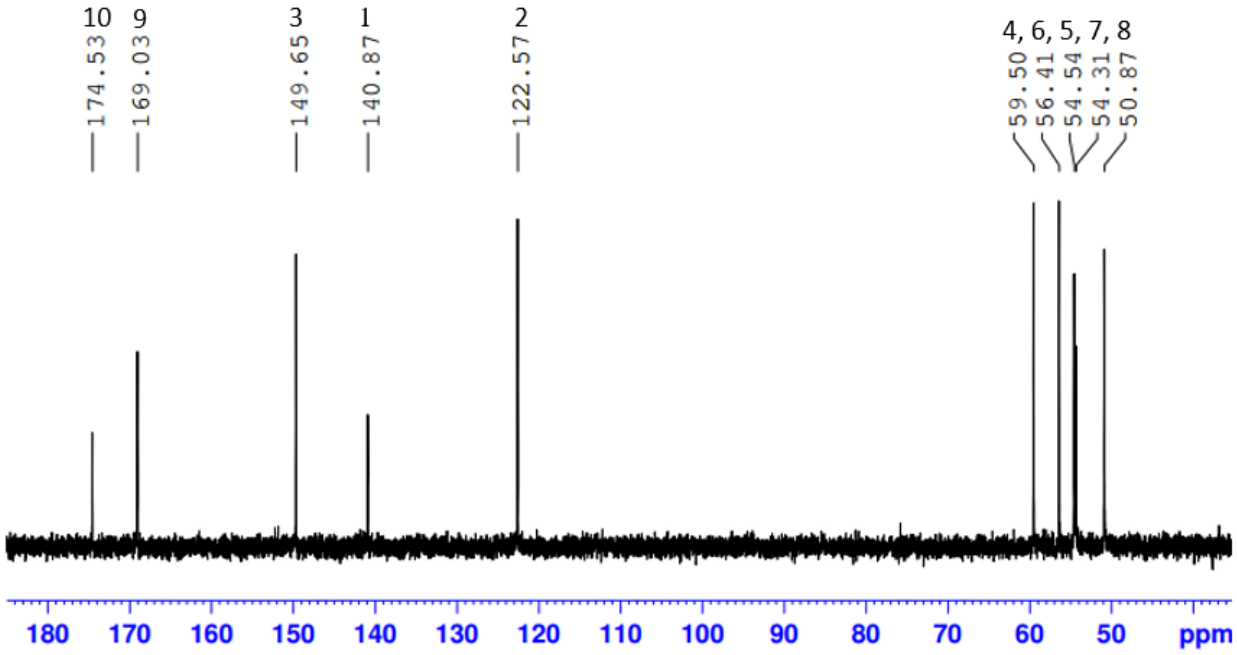

Figure A 19. *[13]C-NMR of* ***PCTA*** *in D_2O.*

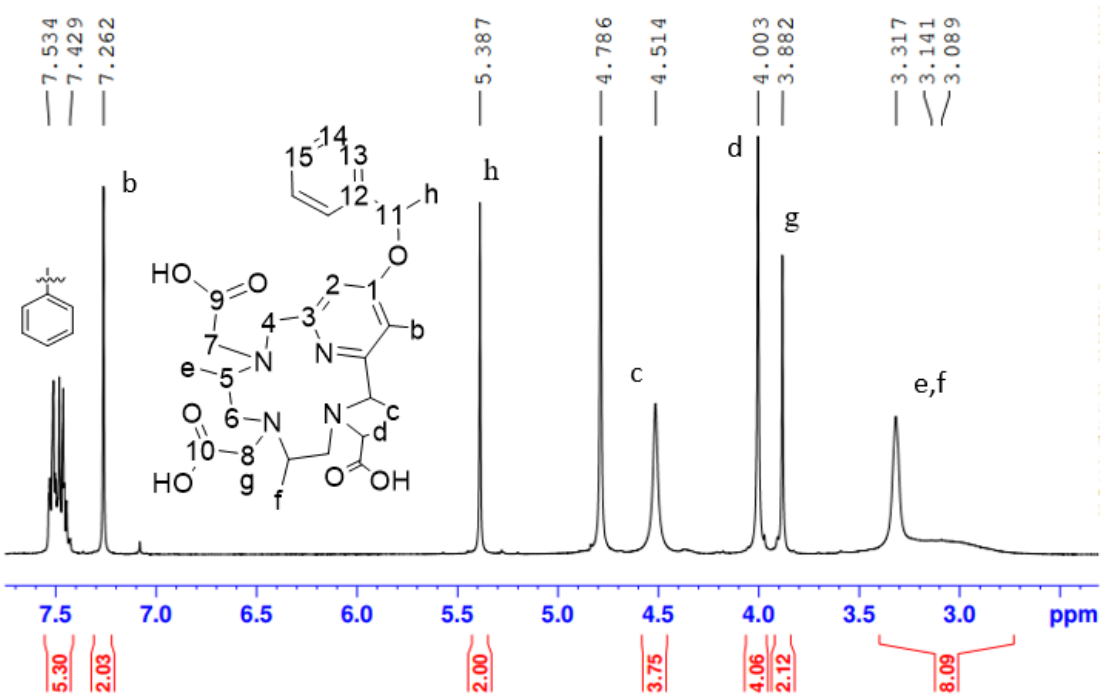

Figure A 20. *^{1}H-NMR of **L11** in D_2O.*

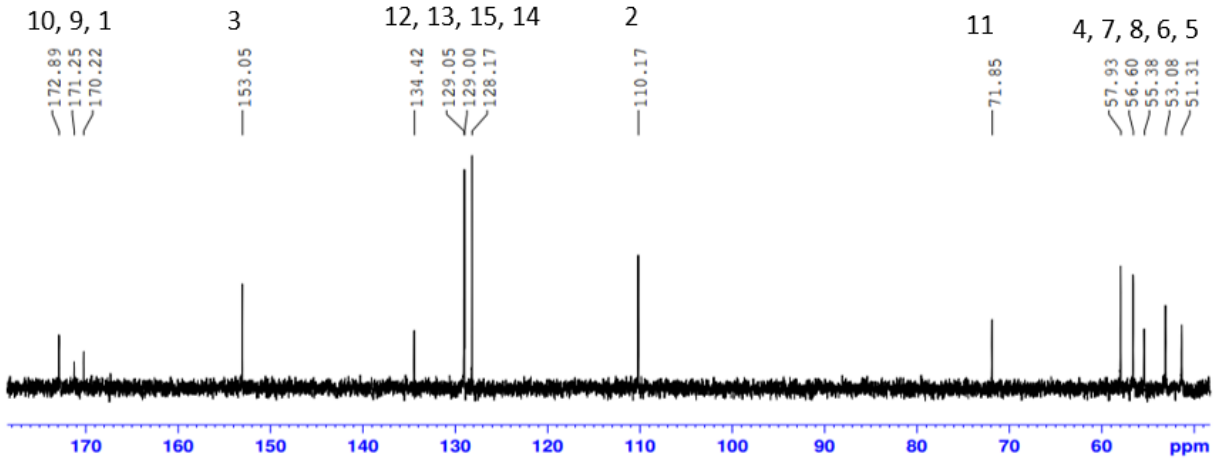

Figure A 21. *^{13}C-NMR of **L11** in D_2O.*

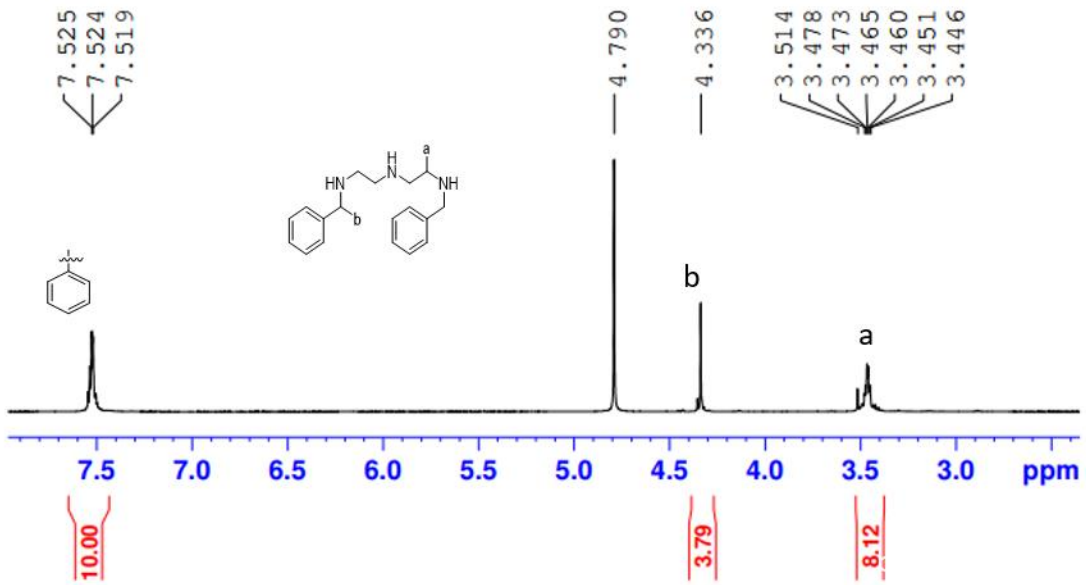

Figure A 22. *^{1}H-NMR of **8** in D_2O.*

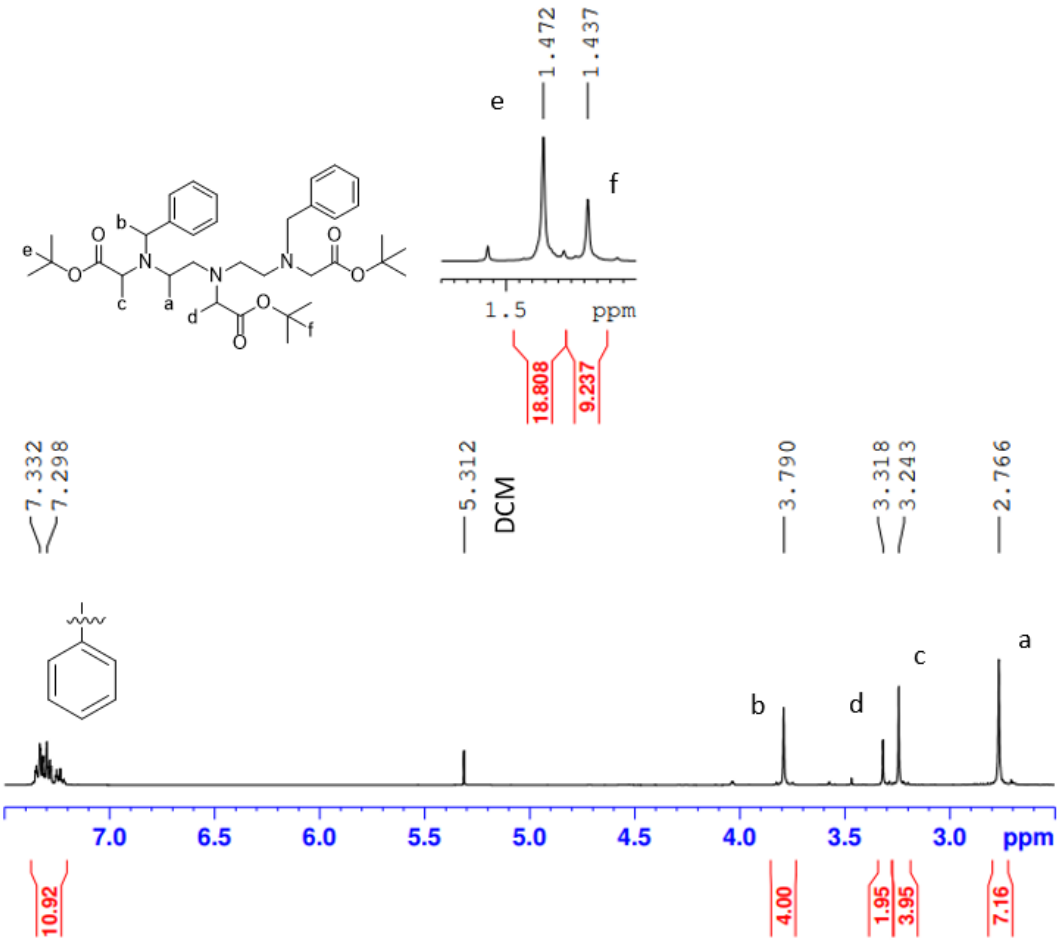

Figure A 23. *^{1}H-NMR of **9** in D_2O.*

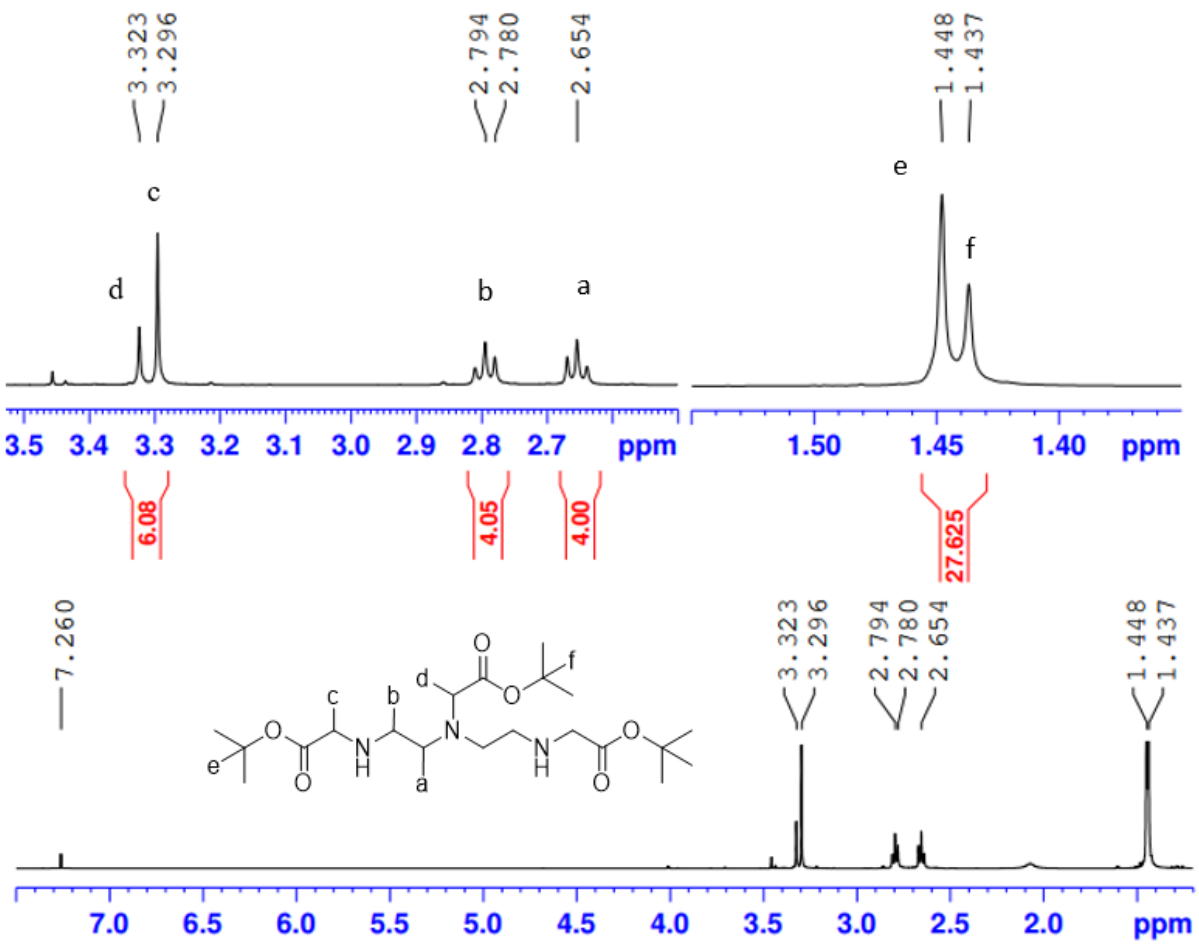

Figure A 24. *^{1}H-NMR of **10** in D_2O.*

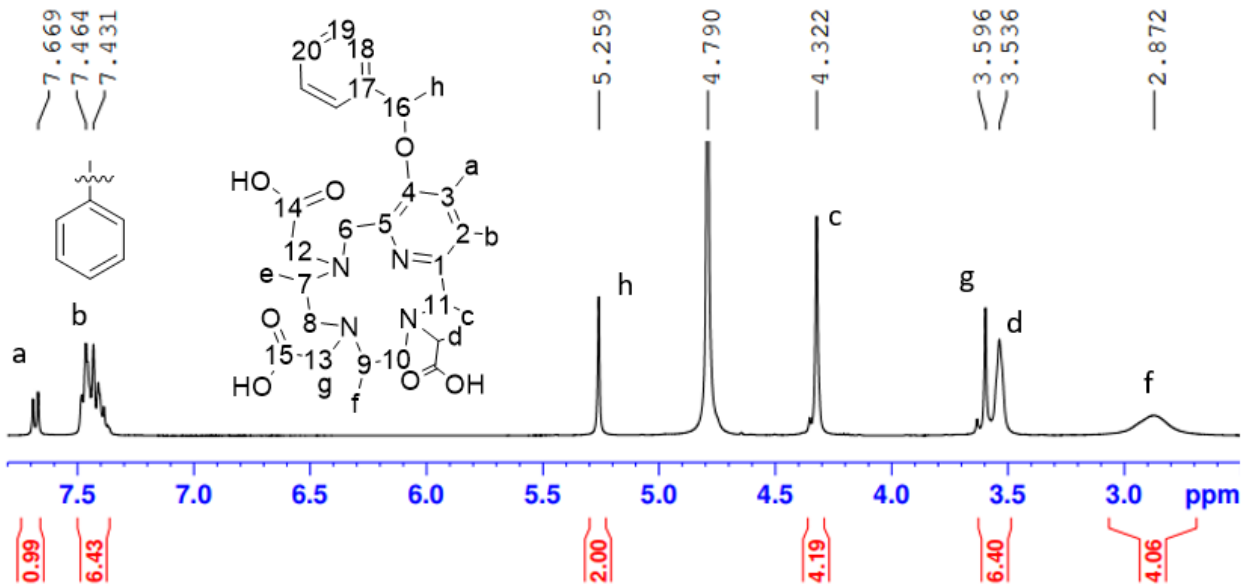

Figure A 25. *^{1}H-NMR of **L12** in D_2O.*

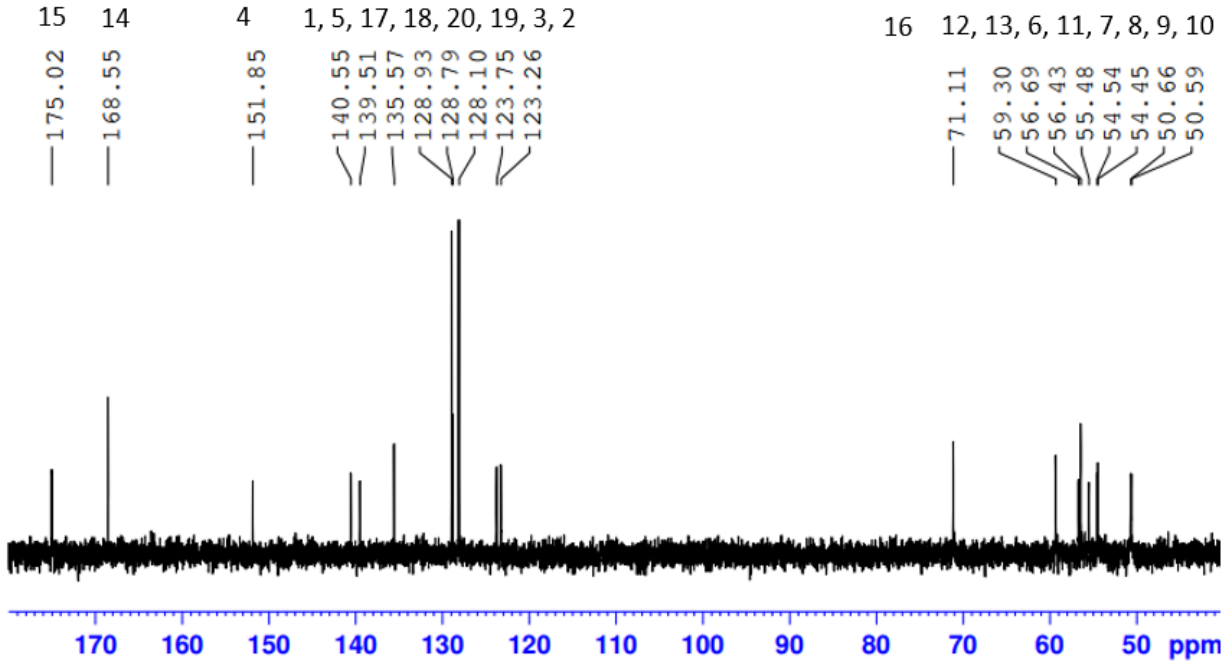

Figure A 26. *^{13}C-NMR of **L12** in D_2O.*

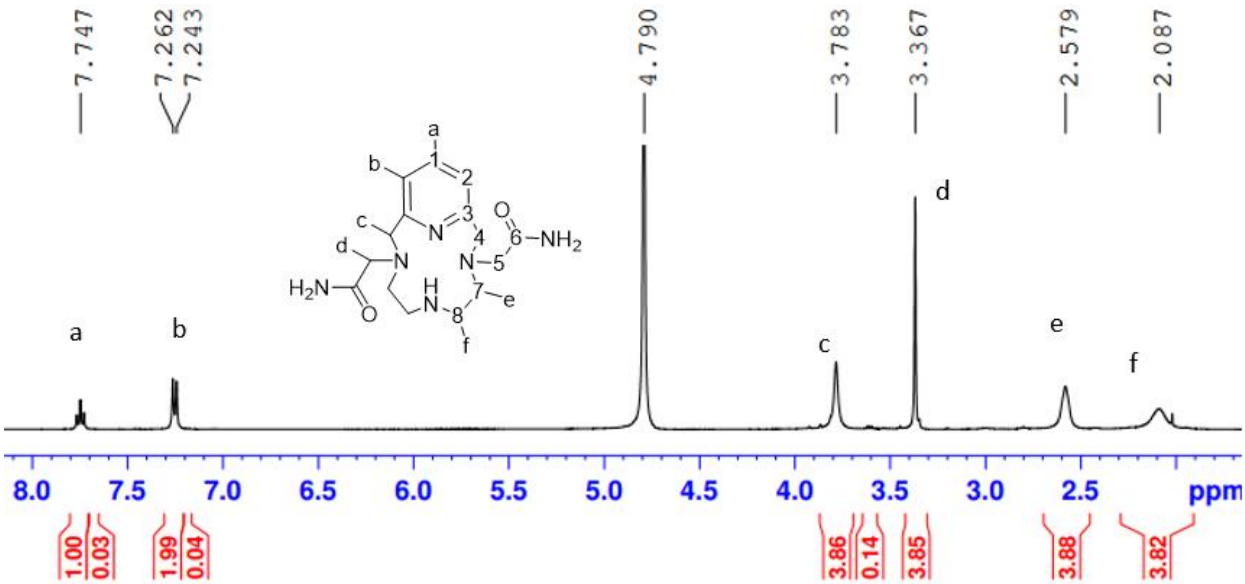

Figure A 27. *^{1}H-NMR of **L16** in D_2O.*

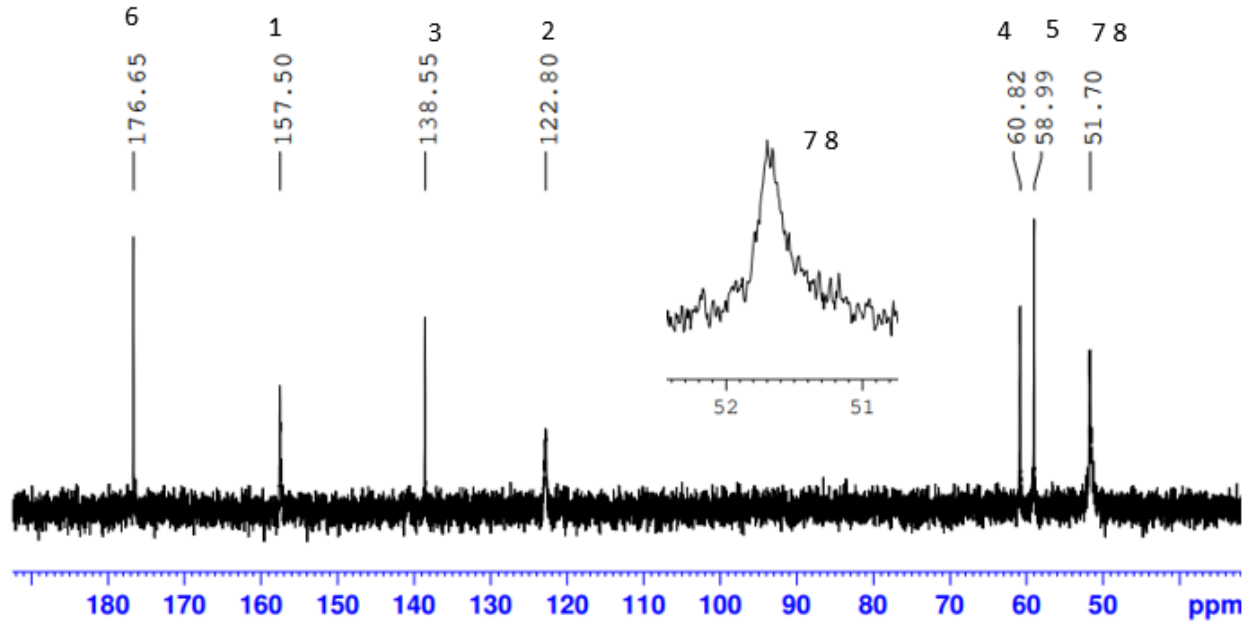

Figure A 28. *^{13}-C-NMR of **L16** in D_2O.*

Table A 24. Crystal data, intensity collections, and structure refinement parameters for **[μ-O(Fe^{3+}L4Cl)($Fe^{3+}Cl_3$)]** and **L3·2Cl·ClO_4**.

Complex	**[μ-O(Fe^{3+}L4Cl)($Fe^{3+}Cl_3$)]**	**L3·2Cl·ClO_4**
Formula	$C_{14}H_{24}Cl_4Fe_2N_4O$	$C_{11}H_{25}N_4Cl_3O_7$
M.W.	517.87	431.70
Unit cell	Monoclinic	Monoclinic
Space group	C2/c	P21/c
a (Å)	33.6834(15)	6.8884(14)
b (Å)	7.4237(3)	17.442(4)
c (Å)	19.0393(8)	14.703(3)
α	90°	90°
β	122.0280(10)°	95.42(3)
γ	90°	90°
Volume ($Å^3$)	4036.2(3)	1758.7(6)
Z	8	4
$D_{calc.}$(g/cm^3)	1.704	1.630
Reflections Collected	126139	5427
Independent Reflections	3991	5427
R_{int}	3.53	10.68
Completeness to θ	99.6%	99.5%
GooF	1.102	1.217
R1,wR2 [I>2sigma(I)]	R_1 = 0.0353 wR_2 = 0.0583	R_1 = 0.1068 wR_2 = 0.1142
R1, wR2	R_1 = 0.0495 wR_2 = 0.0625	R_1 =0.2942 wR_2 = 0.2942

Synthesis of **[μ-O(Fe^{3+}L4Cl)(FeCl$_3$)]**: Sodium perchlorate (24.7 mg, 0.201 mmol) was dissolved in 1.5 ml MeOH and was added to 53.8 mg (0.217 mmol) **L4**. Iron(III) chloride hexahydrate (58.3 mg, 0.216 mmol) was dissolved in 3 ml MeOH and added dropwise to ligand solution. Precipitate formed immediately, the solution was filter through celite and solvent was allowed to evaporate slowly affording yellow X-ray quality crystals. Yield 34% (19 mg, 0.037 mmol). ESI-MS$^+$ Cal(Found)= Parent ion not seen, [Fe^{3+}Me3P1-12(Cl)-(H$^+$)]$^+$ 338.096(338.1770), [Fe^{3+}Me3P1-12(2MeOH)-(2H$^+$)]$^+$ 366.1718(366.1732).

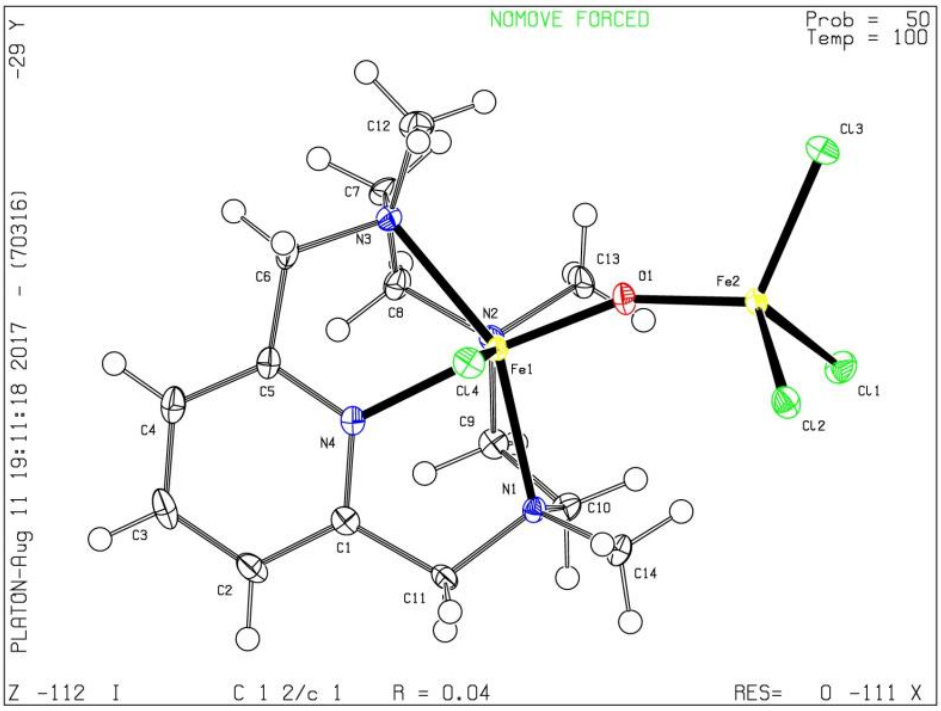

Figure A 30. *Solid-state structure of* ***[μ-O(Fe^{3+}L4Cl)(Fe^{3+}Cl$_3$)]***.

Table A 25. *Bond lengths for* ***[μ-O(Fe^{3+}L4Cl)(Fe^{3+}Cl$_3$)]****.*

Atom	Atom	Length/Å	Atom	Atom	Length/Å
C1	C2	1.384(4)	C11	N1	1.490(3)
C1	C11	1.502(4)	C12	N3	1.488(4)
C1	N4	1.334(3)	C13	N2	1.489(3)
C2	C3	1.383(4)	C14	N1	1.481(3)
C3	C4	1.389(4)	Cl1	Fe2	2.2465(8)
C4	C5	1.375(4)	Cl2	Fe2	2.2459(8)
C5	C6	1.499(4)	Cl3	Fe2	2.2238(8)
C5	N4	1.346(3)	Cl4	Fe1	2.3312(7)
C6	N3	1.492(3)	Fe1	N1	2.234(2)
C7	C8	1.513(4)	Fe1	N2	2.247(2)
C7	N3	1.490(3)	Fe1	N4	2.134(2)
C8	N2	1.485(3)	Fe1	N3	2.252(2)
C9	C10	1.510(4)	Fe1	O1	1.7948(18)
C9	N2	1.485(3)	Fe2	O1	1.7729(17)
C10	N1	1.491(3)			

Table A 26. *Bond angles* ***[μ-O(Fe^{3+}L4Cl)(Fe^{3+}Cl$_3$)]****.*

Atom	Atom	Atom	Angle/˚	Atom	Atom	Atom	Angle/˚
C2	C1	C11	123.6(2)	O1	Fe1	N3	108.39(8)
N4	C1	C2	121.5(2)	Cl2	Fe2	Cl1	107.77(3)
N4	C1	C11	114.8(2)	Cl3	Fe2	Cl1	107.77(3)
C3	C2	C1	118.5(3)	Cl3	Fe2	Cl2	107.56(3)
C2	C3	C4	119.7(3)	O1	Fe2	Cl1	109.47(7)
C5	C4	C3	118.8(3)	O1	Fe2	Cl2	110.33(6)
C4	C5	C6	123.9(2)	O1	Fe2	Cl3	113.73(7)
N4	C5	C4	121.2(3)	C10	N1	Fe1	105.58(15)
N4	C5	C6	114.8(2)	C11	N1	C10	110.6(2)
N3	C6	C5	112.1(2)	C11	N1	Fe1	111.44(15)
N3	C7	C8	111.8(2)	C14	N1	C10	108.7(2)
N2	C8	C7	109.1(2)	C14	N1	C11	108.3(2)
N2	C9	C10	109.5(2)	C14	N1	Fe1	112.17(16)
N1	C10	C9	110.8(2)	C8	N2	C13	109.2(2)
N1	C11	C1	112.7(2)	C8	N2	Fe1	108.37(16)
N1	Fe1	Cl4	100.95(6)	C9	N2	C8	111.7(2)
N1	Fe1	N2	80.23(8)	C9	N2	C13	108.9(2)
N1	Fe1	N3	145.93(8)	C9	N2	Fe1	107.51(15)
N2	Fe1	Cl4	168.77(6)	C13	N2	Fe1	111.15(16)
N2	Fe1	N3	78.49(8)	C1	N4	C5	120.3(2)
N4	Fe1	Cl4	85.37(6)	C1	N4	Fe1	121.11(17)
N4	Fe1	N1	75.51(8)	C5	N4	Fe1	118.58(18)
N4	Fe1	N2	84.13(8)	C6	N3	Fe1	106.86(15)
N4	Fe1	N3	76.11(8)	C7	N3	C6	110.7(2)
N3	Fe1	Cl4	95.14(6)	C7	N3	Fe1	109.44(15)
O1	Fe1	Cl4	97.55(6)	C12	N3	C6	107.7(2)
O1	Fe1	N1	99.07(8)	C12	N3	C7	108.5(2)
O1	Fe1	N2	93.26(8)	C12	N3	Fe1	113.58(16)
O1	Fe1	N4	174.29(9)	Fe2	O1	Fe1	155.49(11)

Synthesis of **L3·2Cl·ClO$_4$**: Ligand (**L3**) (110 mg, 0.332 mmol) was dissolved in 1 mL DI water. Iron(III) perchlorate (105 mg, 0.297 mmol) was dissolved in 5 mL methanol, the metal was added dropwise to the ligand. Slow evaporation of methanol yielded red X-ray quality crystals.

***Figure A 31**. X-ray quality crystals of **L3·2Cl·ClO$_4$**.*

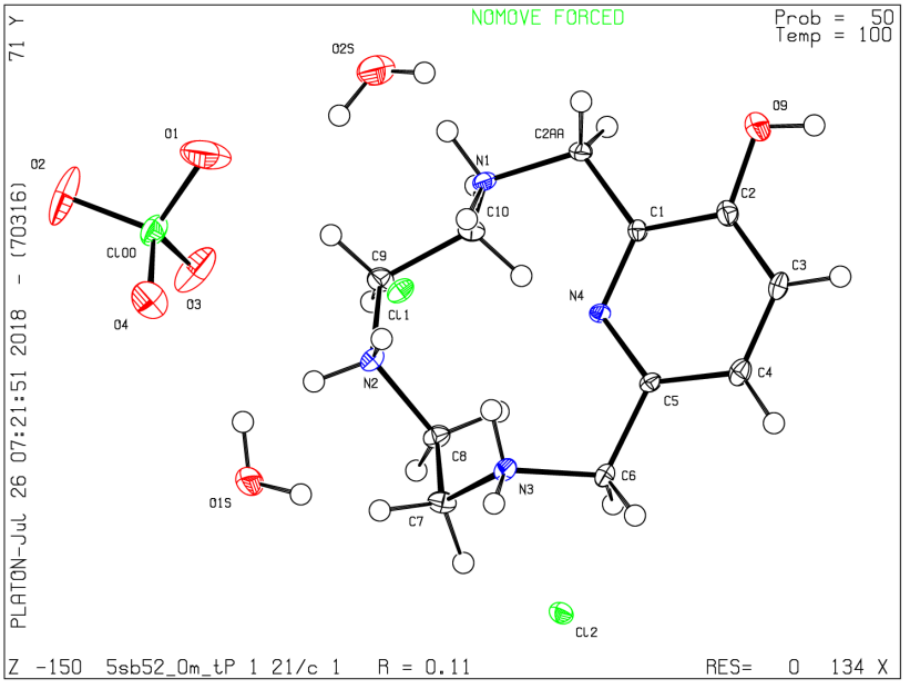

***Figure A 32.** Solid-state structure of **L3·2Cl·ClO$_4$**.*

Table A 27. *Bond lengths for* ***L3·2Cl·ClO$_4$.***

Atom	Atom	Length/Å	Atom	Atom	Length/Å
Cl00	O1	1.430(7)	C4	C3	1.378(9)
Cl00	O2	1.430(6)	C3	C2	1.379(9)
Cl00	O3	1.433(6)	C2	O9	1.337(8)
Cl00	O4	1.432(6)	C2	C1	1.394(8)
C8	C7	1.510(9)	N2	C9	1.498(8)
C8	N2	1.488(8)	C9	C10	1.507(9)
C7	N3	1.504(8)	C10	N1	1.486(8)
N3	C6	1.486(8)	N1	C2AA	1.487(8)
C6	C5	1.506(9)	C2AA	C1	1.500(8)
C5	C4	1.384(8)	C1	N4	1.325(8)
C5	N4	1.336(7)			

Table A 28*. Bond angles for* ***L3·2Cl·ClO$_4$.***

Atom	Atom	Atom	Angle/˚	Atom	Atom	Atom	Angle/˚
O2	Cl00	O1	106.8(5)	C2	C3	C4	119.6(6)
O3	Cl00	O1	112.5(5)	O9	C2	C3	124.5(6)
O3	Cl00	O2	110.3(4)	C1	C2	C3	118.3(6)
O4	Cl00	O1	108.2(4)	C1	C2	O9	117.2(6)
O4	Cl00	O2	110.9(4)	C9	N2	C8	115.0(5)
O4	Cl00	O3	108.0(4)	C10	C9	N2	113.9(5)
N2	C8	C7	111.7(5)	N1	C10	C9	112.6(5)
N3	C7	C8	113.2(5)	C2AA	N1	C10	113.8(5)
C6	N3	C7	115.5(5)	C1	C2AA	N1	110.5(5)
C5	C6	N3	112.4(5)	C2AA	C1	C2	118.7(5)
C4	C5	C6	121.0(5)	N4	C1	C2	122.7(6)
N4	C5	C6	115.6(5)	N4	C1	C2AA	118.6(5)
N4	C5	C4	123.3(6)	C1	N4	C5	118.2(5)
C3	C4	C5	117.9(6)				

References

1. Bedford, R. B. *Acc. Chem. Rev.* **2015,** *48*, 1485-1493.
2. Bedford, R. B.; Brenner, P. B., In *Iron catalysis ii. Topics in organometallic chemistry, vol 50.* , Bauer, E., Ed. Springer: Cham, 2015; Vol. 50, pp 19-46.
3. Dong, L.; Wen, J.; Qin, S.; Yang, N.; Yang, H.; Su, Z.; Yu, X.; Hu, C. *Acs Catal.* **2012,** *2*, 1829-1837.
4. Gustafson, K. P. J.; Guðmundsson, A.; Lewis, K.; Bäckvall, J.-E. *Chem. Eur. J.* **2017,** *23*, 1048-1051.
5. Ford, C. L.; Park, Y. J.; Matson, E. M.; Gordon, Z.; Fout, A. R. *Science* **2016,** *354*, 741-743.
6. Sun, C. L.; Li, B. J.; Shi, Z. J. *Chem. Rev.* **2011,** *111*, 1293-314.
7. He, Y.; Gorden, J. D.; Goldsmith, C. R. *Inorg. Chem.* **2011,** *50*, 12651-12660.
8. Bigi, M. A.; Reed, S. A.; White, M. C. *Nat. Chem.* **2011,** *3*, 216–222.
9. Chen, M. S.; White, M. C. *Science* **2010,** *327*, 566-71.
10. Sherry, B. D.; Furstner, A. *Acc. Chem. Rev.* **2008,** *41*, 1500-1511.
11. Tseberlidis, G.; Intrieri, D.; Caselli, A. *Eur. J. Inorg. Chem.* **2017**, 3589-3603.
12. Daifuku, S. L.; Al-Afyouni, M. H.; Snyder, B. E. R.; Kneebone, J. L.; Neidig, M. L. *J. Am. Chem. Soc.* **2014,** *136*, 9132-9143.
13. Daifuku, S. L.; Kneebone, J. L.; Snyder, B. E. R.; Neidig, M. L. *J. Am. Chem. Soc.* **2015,** *137*, 11432-11444.
14. Agata, R.; Iwamoto, T.; Nakagawa, N.; Isozaki, K.; Hatakeyama, T.; Takaya, H.; Nakamura, M. *Synthesis* **2015,** *47*, 1733-1740.
15. Bedford, R. B.; Brenner, P. B.; Elorriaga, D.; Harvey, J. N.; Nunn, J. *Dalton Trans.* **2016,** *45*, 15811-15817.
16. Bedford, R. B. *Nat. Chem.* **2016,** *8*, 904-905.
17. Serrano-Plana, J.; Oloo, W. N.; Acosta-Rueda, L.; Meier, K. K.; Verdejo, B.; García-España, E.; Basallote, M. G.; Münck, E.; Que, L.; Company, A.; Costas, M. *J. Am. Chem. Soc.* **2015,** *137*, 15833-15842.
18. Serrano-Plana, J.; Aguinaco, A.; Belda, R.; García-España, E.; Basallote, M. G.; Company, A.; Costas, M. *Angew. Chem. Ed. Int.* **2016,** *55*, 6310-6314.

19. Wen, J.; Qin, S.; Ma, L. F.; Dong, L. A.; Zhang, J.; Liu, S. S.; Duan, Y. S.; Chen, S. Y.; Hu, C. W.; Yu, X. Q. *Org. Lett.* **2010,** *12*, 2694-2697.

20. Costas, M.; Mehn, M. P.; Jensen, M. P.; Que, J., L *Chem. Rev.* **2004,** *104*, 939-986.

21. Ilies, L.; Nakamura, E., Iron-catalyzed c-h bond activation. In *C-h bond activation and catalytic functionalization ii*, Dixneuf, P. H.; Doucet, H., Eds. 2016; Vol. 56, pp 1-18.

22. Jia, F.; Li, Z. *Org. Chem. Front.* **2014,** *1*, 194-214.

23. Gamba, I.; Codolà, Z.; Lloret-Fillol, J.; Costas, M. *Coord. Chem. Rev.* **2017,** *334*, 2-24.

24. Jasniewski, A. J.; Que, L. *Chem. Rev.* **2018,** *118*, 2554-2592.

25. Oloo, W. N.; Que, L. *Acc. Chem. Rev.* **2015,** *48*, 2612-2621.

26. Shan, X. P.; Que, L. *J. Inorg. Biochem.* **2006,** *100*, 421-433.

27. Que, J. L. *J. Chem. Soc., Dalton Trans.* **1997**, 3933-3940.

28. Andris, E.; Navrátil, R.; Jašík, J.; Terencio, T.; Srnec, M.; Costas, M.; Roithová, J. *J. Am. Chem. Soc.* **2017,** *139*, 2757-2765.

29. Company, A.; Prat, I.; Frisch, J. R.; Mas-Balleste, R.; Guell, M.; Juhasz, G.; Ribas, X.; Munck, E.; Luis, J. M.; Que, L.; Costas, M. *Chem. Eur. J.* **2011,** *17*, 1622-1634.

30. Bou-Abdallah, F.; McNally, J.; Liu, X. X.; Melman, A. *Chem. Commun. (Camb)* **2011,** *47*, 731-3.

31. Hong, S.; Lee, Y. M.; Cho, K. B.; Seo, M. S.; Song, D.; Yoon, J.; Garcia-Serres, R.; Clemancey, M.; Ogura, T.; Shin, W.; Latour, J. M.; Nam, W. *Chem. Sci.* **2014,** *5*, 156-162.

32. Geiger, D. K. *J. Chem. Ed.* **1991,** *68*, 340.

33. Guengerich, F. P.; Yoshimoto, F. K. *Chem. Rev.* **2018**.

34. Barry, S. M.; Challis, G. L. *ACS Catal.* **2013,** *3*, 2362-2370.

35. Busch, D. H. *Acc. Chem. Rev.* **1978,** *11*, 392-400.

36. Bosnich, B.; Poon, C. K.; Tobe, M. L. *Inorg. Chem.* **1965,** *4*, 1102-1108.

37. Watkins, D. D.; Riley, D. P.; Stone, J. A.; Busch, D. H. *Inorg. Chem.* **1976,** *15*, 387-393.

38. Athey, P. S.; Kiefer, G. E. *J. Org. Chem.* **2002,** *67*, 4081-4085.

39. Constable, E. C., *Coordination chemistry of macrocyclic compounds*. Oxford University Press Inc.: New York, 1999.

40. Lindoy, L. M., *The chemistry of macrocyclic ligand complexes*. Cambridge University Press: Cambridge, UK,, 1989.

41. Meyer, K.; Bill, E.; Mienert; B.; Weyhermuller, T.; Wieghardt, K. *J. Am. Chem. Soc.* **1999,** *121*, 4859-4876.

42. Hubin, T. J.; McCormick, J. M.; Collinson, S. R.; Alcock, N. W.; Clase, H. J.; Busch, D. H. *Inorg. Chim. Acta* **2003,** *346*, 76-86.

43. Olivo, G.; Cussó, O.; Borrell, M.; Costas, M. *J. Biol. Inorg. Chem.* **2017,** *22*, 425-452.

44. Wang, Z.-Q.; Wang, Z.-C.; Zhan, S.; Ye, J.-S. *Appl. Catal., A* **2015,** *490*, 128-132.

45. Que, L. *J. Biol. Inorg. Chem.* **2004,** *9*, 684-690.

46. D., S. L.; Frank, N. *Angew. Chem. Ed. Int.* **2003,** *42*, 2942-2945.

47. Chen, G.; Chen, L.; Ng, S.-M.; Man, W.-L.; Lau, T.-C. *Angew. Chem. Ed. Int.* **2013,** *52*, 1789-1791.

48. Nam, W.; Ho, R.; Valentine, J. S. *J. Am. Chem. Soc.* **1991,** *113*, 7052-7054.

49. Feng, Y.; England, J.; Que, L. *ACS Catal.* **2011,** *1*, 1035-1042.

50. Rohde. J.; In, J.; Lim, M. H.; Brennessel, W. W.; Bukowski, M. R.; Stubna, A.; Munck, E.; Nam, W.; Que Jr., L. *Science* **2003,** *299*, 11037-1039.

51. Annaraj, J.; Suh, Y.; Seo, M. S.; Kim, S. O.; Nam, W. *Chem. Commun.* **2005**, 4529-4531.

52. Li, F.; England, J.; Que, L. *J. Am. Chem. Soc.* **2010,** *132*, 2134-2135.

53. Li, F.; Meier, K. K.; Cranswick, M. A.; Chakrabarti, M.; Van Heuvelen, K. M.; Münck, E.; Que, L. *J. Am. Chem. Soc.* **2011,** *133*, 7256-7259.

54. Ching, W.-M.; Zhou, A.; Klein, J. E. M. N.; Fan, R.; Knizia, G.; Cramer, C. J.; Guo, Y.; Que, L. *Inorg. Chem.* **2017,** *56*, 11129-11140.

55. Tan, P.; Kwong, H.-K.; Lau, T.-C. *Chem. Commun.* **2015,** *51*, 12189-12192.

56. Chow, T. W.-S.; Wong, E. L.-M.; Guo, Z.; Liu, Y.; Huang, J.-S.; Che, C.-M. *J. Am. Chem. Soc.* **2010,** *132*, 13229-13239.

57. To, W.-P.; Wai-Shan Chow, T.; Tse, C.-W.; Guan, X.; Huang, J.-S.; Che, C.-M. *Chem. Sci.* **2015,** *6*, 5891-5903.

58. Koch, W. O.; Krüger, H.-J. *Angew. Chem. Ed. Int. Engl.* **1996,** *34*, 2671-2674.

59. Shin, B.; Sutherlin, K. D.; Ohta, T.; Ogura, T.; Solomon, E. I.; Cho, J. *Inorg. Chem.* **2016,** *55*, 12391-12399.

60. Lee, G.; Oka, M.; Takemura, H.; Miyahara, Y.; Shimizu, N.; Inazu, T. *J. Org. Chem.* **1996,** *61*, 8304-8306.

61. Fronczek, F. R.; Mamo, A.; Pappalardo, S. *Inorg. Chem.* **1989,** *28*, 1419-1422.

62. Miyaura, N.; Suzuki, A. *J. Chem. Soc., Chem. Commun.* **1979**, 866-867.

63. Miyaura, N.; Yamada, K.; Suzuki, A. *Tetrahedron Lett.* **1979,** *20*, 3437-3440.

64. Guillaume, L.; Anny, J. *Chem. Eur. J.* **2014,** *20*, 4796-4805.

65. Wen, J.; Qin, S.; Ma, L.; Dong, L.; Zhang, J.; Liu, S.; Duan, Y.; Chem, S.; Hu, C.; Yu, X. *Org. Lett.* **2010,** *12*, 2694-2697.

66. Dean, S. A.; Peter, C.; E., L. R. *J. Magn. Reson. Imaging* **2009,** *30*, 1240-1248.

67. Viswanathan, S.; Kovacs, Z.; Green, K. N.; Ratnakar, S. J.; Sherry, A. D. *Chem. Rev.* **2010,** *110*, 2960-3018.

68. Dorazio, S. J.; Tsitovich, P. B.; Siters, K. E.; Spernyak, J. A.; Morrow, J. R. *J. Am. Chem. Soc.* **2011,** *133*, 14154-14156.

69. Dorazio, S. J.; Morrow, J. R. *Inorg. Chem.* **2012,** *51*, 7448-7450.

70. Dorazio, S. J.; Tsitovich, P. B.; Gardina, S. A.; Morrow, J. R. *J. Inorg. Biochem.* **2012,** *117*, 212-219.

71. Tsitovich, P. B.; Morrow, J. R. *Inorg. Chim. Acta* **2012,** *393*, 3-11.

72. Dorazio Sarina, J.; Morrow Janet, R. *Eur. J. Inorg. Chem.* **2012,** *2012*, 2006-2014.

73. Olatunde, A. O.; Cox, J. M.; Daddario, M. D.; Spernyak, J. A.; Benedict, J. B.; Morrow, J. R. *Inorg. Chem.* **2014,** *53*, 8311-8321.

74. Jeon, I.-R.; Park, J. G.; Haney, C. R.; Harris, T. D. *Chem. Sci.* **2014,** *5*, 2461-2465.

75. Olatunde Abiola, O.; Bond Christopher, J.; Dorazio Sarina, J.; Cox Jordan, M.; Benedict Jason, B.; Daddario Michael, D.; Spernyak Joseph, A.; Morrow Janet, R. *Chem. Eur. J.* **2015,** *21*, 18290-18300.

76. Doerwald, F. Z.; Dorwald, F. Z., Electrophilic arylation of arenes. In *Side reactions in organic synthesis ii: Aromatic substitutions*, Wiley-VCH Verlag GmbH & Co. KGaA: 2014; pp 61-84.

77. Gribble, G. W.; Fu, L.; Lin, Q.-X., Chapter 3 - attachment at ring positions a2 In *Pyridines: From lab to production*, Scriven, E. F. V., Ed. Academic Press: Oxford, 2013; pp 153-373.

78. Archibald, S. J., Macrocyclic coordination chemistry. In *Annual reports on the progress of chemistry, section a: Inorganic chemistry, vol 107*, Berry, F. J.; Hope, E. G., Eds. 2011; Vol. 107, pp 274-296.

79. Kleij, A. W.; Martinez-Rodriguez, L.; Fiorani, G.; Martin, C., Iron complex-based catalysts. In *Sustainable catalysis: With non-endangered metals, pt 1*, North, M., Ed. 2016; pp 373-406.

80. Maes, J.; Maes, B. U. W., A journey through metal-catalyzed c-h functionalization of heterocycles: Insights and trends. In *Heterocyclic chemistry in the 21st century: A tribute to alan katritzky, vol 120*, Scriven, E. F. V.; Ramsden, C. A., Eds. 2016; Vol. 120, pp 137-194.

81. Bai, Y.; Tang, L.; Huang, H.; Deng, G.-J. *Org. Biomol. Chem.* **2015,** *13*, 4404-4407.

82. Deb, A.; Manna, S.; Maji, A.; Dutta, U.; Maiti, D. *Eur. J. Org. Chem.* **2013,** *2013*, 5251-5256.

83. Du, W.; Zhao, M.-N.; Ren, Z.-H.; Wang, Y.-Y.; Guan, Z.-H. *Chem. Commun.* **2014,** *50*, 7437-7439.

84. Ehlers, P.; Petrosyan, A.; Baumgard, J.; Jopp, S.; Steinfeld, N.; Ghochikyan, T. V.; Saghyan, A. S.; Fischer, C.; Langer, P. *Chemcatchem* **2013,** *5*, 2504-2511.

85. Fier, P. S.; Hartwig, J. F. *J. Am. Chem. Soc.* **2014,** *136*, 10139-10147.

86. Figueira, C. A.; Lopes, P. S.; Gomes, P. T. *Tetrahedron* **2015,** *71*, 4362-4371.

87. Hachiya, H.; Hirano, K.; Satoh, T.; Miura, M. *Chemcatchem* **2010,** *2*, 1403-1406.

88. Hajipour, A. R.; Azizi, G. *Green Chem.* **2013,** *15*, 1030-1034.

89. Hilton, M. C.; Dolewski, R. D.; McNally, A. *J. Am. Chem. Soc.* **2016,** *138*, 13806-13809.

90. Hirano, K.; Miura, M. *J. Syn. Org. Chem. JPN.* **2011,** *69*, 252-265.

91. Hirano, K.; Miura, M. *Synlett* **2011**, 294-307.

92. Huang, G.; Sun, H.; Qiu, X.; Jin, C.; Lin, C.; Shen, Y.; Jiang, J.; Wang, L. *Org. Lett.* **2011,** *13*, 5224-5227.

93. Huang, Y.; Guan, D.; Wang, L. *Chin. J. Org. Chem.* **2014,** *32*, 1294-1298.

94. Hyodo, I.; Tobisu, M.; Chatani, N. *Chem. Asian J.* **2012,** *7*, 1357-1365.

95. Hyodo, I.; Tobisu, M.; Chatani, N. *Chem. Commun.* **2012,** *48*, 308-310.

96. Johnston, A. J. S.; Ling, K. B.; Sale, D.; Lebrasseur, N.; Larrosa, I. *Org. Lett.* **2016,** *18*, 6094-6097.

97. Kaewchangwat, N.; Sukato, R.; Vchirawongkwin, V.; Vilaivan, T.; Sukwattanasinitt, M.; Wacharasindhu, S. *Green Chem.* **2015,** *17*, 460-465.

98. Karadeniz, E.; Zora, M.; Kilicaslan, N. Z. *Tetrahedron* **2015,** *71*, 8943-8952.

99. Kocaoglu, E.; Karaman, M. A.; Tokgoz, H.; Talaz, O. *Acs Omega* **2017,** *2*, 5000-5004.

100. Koley, M.; Wimmer, L.; Schnuerch, M.; Mihovilovic, M. D. *J. Heterocycl. Chem.* **2013,** *50*, 1368-1373.

101. Komeyama, K.; Nagao, Y.; Abe, M.; Takaki, K. *Bull. Chem. Soc. Jpn.* **2014,** *87*, 301-313.

102. Leemans, E.; Colpaert, F.; Mangelinckx, S.; De Brabandere, S.; Denolf, B.; De Kimpe, N. *Synlett* **2011**, 674-678.

103. Li, J.; Liu, K.; Duan, X.; Liu, J. *Chin. J. Org. Chem.* **2017,** *37*, 314-334.

104. Li, X.; Wang, H.-Y.; Shi, Z.-J. *New J. Chem.* **2013,** *37*, 1704-1706.

105. Liu, B.; Guo, Q.; Cheng, Y.; Lan, J.; You, J. *Chem. Eur. J.* **2011,** *17*, 13415-13419.

106. Ma, Z.; Liu, H.; Zhang, C.; Zheng, X.; Yuan, M.; Fu, H.; Li, R.; Chena, H. *Adv. Synth. Catal.* **2015,** *357*, 1143-1148.

107. Maeda, H.; Fukui, A.; Yamakado, R.; Yasuda, N. *Chem. Commun.* **2015,** *51*, 17572-17575.

108. Marin-Hernandez, C.; Santos-Figueroa, L. E.; Moragues, M. E.; Raposo, M. M. M.; Batista, R. M. F.; Costa, S. P. G.; Pardo, T.; Martinez-Manez, R.; Sancenon, F. *J. Org. Chem.* **2014,** *79*, 10752-10761.

109. Midya, G. C.; Paladhi, S.; Dhara, K.; Dash, J. *Chem. Commun.* **2011,** *47*, 6698-6700.

110. Midya, G. C.; Parasar, B.; Dhara, K.; Dash, J. *Org. Biomol. Chem.* **2014,** *12*, 1812-1822.

111. Murakami, K.; Yamada, S.; Kaneda, T.; Itami, K. *Chem. Rev.* **2017,** *117*, 9302-9332.

112. Nakao, Y. *Synthesis-Stuttgart* **2011**, 3209-3219.

113. Nishimoto, Y.; Kondo, H.; Yamaguchi, K.; Yokogawa, D.; Yamaguchi, J.; Itami, K.; Irle, S. *J. Org. Chem.* **2017,** *82*, 4900-4906.

114. Pagar, V. V.; Liu, R.-S. *Org. Biomol. Chem.* **2015,** *13*, 6166-6169.

115. Pan, F.; Wang, H.; Shen, P.-X.; Zhao, J.; Shi, Z.-J. *Chem. Sci.* **2013,** *4*, 1573-1577.

116. Partyka, D. V. *Chem. Rev.* **2011,** *111*, 1529-1595.

117. Perumgani, P. C.; Parvathaneni, S. P.; Keesara, S.; Mandapati, M. R. *J. Organomet. Chem.* **2016,** *822*, 189-195.

118. Qian, Y. Y.; Wong, K. L.; Zhang, M. W.; Kwok, T. Y.; To, C. T.; Chan, K. S. *Tetrahedron Lett.* **2012,** *53*, 1571-1575.

119. Rao Batchu, V.; Romero-Estudillo, I.; Boto, A.; Miguelez, J. *Org. Biomol. Chem.* **2014,** *12*, 9547-9556.

120. Rossi, R.; Lessi, M.; Manzini, C.; Marianetti, G.; Bellina, F. *Adv. Synth. Catal.* **2015,** *357*, 3777-3814.

121. Shang, R.; Ilies, L.; Nakamura, E. *Chem. Rev.* **2017,** *117*, 9086-9139.

122. Shirakawa, E.; Nishikawa, R.; Uchiyama, N.; Hata, I.; Hayashi, T. *Chem. Lett.* **2013,** *42*, 269-271.

123. Singh, P. P.; Aithagani, S. K.; Yadav, M.; Singh, V. P.; Vishwakarma, R. A. *J. Org. Chem.* **2013,** *78*, 2639-2648.

124. Uchiyama, N.; Shirakawa, E.; Nishikawa, R.; Hayashi, T. *Chem. Commun.* **2011,** *47*, 11671-11673.

125. Vakuliuk, O.; Koszarna, B.; Gryko, D. T. *Adv. Synth. Catal.* **2011,** *353*, 925-930.

126. Wang, H. B.; Hu, Y.-L.; Li, D.-J. *J. Mol. Liq.* **2016,** *218*, 429-433.

127. Wang, H.-Y.; Mueller, D. S.; Sachwani, R. M.; Kapadia, R.; Londino, H. N.; Anderson, L. L. *J. Org. Chem.* **2011,** *76*, 3203-3221.

128. Wang, J.; Wang, S.; Wang, G.; Zhang, J.; Yu, X.-Q. *Chem. Commun.* **2012,** *48*, 11769-11771.

129. Wen, J.; Zhang, R.-Y.; Chen, S.-Y.; Zhang, J.; Yu, X.-Q. *J. Org. Chem.* **2012,** *77*, 766-771.

130. Xu, J.; Shao, L.-D.; Li, D.; Deng, X.; Liu, Y.-C.; Zhao, Q.-S.; Xia, C. *J. Am. Chem. Soc.* **2014,** *136*, 17962-17965.

131. Yagoubi, M.; Cruz, A. C. F.; Nichols, P. L.; Elliott, R. L.; Willis, M. C. *Angew. Chem. Ed. Int.* **2010,** *49*, 7958-7962.

132. Yamaguchi, K.; Kondo, H.; Yamaguchi, J.; Itami, K. *Chem. Sci.* **2013,** *4*, 3753-3757.

133. Yilmaz, U.; Deniz, S.; Kucukbay, H.; Sireci, N. *Molecules* **2013,** *18*, 3712-3724.

134. Yu, X.; Li, X.; Wan, B. *Org. Biomol. Chem.* **2012,** *10*, 7479-7482.

135. Zhang, B.; Zhou, Q.; Chen, R.; Jiang, H. *Chin. J. Org. Chem.* **2012,** *32*, 1653-1665.

136. Zhang, Q.; Li, C.; Yang, F.; Li, J.; Wu, Y. *Tetrahedron* **2013,** *69*, 320-326.

137. Zhang, Q.; Yang, F.; Wu, Y. *Chem. Commun.* **2013,** *49*, 6837-6839.

138. Zhu, T.; Li, X.; Chang, H.; Gao, W.; Wei, W. *Synlett* **2016,** *27*, 880-887.

139. Zhuo, F.-F.; Xie, W.-W.; Yang, Y.-X.; Zhang, L.; Wang, P.; Yuan, R.; Da, C.-S. *J. Org. Chem.* **2013,** *78*, 3243-3249.

140. Bauer, I.; Knoelker, H.-J. *Chem. Rev.* **2015,** *115*, 3170-3387.

141. Najafpour, M. M.; Safdari, R.; Ebrahimi, F.; Rafighi, P.; Bagheri, R. *Dalton Trans.* **2016,** *45*, 2618-2623.

142. Raffard, N.; Carina, R.; Simaan, A. J.; Sainton, J.; Riviere, E.; Tchertanov, L.; Bourcier, S.; Bouchoux, G.; Delroisse, M.; Banse, F.; Girerd, J. J. *Eur. J. Inorg. Chem.* **2001**, 2249-2254.

143. Lincoln, K. M.; Offutt, M. E.; Hayden, T. D.; Saunders, R. E.; Green, K. N. *Inorg. Chem.* **2014,** *53*, 1406-1416.

144. Lincoln, K. M.; Arroyo - Currás, N.; Johnston, H. M.; Hayden, T. D.; Pierce, B. S.; Bhuvanesh, N.; Green, K. N. *J. Coord. Chem.* **2015,** *68*, 2810-2826.

145. Lincoln, K. M.; Gonzalez, P.; Richardson, T. E.; Julovich, D. A.; Saunders, R.; Simpkins, J. W.; Green, K. N. *Chem. Commun.* **2013,** *49*, 2712-2714.

146. Alcock, N. W.; Busch, D. H.; Liu, C. Y. *Private Communication* **2007**, CCDC: 639154.

147. McClain Ii, J. M.; Maples, D. L.; Maples, R. D.; Matz, D. L.; Harris, S. M.; Nelson, A. D. L.; Silversides, J. D.; Archibald, S. J.; Hubin, T. J. *Acta. Cryst. C.* **2006,** *62*, m553-m555.

148. Koch, W. O.; Schünemann, V.; Gerdan, M.; Trautwein, A. X.; Krüger, H. *Chem. Eur. J.* **1998,** *4*, 686-691.

149. Shannon, R. D. *Acta. Cryst. A.* **1976,** *32*, 751-767.

150. Koch, W. O.; Barbieri, A.; Grodzicki, M.; Schunemann, V.; Trautwein, A. X.; Kruger, H. J. *Angew. Chem. Ed. Int. Engl.* **1996,** *35*, 422-424.

151. Bard, A.; Faulkerner, L. R., *Electrochemical methods: Fundamentals and applications*. John Wiley & Sons, Inc.: Hoboken, NJ, 2001.

152. Jones, D. G.; Wilson, K. R.; Cannon-Smith, D. J.; Shircliff, A. D.; Zhang, Z.; Chen, Z.; Prior, T. J.; Yin, G.; Hubin, T. J. *Inorg. Chem.* **2015,** *54*, 2221-2234.

153. Hua, W. S.; Ajiboye, S. I.; Haining, G.; Mcghee, L.; Peacock, R. D.; Peattie, G.; Siddique, R. M.; Winfield, J. M. *J. Chem. Soc., Dalton Trans.* **1995**, 3837-3841.

154. Fulmer, G. R.; Miller, A. J. M.; Sherden, N. H.; Gottlieb, H. E.; Nudelman, A.; Stoltz, B. M.; Bercaw, J. E.; Goldberg, K. I. *Organometallics* **2010,** *29*, 2176-2179.

155. Ferraudi, F. *Inorg. Chem.* **1980,** *19*, 438-444.

156. Wakelin, L. P. G.; Bu, X.; Eleftheriou, A.; Parmar, A.; Hayek, C.; Stewart, B. W. *J. Med. Chem.* **2003,** *46*, 5790-5802.

157. Rakowski, M. C.; Wycheck, M.; Busch, D. H. *Inorg. Chem.* **1975,** *14*, 1194-2000.

158. Kalman, F. K.; Vegh, A.; Regueiro-Figueroa, M.; Toth, E.; Platas-Iglesias, C.; Tircso, G. *Inorg. Chem.* **2015,** *54*, 2345-2356.

159. de Sa, A.; Bonnet, C. S.; Geraldes, C. F. G. C.; Toth, E.; Ferreira, P. M. T.; Andre, J. P. *Dalton Trans.* **2013,** *42*, 4522-4532.

160. Nelson, S. M.; Busch, D. H. *Inorg. Chem.* **1969,** *8*, 1859-1863.

161. Hodgkinson, L. C.; Johnson, M. R.; Leigh, S. J.; Spencer, N.; Sutherland, I. O.; Newton, R. F. *J. Chem. Soc., Perkin Trans. 1* **1979**, 2193-2202.

162. Solutions., B. A. X.-R.; APEX2 *(Version 2014.9-0)*, Bruker AXS Inc., Madison, WI (2007).

163. Solutions., B. A. X.-R.; XSHELL *(Version 6.3.1)*, Bruker AXS Inc., Madison, WI (2004).

164. Abragam, A.; Bleaney, B., *Electron paramagnetic resonance of transition ions* 1970; p 912 pp.

165. Hubin, T. J.; McCormick, J. M.; Alcock, N. W.; Busch, D. H. *Inorg. Chem.* **2001,** *40*, 435-444.

166. Goedken, V. L.; Busch, D. H. *J. Am. Chem. Soc.* **1972,** *94*, 7355-7363.

167. Yin, G. C. *Coord. Chem. Rev.* **2010,** *254*, 1826-1842.

168. Hubin, T. J.; McCormick, J. M.; Collinson, S. R.; Buchalova, M.; Perkins, C. M.; Alcock, N. W.; Kahol, P. K.; Raghunathan, A.; Busch, D. H. *J. Am. Chem. Soc.* **2000,** *122*, 2512-2522.

169. Brewer, S. M.; Palacios, P. M.; Johnston, H. M.; Pierce, B. S.; Green, K. N. *Inorg. Chim. Acta* **2018,** *478*, 139-147.

170. Weisman, G. R.; Rogers, M. E.; Wong, E. H.; Jasinski, J. P.; Paight, E. S. *J. Am. Chem. Soc.* **1990,** *112*, 8604-8605.

171. Bazzicalupi, C.; Bencini, A.; Bianchi, A.; Ciampolini, M.; Fusi, V.; Micheloni, M.; Nardi, N.; Paoli, P.; Valtancoli, B. *Supramol. Chem.* **1994,** *3*, 279-290.

172. Wilson, K. R.; Cannon-Smith, D. J.; Burke, B. P.; Birdsong, O. C.; Archibald, S. J.; Hubin, T. J. *Polyhedron* **2016,** *114*, 118-127.

173. Chen, M. S.; White, C. W. *Science* **2007,** *318*, 783-787.

174. Lyakin, O. Y.; Ottenbacher, R. V.; Bryliakov, K. P.; Talsi, E. P. *ACS Catal.* **2012,** *2*, 1196-1202.

175. Sink, R. M.; Buster, D. C.; Sherry, A. D. *Inorg. Chem.* **1990,** *29*, 3645-3649.

176. Collinson, S.; Alcock, N. W.; Raghunathan, A.; Kahol, P. K.; Busch, D. H. *Inorg. Chem.* **2000,** *39*, 757-764.

177. Pulukkody, R.; Kyran, S. J.; Drummond, M. J.; Hseigh, C.-H.; Darensbourg, D. J.; Darensbourg, M. Y. *Chem. Sci.* **2014,** *5*, 3795-3802.

178. Green, K. N.; Jeffery, S. P.; Reibenspies, J. H.; Darensbourg, M. Y. *J. Am. Chem. Soc.* **2006,** *128*, 6493-6498.

179. Green, K. N.; Brothers, S. M.; Thomas, C. W.; Darensbourg, M. Y. *Abstr. Pap. Am. Chem. Soc.* **2007,** *233*, 698-698.

180. Voet, D.; Voet, J. G.; Pratt, C. W., *Fundamentals of biochemistry : Life at the molecular level*. 2nd ed.; Wiley: Hoboken, N.J., 2006.

181. Crabtree, R. H. *Science* **1994,** *266*, 1591-1592.

182. *Concepts and models in bioinorganic chemistry*. Wiley-VCH: Weinheim, 2006.

183. Rothenberg, G., *Catalysis—concepts and green applications* 2ed.; Wiley-VCH: Weineim, Germany 2017; p 65.

184. Busch, D. H., Metals and enzymes - multiple juxtopositional fixedness. *Chem. Eng. News* 1970, p 9.

185. Funwie, N. L.; Cain, A. N.; Fanning, B. Z.; Hageman, S. A.; Mullens, M.; Roberts, T. K.; Turner, D. J.; Valdez, C. N.; Vaughan, R. W.; Ermias, H. G.; Silversides, J. D.; Archibald, S. J.; Hubin, T. J.; Prior, T. J. *Acta. Cryst. E.* **2015,** *71*, 1073-1076.

186. Addison, A. W.; Rao, T. N.; Reedijk, J.; Vanrijn, J.; Verschoor, G. C. *J. Chem. Soc., Dalton Trans.* **1984**, 1349-1356.

187. Amoyaw, P. N. A.; Pham, K.; Cain, A. N.; McClain, J. M.; Hubin, T. J.; Khan, M. O. F. *Curr. Org. Syn.* **2014,** *11*, 916-921.

188. Royal, G.; Dahaoui-Gindrey, V.; Dahaoui, S.; Tabard, A.; Guilard, R.; Pullumbi, P.; Lecomte, C. *Eur. J. Org. Chem.* **1998**, 1971-1975.

189. Sheldrick, G. M. *Acta. Cryst. A.* **2015,** *71*, 3-8.

190. Dolomanov, O. V. B., L.J.; Gildea, R.J.; Howard, J.A.K.; Puschmann, H. *J. Appl. Cryst.* **2009,** *42*, 339-341.

191. Spek, A. *Acta. Cryst. D.* **2009,** *65*, 148-155.

192. Howard, J. K.; Rihak, K. J.; Bissember, A. C.; Smith, J. A. *Chem. Asian J.* **2016,** *11*, 155-167.

193. Choudhury, A. R.; Mukherjee, S. *Org. Biomol. Chem.* **2012,** *10*, 7313-7320.

194. Feig, A. L.; Lippard, S. J. *Chem. Rev.* **1994,** *94*, 759-805.

195. Du Bois, J.; Mizoguchi, T. J.; Lippard, S. J. *Coord. Chem. Rev.* **2000,** *200-202*, 443-485.

196. Patel, R.; Patel, N. *J. Adv. Pharm. Edu. & Res.* **2011,** *1*, 52-68.

197. Thaipong, K.; Boonprakob, U.; Crosby, K.; Cisneros-Zevallos, L.; Byrne, D. H. *J. Food Compost. Anal.* **2006,** *19*, 669-675.

198. Mensor, L. L.; Menezes, F. S.; Leitao, G. G.; Reis, A. S.; dos Santos, T. C.; Coube, C. S.; Leitao, S. G. *Phytothe. Res.* **2001,** *15*, 127-130.

199. Lincoln, K. M.; Gonzalez, P.; Richardson, T. E.; Rutter, L.; Julovich, D. A.; Simpkins, J. W.; Green, K. N. *Chem. Commun.* **2013,** *49*, 2712-2714.

200. Lincoln, K. M.; Richardson, T. E.; Rutter, L.; Gonzalez, P.; Simpkins, J. W.; Green, K. N. *ACS. Chem. Neurosci.* **2012,** *11*, 919-927.

201. Balamurugan, M.; Suresh, E.; Palaniandavar, M. *Dalton Trans.* **2016,** *45*, 11422-11436.

202. Balogh-Hergovich, E.; Speier, G.; Reglier, M.; Giorgi, M.; Kuzmann, E.; Vertes, A. *Eur. J. Inorg. Chem.* **2003**, 1735-1740.

203. Baranwal, B. P.; Das, S. S.; Gupta, T.; Singh, A. K. *Prog. Cryst. Growth & Charact.* **2002,** *45*, 147-153.

204. Bhattacharyya, J.; Das, S.; Mukhopadhyay, S. *Dalton Trans.* **2007**, 1214-1220.

205. Bhattacharyya, J.; Mukhopadhyay, S. *Transition Met. Chem.* **2006,** *31*, 256-261.

206. Chaudhuri, B.; Banerjee, R. *Can. J. Chem.* **1998,** *76*, 350-355.

207. Comba, P.; Gahan, L. R.; Hanson, G. R.; Mereacre, V.; Noble, C. J.; Powell, A. K.; Prisecaru, I.; Schenk, G.; Zajaczkowski-Fischer, M. *Chem. Eur. J.* **2012,** *18*, 1700-1710.

208. Cranswick, M. A.; Meier, K. K.; Shan, X.; Stubna, A.; Kaizer, J.; Mehn, M. P.; Muenck, E.; Que, L., Jr. *Inorg. Chem.* **2012,** *51*, 10417-10426.

209. Das, S.; Bhattacharyya, J.; Mukhopadhyay, S. *Dalton Trans.* **2008**, 6634-6640.

210. Friedle, S.; Kodanko, J. J.; Morys, A. J.; Hayashi, T.; Moenne-Loccoz, P.; Lippard, S. J. *J. Am. Chem. Soc.* **2009,** *131*, 14508-14520.

211. Hazell, A.; Jensen, K. B.; McKenzie, C. J.; Toftlund, H. *Inorg. Chem.* **1994,** *33*, 3127-3134.

212. Ito, S.; Okuno, T.; Itoh, H.; Ohba, S.; Matsushima, H.; Tokii, T.; Nishida, Y. *Z. Naturforsch. B.* **1997,** *52*, 719-727.

213. Ito, S.; Okuno, T.; Matsushima, H.; Tokii, T.; Nishida, Y. *J. Chem. Soc., Dalton Trans.* **1996**, 4479-4484.

214. Ito, S.; Sasaki, Y.; Takahashi, Y.; Ohba, S.; Nishida, Y. *Z. Naturforsch. C.* **1999,** *54*, 554-561.

215. Jozwiuk, A.; Ingram, A. L.; Powell, D. R.; Moubaraki, B.; Chilton, N. F.; Murray, K. S.; Houser, R. P. *Dalton Trans.* **2014,** *43*, 9740-9753.

216. Kejriwal, A.; Bandyopadhyay, P.; Biswas, A. N. *Dalton Trans.* **2015,** *44*, 17261-17267.

217. Kejriwal, A.; Biswas, A. N.; Choudhury, A.; Bandyopadhyay, P. *Transition Met. Chem.* **2014,** *39*, 909-915.

218. Kejriwal, A.; Biswas, S.; Biswas, A. N.; Bandyopadhyay, P. *J. Mol. Catal. A: Chem.* **2016,** *413*, 77-84.

219. Kumbhar, A. S.; Damle, S. G.; Dasgupta, S. T.; Rane, S. Y.; Kumbhar, A. S. *J. Chem. Res.* **1999**, 98-99.

220. Liu, C. L.; Yu, S. W.; Li, D. F.; Liao, Z. R.; Sun, X. H.; Xu, H. B. *Inorg. Chem.* **2002,** *41*, 913-922.

221. Mandal, P. C.; Bhattacharyya, J.; Das, S.; Mukhopadhyay, S.; Kirschenbaum, L. J. *Polyhedron* **2009,** *28*, 3162-3168.

222. Mayilmurugan, R.; Stoeckli-Evans, H.; Suresh, E.; Palaniandavar, M. *Dalton Trans.* **2009**, 5101-5114.

223. Menage, S.; Vincent, J. M.; Lambeaux, C.; Chottard, G.; Grand, A.; Fontecave, M. *Inorg. Chem.* **1993,** *32*, 4766-4773.

224. Menage, S.; Vincent, J. M.; Lambeaux, C.; Fontecave, M. *J. Chem. Soc., Dalton Trans.* **1994**, 2081-2084.

225. Menage, S.; Vincent, J. M.; Lambeaux, C.; Fontecave, M. *J. Mol. Catal. A: Chem.* **1996,** *113*, 61-75.

226. Nayak, S.; Dash, A. C. *Transition Met. Chem.* **2006,** *31*, 813-828.

227. Okuno, T.; Ito, S.; Ohba, S.; Nishida, Y. *J. Chem. Soc., Dalton Trans.* **1997**, 3547-3551.

228. Pardo, E.; Lloret, F.; Carrasco, R.; Munoz, M. C.; Temporal-Sanchez, T.; Ruiz-Garcia, R. *Inorg. Chim. Acta* **2004,** *357*, 2713-2720.

229. Payra, P.; Hung, S. C.; Kwok, W. H.; Johnston, D.; Gallucci, J.; Chan, M. K. *Inorg. Chem.* **2001,** *40*, 4036-4039.

230. Roy, M.; Bhowmick, T.; Santhanagopal, R.; Ramakumar, S.; Chakravarty, A. R. *Dalton Trans.* **2009**, 4671-4682.

231. Taktak, S.; Kryatov, S. V.; Haas, T. E.; Rybak-Akimova, E. V. *J. Mol. Catal. A: Chem.* **2006,** *259*, 24-34.

232. Tanase, S.; Foltz, C.; de Gelder, R.; Hage, R.; Bouwman, E.; Reedijk, J. *J. Mol. Catal. A: Chem.* **2005,** *225*, 161-167.

233. Visvaganesan, K.; Suresh, E.; Palaniandavar, M. *Dalton Trans.* **2009**, 3814-3823.

234. Wang, J.; Jian, F.; Zhuang, R.; Qiao, Y. *Synth. React. Inorg. Met. Org. Chem.* **2012,** *42*, 711-715.

235. Wasser, I. M.; Fry, H. C.; Hoertz, P. G.; Meyer, G. J.; Karlin, K. D. *Inorg. Chem.* **2004,** *43*, 8272-8281.

236. Fleischer, E. B.; Srivastava, T. S. *J. Am. Chem. Soc.* **1969,** *91*, 2403-2405.

237. Shakya, R.; Powell, D. R.; Houser, R. P. *Eur. J. Inorg. Chem.* **2009,** *2009*, 5319-5327.

238. Kurtz, D. M. *Chem. Rev.* **1990,** *90*, 585-606.

239. Chanda, A.; Popescu, D.-L.; de Oliveira, F. T.; Bominaar, E. L.; Ryabov, A. D.; Münck, E.; Collins, T. J. *J. Inorg. Biochem.* **2006,** *100*, 606-619.

240. Bigelow, J. O.; England, J.; Klein, J. E. M. N.; Farquhar, E. R.; Frisch, J. R.; Martinho, M.; Mandal, D.; Münck, E.; Shaik, S.; Que, L. *Inorg. Chem.* **2017,** *56*, 3287-3301.

241. England, J.; Guo, Y.; Farquhar, E. R.; Young Jr, V. G.; Münck, E.; Que Jr, L. *J. Am. Chem. Soc.* **2010,** *132*, 8635-8644.

242. Norman, R. E.; Holz, R. C.; Menage, S.; Que, L.; Zhang, J. H.; O'Connor, C. J. *Inorg. Chem.* **1990,** *29*, 4629-4637.

243. Blackmond, D. G. *J. Am. Chem. Soc.* **2015,** *137*, 10852-10866.

244. Morrow, J. R.; Tóth, É. *Inorg. Chem.* **2017,** *56*, 6029-6034.

245. Green, K. N.; Viswanathan, S.; Rojas-Quijano, F. A.; Kovacs, Z.; Sherry, A. D. *Inorg. Chem.* **2011,** *50*, 1648-1655.

246. Shahid, A.; R., M. J.; H., L. C.; Rowen, C. M. *Angew. Chem. Ed. Int. Engl.* **1994,** *33*, 773-775.

247. Tsitovich, P. B.; Cox, J. M.; Benedict, J. B.; Morrow, J. R. *Inorg. Chem.* **2016,** *55*, 700-716.

248. Tsitovich, P. B.; Cox, J. M.; Spernyak, J. A.; Morrow, J. R. *Inorg. Chem.* **2016,** *55*, 12001-12010.

249. Tsitovich, P. B.; Tittiris, T. Y.; Cox, J. M.; Benedict, J. B.; Morrow, J. R. *Dalton Trans.* **2018,** *47*, 916-924.

250. Thorarinsdottir, A. E.; Gaudette, A. I.; Harris, T. D. *Chem. Sci.* **2017,** *8*, 2448-2456.

251. Aime, S.; Botta, M.; Crich, S. G.; Giovenzana, G. B.; Jommi, G.; Pagliarin, R.; Sisti, M. *J. Chem. Soc., Chem. Commun.* **1995**, 1885-1886.

252. Chin, K. O. A.; Morrow, J. R.; Lake, C. H.; Churchill, M. R. *Inorg. Chem.* **1994,** *33*, 656-664.

253. Aime, S.; Botta, M.; Geninatti Crich, S.; Giovenzana, G. B.; Jommi, G.; Pagliarin, R.; Sisti, M. *Inorg. Chem.* **1997,** *36*, 2992-3000.

254. Brewer, S. M.; Wilson, K. R.; Jones, D. G.; Reinheimer, E. W.; Archibald, S. J.; Prior, T. J.; Ayala, M. A.; Foster, A. L.; Hubin, T. J.; Green, K. N. *Inorg. Chem.* **2018**.

255. Delgado, R.; Quintino, S.; Teixeira, M.; Zhang, A. *J. Chem. Soc., Dalton Trans.* **1997**, 55-64.

256. Stetter, H.; Frank, W.; Mertens, R. *Tetrahedron* **1981,** *37*, 767-772.

257. Prodi, L.; Maestri, M.; Ziessel, R.; Balzani, V. *Inorg. Chem.* **1991,** *30*, 3798-3802.

258. Siaugue, J.-M.; Segat-Dioury, F.; Favre-Réguillon, A.; Madic, C.; Foos, J.; Guy, A. *Tetrahedron Lett.* **2000,** *41*, 7443-7446.

259. Adkins, H.; Kuick, L. F.; Farlow, M.; Wojcik, B. *J. Am. Chem. Soc.* **1934,** *56*, 2425-2428.

260. Skomoroski, R. M.; Schriesheim, A. *J. Phys. Chem.* **1961,** *65*, 1340-1343.

261. Ferroud, C.; Borderies, H.; Lasri, E.; Guy, A.; Port, M. *Tetrahedron Lett.* **2008,** *49*, 5972-5975.

262. Dicke, J. W.; Stibrich, N. J.; Schaefer, H. F. *Chem. Phys. Lett.* **2008,** *456*, 13-18.

263. Hoffmann, R.; Beier, B. F.; Muetterties, E. L.; Rossi, A. R. *Inorg. Chem.* **1977,** *16*, 511-522.

264. Bulhac, I.; Deseatnic-Ciloci, A.; Bourosh, P.; Tiurina, J.; Bologa, O.; Bivol, C.; Clapco, S.; Verejan, A.; Labliuc, S.; Danilescu, O. *Chem. J. Mold.* **2016,** *11*, 39-49.

265. Soo, H. S.; Sougrati, M. T.; Grandjean, F.; Long, G. J.; Chang, C. J. *Inorg. Chim. Acta* **2011,** *369*, 82-91.

266. Dumrath, A.; Lubbe, C.; Beller, M., *Palladium-catalyzed coupling reactions : Practical aspects and future developments*. John Wiley & Sons: Weinheim. Germany 2013.

VITA

Personal Background	Naples, Florida Daughter of Laurie Downey and David Brewer Married Charles Ochoa, November 28, 2015
Education	Diploma, C. F. Brewer High School, White Settlement, Texas, 2006 Associate of Arts, Tarrant County Community College, Fort Worth, Texas, 2008 Bachelor of Science, Chemistry, University of North Texas, Denton, Texas, 2012 Doctor of Philosophy, Chemistry, Texas Christian University, Fort Worth, Texas, 2018
Experience	NSF-REU Fellow, Teas A&M University, College Station, Texas, May - August 2011 TCU Ida Green Fellow, Texas Christian University, Fort Worth, Texas, 2012-2013 Teaching Assistant, Texas Christian University, Fort Worth, Texas, 2013-2018 Departmental Tutor Texas Christian University, Fort Worth, Texas, 2013-2018
Professional Memberships	American Chemical Society

Abstract

SYNTHESIS AND APPLICATIONS OF HIGH-SPIN IRON TETRA-AZAMACROCYCLIC COMPLEXES

By Samantha Brewer Ochoa, Ph.D., 2018
Department of Chemistry and Biochemistry
Texas Christian University

Dissertation Advisor: Kayla N. Green, Associate Professor of Chemistry

Herein we describe the synthesis, charcterization, and role of several iron complexes in the coupling of pyrrole and phenylboronic acid to form 2-phenylpyrrole. The oxidation state and spin state of the iron complexes were characterized using X-ray crystallography, UV-vis absorbance spectroscopy, cyclic voltammetry, and in some cases electron paramagnetic reasonance spectroscopy. Furthermore, the results indicate that the iron(III) complexes are essential for catalytic and regioselective production of the 2-phenylpyrrole product. The complexes were compared to evaluate the effect of five properties on catalyst reaction yields: the coordination requirements of the catalyst, half-potential, topological constraint/rigidity, N-atom modification(s), increasing oxidative stability of the complex, and geometric parameters. The need for two labile *cis*-coordination sites was confirmed based on a 42% decrease in catalytic reaction yield observed when complexes containing penta-dentate ligands were used in place of complexes with tetra-dentate ligands. A strong correlation between iron(III/II) redox potential and catalytic reaction yields was also observed, with **$[Fe^{2+}L6(Cl)_2]$** providing the highest yield (81%, -405 mV). A Lorentzian fitting of redox potential versus yields predicts that these catalysts can undergo more fine tuning to further increase yields. Interestingly, the remaining properties explored did not show a direct, strong relationship to catalytic reaction yields. Furthermore, the role of the sacrificial oxidant, the lack of radical participation, and the formation of μ-oxodiiron species was established leading to a more detailed mechanistic cycle. Finally, a library of five pyclen-based ligands have been developed for use as iron and europium chelators. A preliminary investigation into iron PCTA complexes indicate that the iron center can bind to all seven of the ligand donors, however, the iron complex does not afford a CEST

signal. Establishing that heptadentate ligands containing carboxylic acid pendent arms are not ideal for the developments of iron PARACEST agents.